2016

Strong and selective biomimetic receptors for water-soluble guests through cooperative enhancement and molecular imprinting

Roshan Wajira Gunasekara
Iowa State University

Strong and selective biomimetic receptors for water-soluble guests through cooperative enhancement and molecular imprinting

by

Roshan W. Gunasekara

A dissertation submitted to the graduate faculty

in partial fulfillment of the requirements for the degree of

DOCTOR OF PHILOSOPHY

Major: Organic Chemistry

Program of Study Committee:

Yan Zhao, Major Professor
Aaron D. Sadow
Javier Vela-Becerra
Brett VanVeller
Keith Woo

Iowa State University

Ames, Iowa

2016

TABLE OF CONTENTS

ACKNOWLEDGMENTS

I would like to express the deepest gratitude to my research advisor, Dr. Yan Zhao, for his excellent guidance, support, patience, and wisdom throughout my research work. Without him, this dissertation would not be possible.

I would also like to thank my program of study committee members, Dr. Keith Woo, Dr. Aaron Sadow, Dr. Javier Vela-Becerra, and Dr. Brett VanVeller for their continuous support in my study. Dr. Mei Hong deserves a special thanks for her commitment to serve as my past committee member. They all have dedicated their time to give me advice and useful ideas over the years.

I am thankful to the department of chemistry, Iowa State University, Frank J. Moore and Thoreen Beth Moore Fellowship Award, Alpha Chi Sigma Research Award, National Science Foundation (NSF), and National Institute of Health (NIH) for providing financial support for the research/course work that I have completed. Special appreciation to the members of the chemical instrumentation facility including Dr. Sarah Cady, Dr. Shu Xu, Dr. Kamel Harrata, and Mr. Steve Veysey for their technical assistance to my research.

I wish to thank members of the Yan Zhao group for collaborations, enlightening discussions, support, and for having a pleasant environment in the research laboratory.

Finally, I would extend my humble gratitude for my loving and caring family–my father Somapala Gunasekara, my mother Dayanthi Gunasekara, my brother Chaminda Gunasekara, my wife Roshini Kandawela, and the rest of the family, relatives, and my friends. They all encouraged me and given continuous moral support for my studies.

CHAPTER 1

GENERAL INTRODUCTION

Literature Review

Molecular recognition is a well-documented concept that exhibits host-guest complex formation by exploiting non-covalent interactions.[1] These interactions are mostly from direct binding forces. However, indirect interactions also contribute to the binding. The indirect driving force might come from either altered interactions within the host or guest.[2]

Biological receptors have unparalleled abilities to recognize specific molecules in a competitive aqueous solution. Biotin-streptavidin complex is among the best known examples of molecular recognition in biology. The complex formation interestingly increases the protein's melting point by 37 °C and numerous backbone amide protons of the protein become resistant to H/D exchange. Certainly the binding has tightened the protein host and those indirect and direct interactions together produce an astonishing affinity of $K_a = 10^{13.4}$ M^{-1} in water.[3,4]

Chemists indeed have obtained high binding affinities using the preorganization concept.[5-8] The preorganization reflects the idea of lock-key model in biology.[9] The model has played an important role in developing synthetic host-guest complexes in supramolecular chemistry.[10] However, Williams and co-workers postulated an alternative strategy in which the host-guest interactions can be delocalized over the entire structure instead of being confined at the interface.[11] By combining the two methods, chemists have developed cooperatively enhanced receptors (CERs) to mimic the biological ligands.[12-16] So far, reported CERs appeared to come from accidental discovery rather than by designs, and generally have poor solubility in water. Herein we report a rational design of CERs that

function in water to recognize aromatic amines and citric acid. The key design of our receptors is that the intra-host interactions disengaged prior to binding. The weak host-guest (i.e. carboxylate-ammonium and guanidinium-citrate) direct interactions eliminated the repulsion at the interface to promote intra-host indirect interactions to strengthen the overall binding.

Lectins are a specific class of proteins that bind carbohydrates in aqueous medium.[17-19] They participate in numerous biological functions.[20,21] Understanding their functions in recognition of carbohydrates thus is an important and yet unsolved challenge in bioorganic chemistry. Organoboronic acids have been used widely in sugar recognition.[22] They are well known to form complexes with 1,2- and 1,3- diols of the sugars reversibly and rapidly to form five and six membered ring boronate esters in water.[22,23] As a result, synthetic lectins now can distinguish glucosides from their isomeric sugars and also bind to sugars with a binding affinity ranging from $K_a = 10^3–10^4$ M^{-1}.[23-25] Molecularly imprinted polymers (MIPs) are also commonly used as synthetic lectins to recognize monosaccharaides in water.[26-28] The method involves polymerization of cross-linkers and functional monomers around a template molecule, in the presence of a radical initiator to produce MIPs. These MIPs have displayed long-term stability, template specific pockets, and chemically inert to most of the organic solvents. The vinylboronic acid-functionalized MIPs are the most common in monosaccharide recognition.[26,27] Recently our group has introduced molecularly imprinted nanoparticles (MINPs) that resemble lectins for monosaccharide recognition.[29] The templates for monosaccharide-binding MINPs and MIPs were prepared in organic solvents under azeotropic distillation. Therefore, the method could not be used with oligosaccharides which have very low solubility in nonpolar solvents. Below we report a new technique that allows

us to perform molecular imprinting for monosaccharaides and oligosaccharides directly in aqueous solution, which simplifies the MINP preparation. This technique allows the development of a general method for selective mono-/oligosaccharide recognition based on their building blocks, glycosidic α or β linkages, and chain length.

Lipid composition and membrane curvature play a vital role in biological processes within a cell.[30] In the literature, natural proteins with ADP-ribosylation factor GTPase-activating protein 1 (ArfGAP1) lipid packing sensor (ALPS) motif or Bin-Amphiphysin-Rvs domain are well-known to sense the membrane curvatures.[31-34] These proteins recognize different curvatures of membranes based on the hydrophobic lipid packing deficiencies.[35-39] (i.e. higher lipid curvatures have higher lipid packing deficiencies or vice versa). Interestingly, charge balance between the lipid and the protein seems to play an essential role in the binding process as well.[36,37,40] However, these proteins are limited in biotechnological development due to their cost and low stability. Herein we report bischolate foldamers labeled with environmentally sensitive fluorophores to sense the lipid membrane curvatures as protein mimics.

References

(1) Cerny, J.; Hobza, P. *Phys. Chem. Chem. Phys.* **2007**, *9*, 5291.

(2) Benichou, G.; Tocco, G. *Eur. J. Immunol.* **2013**, *43*, 584.

(3) Weber, P.; Ohlendorf, D.; Wendoloski, J.; Salemme, F. *Science* **1989**, *243*, 85.

(4) Williams, D. H.; Stephens, E.; O'Brien, D. P.; Zhou, M. *Angew. Chem. Int. Ed.* **2004**, *43*, 6596.

(5) Munro, O. Q.; Joubert, S. D.; Grimmer, C. D. *Chem. Eur. J.* **2006**, *12*, 7987.

(6) Isaacs, L. *Accounts Chem Res* **2014**, *47*, 2052.

(7) Jordan, J. H.; Gibb, B. C. *Chem. Soc. Rev.* **2015**, *44*, 547.

(8) Kim, D. S.; Sessler, J. L. *Chem. Soc. Rev.* **2015**, *44*, 532.

(9) Sowdhamini, R.; Srinivasan, N.; Guruprasad, K.; Rufino, S.; Dhanaraj, V.; Wood, S. P.; Emsley, J.; White, H. E.; Blundell, T. *Pharmaceutica Acta Helvetiae* **1995**, *69*, 185.

(10) Schneider, H. J.; Schneider, H. J. *Methods and Principles in Medicinal Chemistry* **2003**, *19*, 21.

(11) Williams, D. H.; Stephens, E.; O'Brien, D. P.; Zhou, M. *Angew. Chem. Int. Ed.* **2004**, *43*, 6596.

(12) Carrillo, R.; Feher-Voelger, A.; Martín, T. *Angew. Chem. Int. Ed.* **2011**, *50*, 10616.

(13) Carrillo, R.; Morales, E. Q.; Martín, V. S.; Martín, T. *Chem. Eur. J.* **2013**, *19*, 7042.

(14) Carrillo, R.; Morales, E. Q.; Martín, V. S.; Martín, T. *J. Org. Chem.* **2013**, *78*, 7785.

(15) Rodriguez-Docampo, Z.; Pascu, S. I.; Kubik, S.; Otto, S. *J. Am. Chem. Soc.* **2006**, *128*, 11206.

(16) Zhong, Z.; Li, X.; Zhao, Y. *J. Am. Chem. Soc.* **2011**, *133*, 8862.

(17) Kennedy, J. F.; Palva, P. M. G.; Corella, M. T. S.; Cavalcanti, M. S. M.; Coelho, L. C. B. B. *Carbohydrate Polymers* **1995**, *26*, 219.

(18) Weis, W. I.; Drickamer, K. *Annu. Rev. Biochem.* **1996**, *65*, 441.

(19) Kilpatrick, D. C. *Biochimica et Biophysica Acta* **2002**, *1572*, 187.

(20) Kamerling, J. P.; Boons, G.-J. *Comprehensive glycoscience : from chemistry to systems biology*; 1st ed.; Elsevier: Amsterdam ; Boston, 2007.

(21) Wang, B.; Boons, G.-J. *Carbohydrate recognition: biological problems, methods, and applications*; Wiley: Hoboken, N.J., 2011.

(22) Jin, S.; Cheng, Y.; Reid, S.; Li, M.; Wang, B. *Med. Res. Rev.* **2010**, *30*, 171.

(23) Miron, C. E.; Petitjean, A. *ChemBioChem* **2015**, *16*, 365.

(24) Kubik, S. *Angew. Chem. Int. Ed.* **2009**, *48*, 1722.

(25) Norrild, J. C.; Eggert, H. *J. Am. Chem. Soc.* **1995**, *117*, 1479.

(26) Wulff, G.; Schauhoff, S. *J. Org. Chem.* **1991**, *56*, 395.

(27) Rajkumar, R.; Warsinke, A.; Möhwald, H.; Scheller, F. W.; Katterle, M. *Biosensors and Bioelectronics* **2007**, *22*, 3318.

(28) Striegler, S. *Macromolecules* **2003**, *36*, 1310.

(29) Awino, J. K.; Gunasekara, R. W.; Zhao, Y. *J. Am. Chem. Soc.* **2016**, *138*, 9759.

(30) Zimmerberg, J.; Kozlov, M. M. *Nat. Rev. Mol. Cell. Biol.* **2006**, *7*, 9.

(31) Mesmin, B.; Drin, G.; Levi, S.; Rawet, M.; Cassel, D.; Bigay, J.; Antonny, B. *Biochemistry* **2007**, *46*, 1779.

(32) Bhatia, V. K.; Madsen, K. L.; Bolinger, P. Y.; Kunding, A.; Hedegård, P.; Gether, U.; Stamou, D. *EMBO J.* **2009**, *28*, 3303.

(33) McMahon, H. T.; Gallop, J. L. *Nature* **2005**, *438*, 590.

(34) Shen, H.; Pirruccello, M.; De Camilli, P. *Cell* **2012**, *150*, 1300.

(35) Drin, G.; Antonny, B. *FEBS Lett.* **2010**, *584*, 1840.

(36) Chong, S. S. Y.; Taneva, S. G.; Lee, J. M. C.; Cornell, R. B. *Biochemistry* **2014**, *53*, 450.

(37) Antonny, B. *Annu. Rev. Biochem.* **2011**, *80*, 101.

(38) Morton, L. A.; Yang, H.; Saludes, J. P.; Fiorini, Z.; Beninson, L.; Chapman, E. R.; Fleshner, M.; Xue, D.; Yin, H. *ACS Chem. Biol.* **2013**, *8*, 218.

(39) Saludes, J. P.; Morton, L. A.; Ghosh, N.; Beninson, L. A.; Chapman, E. R.; Fleshner, M.; Yin, H. *ACS Chem. Biol.* **2012**, *7*, 1629.

(40) Bigay, J.; Antonny, B. *Developmental Cell* **2012**, *23*, 886.

CHAPTER 2

RATIONALLY DESIGNED COOPERATIVELY ENHANCED RECEPTORS TO MAGNIFY HOST–GUEST BINDING IN WATER

A paper published in *Journal of the American Chemical Society* **2015**, 135, 843-849.

Roshan W. Gunasekara and Yan Zhao

Abstract

When disengaged interactions within a receptor are turned on by its guest, these intrahost interactions will contribute to the overall binding energy. Although such receptors are common in biology, their synthetic mimics are rare and difficult to design. By engineering conflictory requirements between intrareceptor electrostatic and hydrophobic interactions, we enabled complementary guests to eliminate the "electrostatic frustration" within the host and turn on the intrahost interactions. The result was a binding constant of K_a $>10^5$ M^{-1} from ammonium–carboxylate salt bridges that typically function poorly in water. These cooperatively enhanced receptors displayed excellent selectivity in binding, despite a large degree of conformational flexibility in the structure.

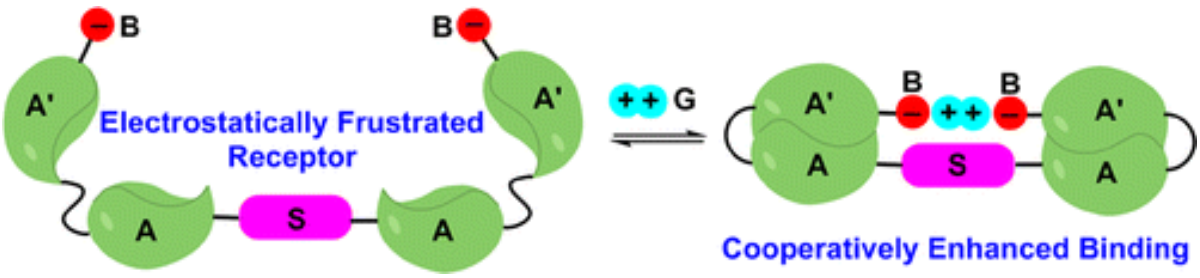

Scheme 1. Design of cooperatively enhanced receptor (CER).

Introduction

Biological hosts have extraordinary abilities to recognize and bind guests in competitive aqueous environments, even well solvated hydrophilic small molecules whose binding is not expected to gain much binding enthalpy. A survey of biological and synthetic host–guest complexes by Houk et al. over a decade ago revealed a large gap between the two groups of receptors: whereas nanomolar or stronger affinities are frequently seen in the former, millimolar affinities represent the average for the latter.[1] Chemists indeed developed extremely tight binders in isolated cases;[2-4] such, nonetheless, remain as rare exceptions to the norm in synthetic supramolecular chemistry.

Interestingly, evident from the large number of tight-binding drugs developed for bioreceptors, there seems to be no fundamental deficiency in chemists' ability to construct tight-binding guests *for* biological hosts. If this is indeed the case, the "deficiency" of synthetic host–guest complexes likely lies in the receptors that admittedly are less complex and smaller in size in comparison to common biological hosts.

The majority of synthetic receptors have been created using the concept of preorganization.[5,6] The concept played vital roles in the development of supramolecular chemistry in the last decades.[7-22] More recently, however, an increasing number of chemists began to wonder whether alternative strategies exist in constructing tight-binding receptors.[23-28] Since bioreceptors are often made of flexible peptide chains with rich conformational dynamics even in the folded state, it seems flexibility cannot be inherently detrimental to high binding affinity. Not only so, flexible bioreceptors must have effective strategies to overcome the problem of negative conformational entropy when they tighten up in the presence of their guests.[29]

After studying protein and other naturally occurring receptors, Williams and co-workers proposed an interesting postulation that the driving force for guest-binding does not all have to come from direct host–guest interactions but may derive from cooperative strengthening of existing interactions *within* the host.[23] Essentially, *binding in bioreceptors can be delocalized over the entire structure, not confined at the host–guest interface*.

Delocalized binding in cooperatively enhanced receptors (CERs) has indeed been realized in several synthetic receptors. Kubik, Otto, and co-workers prepared a peptidic bismacrocyclic anion receptor whose hydrophobic interactions between the two macrocycles assisted the anion binding.[30] Carrillo et al. reported a crown ether-like macrocycle in which a remote intrahost hydrogen bond strengthened the binding of aromatic amino acid ester in an enantioselective fashion.[27] Our group reported an oligocholate foldamer host that exhibited strong cooperativity between the host conformation and guest binding, with the strongest binding occurring at the folding–unfolding transition.[31]

CERs essentially utilize the positive cooperativity between intrahost interactions and (direct) host–guest interactions to reinforce their guest-binding. An exciting implication of such receptors is that high binding affinity can be obtained even from weak (direct) binding forces, as long as sufficient intrahost interactions can be triggered by the guest. Unfortunately, despite the attractiveness and huge potential of such receptors, their rational design represents a formidable task. While preorganization gives chemists a clear path to follow in designing guest-complementary receptors, cooperative enhancement seems more of a rationale for existing phenomena as it stands. Even for the above mentioned synthetic CERs, their discovery appeared to be by accident rather than by design.

In this paper, we report a rational design of CERs that operate in aqueous solution. Weak ammonium–carboxylate salt bridges were enhanced by hydrophobic interactions within the receptor to afford strong binding in water. The key design of the system centers on the "electrostatically frustrated" intrahost interactions that could be strengthened by a suitable guest. Not only strong binding was obtained in water from relatively weak binding forces, excellent selectivity was also achieved for a highly flexible receptor.

Results and Discussion

Design and Synthesis of CERs

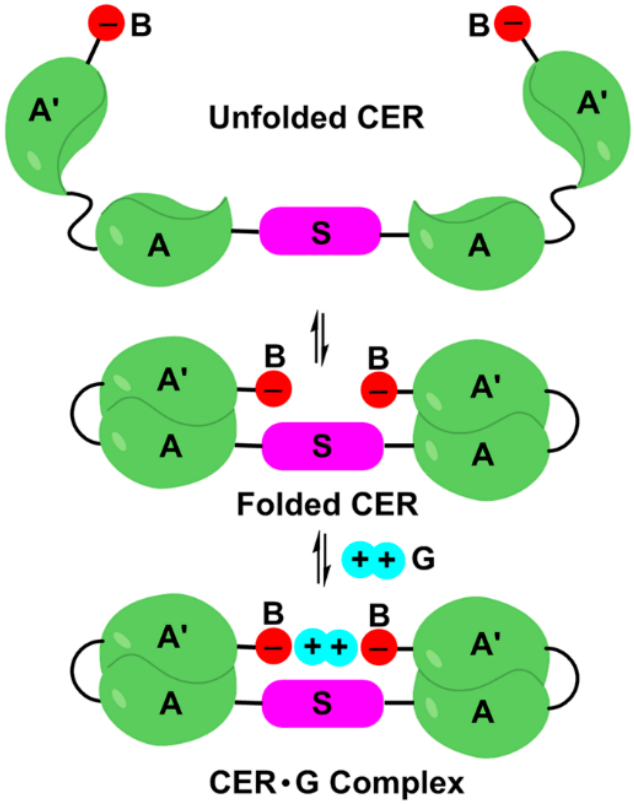

Scheme 2. Design of an electrostatically frustrated CER and its binding of an oppositely charged ligand to trigger intrahost A–A′ interactions.

As shown by Scheme 2, our CER consists of a central scaffold (**S**) to which two insulated "folding arms" are attached. Each arm can fold upon itself by the intrahost **A**–**A′** interactions. The two binding functionalities (**B**) are designed to be far apart in the unfolded CER but in proximity in the folded conformer. As a result, the electrostatic interactions between the two negatively charged **B**'s are in conflict with the **A**–**A′** interactions in the folded conformer and thus interfere with the folding. When a suitable, oppositely charged guest (**G**) binds, it engages direct electrostatic host–guest interactions and, more importantly, by neutralizing the electrostatically repelled **B**'s, strengthens the intrahost **A**–**A′** interactions. In this way, the formerly "frustrated" intrareceptor hydrophobic interactions are "turned on" by the guest and will contribute to the binding energetically. As will be shown by our study, the CER does not have to be fully unfolded prior to binding to be operative. As long as the intrahost **A**–**A′** interactions are not fully engaged before the CER binds the guest, they could contribute to the binding. Similar to biological CERs, the system has the "binding interactions" delocalized over much of the entire structure, with remote **A**–**A′** interactions being utilized to magnify the direct binding forces at the **B**–**G**–**B** interface.

Notably, the CER is highly flexible by design. The guest-induced conformational change is strategically utilized instead of being avoided as in typical preorganized systems. Yet, because the optimal guest needs to match the **B**–**B** distance in the *folded* CER both electrostatically and geometrically, a strong binding selectivity may still be possible despite the flexibility.

To realize the above design, we first synthesized bischolate **1** as the folding arm, with a fluorescent label to study its folding/unfolding (Scheme 3). Our group has a long interest in cholate foldamers except that the earlier examples had their monomers joined by amide

groups on the hydrophilic α-face of the cholate.[32-34] Because the two cholates in **1** need to interact through hydrophobic interactions of the β-faces in water, we connected the cholates by the β-amino group, with a flexible glutamic acid tether to facilitate the choate–cholate interaction. Our previous work shows that a C4 tether in between two cholates allows the facial amphiphiles to interact with each other fairly easily.[35] In Scheme 3, the terminal carboxylate (highlighted by the red circle) corresponds to the binding functionality **B** in Scheme 2 and the two cholates are essentially **A** and **A′**, respectively.

The synthesis of **1** followed standard chemistry employed in other oligocholate synthesis[32] and can be found in the Experimental Section. Our synthesis left an azido group on the cholate, which made it convenient to label the arm with an environmentally sensitive fluorophore (**2**) using click chemistry.

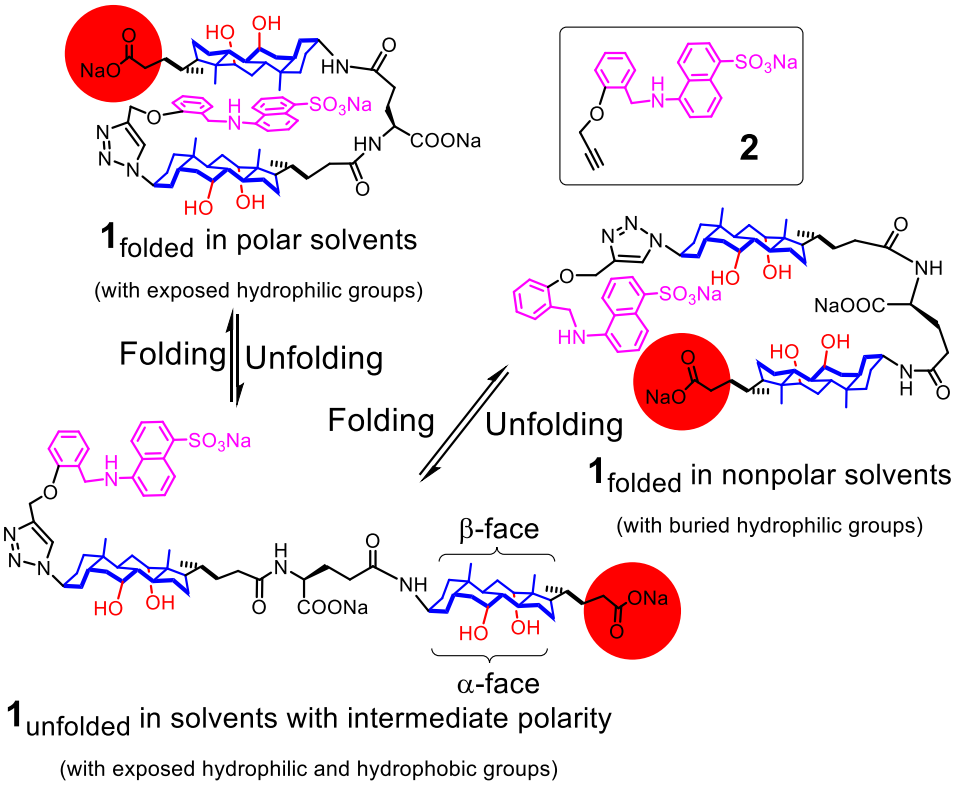

Scheme 3. Folding of bischolate foldamer **1** in polar and nonpolar solvents.

Figure 1 shows the maximum emission intensity of compounds **1** (□) and **2** (△) in two solvent mixtures. The intensity of each compound was normalized to the emission of the same compound in methanol so that the two compounds can be better compared. The x-axes are drawn such that the solvent polarity increases continuously from left to right all the way across Figure 1a,b.

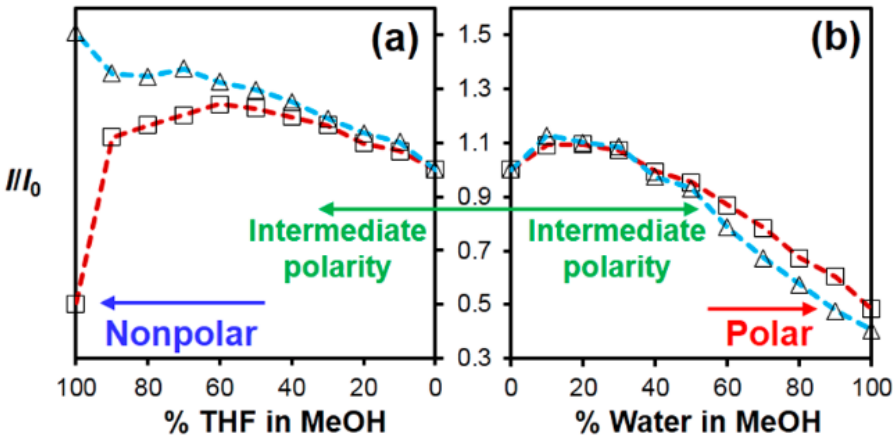

Figure 1. Maximum emission intensity of bischolate **1** (□) and control compound **2** (△) normalized to the intensity of the same compound in methanol as a function of solvent composition in (a) THF/methanol and (b) water/methanol mixtures. The data points are connected by colored lines to guide the eye. λ_{ex} = 340 nm. [Compound] = 2.0 μM.

According to Figure 1, the two compounds responded to solvent polarity similarly at intermediate polarity, evident from the nearly overlapping I/I_0 curves in between 30% THF/methanol and 50% methanol/water (indicated by the green arrow). However, the curves deviated from each other when the solvents became either more polar or less polar. Importantly, as the I/I_0 curves moved apart, **1** (□) had stronger (normalized) emission than **2** (△) toward the polar end but weaker emission toward the nonpolar end.

The aminonaphthalene sulfonate in **1** and **2** is an analogue of the more common fluorophore dansyl, which emits strongly in nonpolar environments and weakly in polar ones.[36] Since a similar effect was operating in **2**, the stronger-than-usual emission of **1** in the most polar solvents suggests that its fluorophore has a higher environmental hydrophobicity than **2** in the most polar solvents, and vice versa in the most nonpolar solvents. This kind of crossing-over in solvent response was identical to what was observed in our cholate-based molecular baskets, which adopted a micelle-like conformation (with exposed hydrophilic faces) in polar solvents and reverse-micelle-like conformation (with buried hydrophilic faces) in nonpolar solvents.[37,38] Conceivably, as **1** folded in polar solvents via the hydrophobic cholate–cholate interactions (Scheme 3), the fluorophore was sensing the hydrophobic local environment and thus emitted more strongly than the control compound. When **1** folded in nonpolar solvents (in THF with low methanol), the hydrophilic faces turned inward, with the many polar groups toward the center of the molecule concentrating methanol near the fluorophore—this type of solvent-induced conformational change has been observed multiple times for both cholate foldamers[32,38] and nonfoldamers[37,38] under similar conditions.

Since the bischolate arm seemed to operate as intended, we prepared CER **3** by clicking three such arms (**5**) to 1,3,5-triethynylbenzene. A control compound **4** was similarly prepared to help us understand the conformation of **3**. We chose the rigid trisubstituted benzene as the central scaffold so that the bischolate arms are separated or "insulated" from one another. Clearly, we did not want cholate–cholate interactions to occur across different arms.

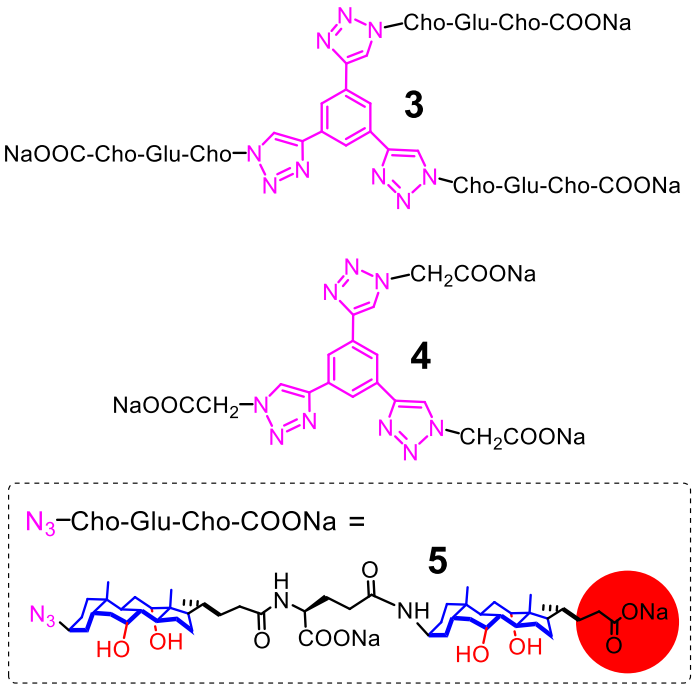

Scheme 4. Structures of Compound **3**, compound **4**, and compound **5**.

Figure 2a shows the I/I_0 curves of **3** and **4**. We focused on the polar side of the solvent scale (i.e., methanol/water mixtures), as the receptor was designed to function in water through the hydrophobic interactions of the β-cholates. Remarkably, the curves for **3** and **4** once again nearly overlapped in <50% water/methanol but moved apart as the solvent became more polar, similar to what happened to **1** and **2** in Figure 1b. Intermolecular aggregation was ruled out by dilution studies. More importantly, the fluorescence in >50% water/methanol displayed a sigmoidal transition, a hallmark of cooperative conformational change.[39,40] The data fit almost perfectly to a two-state unfolding–folding transition model (Figure 2b) that is characteristic of many proteins[41] and solvophobic foldamers,[32,42] suggesting that the proposed cooperative folding indeed was operating.

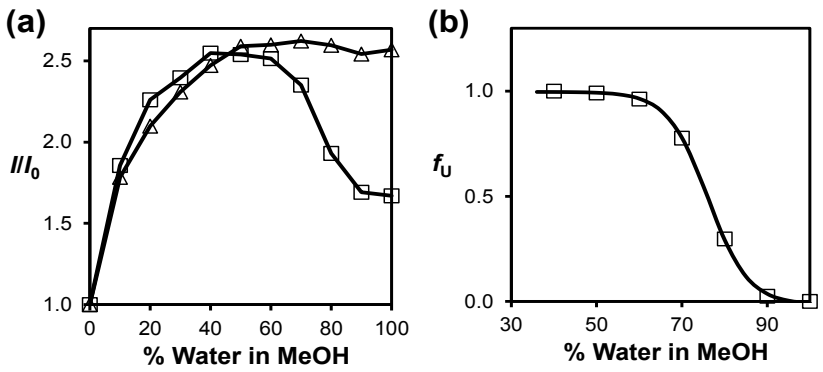

Figure 2. (a) Maximum emission intensity of "3-armed" **3** (□) and control compound **4** (△) normalized to the intensity of the same compound in 100% methanol as a function of solvent composition in water/methanol. λ_{ex} = 240 nm. [Compound] = 2.0 μM. (b) Nonlinear least squares curve fitting of the fluorescence data of **3** in ≥40% water/methanol to a two-state transition model, showing the fraction of unfolded conformer as a function of solvent composition.

Taken together, it seems that the bischolate arms could fold hydrophobically in >50% water/methanol. The similar response of the 1-armed and 3-armed compounds toward solvent polarity suggests that these arms folded independently. The more important questions, however, were whether these arms indeed could enhance the binding of **3** as a receptor and which factors would control the cooperative enhancement.

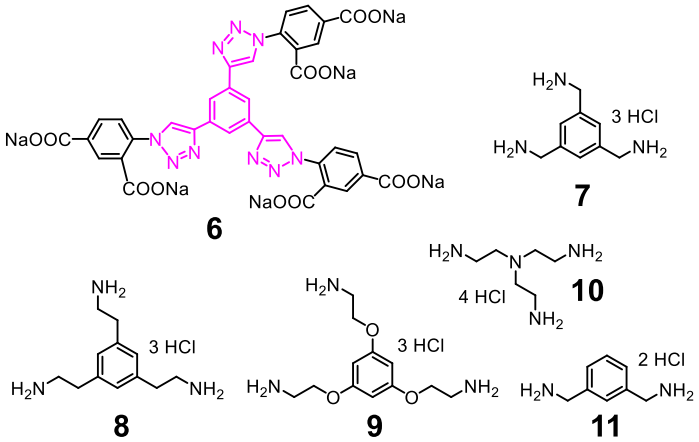

Scheme 5. Structures of receptor **3** and guest molecules.

To evaluate the molecular recognition of **3**, we synthesized a hexacarboxylated analogue **6** as a control receptor, which lacks the key cooperative conformational change of **3**. Its three ortho carboxylates mimic the three terminal carboxylates from the cholates that are responsible for binding triammonium guests such as **7**. Its para carboxylates mimic the three glutamate carboxylates in the midsection of **3** to provide solubility in aqueous solution. Keeping the compounds charged is important to water-solubility of the host–guest complex, especially when the ammonium guest neutralizes the cholate or the ortho carboxylates in **3** and **6**, respectively.

The binding of the two receptors was studied by isothermal titration calorimetry (ITC). ITC is often the method of choice for binding studies. Not only could one determine binding constants (K_a) in a broad range, other important parameters including the binding enthalpy, entropy, and the number of binding sites (N) on the receptor could all be obtained simultaneously.

Both receptors (**3** and **6**) relied on the three introverted carboxylates for binding; the difference between the two was in how the carboxylates were folded back—by conformational changes and a rigid covalent framework, respectively—and whether cooperative conformational change was involved in the binding. As shown by Figure 3, the titration data for both compounds fit nicely to a 1:1 binding model but the two bindings had completely opposite heat of reaction, with **3** showing a positive/unfavorable enthalpy and **6** a large negative/favorable enthalpy.

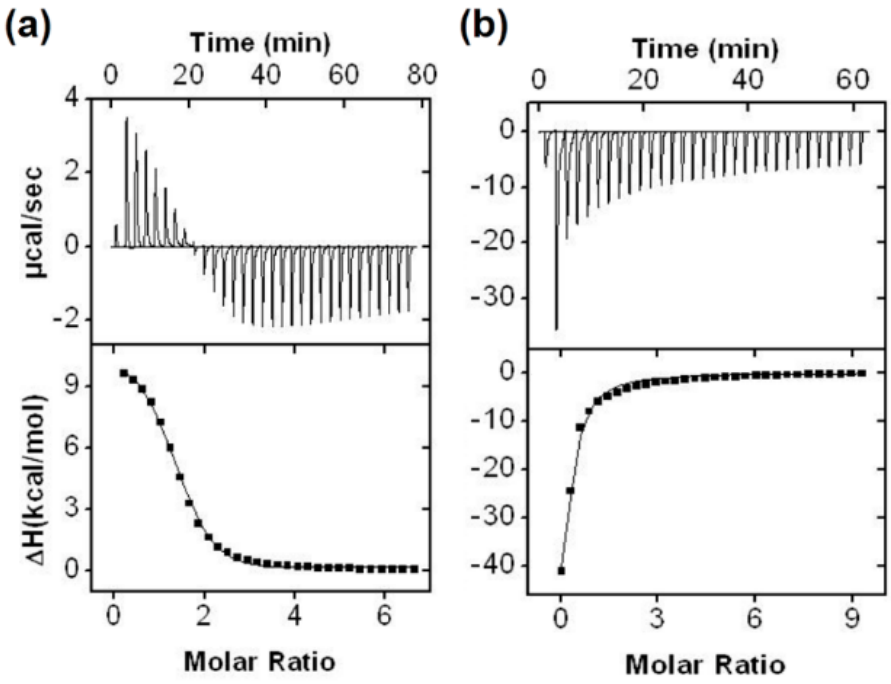

Figure 3. ITC titration curves obtained at 298 K for the binding of **7** by (a) **3** and (b) **6**. The data correspond to entries 1 and 9 in Table 1. In a typical experiment, a 2–6 mM aqueous solution of the guest in Millipore water was injected in equal steps of 10.0 µL into 1.42 mL of 0.05–0.2 mM solution of the host in Millipore water. The top panel shows the raw calorimetric data. The area under each peak represents the amount of heat generated at each ejection and is plotted against the molar ratio of the guest to the host. The smooth solid line is the best fit of the experimental data to the sequential binding of *N* equal and independent binding sites on the MINP. The heat of dilution for the guest, obtained by adding the guest to Millipore water, was subtracted from the heat released during the binding. Binding parameters were auto-generated after curve fitting using Microcal Origin 7.

The thermodynamic parameters for the bindings are summarized in Table 1. Entries 1 and 9 show that the flexible CER (**3**) was able to bind triammonium **7** in water with a K_a of

138×10^3 M^{-1}, ca. 6 times stronger than that of the more rigid control receptor (**6**). The difference corresponds to 1 kcal/mol binding free energy (ΔG). Formation of **3·7** was entropically driven, with a positive/favorable binding entropy ($T\Delta S$ = 17.5 kcal/mol) that more than compensated the unfavorable binding enthalpy of ΔH = 10.5 kcal/mol. In contrast, the rigid receptor **6** has a large favorable enthalpy (ΔH = -35.6 kcal/mol) that was offset by an also large entropic term ($T\Delta S$ = -29.6 kcal/mol). To our delight, the number of independent binding sites (N) for all the receptors (**3**, **6**, and **12** to be discussed later) was 1.1 ± 0.2 according to the ITC titrations, indicating that 1:1 binding stoichiometry was indeed in operation as designed.

The binding data so far are consistent with the designed cooperatively enhanced binding. Not only was the flexible CER able to bind more strongly than the more "preorganized" control receptor **6** with the same number of salt bridges,[43] the two bindings had opposite driving forces. The entropically driven binding of **3** also strongly supports our CER design: since the intrahost hydrophobic interactions were expected to contribute to the binding and a large number of water molecules will be released to the bulk solution during hydrophobic association of the cholates, a strong entropic driving force is anticipated. According to Figure 2b, **3** was fully folded in 100% water. Since the folding was hydrophobically driven, the cholate–cholate hydrophobic interactions must have been already engaged to a large degree prior to binding. The fact that additional hydrophobic driving force could be "transferred" to the guest-binding suggests that the cholates were not tightly packed in folded **3** prior to the binding, as expected from the proposed repulsion between the terminal carboxylates.

Table 1. Binding data obtained by ITC[a]

Entry	Complex	K_a (10^3 M^{-1})	ΔG (kcal/mol)	ΔH (kcal/mol)	$T\Delta S$ (kcal/mol)
1	3·7	138 ± 2	-7.0	10.5	17.5
2	3·7[b]	49 ± 9	-6.4	71.0	77.4
3	3·7[c]	6.8 ± 0.2	-5.2	114.0	119.2
4	3·7[d]	19 ± 1.6	-5.8	-1.6	4.2
5	3·8	11 ± 6	-5.5	35.4	40.9
6	3·9	8.0 ± 1.0	-5.3	-1.7	3.6
7	3·10[e]	--	--	--	--
8	3·11	23 ± 1	-5.9	2.8	8.7
9	6·7	24 ± 10	-6.0	-35.6	-29.6
10	6·8[e]	--	--	--	--
11	6·9[e]	--	--	--	--
12	12·13	2.2 ± 0.5	-4.6	9.9	14.5
13	12·14	150 ± 30	-7.1	-8.3	-1.3

[a] The titrations were generally performed in duplicates in water and the errors between the runs were generally <10%. The number of independent binding sites (N) was found to be 1.1 ± 0.2. [b] The binding was determined in a 80:20 water/methanol mixture. [c] The binding was determined in a 60:40 water/methanol mixture. [d] The binding was determined in PBS buffer (pH 7.4, 137 mM NaCl, 2.7 mM KCl). [e] The binding was too weak to be determined by ITC.

The formation of **6·7** was enthalpically driven (Table 1, entry 9). The binding affinity for triammonim **7** by **6** in water was ~6 times stronger than that by a triphosphonate receptor (K_a = 4 × 10^3 M^{-1} in D_2O) in the literature for the same guest.[44] The stronger binding by **6** likely comes from the secondary electrostatic interactions between the ammoniums on the guest and the para carboxylates of **6**. The enthalpic driving force seems reasonable. Although ionic interactions have been reported to afford positive entropy in some cases,[45-48] it is also well known that strong ionic interactions have favorable enthalpic contribution.[47,49] In the case of **6**, any favorable entropy obtained through release of water molecules during desolvation was probably overcome by increased order of the complex. One source for the

higher order could come from the loss of conformational freedom in the receptor during binding. The free receptor is unlikely to have all the carboxylates on the same side of the molecule, due to electrostatic repulsion of the ortho carboxylates and multiple rotatable bonds in the 1,3,5-tris(triazolyl)benzene scaffold. Binding between **6** and **7** would undoubtedly freeze the conformation of the host, leading to a reduction of entropy.

The intrahost hydrophobic contribution to the formation of **3·7** was additionally confirmed by the addition of methanol to the aqueous solution. As shown by entries 2 and 3 of Table 1, the binding affinity continued to decline with increasing amounts of methanol. Additionally, in PBS buffer, which contained significant amounts of electrolytes (NaCl, KCl, and sodium phosphate), the binding was also weakened significantly (entry 4). The result is consistent with our proposed binding mechanism. As the electrolytes lowered the repulsion among the negatively charged carboxylates in the folded CER, the intrahost cholate–cholate hydrophobic interactions become more fully engaged *prior to* the guest binding, destroying the very basis of the cooperative enhancement. These results are also in agreement with our earlier conclusion that, even though **3** was fully folded (Figure 2b), the cholates were not tightly packed due to the repulsion among the cholate carboxylates.

Our CER model in Scheme 2 predicts selectivity in the binding, as the optimal guest needs to fit in between the binding groups in the folded CER. The prediction was confirmed in the bindings of guests **8**–**11**. The addition of a single methylene spacer (**8** vs. **7**) lowered the binding affinity (of **8**) by an order of magnitude. Compound **9** differs from **8** by another oxygen spacer; its binding by **3** was similarly weak. Thus, despite the tremendous flexibility of the conformationally mobile CER, not only could it bind its guest tightly in water, it also did so with quite impressive selectivity.

Somewhat surprisingly, **3** had no detectable binding for the ammonium salt of TREN (**10**). It is unclear to us why this compound could not bind, given its similarity to **7** in size and the terminal amine groups. On the other hand, it is interesting to note that diammonium salt **11** was bound with quite a remarkable affinity in water. Even though its binding constant was weaker than that for **7** (as expected), a K_a of 23×10^3 M^{-1} was 2–3 times higher than the "slightly-mismatched" triammonium **8** and **9**. We believe this result actually derived from our CER binding mechanism. Although three ammoniums are optimal for binding CER **3**, two such groups are sufficient to "disarm" the electrostatically frustrated bischolates. This is because when two salt bridges are formed between **3** and **11**, the third cholate carboxylate would not face significant repulsion in the guest-binding folded state. As a result, even when the third salt bridge was absent, all the other intrahost hydrophobic interactions among the cholates could be turned on by **11** to enhance its binding.

If the folding arms are essential to the CER, reducing its number should weaken the binding dramatically. To verify this hypothesis, we synthesized 2-armed CER **12** and studied its binding of diammonium **13** and diguanidinium **14**. As predicted, the 2-armed receptor displayed weaker binding for diammonium **13**, with a K_a of 2.2×10^3 M^{-1} (Table 1, entry 12) or about 60 times weaker than that of **3·7**. It is worth noting that, although two salt bridges are formed in both **3·11** and **12·13**, the former complex was 10 times more stable than the latter. The result once again confirms that the intrahost cholate–cholate interactions were critical to the binding. Since three such interactions can be formed in **3·11** but only two in **12·13**, the higher stability of the former is anticipated, despite the same number of salt bridges formed in both complexes.

A stronger direct binding force between the carboxylate and guanidinium not surprisingly enhanced the binding even further, giving an impressive K_a of 150 × 10^3 M^{-1} with ΔG = -7.1 kcal/mol for **12·14** in water (Table 1, entry 13). As shown by Figure 4, the ITC curves for **13** and **14** once again displayed different types of driving forces, with the binding of diammonium **13** endothermic and the binding of diguanidinium **14** exothermic. If we assume the intrahost cholate–cholate interactions are hydrophobic and entropic in origin, the switching from entropy- to enthalpy-driven binding from **13** to **14** could suggest that cooperative enhancement by the intrahost interactions is more important to a receptor whose direct host–guest binding forces are weaker. Stated differently, the stronger the direct binding forces, the less the binding needs to rely on intrahost interactions to afford high binding affinity. Many bis- and tris-guanidinium–carboxylate host–guest complexes have been reported in the literature,[46,50-52] they often did not function in pure aqueous solution or displayed much weaker binding than what was observed for **12·14**. The enhanced binding in the CER suggests that cooperative hydrophobic intrahost interactions could indeed magnify polar interactions that are compromised by water.

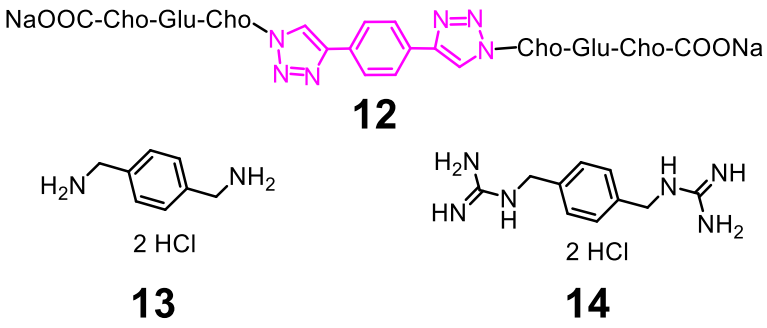

Scheme 6. Structures of receptor **12** and guest molecules.

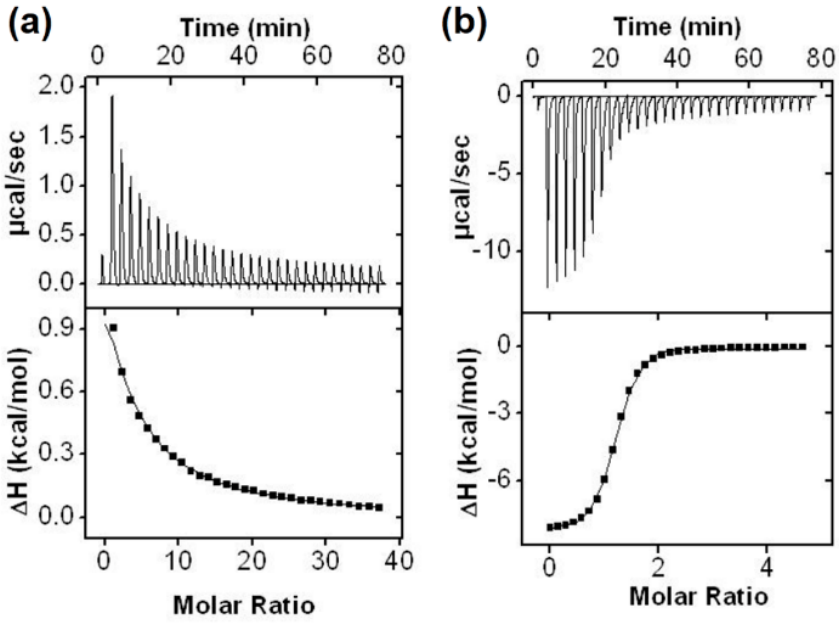

Figure 4. ITC titration curves obtained at 298 K for the binding of (a) **13** and (b) **14** by **12**. The data correspond to entries 12 and 13 in Table 1.

Conclusion

The significance of this work lies in the rational design of cooperatively enhanced receptors (CERs) that employ "hidden" intrahost interactions to magnify weak polar binding forces. Our strategy makes the binding delocalized over the entire structure of the receptor instead of being confined at the binding interface.[53] Despite the flexibility of the receptor, high binding selectivity is still possible, even though the selection rule is quite different from what governs a preorganized receptor: instead of fitting snuggly into a rigid pocket, the best guest needs to turn on the most number of non-engaged intrahost interactions prior to binding.

There is strong support for Williams's postulation of delocalized, cooperatively enhanced binding in biology. When streptavidin binds biotin, the melting point of the protein host increases by 37 °C and numerous backbone amide protons become resistant to H/D exchange.[23] In contrast to hundreds or thousands preorganized synthetic receptors already synthesized, very few CERs have been made by chemists. Hopefully, the rational design of CERs will accelerate the development of these biomimetic receptors and help chemists create ultrastable host–guest complexes even when strong direct host–guest interactions are unavailable—this could be one of many of nature's secrets in making the impossible possible. The electrostatic frustration illustrated in this work certainly is not the only strategy for CERs. We believe additional designs will emerge as more researchers join this pursuit.

Acknowledgement

We thank NSF (CHE-1303764) for financial support of the research.

Experimental Section

General Method

For spectroscopic purpose, methanol, tetrahydrofuran, hexanes, and ethyl acetate were of HPLC grade. All other reagents and solvents were of ACS-certified grade or higher, and were used as received from commercial suppliers. Routine ^{1}H and ^{13}C NMR spectra were recorded on a Bruker DRX-400, on a Bruker AV II 600 or on a Varian VXR-400 spectrometer. MALDI-TOF mass was recorded on a Thermobioanalysis Dynamo mass spectrometer. UV-vis spectra were recorded at ambient temperature on a Cary 100 Bio UV-visible spectrophotometer. Fluorescence spectra were recorded at ambient temperature on a Varian Cary Eclipse Fluorescence spectrophotometer. ITC was performed using a MicroCal

VP-ITC Microcalorimeter with Origin 7 software and VPViewer2000 (GE Healthcare, Northampton, MA).

Syntheses

Syntheses of compounds **7**,[54] **8**,[55] **18**,[56] **19**,[57] **20**,[57] **21**,[57] **22**,[57] **23**,[57] **25**,[58] **27**,[59] **28**,[60] **29**,[61] **33**,[62] **34**,[54] **35**,[63] and **36**[64] were previously reported.

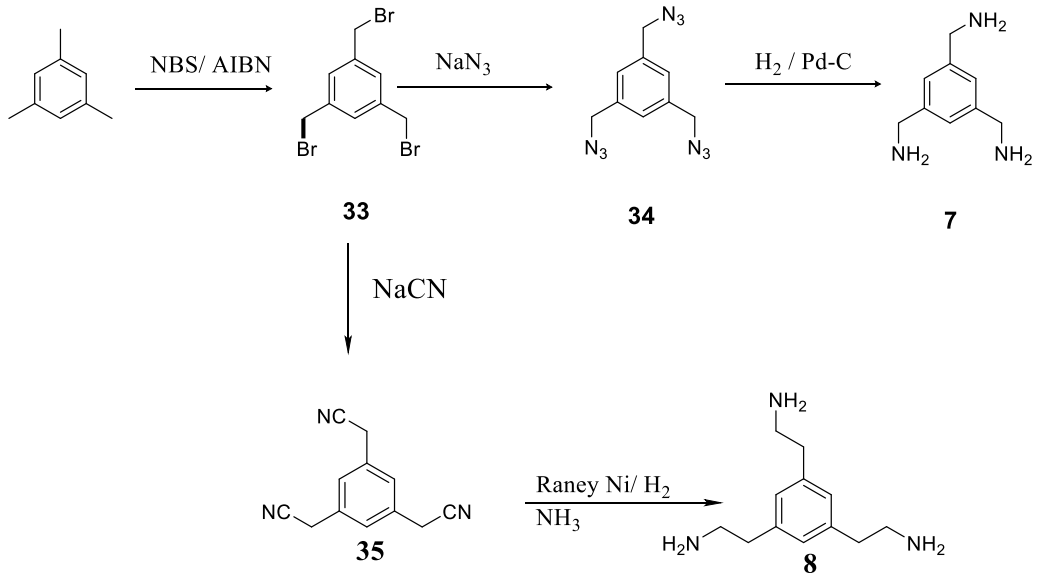

Scheme 7. Synthesis of compound **7** and **8.**

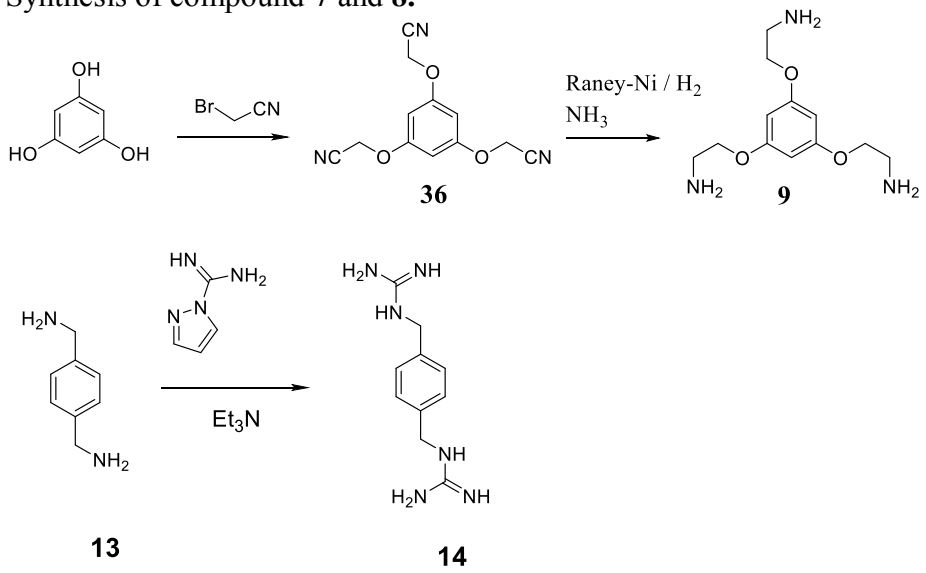

Scheme 8. Synthesis of compound **9** and **14.**

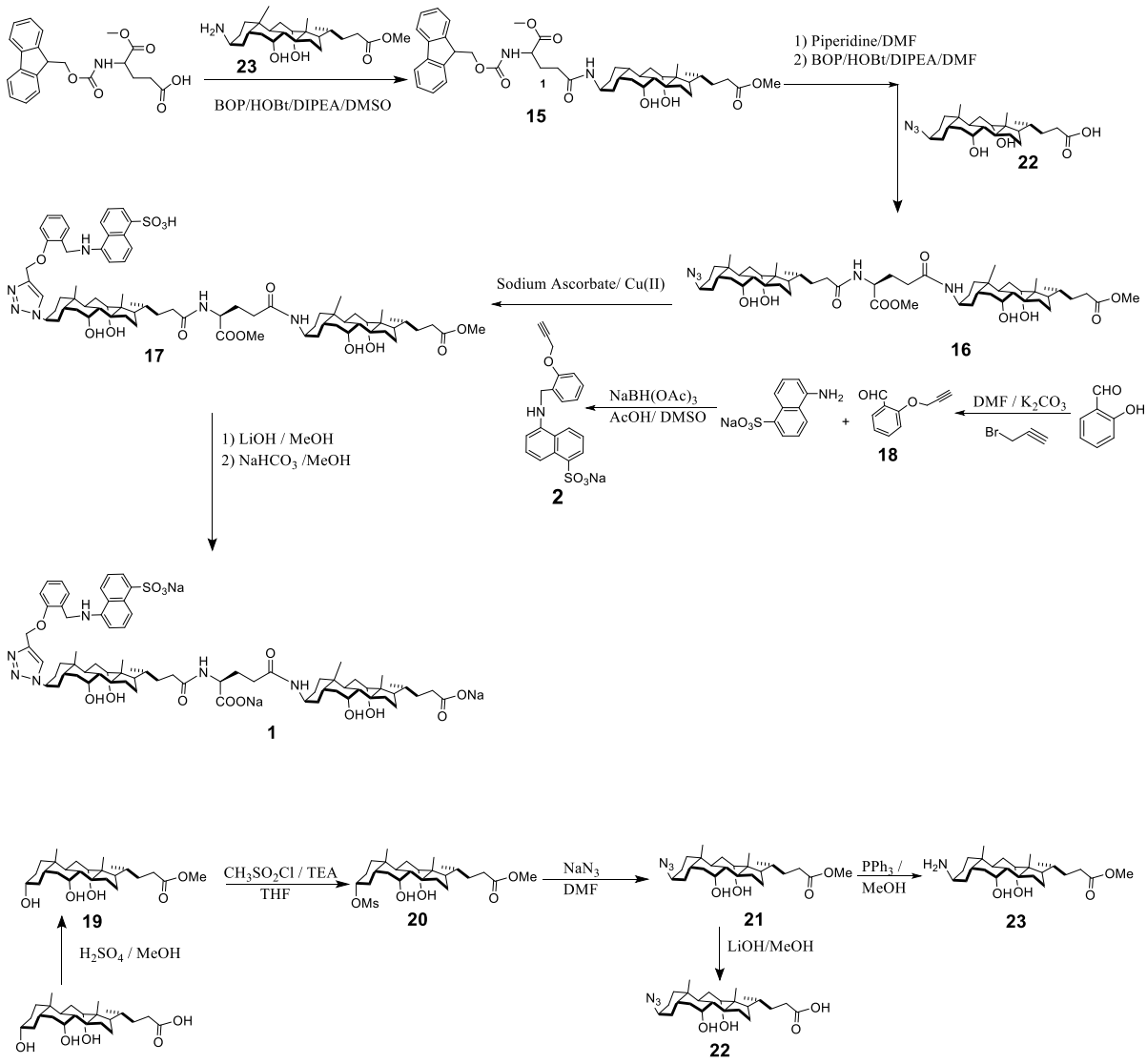

Scheme 9. Synthesis of compound **1.**

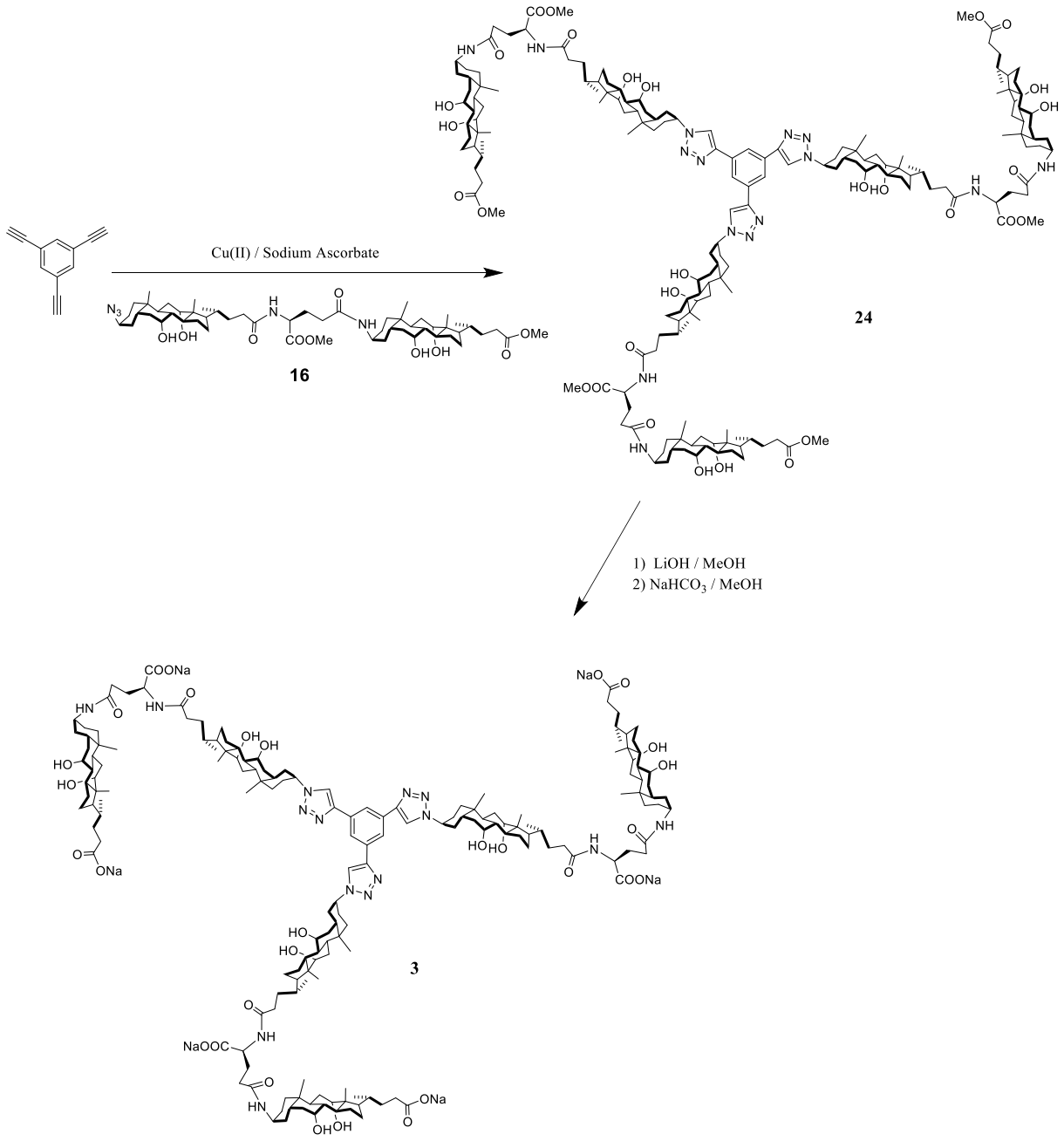

Scheme 10. Synthesis of compound **3.**

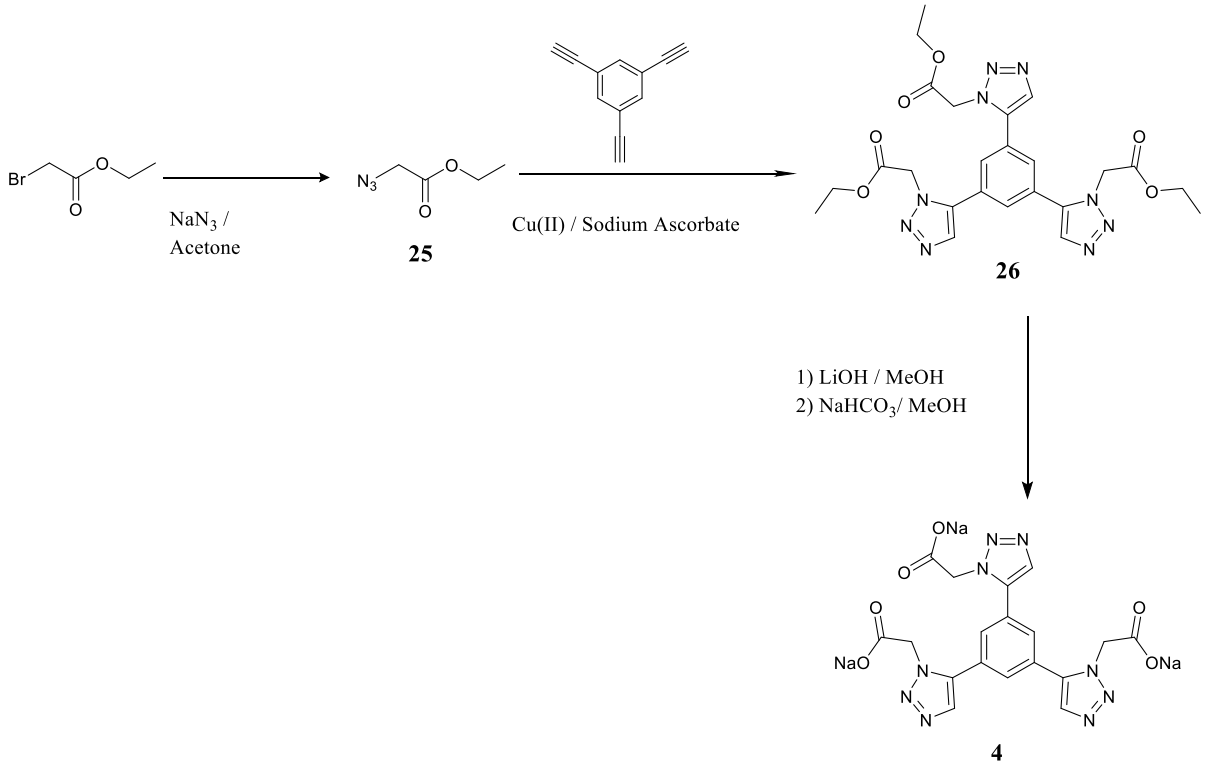

Scheme 11. Synthesis of compound **4.**

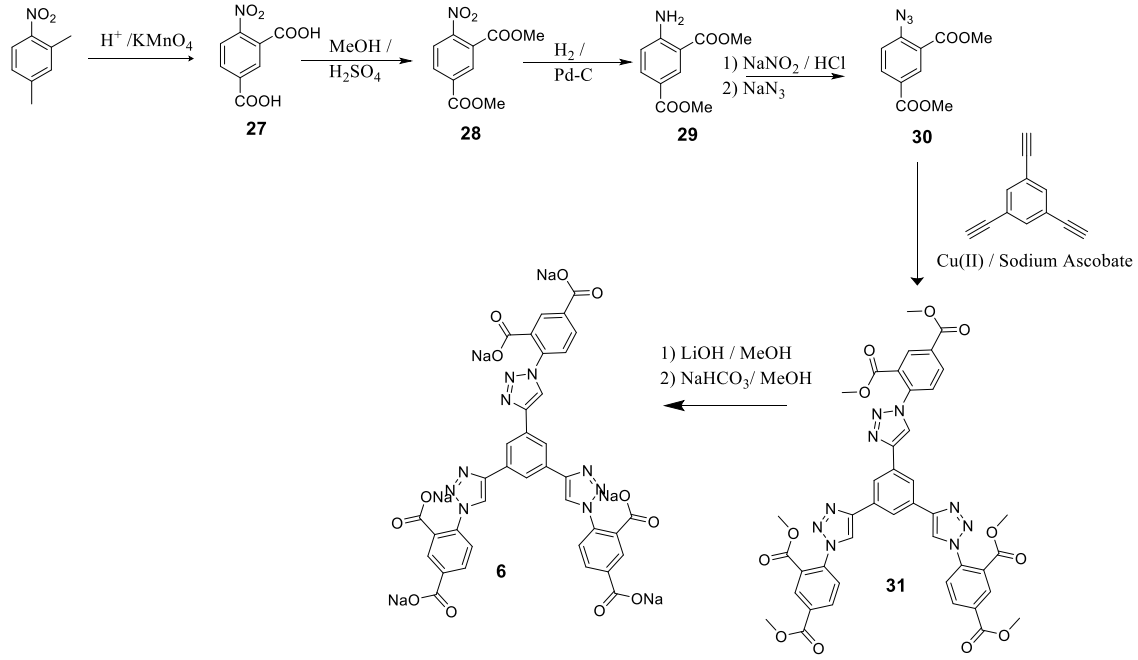

Scheme 12. Synthesis of compound **6.**

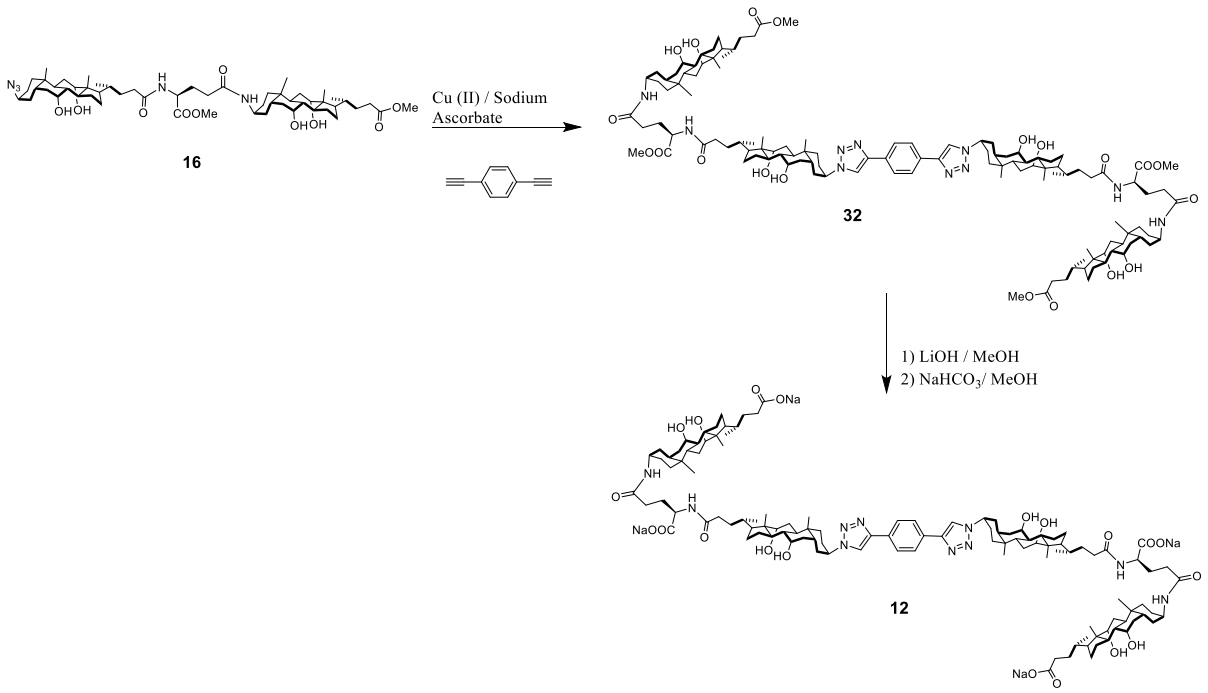

Scheme 13. Synthesis of compound **12.**

Compound 2. A mixture of compound **18** (0.5 g, 3.12 mmol), 5-amino-1-naphthalenesulfonic acid (0.46 g, 2.08 mmol), sodium triacetoxyborohydride (0.88 mL, 4.16 mmol), and glacial acetic acid (0.75 mL, 12.48 mmol) in dimethyl sulfoxide (12 mL) was stirred at room temperature overnight. The reaction was monitored by TLC. Sodium bicarbonate (25 mL) was added to the reaction mixture, followed by sodium chloride (100 mg). The precipitate formed was collected by suction filtration to give a brown powder. (0.68 g, 89%). ^{1}H NMR (400 MHz, $DMSO_4$-D_6, δ): 8.22 (d, J = 8.5 Hz, 1H), 8.10 (d, J = 8.7 Hz, 1H), 7.93 (dd, J = 7.2, 1.1 Hz, 1H), 7.36 (dd, J = 8.5, 7.1 Hz, 1H), 7.16 (m, 5H), 6.87 (m, 1H), 6.31 (d, J = 7.5 Hz, 1H), 4.93 (d, J = 2.4 Hz, 2H), 4.45 (s, 2H), 3.63 (t, J = 2.3 Hz, 1H). ^{13}C NMR (400 MHz, $DMSO_4$-D_6, δ): 166.8, 157.1, 155.6, 144.7, 136.7, 132,6, 130.6, 128.7,

126.3, 125.0, 123.7, 123.7, 123.3, 122.0, 121.5, 114.8, 112.8, 79,9, 78.8, 56.3. ESI-MS (*m/z*): $[M+Na]^+$ cacld for $C_{20}H_{17}NO_4SNa$, 390.0771; found, 390.0774.

Compound 15. Compound **1** (0.72 g, 1.8 mmol), compound **10** (0.87 g, 2.05 mmol), (benzotriazol-1-yloxy)tris(dimethylamino)phosphonium hexafluorophosphate (BOP, 1.59 g, 3.6 mmol), 1-hydroxybenzotriazole hydrate (HOBt, 0.486 g, 3.6 mmol), and N,N-diisopropylethyl-amine (DIPEA, 2.51 mL, 1.44 mmol) were dissolved in dimethyl sulfoxide (6 mL). The reaction mixture was stirred for 1 h in a microwave reactor at 65 °C (150 W), cooled down to room temperature, and poured into a dilute HCl aqueous solution (0.05 M, 15 mL). The precipitate formed was collected by suction filtration, washed with water, dried in air, and purified by column chromatography over silica gel with 20:1 dichloromethane/methanol as the eluent to give an off-white powder (1.12 g, 79%). ^{1}H NMR (600 MHz, $CD_3OD/CDCl_3$, 1:1, δ): 7.75 (d, J = 7.5 Hz, 2H), 7.62 (dd, J = 10.7, 7.5 Hz, 2H), 7.37 (t, J = 7.4 Hz, 2H), 7.29 (t, J = 7.3 Hz, 2H), 4.41 (dd, J = 10.5, 6.9 Hz, 1H), 4.34 (dd, J = 10.7, 7.1 Hz, 1H), 4.24 (t, J = 7.1 Hz, 2H), 4.02 (s, 1H), 4.45 (s, 2H), 3.63 (t, 1H), 4.02 (s, 1H), 3.95 (s, 1H), 3.82 (s, 1H, 3.72 (S, 3H), 3.64 (s, 3H), 2.59-0.80 (series of m, 38H), 0.67 (s, 3H). ^{13}C NMR (150 MHz, $CD_3OD/CDCl_3$, 1:1, δ): 175.5, 172.8, 172.6, 157.1, 143.8, 143.6, 141.3, 141.2, 127.6, 127.6, 126.9, 124.9, 124.9, 119.8, 72.8, 67.9, 66.8, 53.6, 52.1, 51.2, 48.3, 48.0, 47.1, 46.7, 46.3, 45.8, 41.6, 36.9, 36.2, 36.2, 35.3, 35.0, 34.1, 33.2, 32.2, 30.9, 30.7, 38.3, 27.9, 27.39, 25.9, 24.3, 23.0, 22.6, 16.7, 12.2. ESI-MS (*m/z*): $[M+H]^+$ cacld for $C_{46}H_{63}N_2O_9$, 787.4538; found, 787.4529.

Compound 16. Compound **15** (0.30 g, 0.038 mmol) was dissolved in an aqueous solution of piperidine (0.2 mL, 20%). After the reaction mixture was stirred for 2 h at room temperature, it was concentrated by rotary evaporation. The residue (0.020 mg, 0.0381 mmol) was then

mixed with compound **22** (0.017 mg, 0.040 mg), (benzotriazol-1-yloxy)tris(dimethylamino)phospho-nium hexafluorophosphate (BOP, 0.057 mg, 0.042 mmol), 1-hydroxybenzotriazole hydrate (HOBt, 0.077 mg, 0.040 mg), and N,N-diisopropylethylamine (DIPEA, 0.053 mL, 0.305 mmol) in dry DMF (1 mL). The reaction mixture was stirred for 2 h in a microwave reactor at 90 °C (150 W), extracted with ethyl acetate (3 × 5 mL), washed with water (5 mL), and dried with $MgSO_4$. The solvent was removed by rotary evaporation, and the residue was purified by a flash column chromatograph over silica gel with 10:1 dichloromethane/methanol as the eluent to give a white powder (30 mg, 77%). ^{1}H NMR (600 MHz, $CD_3OD/CDCl_3$, 1:1, δ): 7.55 (d, J = 7.0 Hz, 1H), 4.39 (dd, J = 9.3, 4.8 Hz, 1H), 3.99 (s, 1H), 3.93 (d, 2H), 3.88 (s, 1H), 3.80 (3.80 (d, J = 4.0 Hz, 2H), 3.71 (s, 3H), 3.64 (s, 3H), 2.60-0.80 (series of m), 0.68 (s, 6H). ^{13}C NMR (150 MHz, $CD_3OD/CDCl_3$, 1:1, δ): 175.5, 172.7, 172.6, 77.7, 77.5, 77.3, 72.8, 72.8, 67.9, 67.9, 58.8, 52.1, 51.9, 51.2, 48.3, 48.1, 47.9, 47.8, 46.8, 46.3, 46.3, 45.8, 41.6, 41.6, 39.4, 39.4, 36.9, 36.9, 35.5, 35.3, 35.1, 35.1, 34.2, 33.9, 33.2, 32.8, 32.2, 31.7, 30.9, 30.7, 30.6, 28.4, 27.5, 27.4, 26.0, 24.2, 23.0, 22.6, 22.5, 18.4, 16.8, 16.7, 12.2. ESI-MS (*m/z*): $[M+H]^+$ cacld for $C_{55}H_{90}N_5O_{10}$, 980.6688; found, 980.6680.

Compound 17. Compound **16** (0.060 g, 0.062 mmol), compound **2** (0.026 g, 0.067 mmol), $CuSO_4 \cdot 5H_2O$ (0.015 g, 0.062 mmol), and sodium ascorbate (0.024 g, 0.122 mmol) were dissolved in a 2:1:1 THF/MeOH/H_2O mixture (1.2 mL). The reaction mixture was stirred overnight at 45 °C. TLC showed completion of the reaction. The organic solvents were removed *in vacuo* and the residue was combined with water (10 mL). The precipitate formed was collected by suction filtration, dried in air, and purified by preparative TLC using 5:1 dichloromethane/methanol as the developing solvent to give a white powder (67 mg ,79%).

^{1}H NMR (600 MHz, $CD_3OD/CDCl_3$, 1:1, δ): 8.20 (d, *J* = 8.7 Hz, 1H), 8.15 (d, *J* = 7.2 Hz, 1H), 8.03 (d, *J* = 8.5 Hz, 1H), 7.59 (m, 2H), 7.35 (m, 3H), 7.26 (td, *J* = 7.8, 1.7 Hz, 1H), 7.07 (d, *J* = 8.2 Hz, 2H), 6.92 (td, *J* = 7.5, 1.0 Hz, 1H), 6.64 (d, *J* = 7.6 Hz, 1H), 5.26 (s, 2H), 4.46 (d, *J* = 4.0 Hz, 2H), 4.39 (m, 2H), 4.33 (s, 1H), 4.00 (s, 1H), 3.97 (d, *J* = 3.2 Hz, 1H), 3.93 (t, *J* = 2.9 Hz, 2H), 3.81 (m, 2H), 3.77 (m, 2H), 3.71 (s, 3H), 3.63 (s, 3H), 2.78 (t, *J* = 14.3 Hz, 1H), 2.52 (t, *J* = 14.2, 4.3 Hz, 1H), 2.40-0.80 (series of m), 0.68 (s, 6H). ^{13}C NMR (150 MHz, $CD_3OD/CDCl_3$, 1:1, δ): 175.6, 175.4, 172.8, 172.6, 156.3, 149.4, 143.9, 140.7, 136.0, 130.1, 129.3, 128.3, 127.4, 127.3, 125.5, 124.4, 123.7, 122.5, 121.1, 115.5, 112.0, 105.2, 77.9, 77.7, 77.5, 72.7, 72.7, 67.9, 67.6, 61.9, 57.3, 53.4, 52.1, 51.8, 51.0, 48.9, 47.8, 47.6, 46.7, 46.2, 46.2, 45.8, 43.8, 41.7, 41.6, 39.4, 36.9, 35.5, 35.3, 35.0, 34.6, 34.2, 33.7, 33.2, 32.6, 32.1, 32.0,31.7, 30.9, 30.8, 30.7, 30.6, 30.2, 29.5, 28.4, 27.4, 26.5, 25.9, 24.2, 23.0, 22.4, 18.3, 16.6, 16.6, 12.0. ESI-MS (*m/z*): $[M+H]^+$ cacld for $C_{75}H_{107}N_6O_{14}S$, 1347.7566; found 1347.7366.

Compound 1. A solution of compound **17** (0.044 g, 0.033 mmol) in 2 M lithium hydroxide (0.32 mL, 0.64 mmol) and methanol (2 mL) was stirred at room temperature for 4 h. The organic solvent was removed by rotary evaporation. After a dilute HCl solution (0.05 M, 30 mL) was added to the mixture, the precipitate formed was collected by suction filtration, washed with cold water, and dried *in vacuo* to get a white powder (43 mg, 99%). To obtain the sodium salt of this compound, the above acid was mixed with saturated sodium bicarbonate (0.5 mL) and methanol (5 mL). The reaction mixture was stirred for 5 h. After the solvents were removed by rotary evaporation, the residue was dissolved in methanol (5 mL). The solution was filtered and then concentrated by rotary evaporation to give the sodium salt as a white powder. ^{1}H NMR (600 MHz, $CD_3OD/CDCl_3$, 1:1, δ): 8.20 (d, *J* = 8.7

Hz, 1H), 8.15 (d, *J* = 7.2 Hz, 1H), 8.03 (d, *J* = 8.5 Hz, 1H), 7.59 (m, 2H), 7.35 (m, 3H), 7.26 (td, *J* = 7.8, 1.7 Hz, 1H), 7.07 (d, *J* = 8.2 Hz, 2H), 6.92 (td, *J* = 7.5, 1.0 Hz, 1H), 6.64 (d, *J* = 7.6 Hz, 1H), 5.26 (s, 2H), 4.46 (d, *J* = 4.0 Hz, 2H), 4.39 (m, 2H), 4.33 (s, 1H), 4.00 (s, 1H), 3.97 (d, *J* = 3.2 Hz, 1H), 3.93 (t, *J* = 2.9 Hz, 2H), 3.81 (m, 2H), 3.77 (m, 2H), 2.78 (t, *J* = 14.3 Hz, 1H), 2.52 (t, *J* = 14.2, 4.3 Hz, 1H), 2.40-0.80 (series of m), 0.68 (s, 6H). ^{13}C NMR (150 MHz, $CD_3OD/CDCl_3$, 1:1, δ): 189.8, 174.5, 173.7, 156.2, 143.9, 143.3, 130.1, 128.5, 127.8, 127.7, 126.9, 126.7, 125.2, 124.3, 123.8, 123.1, 122.2, 120.8, 115.1, 112.0, 99.5, 78.2, 77.8, 77.5, 72.7, 72.5, 67.7, 67.5, 61.5, 57.2, 54.3, 52.9, 47.6, 47.2, 47.0, 46.9, 46.7, 46.2, 46.2, 42.9, 41.6, 41.5, 39.5, 39.5, 37.0, 36.8, 35.6, 34.9, 34.6, 34.6, 34.1, 33.6, 33.2, 33.0, 32.6, 32.1, 31.8, 30.5, 30.2, 29.6, 29.3, 27.3, 26.5, 25.9, 24.2, 22.9, 22.8, 22.1, 22.1, 22.0, 16.4, 16.4, 11.6. ESI-MS (*m/z*): $[M+H]^+$ cacld for $C_{73}H_{103}N_6O_{14}S$, 1319.7253; found, 1319.7199.

Compound 24. Compound **16** (0.070 g, 0.071 mmol), 1, 3, 5-triethynylbenzene (0.026 g, 0.017 mmol), $CuSO_4 \cdot 5H_2O$ (0.013 g, 0.053 mmol), and sodium ascorbate (0.021 g, 0.107 mmol) were dissolved in a 2:1:1 THF/MeOH/H_2O mixture (1.6 mL). The reaction mixture was stirred overnight at 45 °C. TLC showed completion of the reaction. The organic solvents were removed *in vacuo* and the residue was combined with water (10 mL). The precipitate formed was collected by suction filtration, dried in air, and purified by preparative TLC using 5:1 dichloromethane/methanol as the developing solvent to give a white powder (25 mg, 48%). ^{1}H NMR (600 MHz, $CD_3OD/CDCl_3$, 1:1, δ): 8.34 (s, 3H), 8.29 (s, 3H), 7.54 (d, *J* = 7.1 Hz, 3H), 4.40 (dd, *J* = 9.1, 4.8 Hz, 3H), 3.99 (d, *J* = 12.2 Hz, 6H), 3.93 (d, *J* = 3.0 Hz, 3H), 3.85 (d, *J* = 3.9 Hz, 3H), 3.80 (m, 3H), 3.71 (s, 9H), 3.63 (s, 9H), 3.03 (t, *J* = 13.8 Hz, 3H), 2.52 (td, *J* = 14.3, 4.4 Hz, 3H),), 2.40-0.80 (series of m), 0.69 (s, 18H). ^{13}C NMR (150

MHz, $CD_3OD/CDCl_3$, 1:1, δ): 176.2, 176.1, 173.4, 173.2, 147.2, 135.8, 132.6, 122.8, 121.1, 78.6, 78.4, 78.2, 77.9, 73.5, 68.6, 68.5, 58.1, 52.8, 52.6, 51.9, 49.6, 49.4, 49.4, 49.2, 49.0, 48.7, 48.5, 48.3, 47.4, 47.0, 47.0, 46.5, 42.4, 42.3, 40.1, 40.1, 37.7, 37.6, 36.2, 36.0, 35.7, 35.6, 34.9, 34.6, 33.9, 33.4, 33.0, 32.9, 32.4, 31.6, 31.4, 31.3, 30.2, 29.1, 28.2, 28.1, 27.3, 26.6, 25.1, 24.9, 23.7, 23.3, 23.2, 17.5, 17.4, 12.9. ESI-MS (*m/z*): $[M+3H]^+$ cacld for $C_{177}H_{276}N_{15}O_{30}$, 3094.0600; found, 3094.5205.

Compound 3. A solution of compound **24** (0.050 g, 0.016 mmol) in 2 M lithium hydroxide (0.48mL, 0.97 mmol) and methanol (4 mL) was stirred at room temperature for 4 h. The organic solvent was removed by rotary evaporation. After a dilute HCl solution (0.05 M, 30 mL) was added to the reaction mixture, the precipitate formed was collected by suction filtration, washed with cold water, and dried *in vacuo* to get a white powder (48 mg, 100%). To obtain the sodium salt of this compound, the above acid was mixed with saturated sodium bicarbonate (0.5 mL) and methanol (5 mL). The reaction mixture was stirred for 5 h. After the solvents were removed by rotary evaporation, the residue was dissolved in methanol (5 mL). The solution was filtered and then concentrated by rotary evaporation to give the sodium salt as a white powder. ^{1}H NMR (600 MHz, $CD_3OD/CDCl_3$, 1:1, δ): 9.01 (s, 3H), 8.55 (s, 3H), 4.79 (s, 3H), 4.39 (dd, J = 9.1, 4.7 Hz, 3H), 4.01 (s, 3H), 3.97 (s, 3H), 3.92 (t, J = 2.7 Hz, 3H), 3.85 (s, 3H), 3.80 (d, J = 2.9 Hz, 3H), 3.06 (s, 2H), 2.50 (t, J = 13.6 Hz, 3H), 2.40-0.80 (series of m), 0.67 (d, J = 7.5 Hz, 18H). ^{13}C NMR (150 MHz, $CD_3OD/CDCl_3$, 1:1, δ): 176.2, 176.1, 173.4, 173.2, 147.2, 135.8, 132.6, 122.8, 121.1, 78.6, 78.4, 78.2, 77.9, 73.5, 68.6, 68.5, 58.1, 52.8, 52.6, 51.9, 47.0, 47.0, 46.5, 42.4, 42.3, 40.1, 40.1, 37.7, 37.6, 36.2, 36.0, 35.7, 35.6, 34.9, 34.6, 33.9, 33.4, 33.0, 32.9, 32.4, 31.6, 31.4, 31.3, 30.2, 29.1, 28.2,

28.1, 27.3, 26.6, 25.1, 24.9, 23.7, 23.3, 23.2, 17.5, 17.4, 12.9. ESI-MS (*m/z*): $[M]^+$ cacld for $C_{171}H_{261}N_{15}O_{30}$, 3005.9392; found, 3005.2965.

Compound 26. Compound **25** (0.316 g, 2.45 mmol,) 1,3,5-triethynylbenzene (0.105 g, 0.7 mmol), $CuSO_4 \cdot 5H_2O$ (0.349 g, 1.4 mmol), and sodium ascorbate (0.55 g, 2.8 mmol) were dissolved in a 2:1:1 THF/MeOH/H_2O mixture (2 mL). The reaction mixture was stirred overnight at 45 °C. TLC showed completion of the reaction. The organic solvents were removed *in vacuo* and the residue was combined with water (10 mL). The precipitate formed was collected by suction filtration, dried in air, and purified by preparative TLC using 10:1 dichloromethane/methanol as the developing solvent to give a white powder (25 mg, 48%). ^{1}H NMR (400 MHz, $CDCl_3$, δ): 8.11 (d, J = 3.6 Hz, 3H), 8.04 (d, J = 3.3 Hz, 3H), 5.22 (d, J = 7.1 Hz, 6H), 4.25 (q, J = 7.1 Hz, 6H), 3.79 (m, 3H), 1.27 (t, J = 2.1 Hz, 9H). ^{13}C NMR (100 MHz, $CDCl_3$, δ): 166.9, 147.3, 131.4, 131.3, 122.4, 51.0, 14.1. ESI-MS (*m/z*): $[M+H]^+$ cacld for $C_{24}H_{28}N_9O_6$, 538.2157; found, 538.2155.

Compound 4. A solution of compound **26** (0.080 g, 0.015 mmol) in 2 M lithium hydroxide (4.8 mL, 8.92 mmol) and methanol (6 mL) was stirred at room temperature for 4 h. The organic solvent was removed by rotary evaporation. After a dilute HCl solution (0.05 M, 30 mL) was added to the reaction mixture, the precipitate formed was collected by suction filtration, washed with cold water, and dried *in vacuo* to get a white powder (80 mg, 100%). To obtain the sodium salt of this compound, the above acid was mixed with saturated sodium bicarbonate (0.5 mL) and methanol (5 mL). The reaction mixture was stirred for 5 h. After the solvents were removed by rotary evaporation, the residue was dissolved in methanol (5 mL). The solution was filtered and then concentrated by rotary evaporation to give the sodium salt as a white powder. ^{1}H NMR (600 MHz, $CDCl_3$, δ): 8.53 (s, 3H), 8.31 (s, 3H),

5.16 (s, 6H). ^{13}C NMR (150 MHz, $CDCl_3$, δ): 146.5, 131.9, 123.2, 122.0, 62.8. ESI-MS (*m/z*): $[M-H]^+$ cacld for $C_{18}H_{14}N_9O_6$, 452.1073; found, 452.1075.

Compound 30. A solution of 4-aminioisophthalate (400 mg, 1.91 mmol) in conc. HCl (3.5 mL), and H_2O (1.5 mL) was cooled below 5 °C in an ice bath. A solution of $NaNO_2$ (197 mg, 2.86 mg) in water (0.80 mL) chilled to 0 °C was added dropwise over 1 h to the 4-aminioisophthalate solution while the temperature of the reaction mixture was maintained below 5 °C. After 1 h, NaN_3 (186 mg, 2.86 mmol) was added slowly. After the reaction mixture was stirred for 3 h, the precipitate was collected by suction filtration to give a while powder (0.445, 97%). ^{1}H NMR (400 MHz, $CDCl_3$, δ): 8.53 (s, 1H), 8.18 (m, 1H), 7.30 (d, *J* = 8.5 Hz, 1H), 3.93 (s, 7H). ^{13}C NMR (600 MHz, $CDCl_3$, δ): 133.9, 133.3, 119.7, 52.4, 52.3. ESI-MS (*m/z*): $[M+H]^+$ cacld for $C_{10}H_{10}N_3O_4$, 236.0671; found, 236.0681.

Compound 31. Compound **30** (0.360 g, 1.15 mmol), 1,3,5-triethynylbenzene (0.075 g, 0.490 mmol), $CuSO_4 \cdot 5H_2O$ (0.248 g, 0.990 mmol), and sodium ascorbate (0.395 g, 1.99 mmol) were dissolved in a 2:1:1 THF/MeOH/H_2O mixture (4 mL). The reaction mixture was stirred overnight at 45 °C. TLC showed completion of the reaction. The organic solvents were removed *in vacuo* and the residue was combined with water (10 mL). The precipitate formed was collected by suction filtration, dried in air, and purified by preparative TLC using 10:1 dichloromethane/methanol as the developing solvent to give a white powder (110 mg, 33%). ^{1}H NMR (400 MHz, $CDCl_3$, δ): 8.69 (q, *J* = 2.0 Hz, 3H), 8.52 (m, 3H), 8.39 (dt, *J* = 8.2, 2.1 Hz, 3H), 8.36 (d, *J* = 2.1 Hz, 3H), 7.70 (dd, *J* = 8.2, 2.1 Hz, 3H), 4.02 (s, 9H), 3.82 (m, 9H). ^{13}C NMR (150 MHz, $CDCl_3$, δ): 165.0, 147.2, 139.0, 133.7, 132.6, 131.6, 127.5, 126.4, 122.9, 121.9, 53.0. ESI-MS (*m/z*): $[M+H]^+$ cacld for $C_{42}H_{34}N_9O_{12}$, 856.2321; found, 856.2322.

Compound 6. A solution of compound **31** (0.110 g, 0.128 mmol) in 2 M lithium hydroxide (3.80 mL, 7.70 mmol) and methanol (15 mL) was stirred at room temperature for 7 h. The organic solvent was removed by rotary evaporation. After a dilute HCl solution (0.05 M, 30 mL) was added to the reaction mixture, the precipitate formed was collected by suction filtration, washed with cold water, and dried *in vacuo* to get a yellow powder (109 mg, 100%). To obtain the sodium salt of this compound, the above acid was mixed with saturated sodium bicarbonate (0.8 mL) and methanol (5 mL). The reaction mixture was stirred for 5 h. After the solvents were removed by rotary evaporation, the residue was dissolved in methanol (5 mL). The solution was filtered and then concentrated by rotary evaporation to give the sodium salt as a yellow powder. ^{1}H NMR (400 MHz, $CDCl_3$, δ): 8.69 (q, J = 2.0 Hz, 3H), 8.52 (m, 3H), 8.39 (dt, J = 8.2, 2.1 Hz, 3H), 8.36 (d, J = 2.1 Hz, 3H), 7.70 (dd, J = 8.2, 2.1 Hz, 3H). ^{13}C NMR (150 MHz, $CDCl_3$, δ): 165.0, 147.2, 139.0, 133.7, 132.6, 131.6, 127.5, 126.4, 122.9, 121.9. ESI-MS (*m/z*): $[M+H]^+$ cacld for $C_{36}H_{22}N_9O_{12}$, 772.1382; found, 772.1369.

Compound 32. Compound **16** (0.230 g, 0.234 mmol), 1,4-diethynylbenzene (0.015 g, 0.117 mmol), $CuSO_4 \cdot 5H_2O$ (0.058 g, 0.234 mmol), and sodium ascorbate (0.046 g, 0.234 mmol) were dissolved in a 2:1:1 THF/MeOH/H_2O mixture (2 mL). The reaction mixture was stirred overnight at 45 °C. TLC showed completion of the reaction. The organic solvents were removed *in vacuo* and the residue was combined with water (10 mL). The precipitate formed was collected by suction filtration, dried in air, and purified by preparative TLC using 5:1 dichloromethane/methanol as the developing solvent to give a white powder (43 mg, 18%). ^{1}H NMR (600 MHz, $CD_3OD/CDCl_3$ = 1:1, δ): 8.23 (s, 2H), 7.89 (s, 3H), 7.60 (d, J = 7.2 Hz, 1H), 4.39 (dd, J = 9.2, 4.9 Hz, 2H), 3.99 (d, J = 9.8 Hz, 4H), 3.93 (t, J = 3.1 Hz, 2H), 3.85 (d,

J = 3.9 Hz, 2H), 3.80 (d, *J* = 3.8 Hz, 3H), 3.71 (s, 6H), 3.64 (s, 6H), 3.01 (t, *J* = 13.8 Hz, 2H), 2.53 (td, *J* = 13.8 and 4.4 Hz, 2H), 2.51-0.80 (series of m), 0.70 (s, 12H). ^{13}C NMR (150 MHz, $CD_3OD/CDCl_3$ = 1:1, δ): 175.5, 175.4, 172.8, 172.5, 146.7, 130.3, 126.0, 120.0, 77.8, 77.6, 77.4, 72.8, 67.9, 67.8, 57.3, 52.1, 51.9, 51.1, 48.2, 47.7, 47.7, 46.8, 46.7, 46.3, 46.2, 45.8, 41.7, 41.6, 39.5, 39.4, 37.0, 36.9, 35.5, 35.3, 35.0, 34.9, 34.2, 33.8, 33.2, 32.7, 32.4, 32.2, 31.7, 30.9, 30.8, 30.7, 30.6, 28.4, 27.5, 27.4, 26.6, 25.9, 24.5, 24.2, 23.0, 22.5, 22.5, 16.7, 16.6, 12.1, 12.1. ESI-MS (*m*/*z*): $[M+Na]^+$ cacld for $C_{120}H_{184}N_{10}O_{20}Na$, 2108.3581; found, 2109.3555.

Compound 12. A solution of compound **32** (0.043 g, 0.021 mmol) in 2 M lithium hydroxide (0.40 mL, 0.80 mmol) and methanol (2 mL) was stirred at room temperature for 4 h. The organic solvent was removed by rotary evaporation. After addition of a dilute HCl solution (0.05 M, 20 mL), the precipitate formed was collected by suction filtration, washed with cold water, and dried *in vacuo* to get a white powder (109 mg, 100%). To obtain the sodium salt of this compound, the above acid was mixed with saturated sodium bicarbonate (0.8 mL) and methanol (5 mL). The reaction mixture was stirred for 5 h. After the solvents were removed by rotary evaporation, the residue was dissolved in methanol (5 mL). The solution was filtered and then concentrated by rotary evaporation to give the sodium salt as a white powder. ^{1}H NMR (600 MHz, $CD_3OD/CDCl_3$, 1:1, δ): 8.23 (s, 2H), 7.89 (s, 3H), 7.60 (d, *J* = 7.2 Hz, 1H), 4.39 (dd, *J* = 9.2, 4.9 Hz, 2H), 3.99 (d, *J* =.8 Hz, 4H), 3.93 (t, *J* = 3.1 Hz, 2H), 3.85 (d, *J* = 3.9 Hz, 2H), 3.80 (d, *J* = 3.8 Hz, 3H), 3.01 (t, *J* = 13.8 Hz, 2H), 2.53 (td, *J* = 13.8, 4.4 Hz, 2H),), 2.51-0.80 (series of m), 0.70 (d, *J* = 12.9 Hz, 12H). ^{13}C NMR (150 MHz, $CD_3OD/CDCl_3$, 1:1, δ): 177.6, 176.0, 174.1, 145.1, 130.7, 128.8, 127.4, 123.1, 78.3, 78.2, 78.0, 77.7, 73.4, 73.3, 68.5, 68.3, 60.0, 52.7, 52.5, 47.3, 47.2, 46.9, 46.8, 42.1, 39.9,

39.8, 37.5, 37.4, 36.0, 35.8, 35.6, 35.4, 34.6, 34.2, 33.6, 33.2, 32.7, 32.5, 32.1, 31.5, 31.2, 31.0, 28.9, 28.0, 27.1, 26.4, 24.7, 23.6, 23.1, 17.4, 17.3, 12.8. ESI-MS (*m*/*z*): $[M+Na]^+$ cacld for $C_{116}H_{176}N_{10}O_{20}Na$, 2053.7340; found, 2053.1953.

Compound 9. A reaction mixture of compound **36** (180 mg, 0.74 mg) and Raney-Ni (50 mg, suspension in water) in methanol (4 mL) saturated with NH_3 (3.8 mL) was sealed in an autoclave and stirred under hydrogen (16 bar) for 10 h at room temperature. The catalyst was removed by filtration through a layer of celite. The filtrate was concentrated by rotary evaporation to give a yellow powder (180 mg, 97%). ^{1}H NMR (400 MHz, MeOH/D_2O, δ): 6.09 (s, 3H), 4.19 (br, 6H), 3.28 (br, 6H). ^{13}C NMR (100 MHz, MeOH/D_2O, δ): 159.8, 97.1, 65.4, 48.7, 39.1 ESI-MS (*m*/*z*): $[M]^+$ cacld for $C_{12}H_{21}N_3O_3$, 255.1583; found, 255.2261.

Compound 14. A mixture of 1,4-phenylenedimethanamine (0.100 g, 0.74 mmol), 1H-pyrazole-1-carboxamidine hydrochloride (0.226 g 1.54 mmol), and triethyl amine (0.1 mL) in DMF (2 mL) was stirred at 60 °C under nitrogen. After 8 h, ether was added to the reaction mixture. The precipitate formed was collected by suction filtration, washed with ether, and dried in air. The crude product was crystallized from 1:1:0.5 ether/acetonitrile/ethanol (2.5 mL) to give a white powder (146 mg, 90%). ^{1}H NMR (600 MHz, D_2O, δ): 7.39 (s, 1H), 4.46 (s, 1H). ^{13}C NMR (600 MHz, D_2O, δ): 156.9, 135.8, 127.4, 44.2, . ESI-MS (*m*/*z*): $[M+H]^+$ cacld for $C_{10}H_{17}N_6$, 221.1509; found, 221.1507.

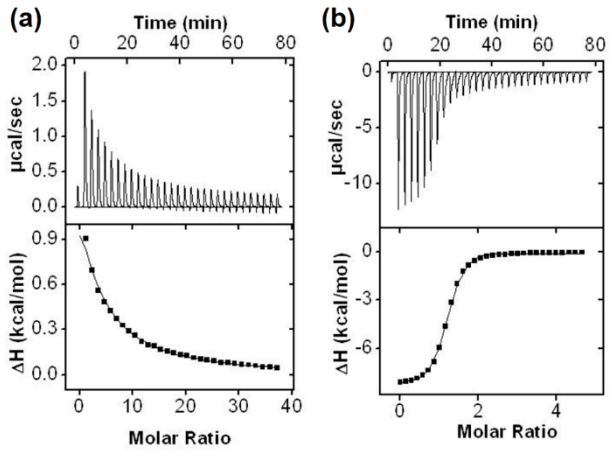

Figure 5. ITC titration curves obtained at 298 K for the binding of (a) **13** and (b) **14** by **12**. The data correspond to entries **12** and **13** in Table 1. In a typical experiment, a 2–6 mM aqueous solution of the guest in Millipore water was injected in equal steps of 10.0 µL into 1.42 mL of 0.05–0.2 mM solution of the host in Millipore water. The top panel shows the raw calorimetric data. The area under each peak represents the amount of heat generated at each ejection and is plotted against the molar ratio of the guest to the host. The smooth solid line is the best fit of the experimental data to the sequential binding of N equal and independent binding sites on the receptor. The heat of dilution for the guest, obtained by adding the guest to Millipore water, was subtracted from the heat released during the binding. Binding parameters were auto-generated after curve fitting using Microcal Origin 7.

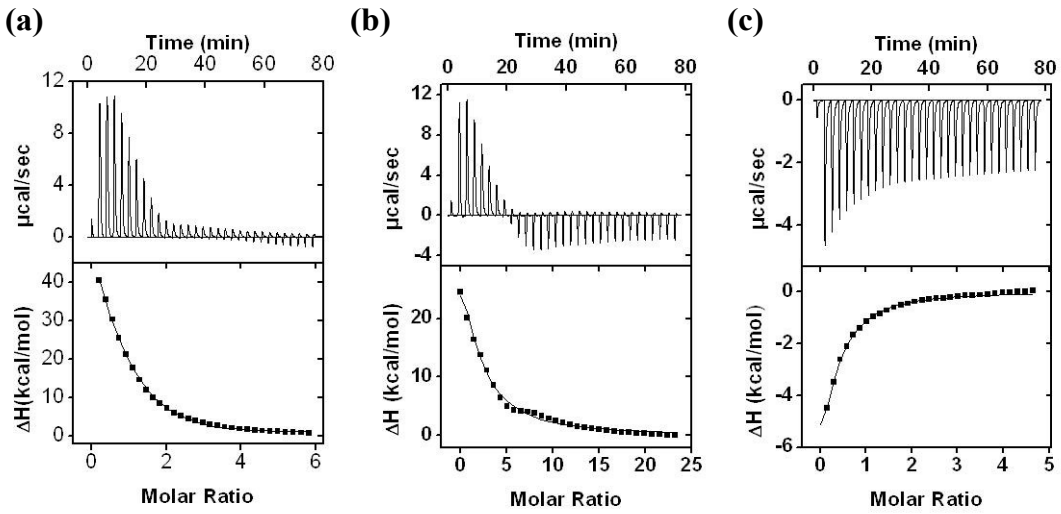

Figure 6. ITC titration curves obtained at 298 K for the binding of **7** by **3** in **(**a) 80:20 water/methanol, (b) 60:40 water/methanol, and (c) PBS buffer (pH 7.4, 137 mM NaCl, 2.7 mM KCl) mixture. The data correspond to entries 2–4 in Table 1. The top panel shows the raw calorimetric data. The area under each peak represents the amount of heat generated at each ejection and is plotted against the molar ratio of the guest to the host. The smooth solid line is the best fit of the experimental data to the sequential binding of *N* equal and independent binding sites on the receptor. The heat of dilution for the guest, obtained by adding the guest to Millipore water, was subtracted from the heat released during the binding. Binding parameters were auto-generated after curve fitting using Microcal Origin 7.

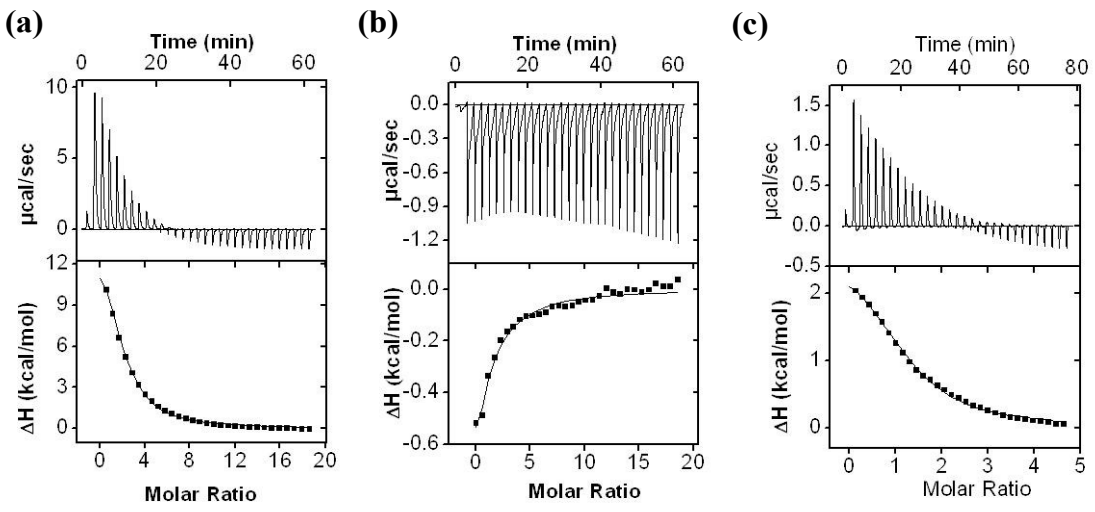

Figure 7. ITC titration curves obtained at 298 K for the binding of (a) **8**, (b) **9**, and (c) **11** by **3** in water. The data correspond to entries 5, 6, and 8 in Table 1. The top panel shows the raw calorimetric data. The area under each peak represents the amount of heat generated at each ejection and is plotted against the molar ratio of the guest to the host. The smooth solid line is the best fit of the experimental data to the sequential binding of *N* equal and independent binding sites on the receptor. The heat of dilution for the guest, obtained by adding the guest to Millipore water, was subtracted from the heat released during the binding. Binding parameters were auto-generated after curve fitting using Microcal Origin 7.

^{1}H and ^{13}C NMR spectra

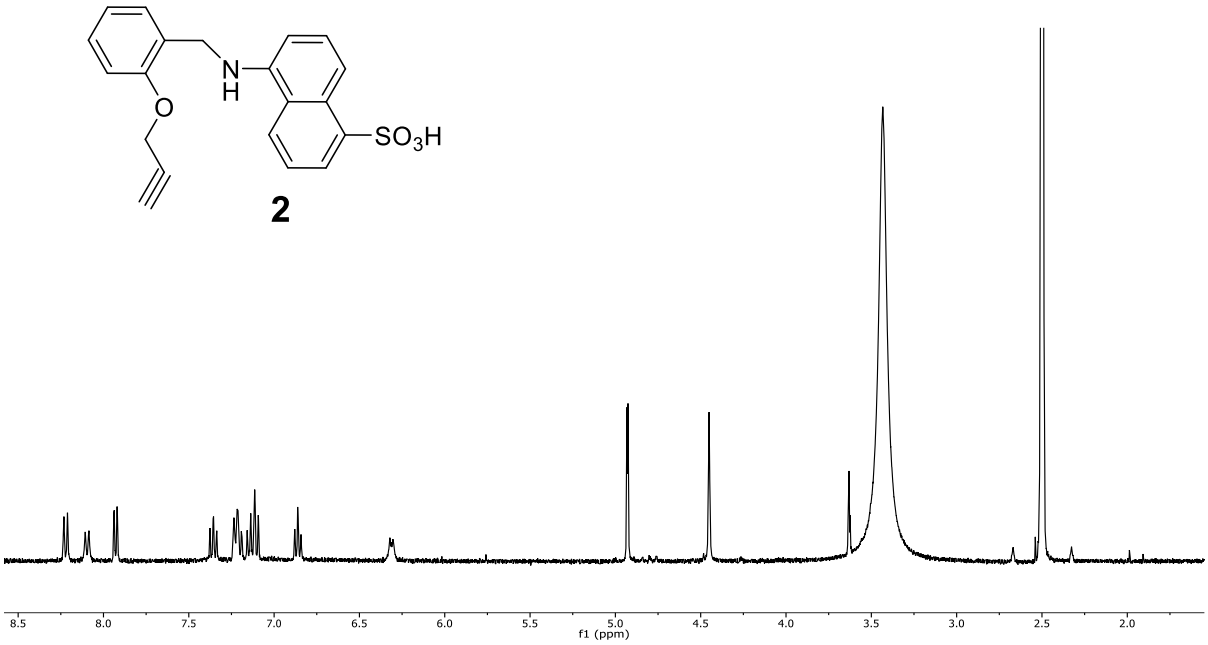

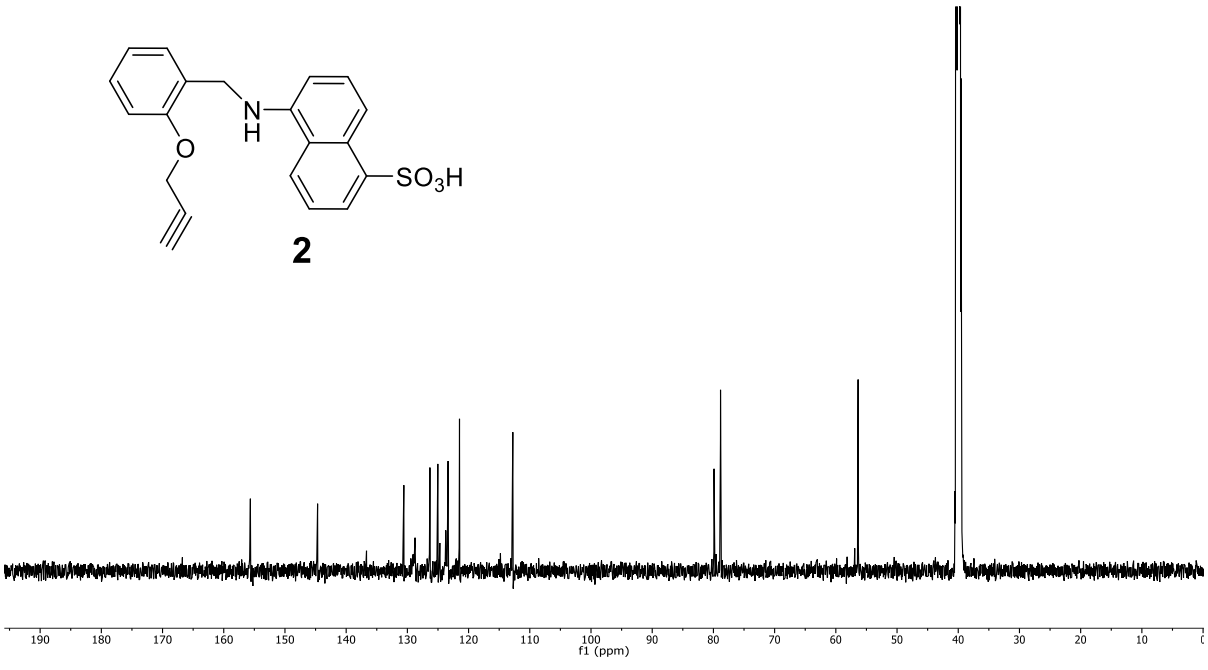

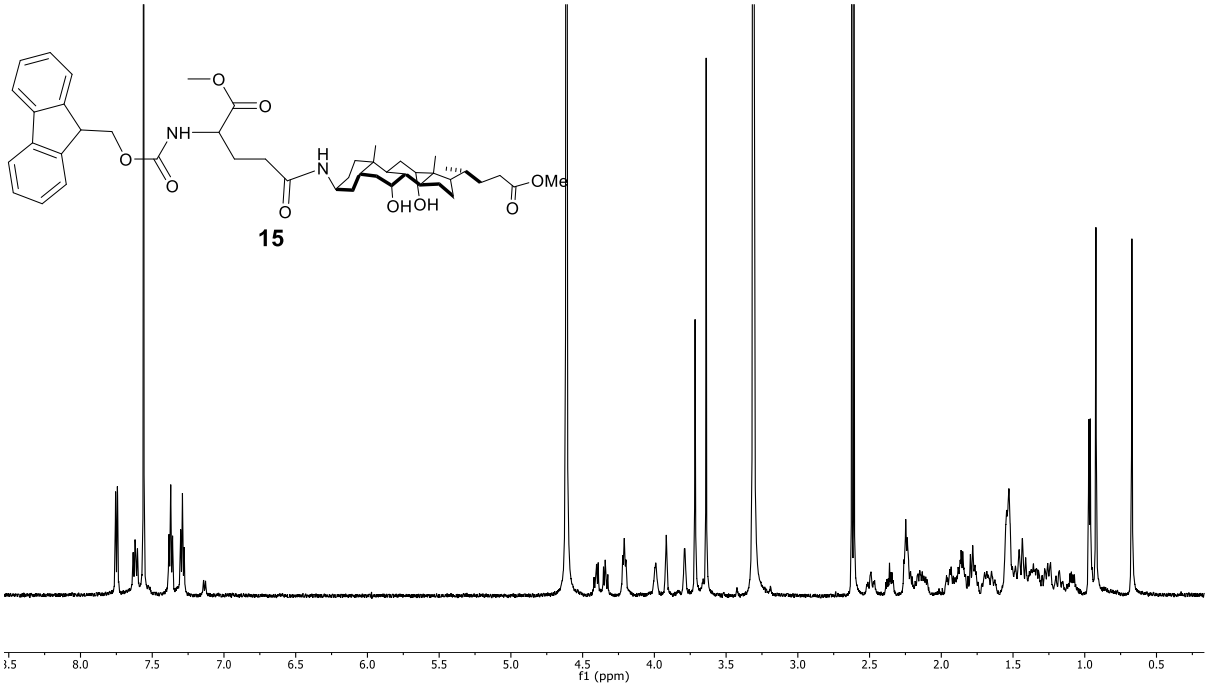

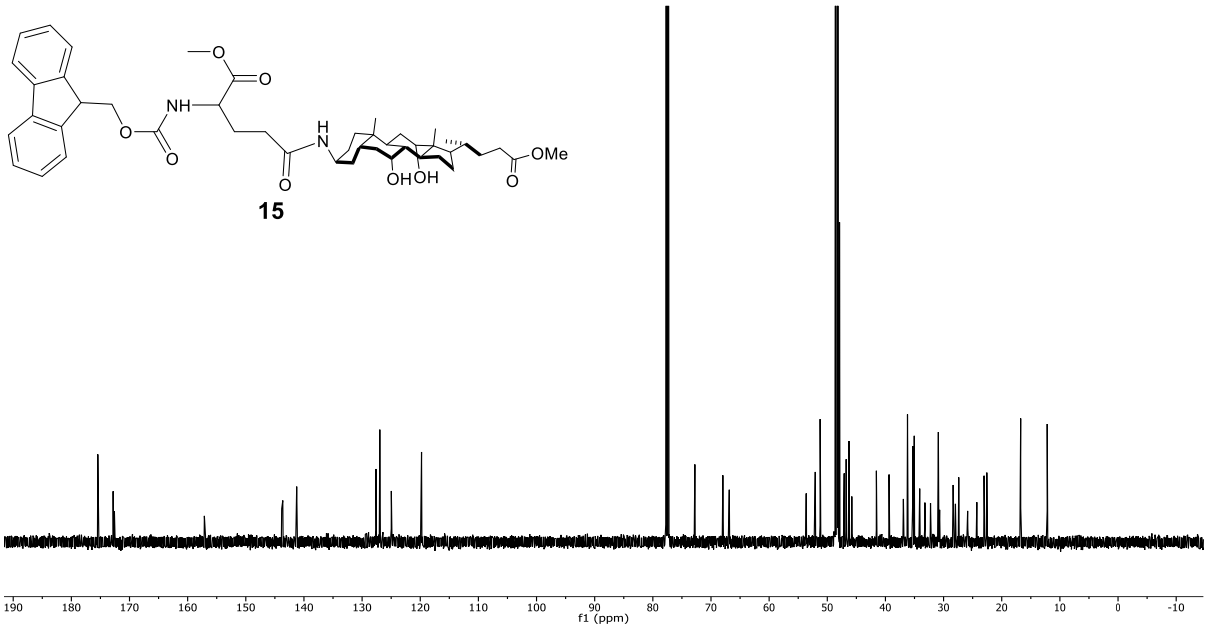

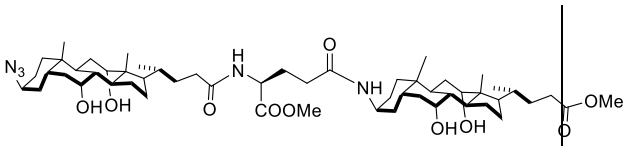

16

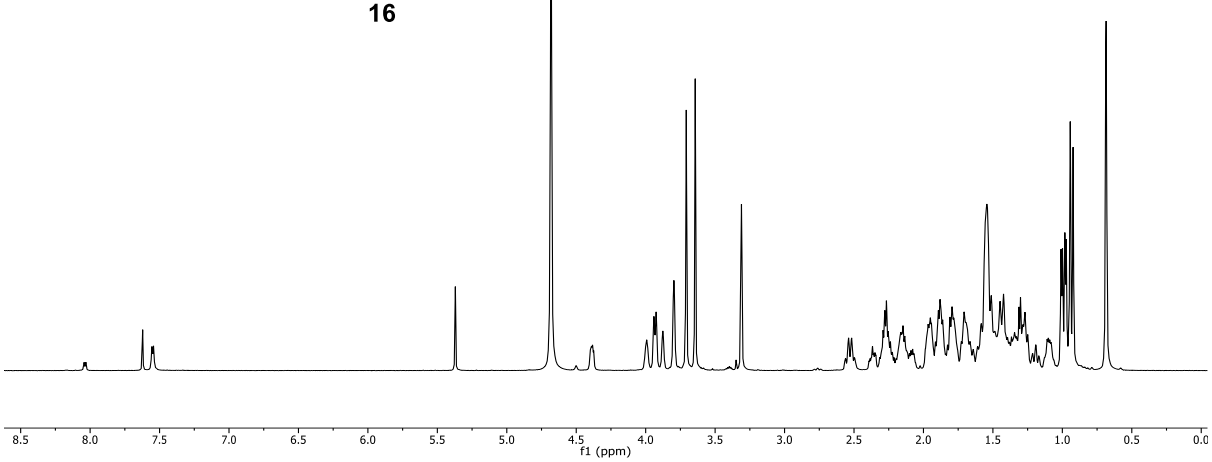

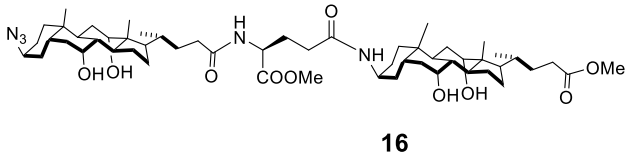

16

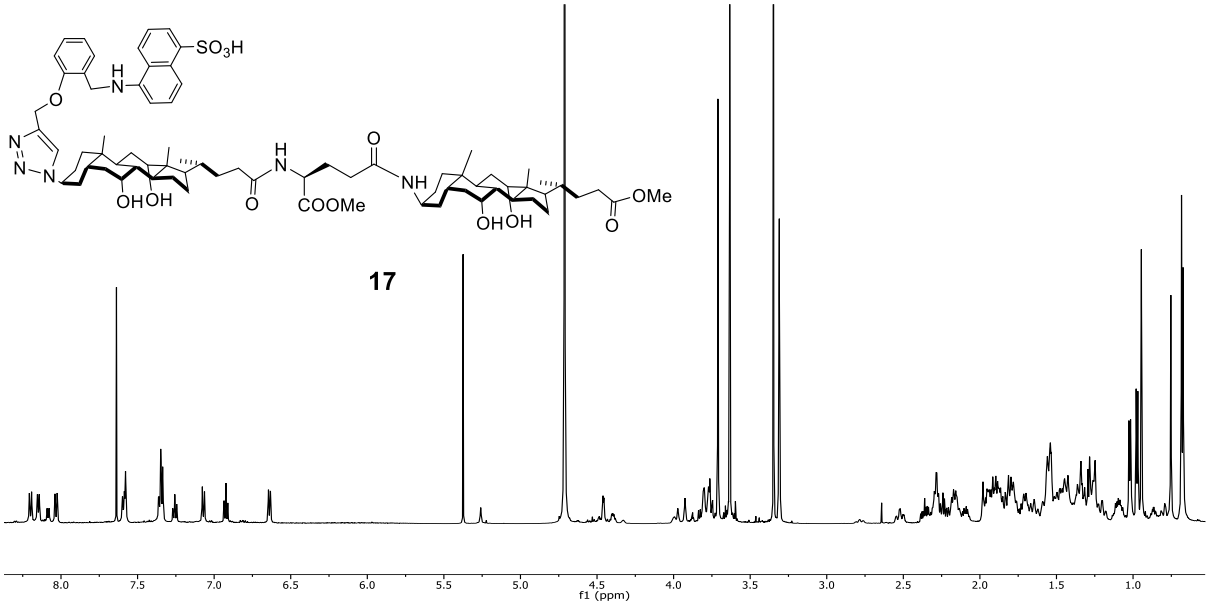

17

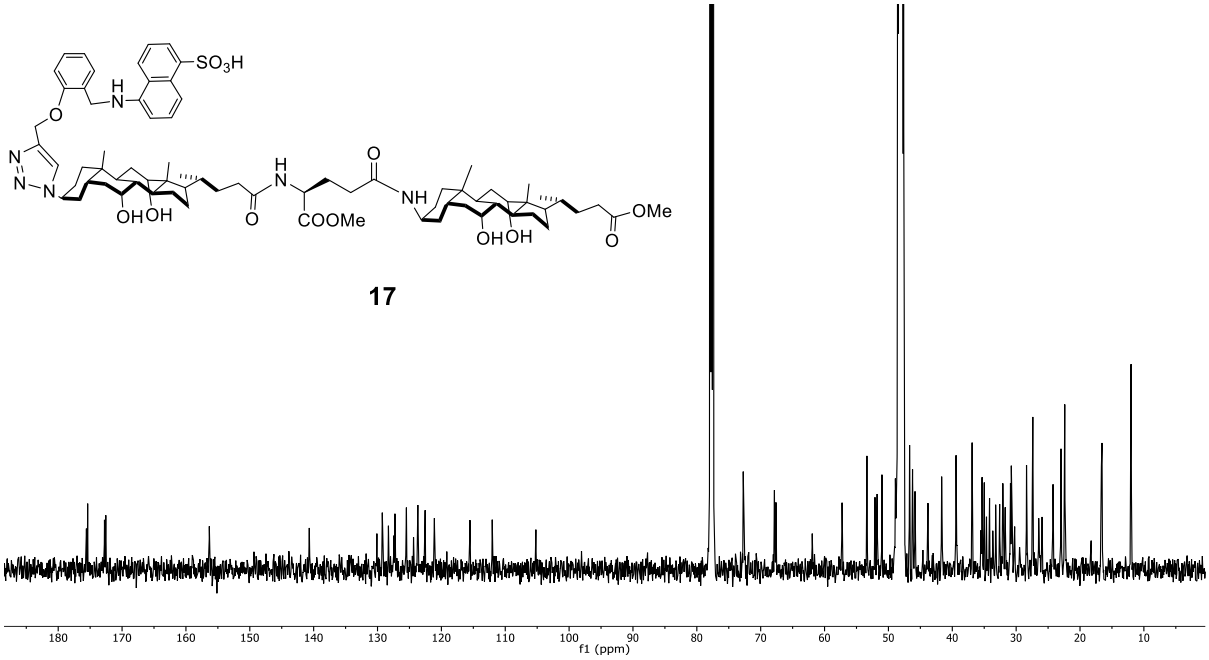

17

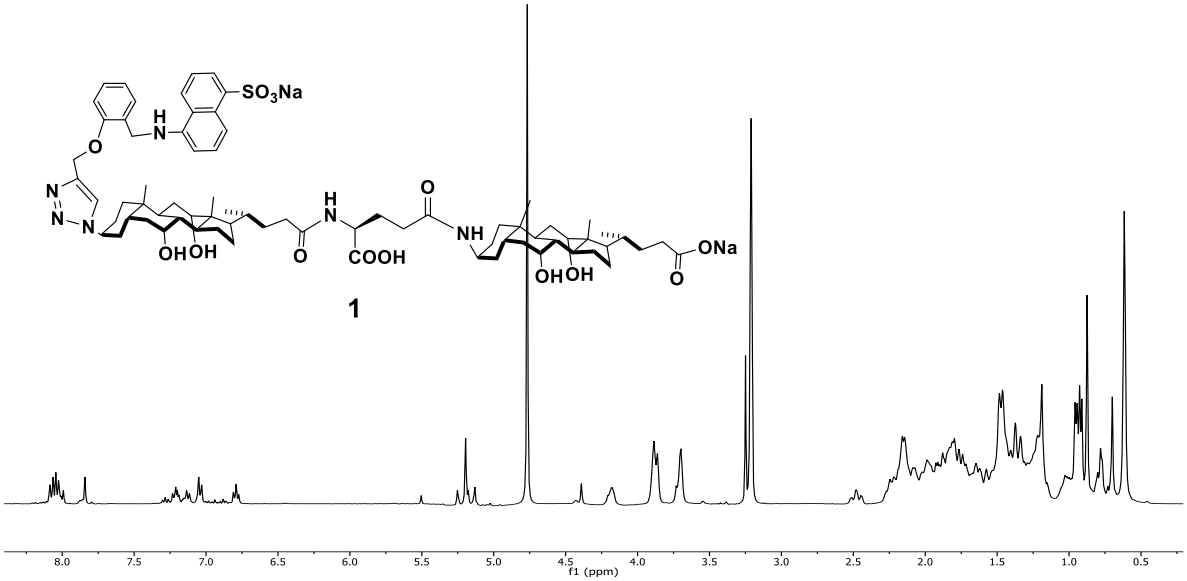

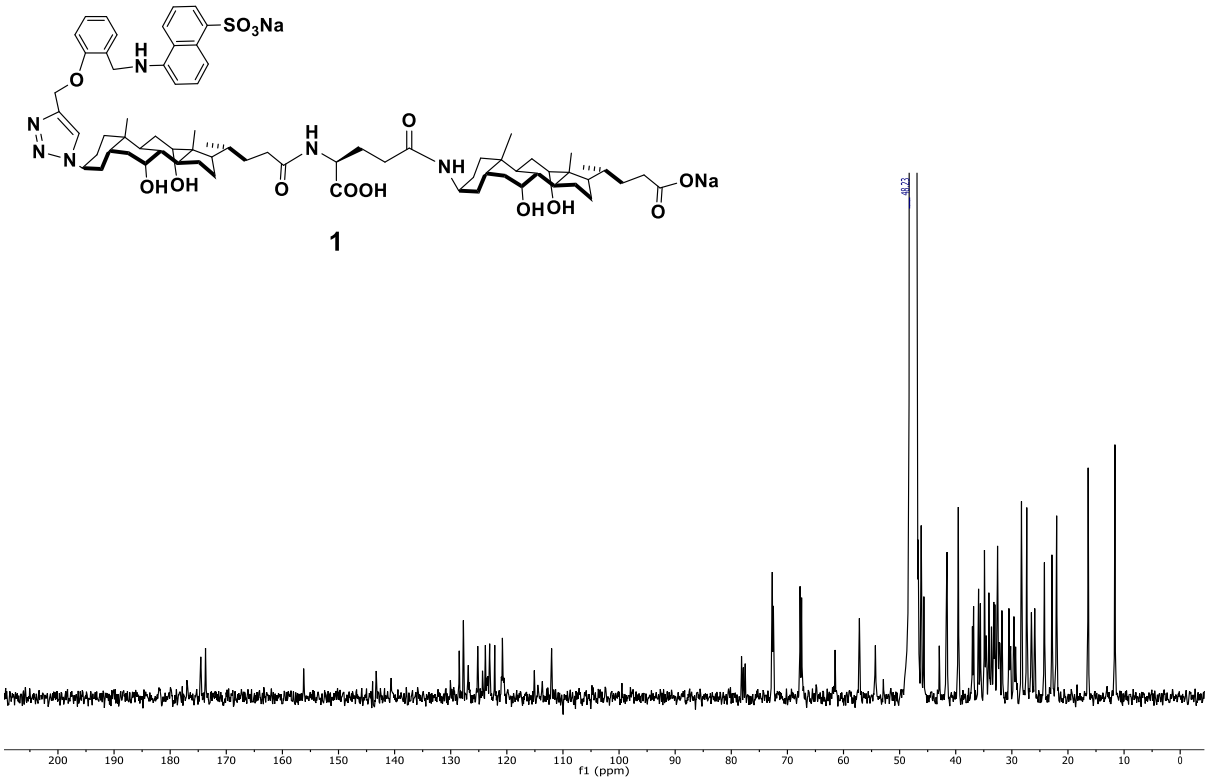

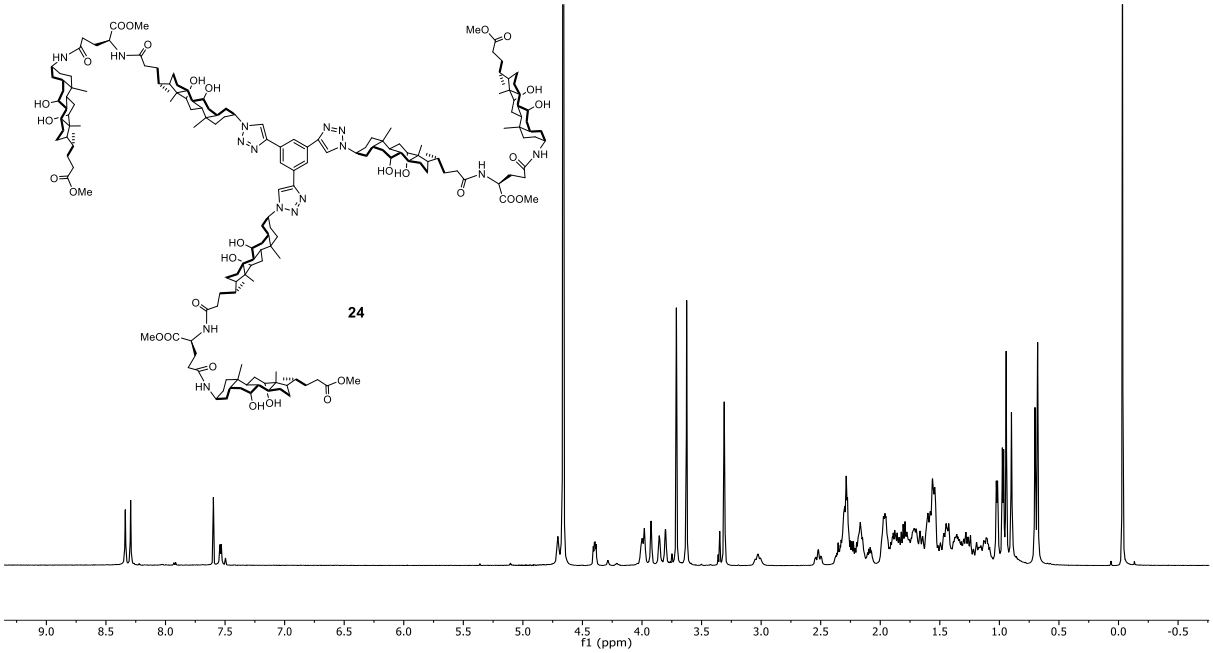

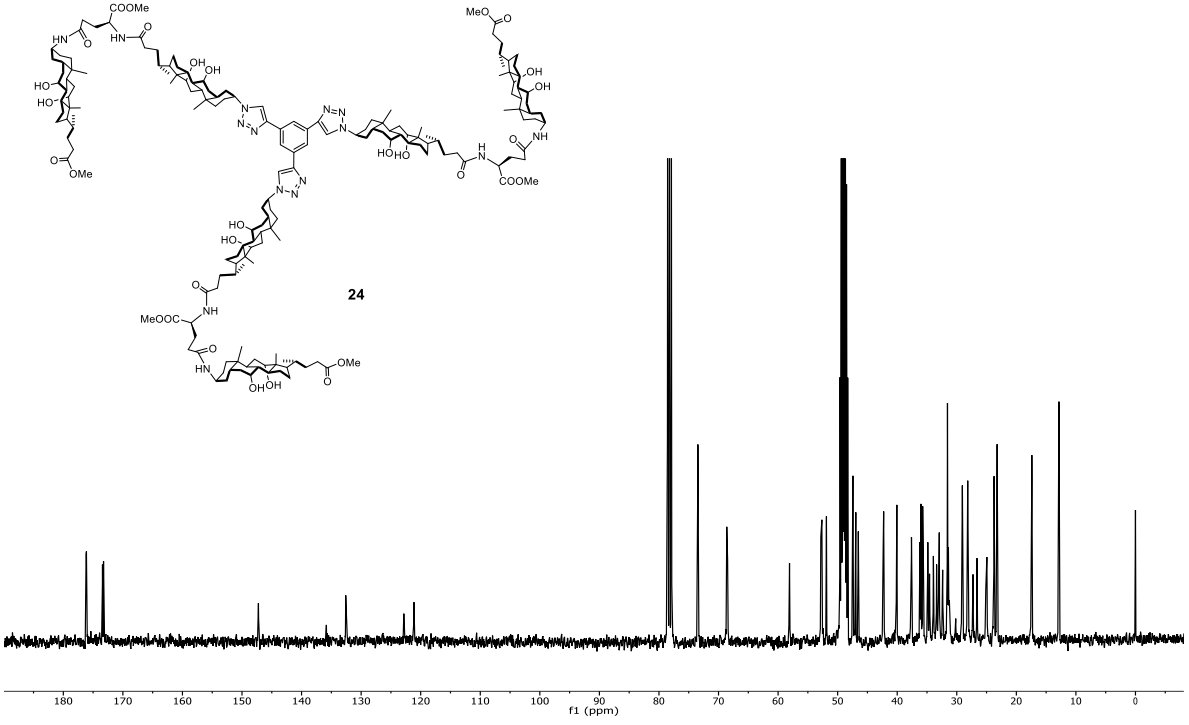

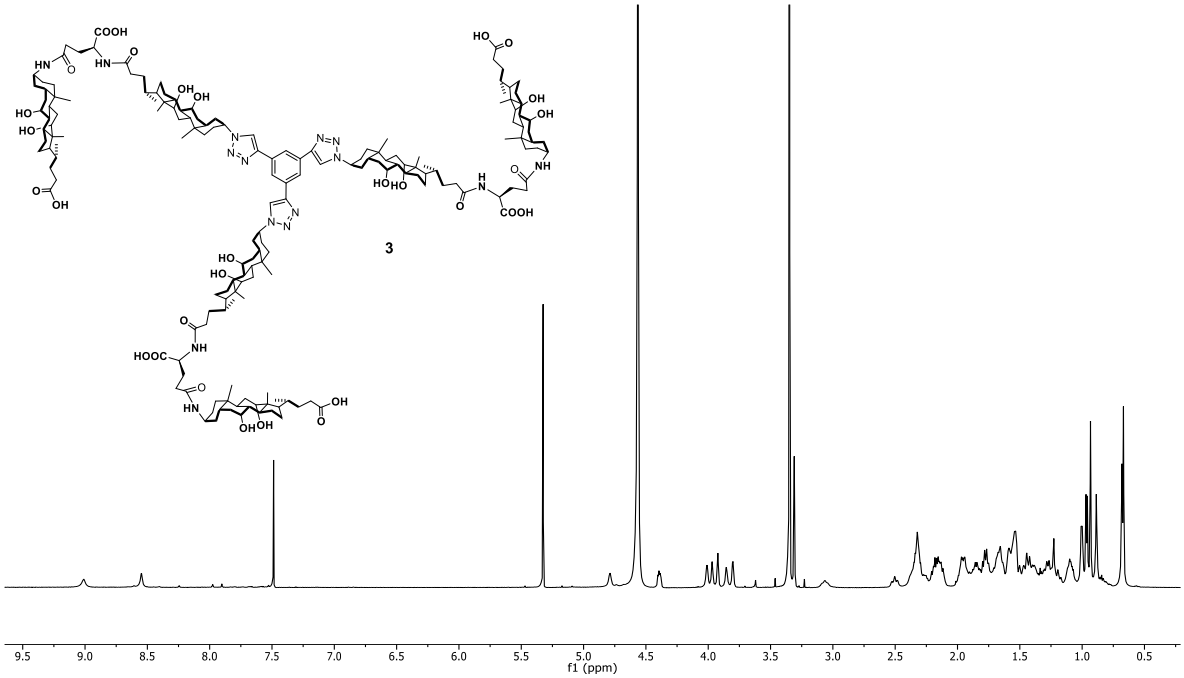

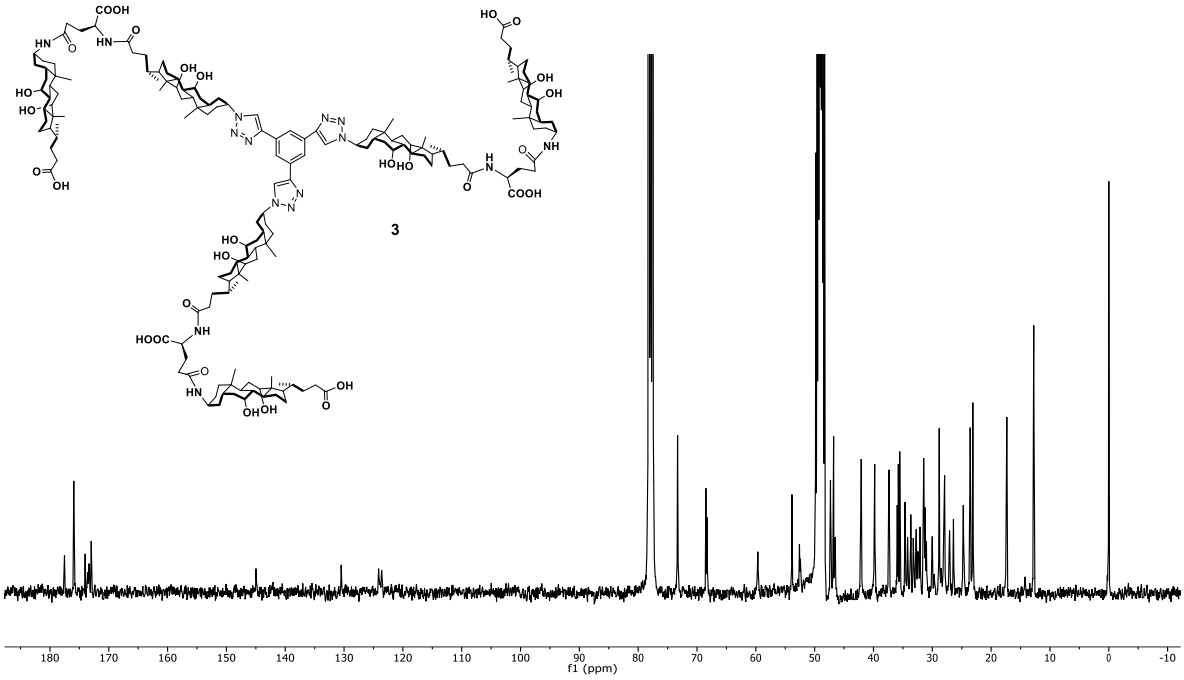

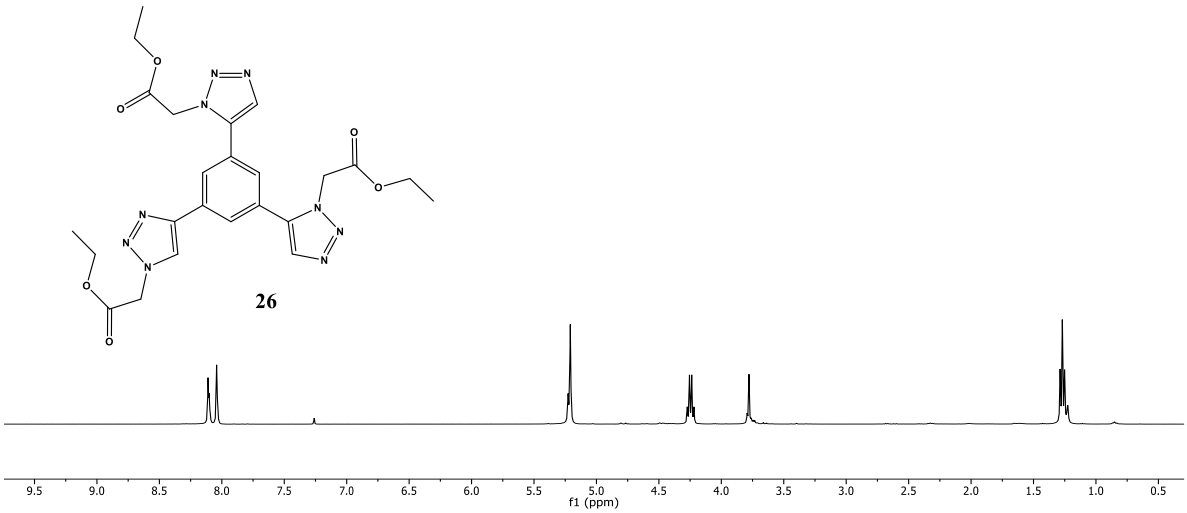

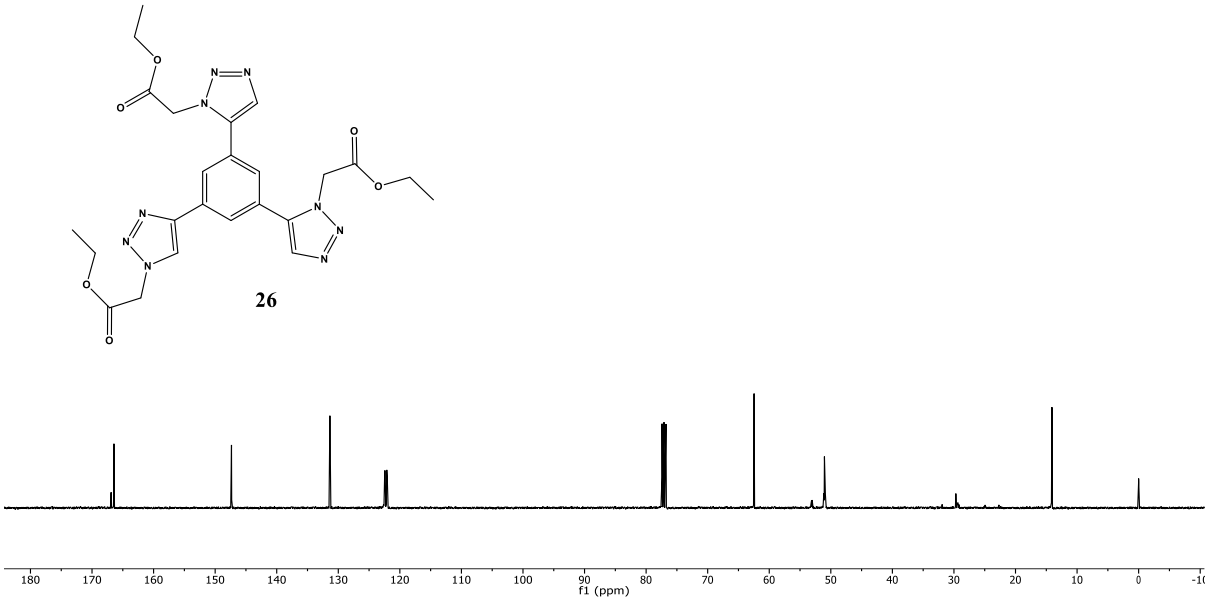

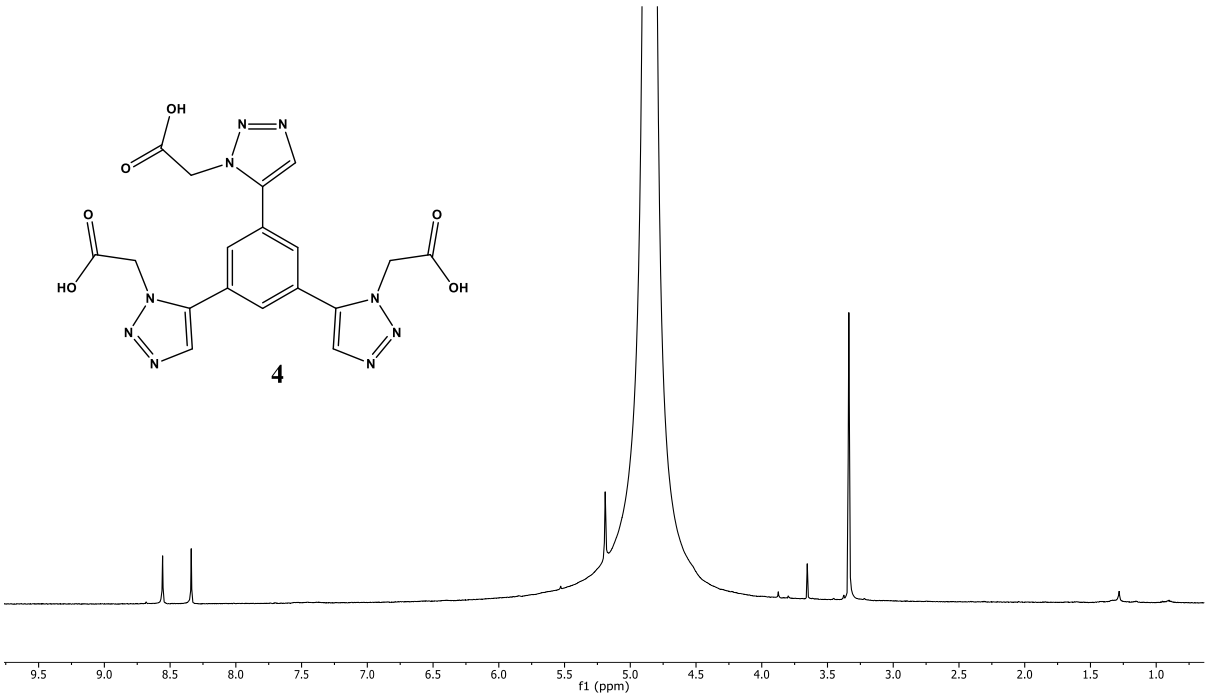

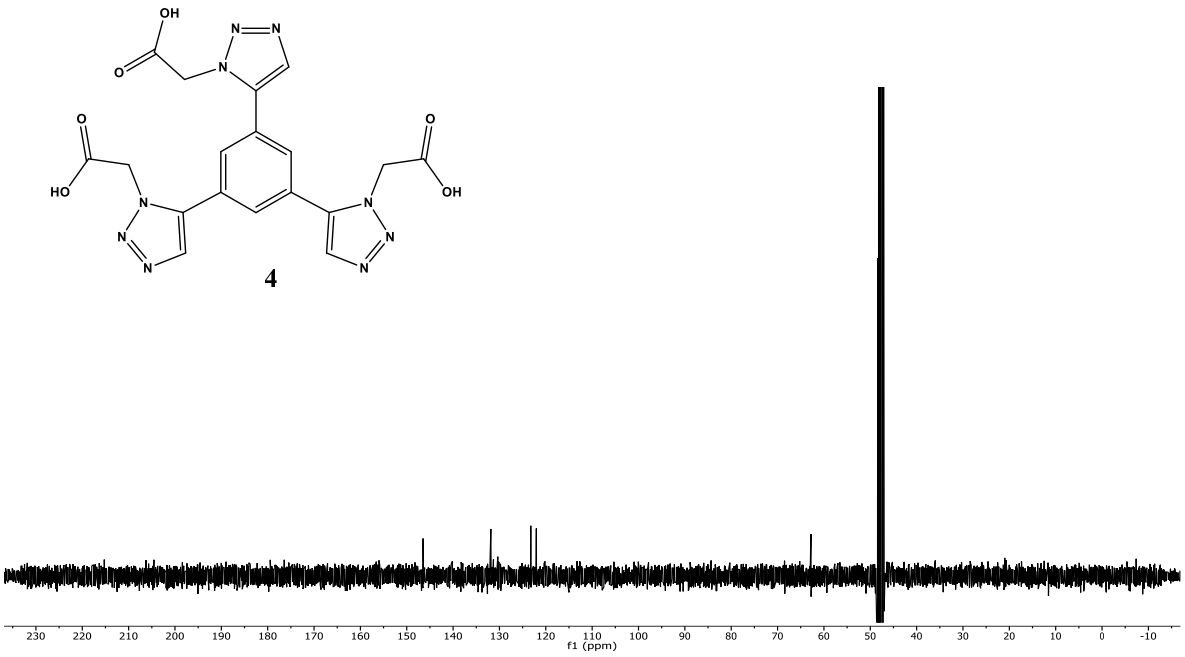

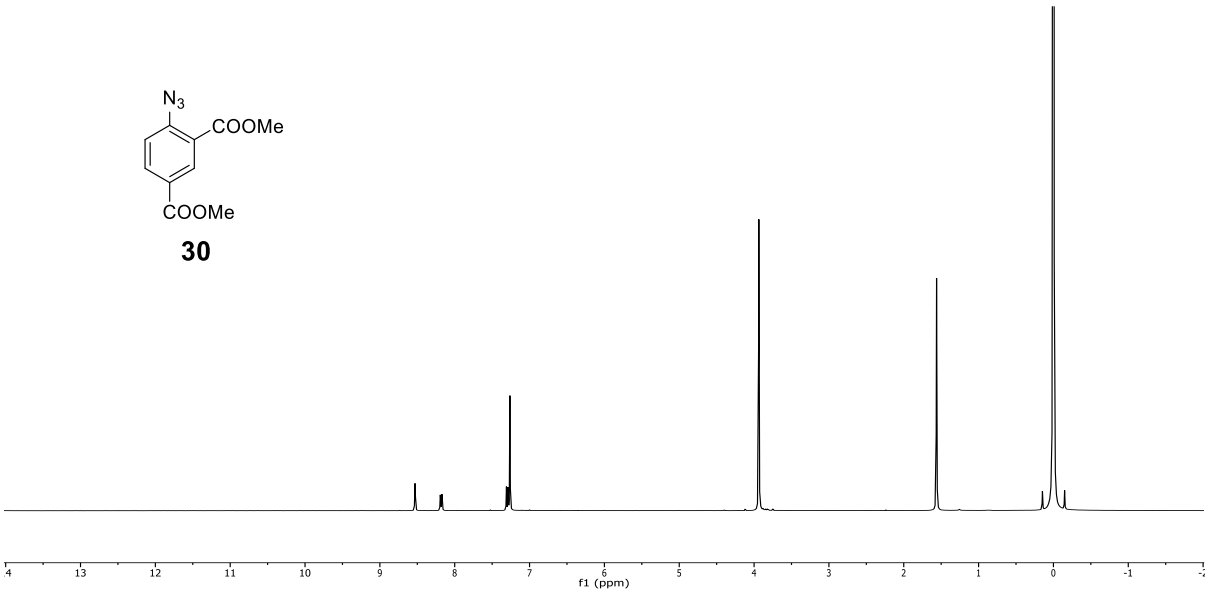

30

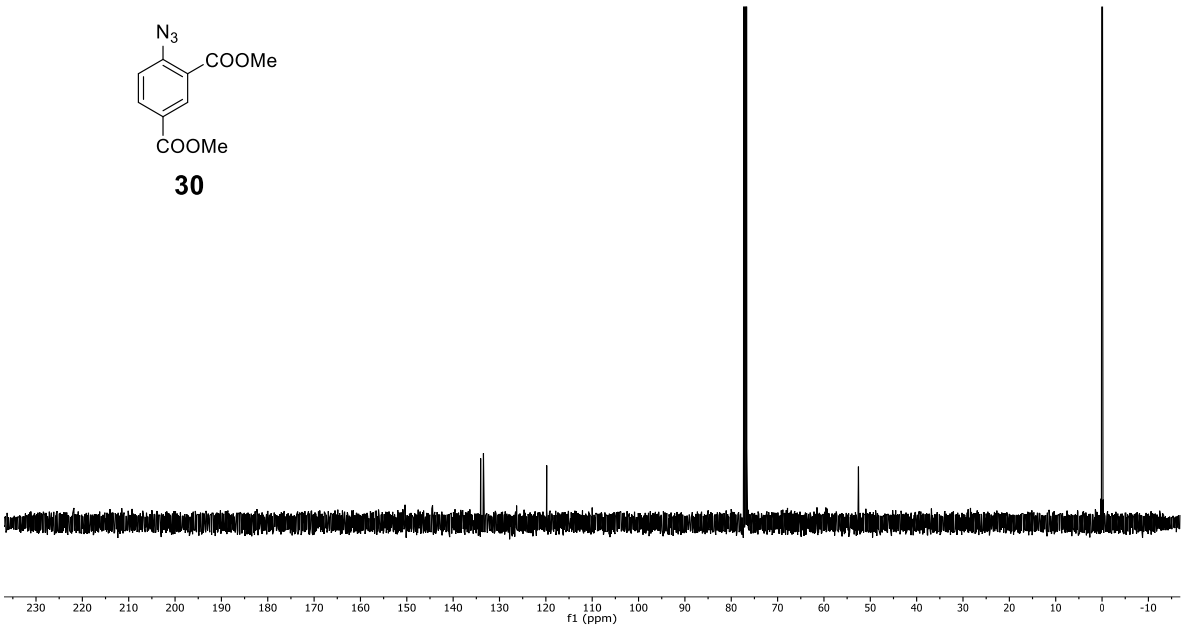

30

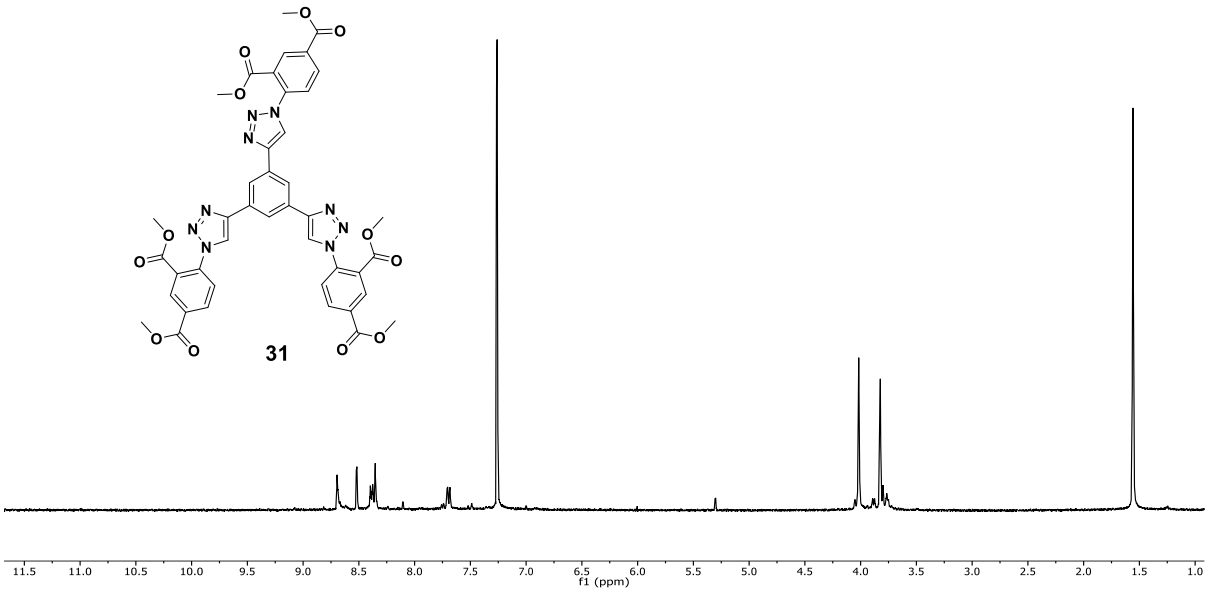

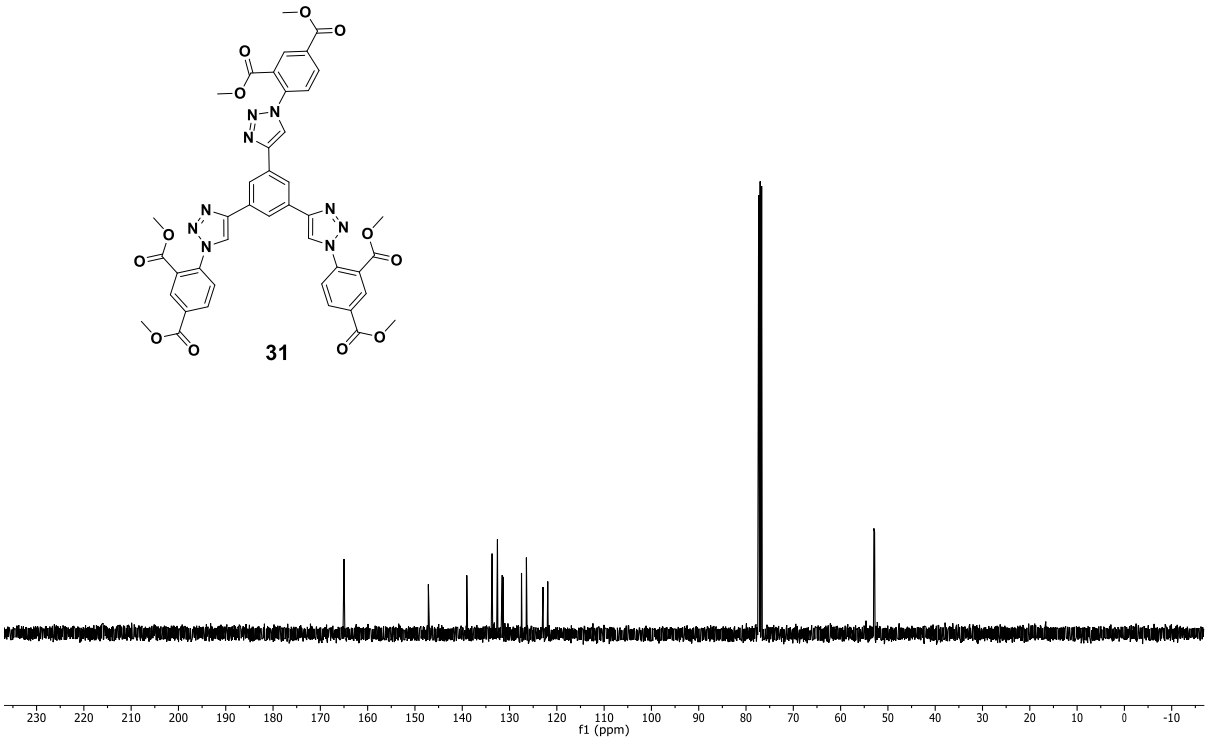

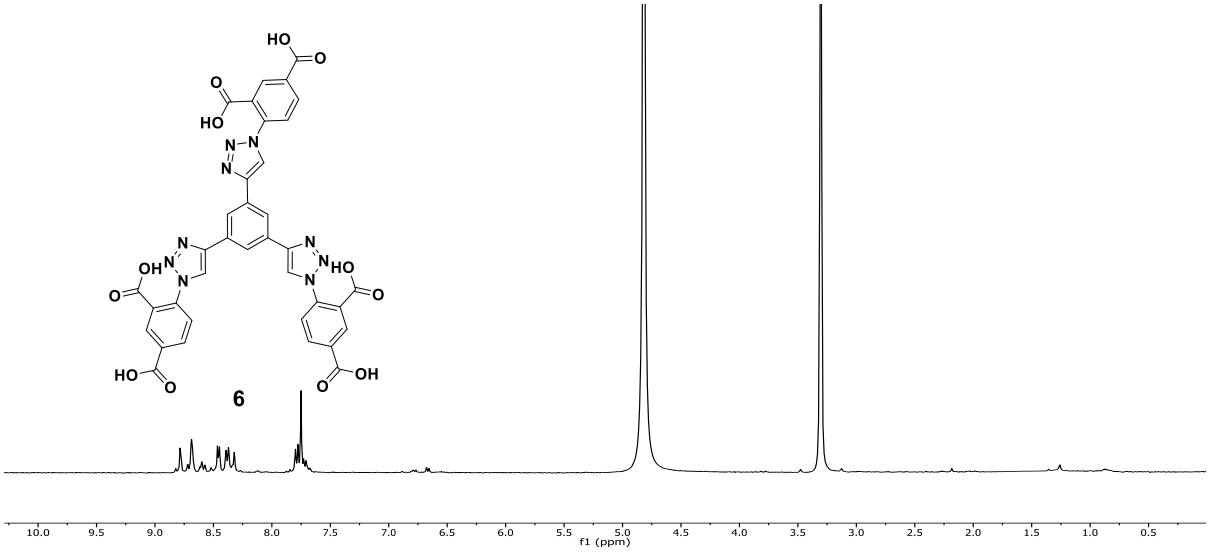

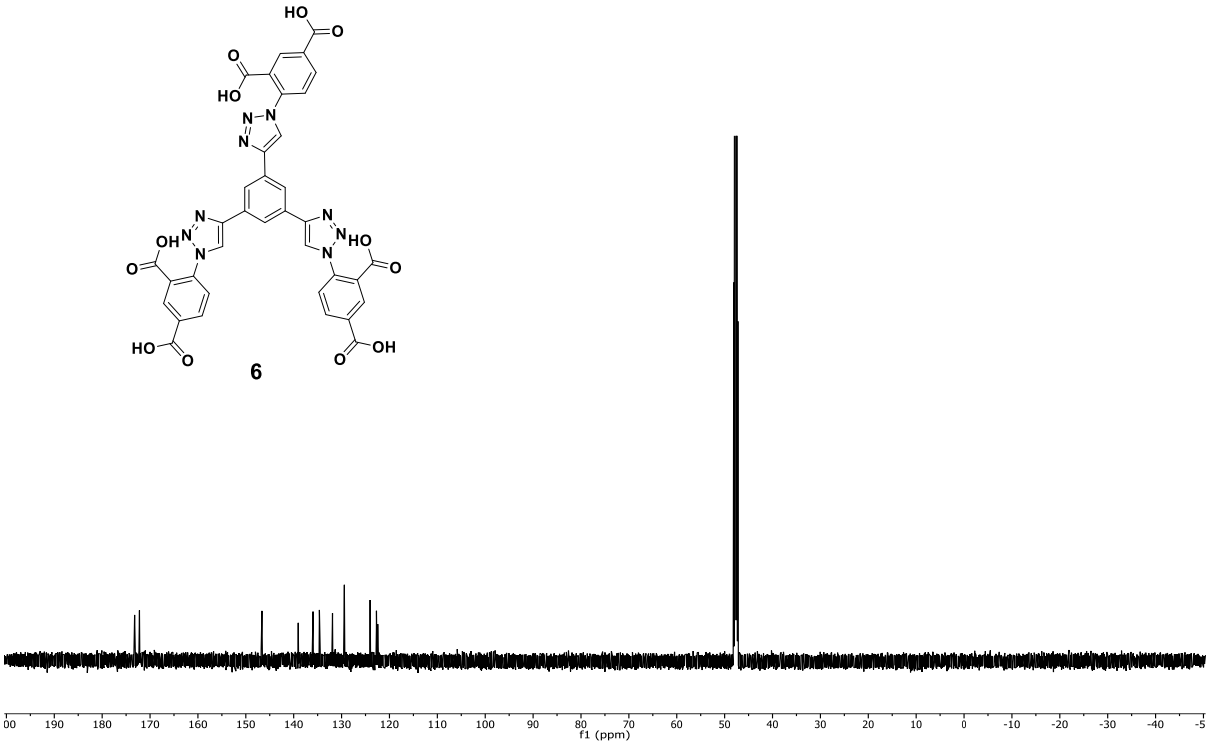

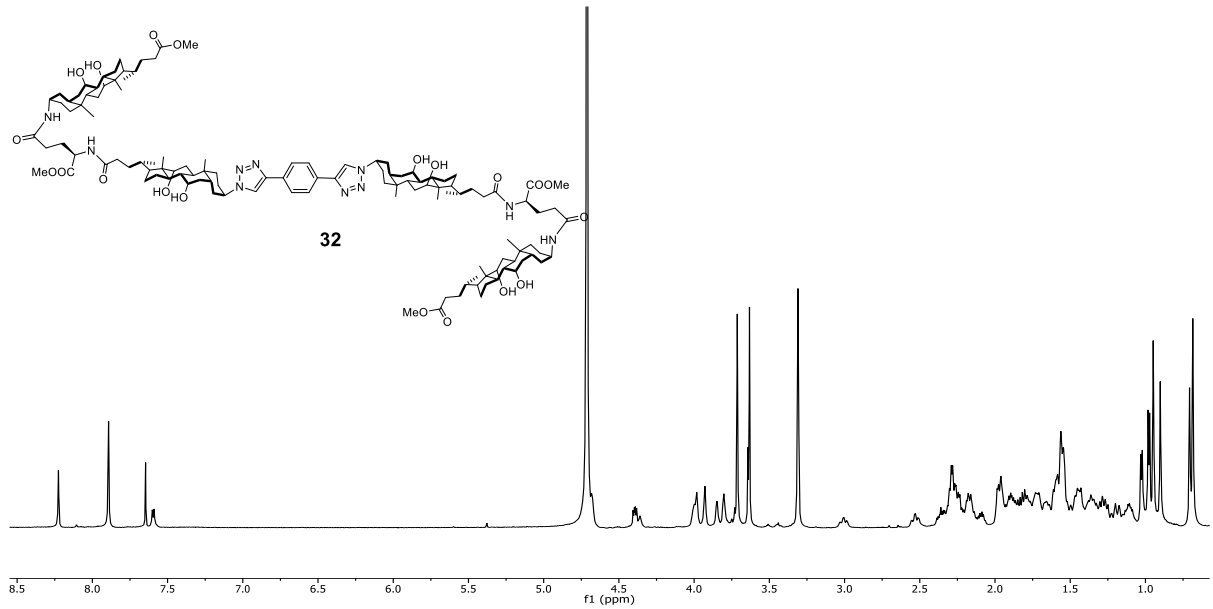

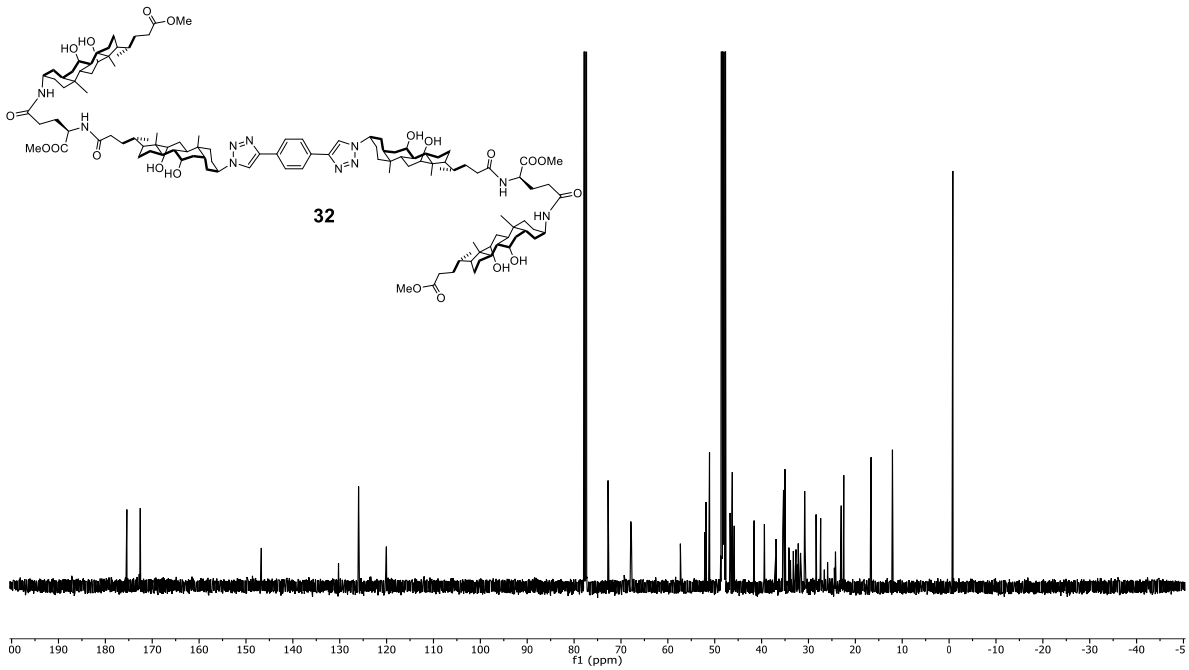

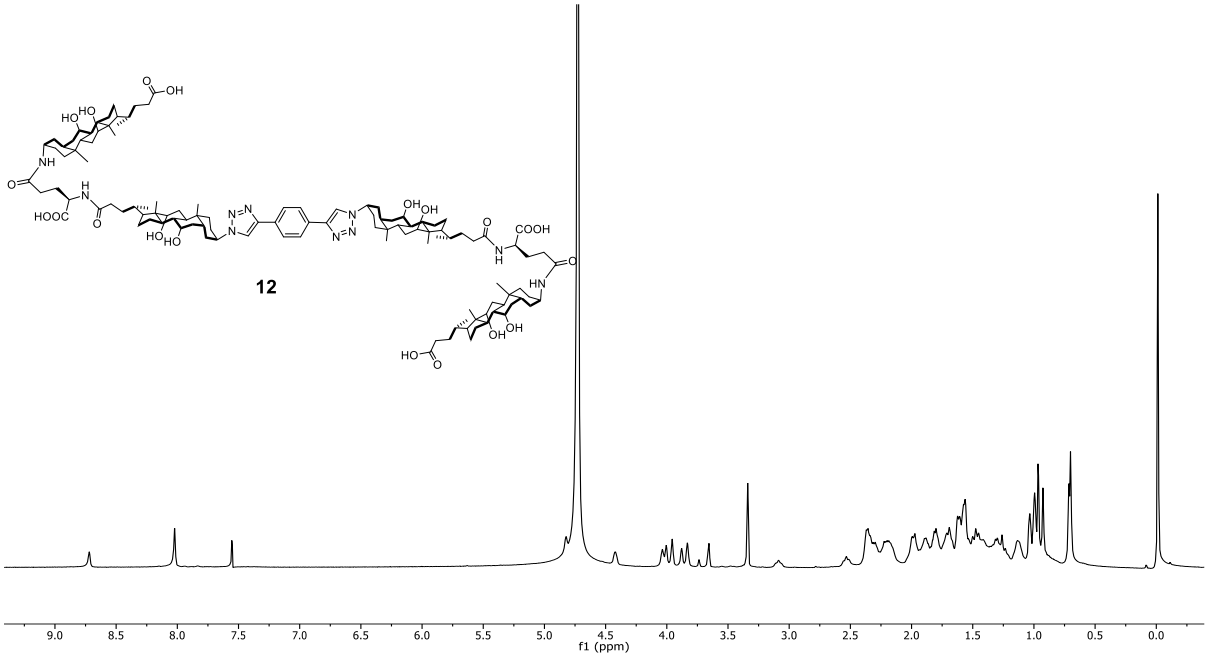

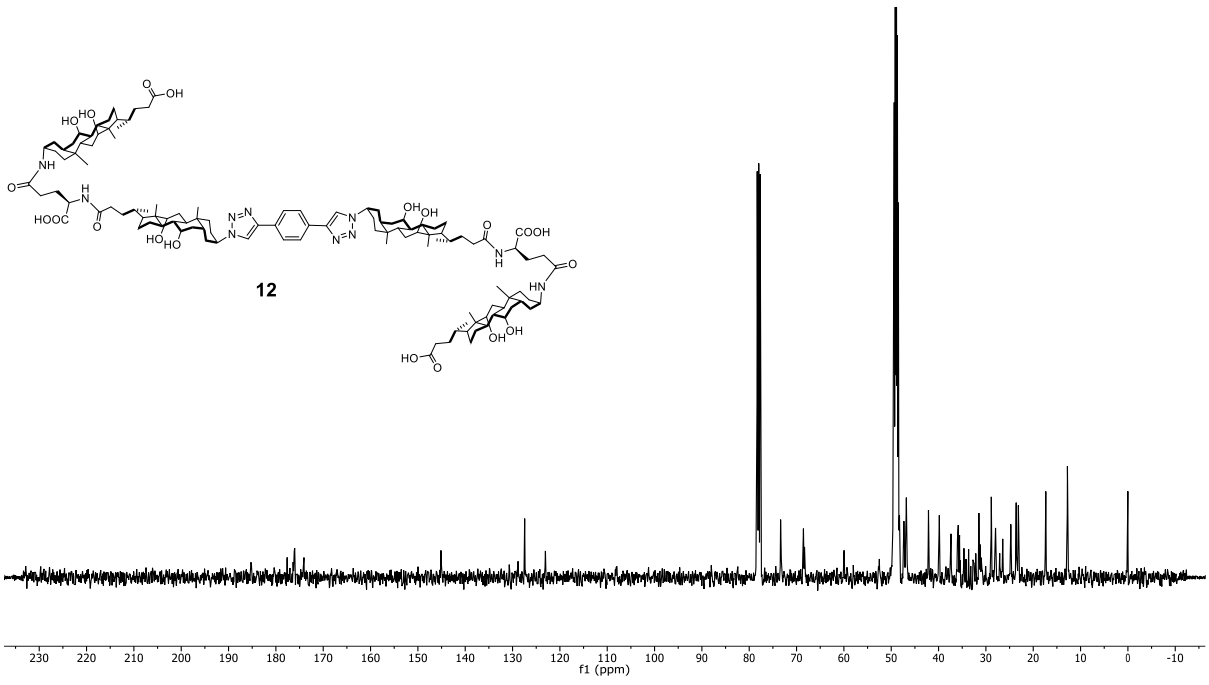

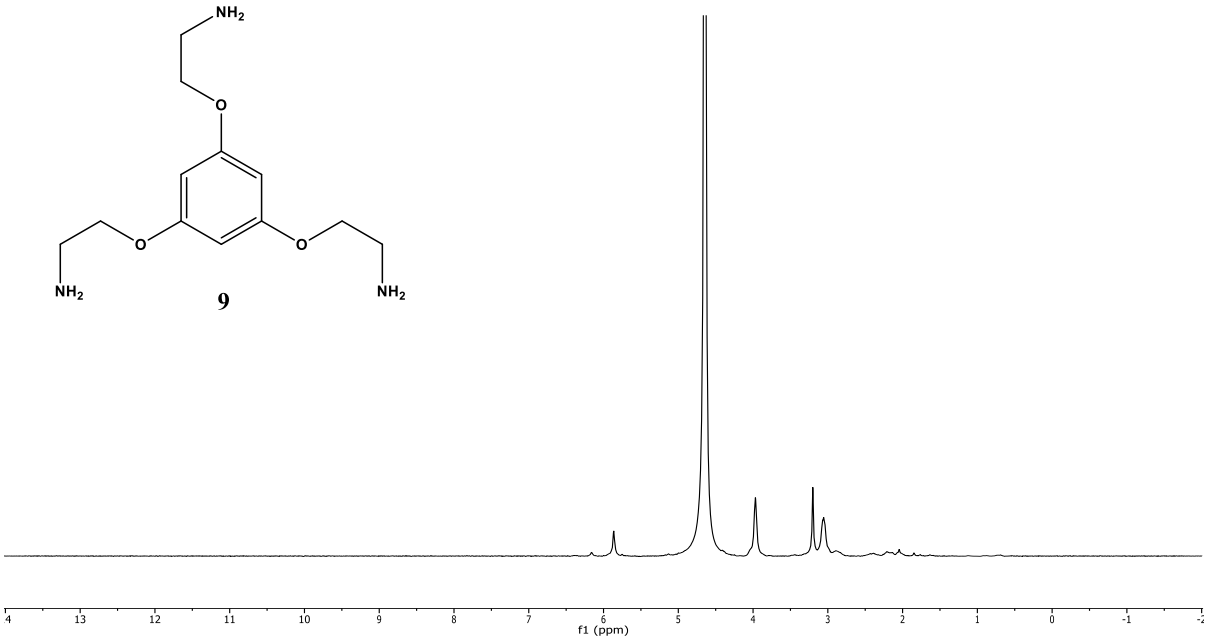

9

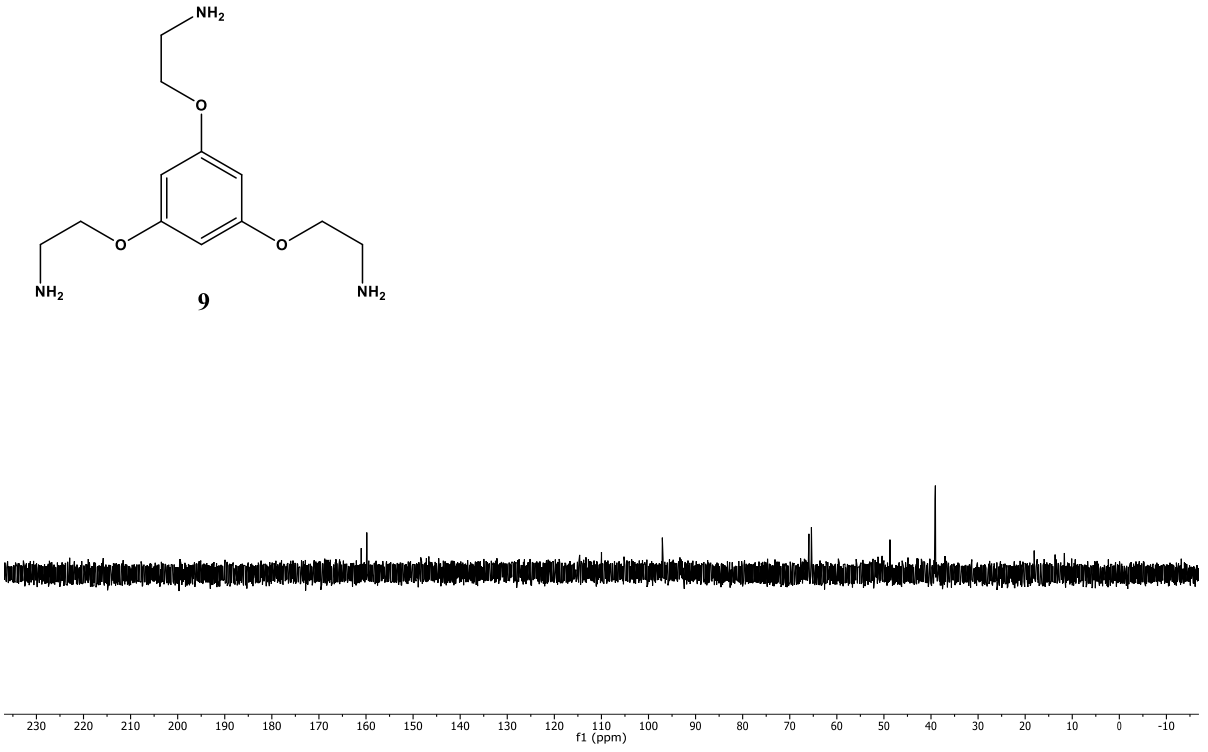

9

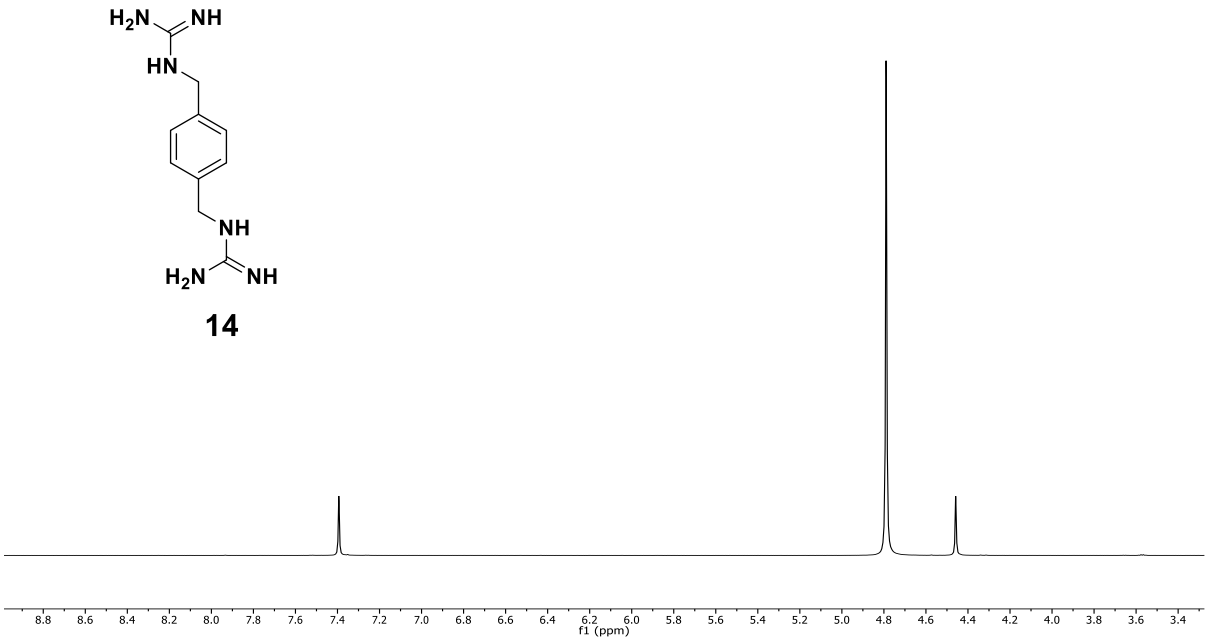

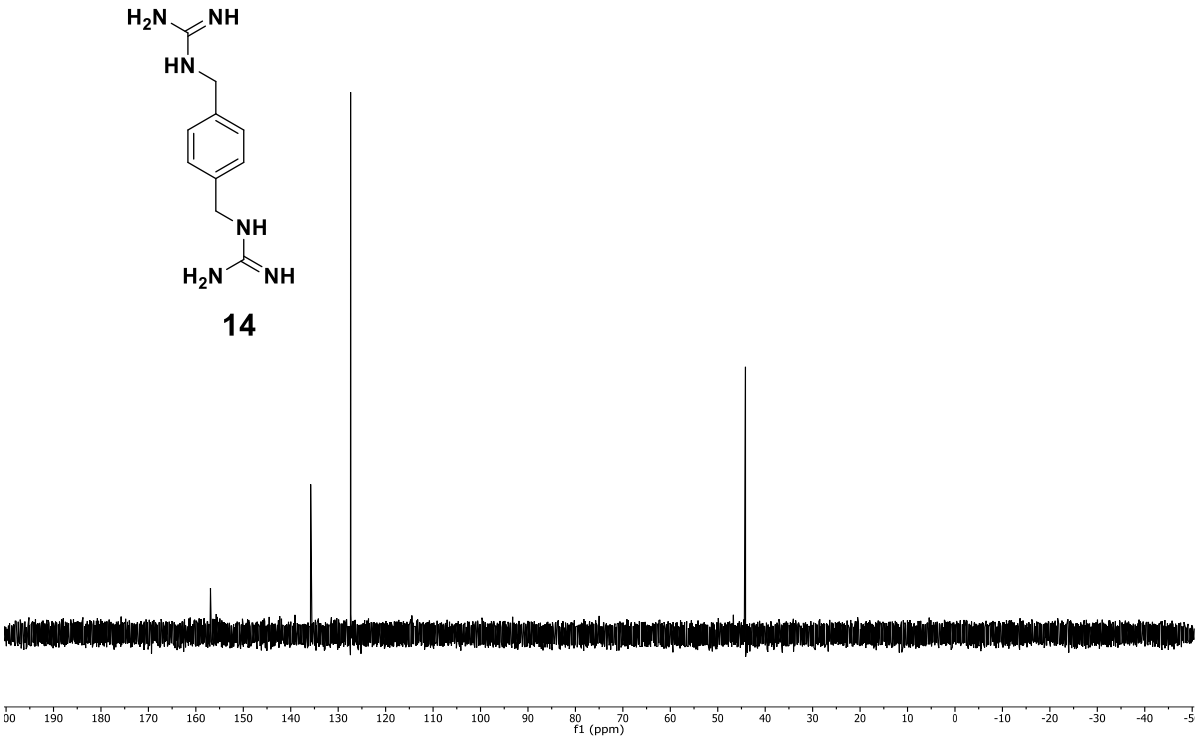

Notes and References

(1) Houk, K. N.; Leach, A. G.; Kim, S. P.; Zhang, X. Y. *Angew. Chem. Int. Ed.* **2003**, *42*, 4872-4897.

(2) Rekharsky, M. V.; Mori, T.; Yang, C.; Ko, Y. H.; Selvapalam, N.; Kim, H.; Sobransingh, D.; Kaifer, A. E.; Liu, S.; Isaacs, L.; Chen, W.; Moghaddam, S.; Gilson, M. K.; Kim, K.; Inoue, Y. *Proc. Natl. Acad. Sci. U. S. A.* **2007**, *104*, 20737-20742.

(3) Hogben, H. J.; Sprafke, J. K.; Hoffmann, M.; Pawlicki, M.; Anderson, H. L. *J. Am. Chem. Soc.* **2011**, *133*, 20962-20969.

(4) Cao, L. P.; Sekutor, M.; Zavalij, P. Y.; Mlinaric-Majerski, K.; Glaser, R.; Isaacs, L. *Angew. Chem. Int. Ed.* **2014**, *53*, 988-993.

(5) Atwood, J. L.; Lehn, J. M. *Comprehensive Supramolecular Chemistry*; Pergamon: New York, 1996.

(6) Steed, J. W.; Gale, P. A. *Supramolecular Chemistry: From Molecules to Nanomaterials*; Wiley: Weinheim, 2012.

(7) Cram, D. J. *Angew. Chem. Int. Ed. Engl.* **1986**, *25*, 1039-1057.

(8) Lehn, J. M. *Proc. Natl. Acad. Sci. U. S. A.* **2002**, *99*, 4763-4768.

(9) Leininger, S.; Olenyuk, B.; Stang, P. J. *Chem. Rev.* **2000**, *100*, 853-908.

(10) Meyer, E. A.; Castellano, R. K.; Diederich, F. *Angew. Chem. Int. Ed.* **2003**, *42*, 1210-1250.

(11) Hunter, C. A. *Angew. Chem. Int. Ed.* **2004**, *43*, 5310-5324.

(12) Rebek, J. *Angew. Chem. Int. Ed.* **2005**, *44*, 2068-2078.

(13) Vriezema, D. M.; Aragones, M. C.; Elemans, J.; Cornelissen, J.; Rowan, A. E.; Nolte, R. J. M. *Chem. Rev.* **2005**, *105*, 1445-1489.

(14) Hoeben, F. J. M.; Jonkheijm, P.; Meijer, E. W.; Schenning, A. P. H. J. *Chem. Rev.* **2005**, *105*, 1491-1546.

(15) Corbett, P. T.; Leclaire, J.; Vial, L.; West, K. R.; Wietor, J. L.; Sanders, J. K. M.; Otto, S. *Chem. Rev.* **2006**, *106*, 3652-3711.

(16) Oshovsky, G. V.; Reinhoudt, D. N.; Verboom, W. *Angew. Chem. Int. Ed.* **2007**, *46*, 2366-2393.

(17) Serreli, V.; Lee, C. F.; Kay, E. R.; Leigh, D. A. *Nature* **2007**, *445*, 523-527.

(18) Horne, W. S.; Gellman, S. H. *Acc. Chem. Res.* **2008**, *41*, 1399-1408.

(19) Yoshizawa, M.; Klosterman, J. K.; Fujita, M. *Angew. Chem. Int. Ed.* **2009**, *48*, 3418-3438.

(20) Stoddart, J. F. *Chem. Soc. Rev.* **2009**, *38*, 1802-1820.

(21) Schneider, H. J. *Angew. Chem. Int. Ed.* **2009**, *48*, 3924-3977.

(22) Ahn, Y.; Jang, Y.; Selvapalam, N.; Yun, G.; Kim, K. *Angew. Chem. Int. Ed.* **2013**, *52*, 3140-3144.

(23) Williams, D. H.; Stephens, E.; O'Brien, D. P.; Zhou, M. *Angew. Chem. Int. Ed.* **2004**, *43*, 6596-6616.

(24) Badjic, J. D.; Nelson, A.; Cantrill, S. J.; Turnbull, W. B.; Stoddart, J. F. *Acc. Chem. Res.* **2005**, *38*, 723-732.

(25) Otto, S. *Dalton Trans.* **2006**, 2861-2864.

(26) Hunter, C. A.; Anderson, H. L. *Angew. Chem. Int. Ed.* **2009**, *48*, 7488-7499.

(27) (a) Carrillo, R.; Feher-Voelger, A.; Martín, T. *Angew. Chem. Int. Ed.* **2011**, *50*, 10616-10620. (b) Carrillo, R.; Morales, E. Q.; Martín, V. S.; Martín, T. *Chem. -Eur.*

J. **2013**, *19*, 7042-7048. (c) Carrillo, R.; Morales, E. Q.; Martín, V. S.; Martín, T. *J. Org. Chem.* **2013**, *78*, 7785-7795.

(28) Zhao, Y. *ChemPhysChem* **2013**, *14*, 3878-3885.

(29) Whitty, A. *Nat. Chem. Biol.* **2008**, *4*, 435-439.

(30) (a) Rodriguez-Docampo, Z.; Pascu, S. I.; Kubik, S.; Otto, S. *J. Am. Chem. Soc.* **2006**, *128*, 11206-11210. (b) Kubik, S.; Goddard, R.; Kirchner, R.; Nolting, D.; Seidel, J. *Angew. Chem. Int. Ed.* **2001**, *40*, 2648-2651.

(31) Zhong, Z.; Li, X.; Zhao, Y. *J. Am. Chem. Soc.* **2011**, *133*, 8862-8865.

(32) Zhao, Y.; Zhong, Z. *J. Am. Chem. Soc.* **2005**, *127*, 17894-17901.

(33) Cho, H.; Zhao, Y. *J. Am. Chem. Soc.* **2010**, *132*, 9890-9899.

(34) Zhao, Y.; Cho, H.; Widanapathirana, L.; Zhang, S. *Acc. Chem. Res.* **2013**, *46*, 2763-2772.

(35) Zhao, Y. *J. Org. Chem.* **2009**, *74*, 834-843.

(36) Li, Y. H.; Chan, L. M.; Tyer, L.; Moody, R. T.; Himel, C. M.; Hercules, D. M. *J. Am. Chem. Soc.* **1975**, *97*, 3118-3126.

(37) Ryu, E.-H.; Yan, J.; Zhong, Z.; Zhao, Y. *J. Org. Chem.* **2006**, *71*, 7205-7213.

(38) Zhao, Y.; Zhong, Z.; Ryu, E.-H. *J. Am. Chem. Soc.* **2007**, *129*, 218-225.

(39) Chan, H. S.; Bromberg, S.; Dill, K. A. *Philos. Trans. R. Soc. London B* **1995**, *348*, 61-70.

(40) Hill, D. J.; Mio, M. J.; Prince, R. B.; Hughes, T. S.; Moore, J. S. *Chem. Rev.* **2001**, *101*, 3893-4012.

(41) Creighton, T. E. *Protein Structure: A Practical Approach, 2nd Ed.*; IRL Press: Oxford, 1997.

(42) Prince, R. B.; Saven, J. G.; Wolynes, P. G.; Moore, J. S. *J. Am. Chem. Soc.* **1999**, *121*, 3114-3121.

(43) If secondary electrostatic interactions, i.e., those between the ammoniums and the more distant carboxylates in **3** and **6**, are considered, **6** should be favored over **3** because its para carboxylates are closer to ammoniums on the guest than the glutamate carboxylates in **3**.

(44) Grawe, T.; Schrader, T.; Zadmard, R.; Kraft, A. *J. Org. Chem.* **2002**, *67*, 3755-3763.

(45) Berger, M.; Schmidtchen, F. P. *Angew. Chem. Int. Ed.* **1998**, *37*, 2694-2696.

(46) Linton, B. R.; Goodman, M. S.; Fan, E.; van Arman, S. A.; Hamilton, A. D. *J. Org. Chem.* **2001**, *66*, 7313-7319.

(47) Rekharsky, M.; Inoue, Y.; Tobey, S.; Metzger, A.; Anslyn, E. *J. Am. Chem. Soc.* **2002**, *124*, 14959-14967.

(48) Tobey, S. L.; Anslyn, E. V. *J. Am. Chem. Soc.* **2003**, *125*, 14807-14815.

(49) Linton, B.; Hamilton, A. D. *Tetrahedron* **1999**, *55*, 6027-6038.

(50) Schmidtchen, F. P.; Berger, M. *Chem. Rev.* **1997**, *97*, 1609-1646.

(51) Orner, B. P.; Hamilton, A. D. *J. Incl. Phenom. Macro.* **2001**, *41*, 141-147.

(52) Best, M. D.; Tobey, S. L.; Anslyn, E. V. *Coord. Chem. Rev.* **2003**, *240*, 3-15.

(53) Micelles of ionic surfactants are also known to be electrostatically frustrated and the electrostatic frustration has been shown to enhance its binding of oppositely charged species. For examples, see: (a) Woo, H. J.; Carraro, C.; Chandler, D. *Faraday Discuss.* **1996**, *104*, 183-191. (b) Kostereli, Z.; Severin, K. *Chem. Commun.* **2012**, *48*, 5841-5843.

(54) Granzhan, A.; Schouwey, C.; Riis-Johannessen, T.; Scopelliti, R.; Severin, K. *J. Am. Chem. Soc.* **2011**, *133*, 7106-7115.

(55) Bostoen, C. L.; Janssen, K. J. G.; Google Patents: 1998.

(56) Khatri, A. I.; Samant, S. D. *Tetrahedron Lett.* **2014**, *55*, 2362-2365.

(57) Ryu, E.-H.; Ellern, A.; Zhao, Y. *Tetrahedron* **2006**, *62*, 6808-6813.

(58) Gann, A. W.; Amoroso, J. W.; Einck, V. J.; Rice, W. P.; Chambers, J. J.; Schnarr, N. A. *Org Lett.* **2014**, *16*, 2003-2005.

(59) Polaske, N. W.; Szalai, M. L.; Shanahan, C. S.; McGrath, D. V. *Org Lett.* **2010**, *12*, 4944-4947.

(60) Andrianjara, C.; Barvian, N.; Gaudilliere, B.; Jacobelli, H.; Ortwine, D.; Patt, W.; Pham, L.; Kostlan, C.; Wilson, M.; Google Patents: 2002.

(61) Hallberg, A.; Westman, J.; Post, C.; Google Patents: 2008.

(62) Hermann, K.; Turner, D. A.; Hadad, C. M.; Badjić, J. D. *Chem. Eur. J.* **2012**, *18*, 8301-8305.

(63) Aakeroy, C. B.; Smith, M. M.; Desper, J. *CrystEngComm* **2012**, *14*, 71-74.

(64) Luo, H.-Z.; Ye, H.-Y. *Acta Cryst. E.* **2008**, *64*, 0136.

CHAPTER 3

ENHANCING BINDING AFFINITY AND SELECTIVITY THROUGH PREORGANIZATION AND COOPERATIVE ENHANCEMENT OF THE RECEPTOR

A paper published in *Chemical Communication* **2016**, *52*, 4345-4348.

Roshan W. Gunasekara and Yan Zhao

Abstract

When direct host–guest binding interactions are weakened by unfavorable solvent competition, guest-triggered intrareceptor interactions could be used to augment the binding. This strategy of cooperative enhancement, when combined with the principle of preorganization, yielded a strong and selective receptor for binding citrate in water.

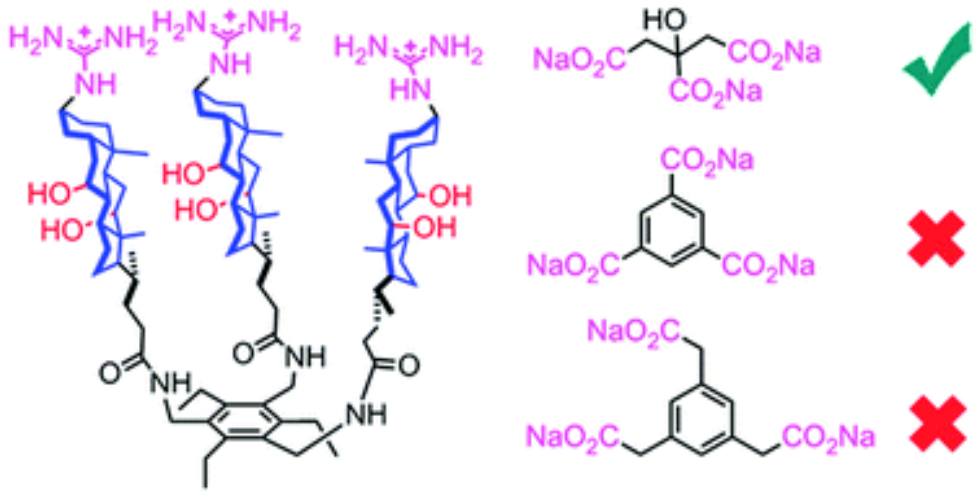

Scheme 1. Design of cooperatively enhanced receptor and guest molecules.

Introduction

Molecular recognition is at the heart of biology and vital to countless processes including ligand–receptor interactions, gene expression, transport, and catalysis.[1,2] Over the last decades, chemists have made remarkable progress in constructing receptors functional in organic solvents, doing so in aqueous solution, however, remains challenging.[3,4] The difficulty in the latter partly derives from the nature of the noncovalent forces used in the binding: whereas polar interactions such as hydrogen bonds are directional and highly programmable, they tend to be ineffective in protic solvents due to competition from solvent. Conversely, although hydrophobic interactions can be strong in water, their nondirectionality makes it difficult to achieve high selectivity in binding.

We recently reported a method to create guest-complementary hydrophobic binding pockets within water-soluble nanoparticles through molecular imprinting of surfactant micelles.[5-8] Strong and selective binding was achieved for a variety of water-soluble molecules including bile salt derivatives,[5] aromatic carboxylates and sulfonates,[6,7] and nonsteroidal anti-inflammatory drugs (NSAIDs).[8] To be successfully imprinted within the micelles, however, the guest needs to possess significant hydrophobicity.

Citric acid is a natural preservative found in citrus fruits. It is also an important intermediate in the citric acid cycle. To create receptors for such guest molecules with little or no hydrophobicity, we have to deal with the challenge in utilizing inherently weak polar binding forces in water. One possible solution to the problem is multivalency.[9-11] If multiple binding groups in a concave receptor can be oriented to interact with the (polar) guest, strong binding should be achievable even if the individual interaction are weak. Anslyn and co-workers, indeed, in a classic paper described such a tripodal receptor that bound citrate in

D_2O with an impressive binding constant (K_a) of 6.9×10^3 M^{-1}.[12] Many citrate receptors have been reported using similar strategies, sometimes using metal–ligand complexation for higher binding affinity.[13-22]

Nature has a different strategy to deal with weak binding forces. Streptavidin binds biotin with a K_a of $10^{13.4}$ M^{-1}. Having two highly polar functional groups (i.e., carboxylic acid and urea) and a rather small size (M.W. = 244.3), its tight binding cannot be fully explained by enthalpy gain or displaced water molecules in the binding pocket. Upon binding with biotin, the melting point of the protein increases by 37 °C and numerous backbone amide proteins become resistant to H/D exchange.[23] These results suggest that the guest-binding has turned on previously disengaged intrareceptor interactions, which contribute to the binding equilibrium even though they are not at the binding interface. With these hidden "binding interactions" delocalized throughout the protein, nature is able to achieve high binding affinity even when direct host–guest binding forces are of limited strength. Similar synthetic cooperatively enhanced receptors (CERs),[24] although still few and far between, began to emerge in the literature in recent years.[25-30]

Results and Discussion

Design and synthesis of CERs

To bind citrate in water, we designed CERs **1** and **2**. The C3-symmetrical receptors have three facially amphiphilic cholates functionalized with guanidinium groups on the top. The positively charged guanidinium groups are on the β face of the cholate, opposite to the hydroxyl groups. Their electrostatic repulsion is engineered to hinder close contact of the cholate groups, making it difficult for the intrahost hydrophobic interactions to fully engage.

When citrate, a trianonic guest, binds the receptor, the repulsion among the guanidinium groups is eliminated while the citrate carboxylate groups, being close to one another, promote the intermolecular aggregation of the cholates. The guest-triggered hydrophobic interactions are expected to contribute to the binding, even though the guest itself has negligible hydrophobicity.

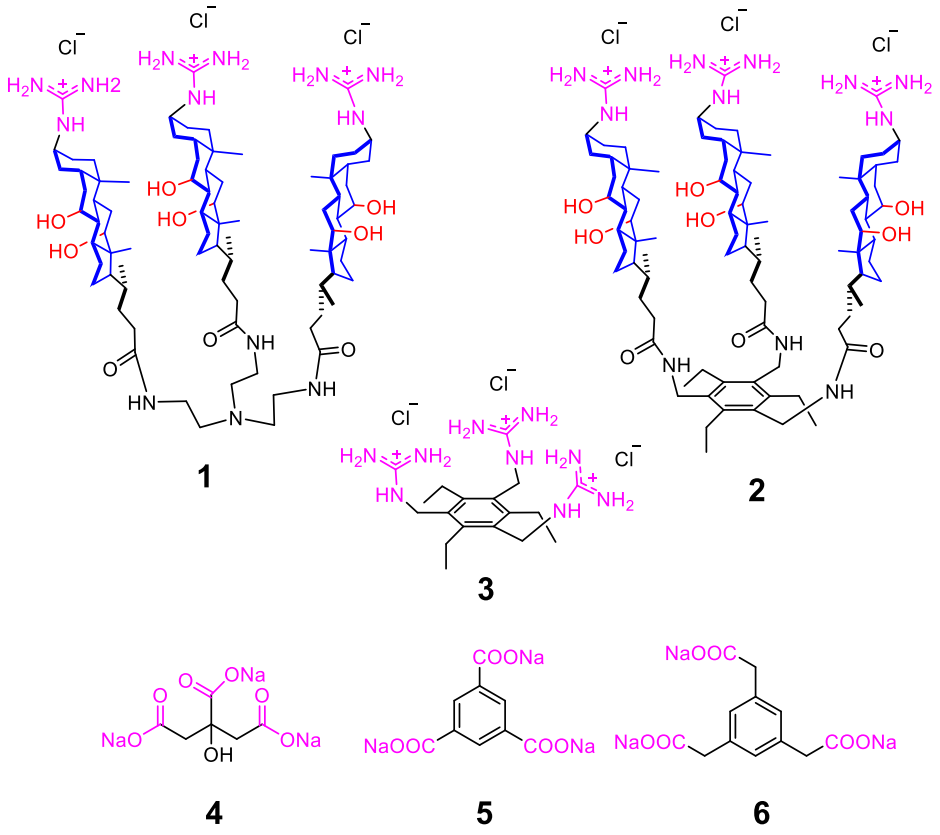

Scheme 2. Structures of CERs and guest molecules used in study.

The major difference between 1 and 2 is the scaffold on which the cholates were assembled: one was built on a flexible scaffold and the other on the preorganized 1,3,5-tris(aminomethyl)-2,4,6-triethylbenzene.[31,32] To compare our CERs with conventional receptors, we also prepared 3, based on the same hexasubstituted benzene, without the cholate groups responsible for the hypothesized intramolecular hydrophobic enhancement.

Table 1. Binding data for receptors 1–3 obtained by ITC.[a]

Entry	Complex	K_a (10^3 M^{-1})	K_{rel}	ΔG (kcal/mol)	ΔH (kcal/mol)	TΔS (kcal/mol)
1	**1•4**	10.4 ± 1.1	1	-5.5 ± 0.04	10.4 ± 0.3 0.04	15.9
2	**1•5**	7.6 ± 0.9	0.73	-5.3 ± 0.05	-4.5 ± 0.5	0.8
3	**1•6**	3.2 ± 0.2	0.31	-4.8 ± 0.06	-9.7 ± 1.0	-4.9
4	**2•4**	77.9 ± 4.5	1	-6.7 ± 0.04	2.5 ± 0.1	9.2
5	**2•5**	2.1 ± 0.7	0.03	-4.5 ± 0.3	-14.0 ± 0.2	-9.5
6	**2•6**	-[b]	-[b]	-[b]	-[b]	-[b]
7	**3•4**	16.3 ± 2.7	1	-5.7 ± 0.1	-1.6 ± 0.4	4.1
8	**3•5**	3.9 ± 0.8	0.24	-4.8 ± 0.5	-5.8 ± 2.4	-0.9
9	**3•6**	-[b]	-[b]	-[b]	-[b]	-[b]

[a]The titrations were performed in duplicates in Millipore water and the errors in K_a between the runs were generally < 20%. The number of binding site (N) determined by ITC averaged ~0.4 for **4** and ~0.8 for **5** and **6** for all three receptors. The lower-than-unity N in the citrate–receptor complexes could be caused by the presence of small amounts of higher order complexation, as in Anslyn's tripodal guanidinium receptor which bound citrate mainly in the 1:1 stoichiometry but formed small amounts of higher order complexes. In our hands, ESI-MS confirmed the 1:1 complex between **4** and the preorganized receptor **3** (Figure 8 ESI†).Since the diffusion coefficient of **2** (our strongest and most selective citrate receptor) changed very little upon binding citrate (vide infra), the higher order binding processes must be minor. [b] Binding was not detectable by ITC.

Table 1 shows the binding data for the three receptors. Selected ITC titrations curves are shown in Figure 1 and more in the Supplementary Information (Figures S1–S3, ESI†). We chose to study two anionic guests (**5** and **6**) in addition to citrate (**4**). All the guests possess three carboxylates, with the distance between the binding groups more or less increasing from **4** to **5** to **6**. Our hypothesis was that, as the carboxylate groups in the guest are separated by a larger distance, their ion-pairing interactions with the host would keep the

cholates apart, preventing their effective intramolecular hydrophobic contact. Consequently, the cooperative enhancement designed in the citrate binding will either diminish or disappear in **5** and **6**.

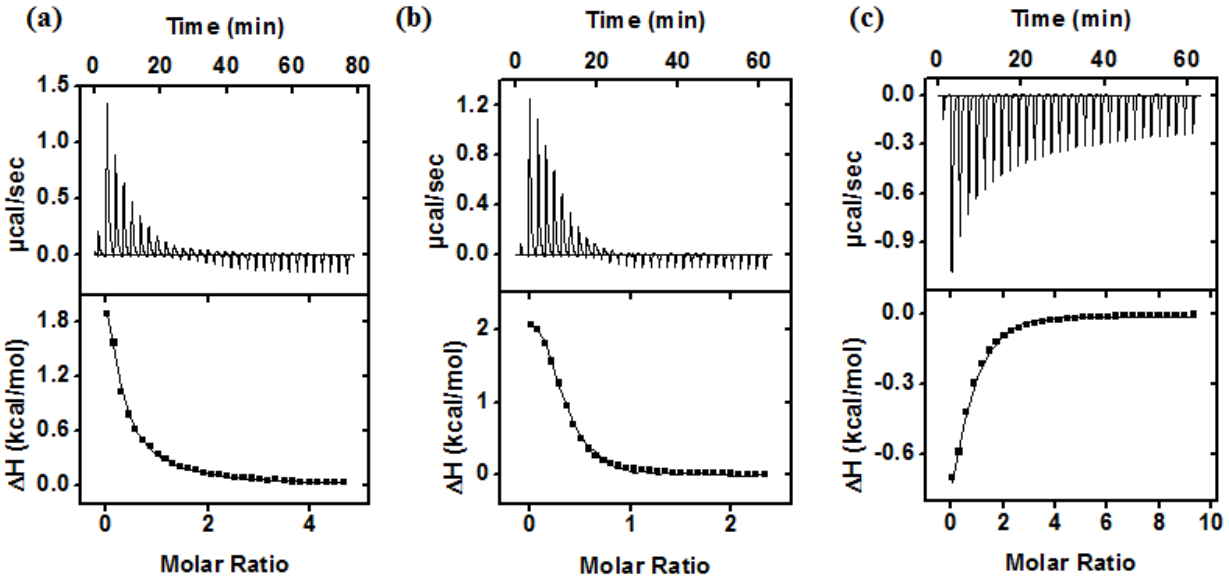

Figure 1. ITC titration curves obtained at 298 K for the binding of citrate **4** by (a) **1**, (b) **2**, and (c) **3**. The data correspond to entries 1, 4, and 7, respectively, in Table 1.

The binding data support our hypothesis. Receptor **1** bound citrate **4** with a very significant K_a of 10.4×10^3 M^{-1} in water (Table 1, entry 1). Although the binding was weaker than that of the preorganized control receptor **3** (K_a = 16.3×10^3 M^{-1}, entry 7), it is encouraging to see that a highly flexible receptor could bind citrate with such an affinity. The preorganized cholate receptor was clearly the best among the three to afford a K_a of 77.9×10^3 M^{-1} or a binding free energy of $-\Delta G$ = 6.7 kcal/mol (entry 4). Its ^{1}H NMR spectrum in D_2O showed well-resolved peaks at submillimolar concentrations (Figure 9 ESI†). Because

the ITC was performed with the concentration of the receptor at 0.1–0.2 mM, host aggregation was not expected to be a problem under our experimental conditions.

We also studied the most stable host–guest complex (**2**•**4**) by two additional NMR techniques. 2D diffusion-ordered NMR spectroscopy (DOSY) experiments showed that **2** and **4** (both at 1.5 mM) had a diffusion coefficient of 2.43 and 5.57 × 10^{-10} m^2s^{-1} in D_2O, respectively (Figures 11 and 10, ESI†). The slower movement of the former was expected from its larger size. The homogeneous distribution of the diffusion peaks rules out any significant host aggregation at 1.5 mM. Most importantly, citrate in a 1:1 mixture of **2** and **4** had a diffusion coefficient of 2.16 × 10^{-10} m^2 s^{-1} in D_2O (Figure 12 ESI†), slightly slower than that of **2** and thus fully in agreement with the host–guest complexation.

The complexation was further supported by 2D NOESY experiments, which showed close contact between **2** and **4**, as well as cholate–cholate contact that resulted from the citrate-triggered intramolecular aggregation of the cholates (for details, see Figures S9 and S10, ESI†).

An interesting difference between the cholate receptors and the control receptor was in the driving force for the binding. Table 1 indicates that the binding of citrate by either **1** or **2** was endothermic with a positive ΔH, but was exothermic by **3** (compare entries 1, 4, and 7). The endo- and exothermic difference is seen clearly in the ITC titration curves (Figure 1). Note that all three bindings have significant entropic contributions, with $T\Delta S$ being 15.9, 9.2, and 4.1 kcal/mol, respectively, for receptors **1**, **2**, and **3**.

For ionic binding between citrate and the preorganized receptor **3**, the entropic contribution normally is considered to come from the release of water molecules that solvate

the ionic groups prior to the binding.[9,33-35] The two cholate receptors are considerably more flexible than **3**. Because binding reduces freedom of the cholate hosts substantially, the entropic driving force normally is expected to decrease but increased instead. In fact, receptor **1**, the most flexible among the three, had the largest entropic driving force (15.9 kcal/mol). Since the enthalpy of binding citrate was positive/unfavorable for the two cholate receptors, the only reason the complex could form at all was the increased entropy.

The unusually large entropic driving force for **1** and **2** are consistent with our hypothesized hydrophobically enhanced binding.[36] When citrate ion-pairs with the three guanidinium groups, hydrophobic contact among the cholates is anticipated to improve as the electrostatic repulsion among the guanidinium groups is eliminated. Since (tighter) contact among the cholates would release water molecules formerly associated with the cholate β faces, strong entropic driving forces in the citrate binding of **1** and **2** are predicted by our binding model. The flexible tether in **1** probably makes it easier for the cholates to interact with one another, thus creating the strongest hydrophobic/entropic driving force. The large entropic driving force in receptor **1** was compensated by a significant enthalpic penalty, making its overall binding weaker than that of **2**.

Receptor **2** was not only the strongest but also the most selective among the three citrate receptors. Table 1 lists the relative binding constants (K_{rel}) of guests **5** and **6** to that of citrate. According to our data, the flexible cholate receptor **1** had the poorest selectivity, with K_{rel} being 0.73 and 0.31 for **5** and **6**, respectively. The preorganized cholate receptor **2** afforded a K_{rel} of 0.03 for **5** and showed nondetectable binding for **6**. Although the control receptor **3** also exhibited no binding for **6**, it bound **5** with a K_{rel} of 0.24, thus less discriminating than cholate receptor **2**. Stronger citrate-binding receptors have been prepared

by Schmuck and Schwegmann using the principle of preorganization and multivalency, but the selectivity was lower.[37]

Figure 2. CPK model of complex **2•4**, showing the hydrogen-bonded citrate on the top and tightly packed cholates groups.

Our data so far strongly supports the intimate contact among the cholates being responsible for the unusual stability of complex **2•4** in water. Our hypothesized binding model also suggests that poor contact among the cholates should be the cause of the lower stability of **2•5**. If these predictions are true, a hydrophobic "gap" should exist among the cholates of **2•5**, which is lacking in the former. To confirm these features, we titrated receptor **2** with **4** and **5**, respectively, in the presence of 1.0 μM pyrene in water. Pyrene has five vibronic bands in emission. The first band (I_1) near 372 nm becomes more intense in more polar environment and the third (I_3) near 384 is rather insensitive to the environmental

polarity. As a result, the I_3/I_1 ratio becomes larger as the probe enters a nonpolar microenvironment.[38] If indeed a hydrophobic gap is created when **5** binds **2**, pyrene, being hydrophobic, should insert itself into the gap, provided that the gap is large enough to accommodate the probe. With the cholates tightly associated with one another in **2•4** (CPK model shown in Figure 2), pyrene is expected to remain in the aqueous phase, displaying a nearly constant and rather low I_3/I_1 value.

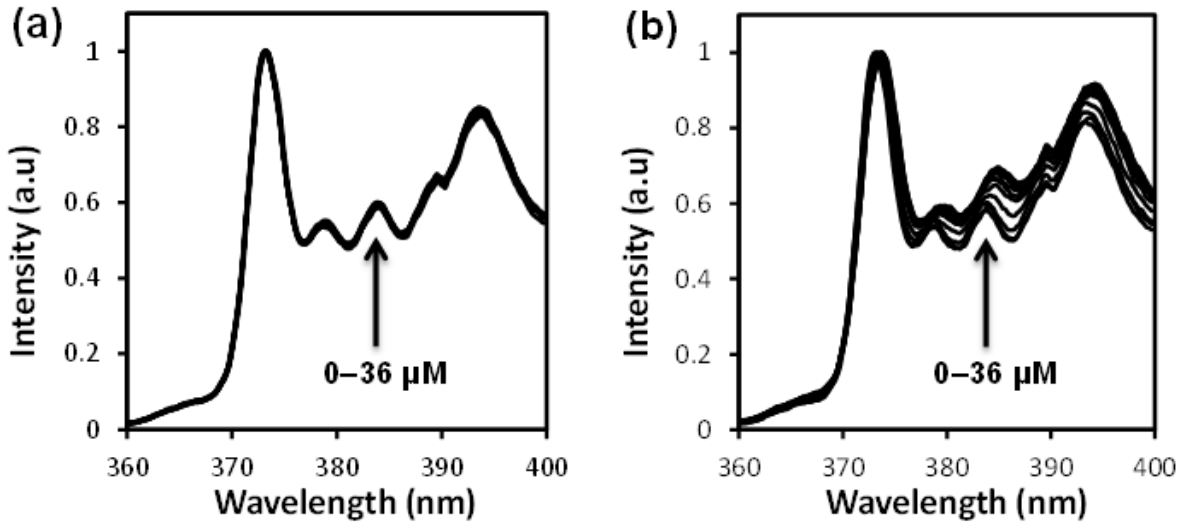

Figure 3. Emission spectra of pyrene normalized to vibronic band I_1 in different concentrations of (a) citrate **4** and (b) benzene-1,3,5-tricarboxlate **5** in the presence of receptor **2** in Millipore water. [Pyrene] = 1.0 μM; [**2**] = 20 μM.

Figure 3a shows the normalized emission spectra of pyrene as 0–36 μM of citrate **4** was added to 20 μM of receptor **2**. As predicted, the emission of pyrene stayed unchanged, suggesting that pyrene remained in water throughout the titration. Calculated from the binding constant and the concentrations, the percentage of **2** being complexed with citrate ranged from 0 to 67% during the titration. The nearly constant I_3/I_1 indicates that pyrene under our experimental conditions bound neither the free receptor nor the **2•4** complex.

When **2** was titrated with benzene-1,3,5-tricarboxlate **5**, the results were completely different (Figure 3b). The I_3 band intensified continuously relative to I_1, shown also by Figure 4, in which the I_3/I_1 ratio was plotted against the concentration of the guest. The gradual increase of I_3/I_1 suggests that a hydrophobic gap indeed was created in complex **2•5** that could accommodate pyrene. The three carboxylate groups in **5** are separated by a phenyl spacer. Formation of three amidinium–carboxylate salt bridges, therefore, is anticipated to keep the cholates apart—this is how the hydrophobic gap is formed in the complex. The net result is that, when a CER binds a mismatched guest, the intrareceptor interactions that have enhanced the binding of a well-matched guest turn against the poorly-fitted guest because the guest-binding creates unfavorable intrareceptor interactions. Put it in a different way, the guest-triggered intrareceptor interactions are a double-edged sword: they reward the "fittest" guest by contributing to their binding and penalize the "misfitted" ones by taking away what can be obtained through direct host–guest binding interactions.

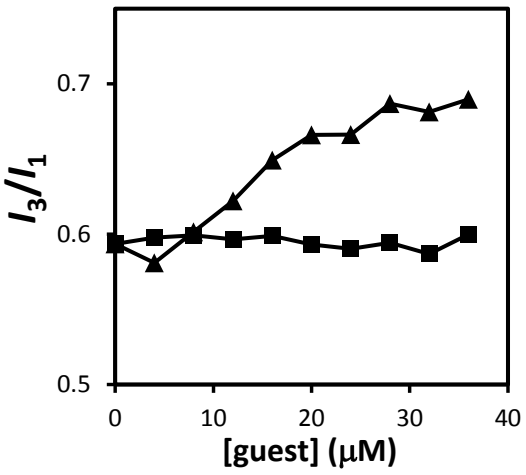

Figure 4. Pyrene I_3/I_1 ratio as a function of the concentration of citrate **4** (■) and benzene-1,3,5-tricarboxylate **5** (▲) in Millipore water. [Pyrene] = 1.0 μM. [2] = 20 μM.

Cooperative enhancement is beneficial to selectivity only if the CER is properly preorganized, as demonstrated by receptor **2** in our study. For nonpreorganized CER **1**, the flexible scaffold gives the cholates too much freedom to adjust themselves, both in the free receptor and after binding the guest. The result is very poor selectivity of binding, as shown by the binding data.

Conclusion

One of the most interesting properties of the CERs is that what controls the binding both in terms of affinity and selectivity could be completely away from the binding interface. This feature is the key difference between a CER and traditional preorganized hosts whose binding action mainly happens at the host–guest binding interface. The most significant finding of this work is that the intrareceptor interactions can be rationally engineered to favor one guest over others to magnify both the affinity and selectivity. As supramolecular chemistry continues to evolve, this strategy should be very useful in the design of biomimetic receptors, even when direct binding forces are weak due to either environmental or structural reasons.

Acknowledgement

We thank NSF (CHE-1303764) for supporting this research.

Experimental Section

General Method

For spectroscopic purpose, methanol, tetrahydrofuran, hexane, and ethyl acetate were of HPLC grade. All other reagents and solvents were of ACS-certified grade or higher, and were used as received from commercial suppliers. Routine ^{1}H and ^{13}C NMR spectra were

recorded on a Bruker DRX-400, on a Bruker AV II 600 or on a Varian VXR-400 spectrometer. MALDI-TOF mass was recorded on a Thermobioanalysis Dynamo mass spectrometer. ITC was performed using a MicroCal VP-ITC Microcalorimeter with Origin 7 software and VPViewer2000 (GE Healthcare, Northampton, MA). Fluorescence spectra were recorded at ambient temperature on a Varian Cary Eclipse Fluorescence spectrophotometer.

Syntheses

Syntheses of compounds **6**,[39] **7**,[40] **8**,[40] **9**,[40] **10**,[40] **14**,[41] **15**,[41] **16**,[42] and **17**[43] were previously reported.

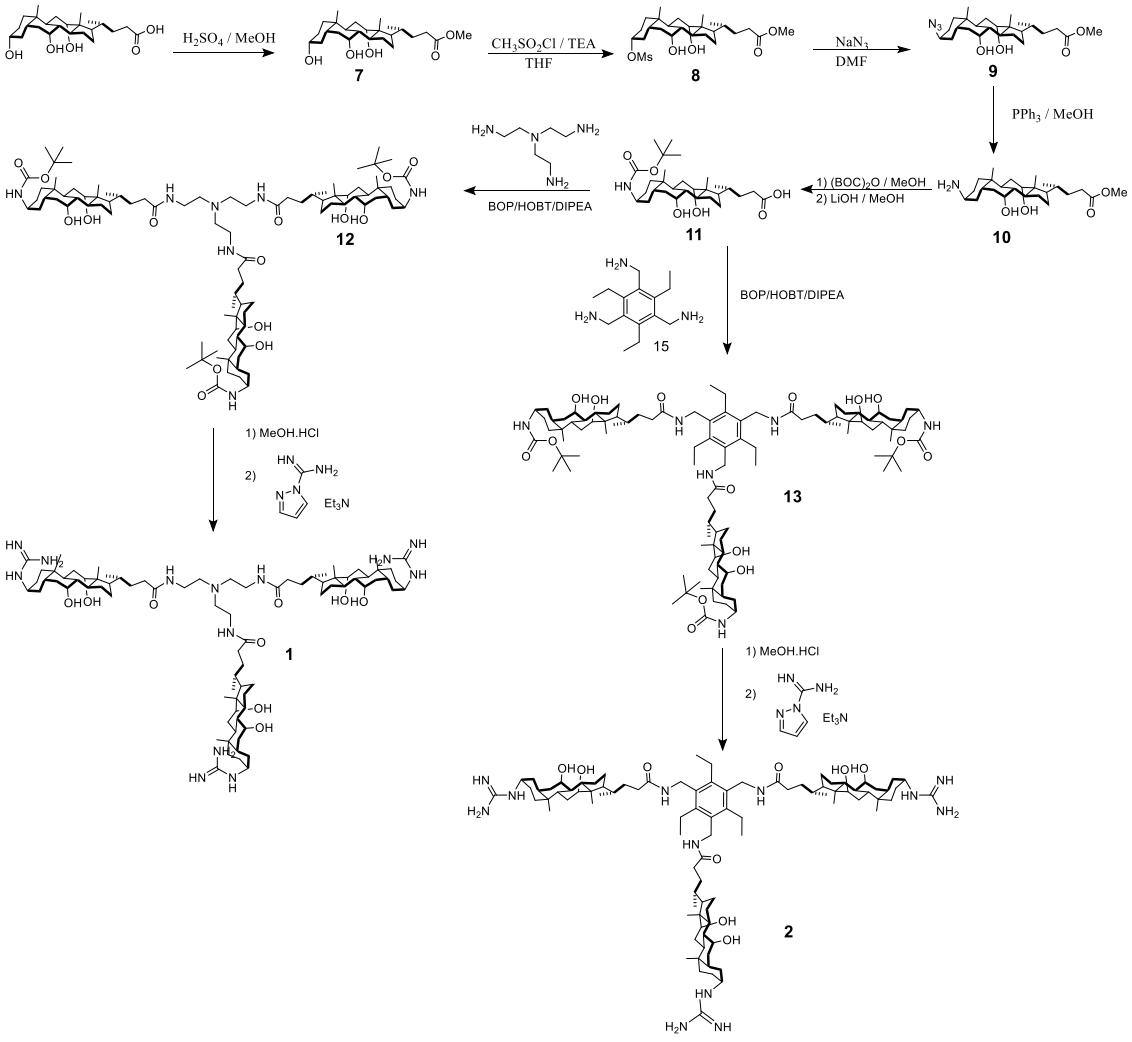

Scheme 3. Synthesis of compound **1** and compound **2.**

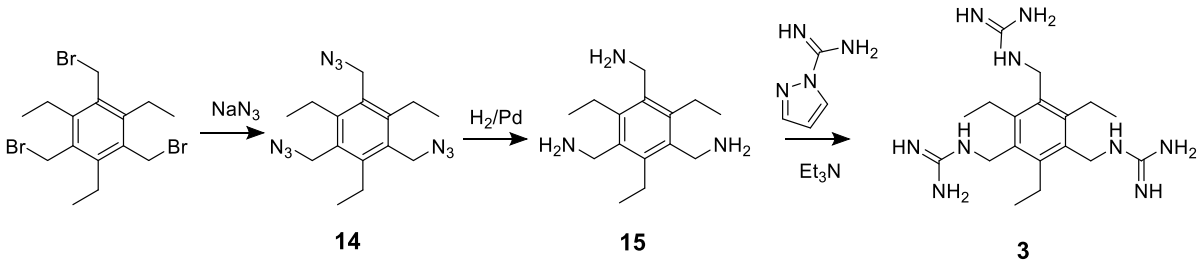

Scheme 4. Synthesis of compound **3.**

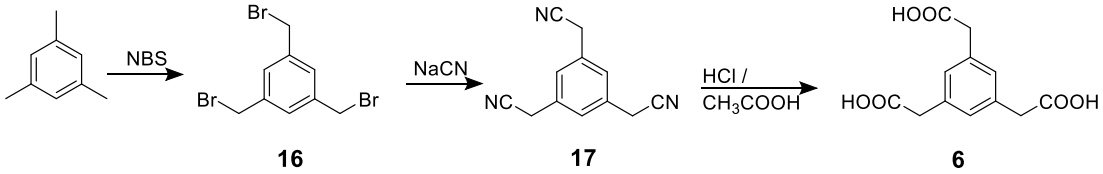

Scheme 5. Synthesis of compound **6.**

Compound 11. Compound **10** (0.9 g, 2.13 mmol) was dissolved in methanol (25.00 mL) and sodium bicarbonate (0.35g, 4.2 mmol) was added to it. Di-tert-butyl dicarbonate (0.511g, 2.34 mmol) was added to the reaction content and stirred at room temperature under nitrogen gas. The reaction was monitored by TLC and completed in 12 h. 2 M lithium hydroxide (11 mL, 21.30 mmol) was then added to it. The mixture was stirred at room temperature for 4 h. The reaction was monitored by TLC. The organic solvent was removed by rotary evaporation. After a dilute HCl solution (0.05 M, 30 mL) was added to the reaction mixture, the precipitate formed was collected by suction filtration, washed with cold water, and dried *in vacuo* to get a white powder (1.00 g, 99%). ^{1}H NMR (400 MHz, $CD_3OD/CDCl_3$, 1:1, δ): 5.44(s, 1H), 3.93 (s, 1H), 3.78 (s, 1H), 3.73 (s, 1H), 2.60-0.92 (series of m), 0.66 (s, 3H). ESI-MS (*m/z*): $[M+H]^+$ cacld for $C_{29}H_{50}NO_6$, 508.3633; found, 508.3631.

Compound 12. Compound **11** (0.91 g, 1.8 mmol), tris(2-aminoethyl)amine (0.087 mL, 0.58 mmol), (benzotriazol-1-yloxy)tris(dimethylamino)phosphonium hexafluorophosphate (BOP, 1.53 g, 3.48 mmol), 1-hydroxybenzotriazole hydrate (HOBt, 0.47 g, 3.48 mmol), and N,N-diisopropylethylamine (DIPEA, 1.21 mL, 6.96 mmol) were dissolved in dimethyl formamide (6 mL). The reaction was stirred for 1 h in a microwave reactor at 65 °C (150 W), cooled down to room temperature, and poured into a dilute HCl aqueous solution (0.05 M, 20 mL). The precipitate formed was collected by suction filtration, washed with water, dried in air, and purified by column chromatography over silica gel with 6:1 dichloromethane/methanol as the eluent to give an off-white powder (0.655 g, 70%). ^{1}H NMR (600 MHz, $CD_3OD/CDCl_3$, 1:1, δ): 6.21 (s, 3H), 3.94 (s, 3H), 3.79 (s, 3H), 3.72 (s, 3H), 3.22 (t, 6H), 2.60-0.92 (series of m), 0.70 (s, 9H). ^{13}C NMR (150 MHz, $CD_3OD/CDCl_3$, 1:1, δ): 175.5, 156.4, 77.6, 72.7, 67.8, 53.8, 47.7, 46.6, 43.2, 41.6, 39.5, 37.5, 36.8, 35.6, 34.9, 34.2, 34.0, 33.7, 33.0, 32.0, 30.5, 28.4, 27.6, 27.4, 25.9, 24.7, 23.0, 22.3, 20.6, 16.7, 11.9. ESI-MS (*m/z*): $[M+H]^+$ cacld for $C_{93}H_{160}N_7O_{15}$, 1615.1894; found, 1615.1950.

Compound 1. Compound **12** (0.45 g, 0.28 mmol) was stirred with methanolic hydrochloric acid (6 mL, pH = 1) at room temperature for 6 h. The reaction was monitored by TLC. The solvent was removed by rotary evaporation (bath temperature <40 °C), to give an off-white powder (0.37 g, 100%). The off-white powder (0.370 g, 0.28 mmol), 1H-Pyrazole-1-carboxamidine hydrochloride (0.132 g, 0.90 mmol) and triethyl amine (4 mL) in DMF (2 mL) was stirred at 60 °C under nitrogen. After 17 h, ether was added to the reaction mixture. The precipitate formed was collected by suction filtration, washed with ether, and dried in air. The crude product was crystallized from 1:1:1 ether/acetonitrile/ethanol (15 mL) to give yellow color powder. (0.360 g, 89%). ^{1}H NMR (600 MHz, $CD_3OD/CDCl_3$, 1:1, δ): 3.96 (s,

3H), 3.81 (s, 3H), 3.50 (s, 6H), 3.17 (q, J = 7.4 Hz, 6H), 2.78 (t, J = 14.6 Hz, 3H), 2.60-0.92 (series of m), 0.70 (s, 9H). ^{13}C NMR (150 MHz, $CD_3OD/CDCl_3$, 1:1, δ): 175.5, 156.3, 78.1, 77.7, 77.4, 72.6, 72.5, 67.9, 67.6, 67.4, 56.5, 55.6, 53.8, 48.6, 48.4, 48.2, 48.0, 47.9, 47.8, 47.7, 47.5, 47.4, 47.3, 46.8, 46.6, 46.4, 46.2, 41.6, 39.4, 37.5, 37.0, 36.7, 35.7, 35.7, 34.9, 33.9, 33.6, 33.1, 32.0, 31.5, 30.6, 30.2, 29.1, 28.4, 27.5, 25.9, 24.3, 23.0, 22.5, 22.3, 21.9, 21.8, 16.7, 12.0, 8.4, 6.9. ESI-MS (m/z): [M+H]+ cacld for $C_{81}H_{142}N_{13}O_9$, 1441.0975; found, 1441.1048.

Compound 13. Compound **11** (0.46 g, 0.89 mmol), compound **15** (0.070 g, 0.28 mmol), (benzotriazol-1-yloxy)tris(dimethylamino)phosphonium hexafluorophosphate (BOP, 0.495 g, 1.12 mmol), 1-hydroxybenzotriazole hydrate (HOBt, 0.15 g, 1.12 mmol), and N,N-diisopropylethylamine (DIPEA, 0.585 mL, 3.36 mmol) were dissolved in dimethyl sulfoxide (4 mL). The reaction was stirred for 3 h in a microwave reactor at 65 °C (150 W), cooled down to room temperature, and poured into a dilute HCl aqueous solution (0.05 M, 20 mL). The precipitate formed was collected by suction filtration, washed with water, dried in air, and purified by column chromatography over silica gel with 10:1 dichloromethane/methanol as the eluent to give an off-white powder (0.320 g, 67%). ^{1}H NMR (600 MHz, $CD_3OD/CDCl_3$, 1:1, δ): 4.39 (s, 6H), 3.92 (t, *J* = 2.8 Hz, 3H), 3.79 (m, 3H), 3.72 (s, 3H), 2.68 (m, 6H), 2.60-0.92 (series of m), 0.68 (s, 9H). ^{13}C NMR (150 MHz, $CD_3OD/CDCl_3$, 1:1, δ): 175.0, 143.8, 131.6, 126.8, 77.9, 77.8, 77.6, 77.2, 72.8, 67.9, 48.1, 47.9, 47.7, 47.5, 46.7, 46.2, 41.6, 39.2, 37.8, 36.9, 35.5, 35.0, 34.1, 32.6, 31.9, 28.3, 27.9, 27.5, 25.8, 23.0, 22.5, 17.8, 16.7, 15.7, 12.03. ESI-MS (*m/z*): $[M+H]^+$ cacld for $C_{102}H_{169}N_6O_{15}$, 1618.2568; found, 1618.2640.

Compound 2. Compound **13** (0.32 g, 0.18 mmol) was stirred with methanolic hydrochloric acid (5 mL, pH = 1) at room temperature for 6 h. The solvent was removed by rotary evaporation (bath temperature <40 °C) to give an off-white powder (0.37 g, 100%). The material obtained (0.31 g, 0.22 mmol) was combined with 1H-Pyrazole-1-carboxamidine hydrochloride (0.101 g, 0.69 mmol) and triethyl amine (3 mL) in DMF (2 mL) and the mixture was stirred at 60 °C under nitrogen. The reaction was monitored by TLC. After 17 h, ether was added to the reaction. The precipitate formed was collected by suction filtration, washed with ether, and dried in air. The crude product was crystallized from 1:1:1 ether/acetonitrile/ethanol (10 mL) to give a white color powder (0.29 g, 86%). ^{1}H NMR (600 MHz, $CD_3OD/CDCl_3$, 1:1, δ): 7.63 (s, 3H), 4.39 (s, 6H), 3.95 (s, 3H), 3.80 (s, 3H), 3.71 (s, 3H), 2.65 (d, *J* = 8.6 Hz, 6H), 2.68 (m, 6H), 2.60-0.92 (series of m), 0.69 (s, 9H). ^{13}C NMR (150 MHz, $CD_3OD/CDCl_3$, 1:1, δ): 175.0, 156.3, 143.9, 131.4, 72.7, 67.7, 65.7, 57.2, 48.4, 47.8, 47.7, 47.7, 47.5, 46.8, 46.6, 46.3, 46.3, 41.6, 39.5, 39.4, 37.9, 36.8, 35.6, 35.0, 33.9, 33.2, 32.7, 31.9, 30.7, 30.2, 28.3, 27.5, 25.9, 24.3, 23.0, 22.8, 22.5, 22.0, 17.4, 16.7, 15.7, 15.7, 14.5, 12.1. ESI-MS (*m/z*): $[M+3H]^{3+}$ cacld for $C_{90}H_{151}1N_{12}O_9$, 515.7299; found, 515.7310.

Compound 3. Compound **15** (0.10 g, 0.40 mmol), 1H-Pyrazole-1-carboxamidine hydrochloride (0.19 g, 0.69 mmol), and triethyl amine (0.5 mL) in in DMF (2 mL) was stirred at 60 °C under nitrogen. After 17 h, ether was added to the reaction mixture. The precipitate formed was collected by suction filtration, washed with ether, and dried in air. The crude product was crystallized from 1:1:1 ether/acetonitrile/ethanol (5 mL) to give white color powder (0.13 g, 89%). ^{1}H NMR (400 MHz, $CD_3OD/CDCl_3$, 1:1, δ): 4.42 (s, 2H), 2.71 (d, *J* = 7.4, 2H), 2.05 (s, 1H), 1.18 (t, *J* = 8.1 Hz, 3H).^{13}C NMR (100 MHz, $CD_3OD/CDCl_3$,

1:1, δ): 156.3, 145.3, 129.6, 39.6, 22.4, 15.2. ESI-MS (*m/z*): $[M+H]^+$ cacld for $C_{18}H_{34}N_9$, 376.2859; found, 376.2932.

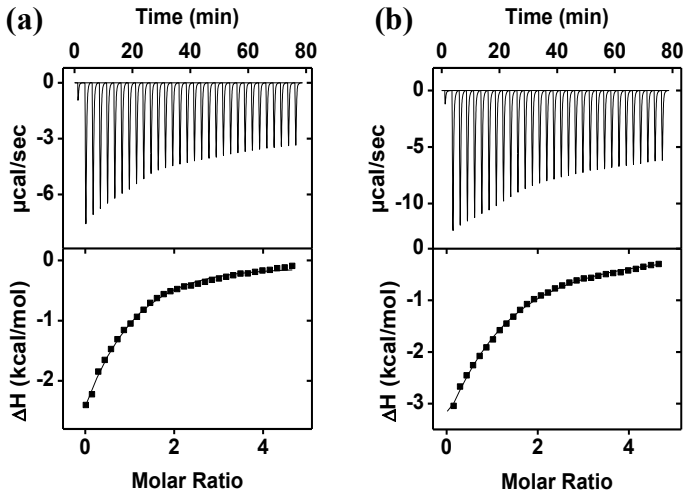

Figure 5. ITC titration curves obtained at 298 K for the binding of (a) **5** (4 mM) by CER **1** (0.2 mM) in D.I. water (pH = 7.0) and (b) **6** (4 mM) by CER **1** (0.2 mM) in D.I. water (pH = 7.0). The data correspond to entries 2 and 3 respectively, in Table 1. The top panel shows the raw calorimetric data. The area under each peak represents the amount of heat generated at each ejection and is plotted against the molar ratio of CER to the substrate. The solid line is the best fit of the experimental data to the sequential binding of N equal and independent binding sites on the CER. The heat of dilution for the substrate, obtained by adding the substrate to D.I. water (pH = 7.0), was subtracted from the heat released during the binding. Binding parameters were auto-generated after curve fitting using Microcal Origin 7.

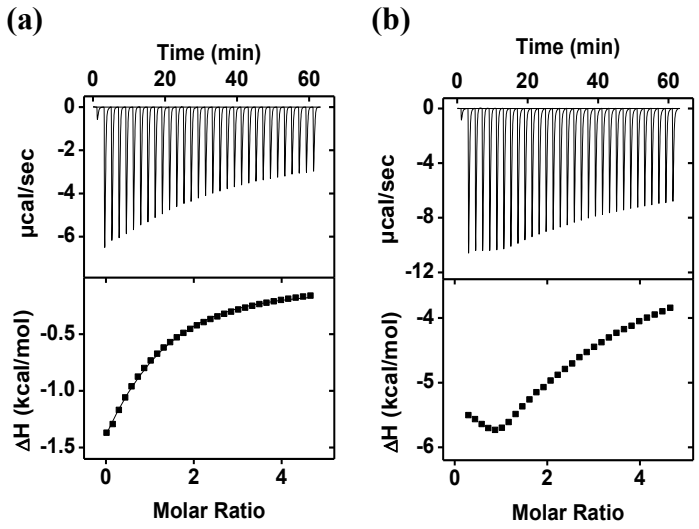

Figure 6. ITC titration curves obtained at 298 K for the binding of (a) **5** (4 mM) by CER **2** (0.2 mM) in D.I. water (pH = 7.0) and (b) **6** (4 mM) by CER **2** (0.2 mM) in D.I. water (pH = 7.0). The data correspond to entries 5 and 6 respectively, in Table 1. The top panel shows the raw calorimetric data. The area under each peak represents the amount of heat generated at each ejection and is plotted against the molar ratio of CER to the substrate. The solid line is the best fit of the experimental data to the sequential binding of N equal and independent binding sites on the CER. The heat of dilution for the substrate, obtained by adding the substrate to D.I. water (pH = 7.0), was subtracted from the heat released during the binding. Binding parameters were auto-generated after curve fitting using Microcal Origin 7.

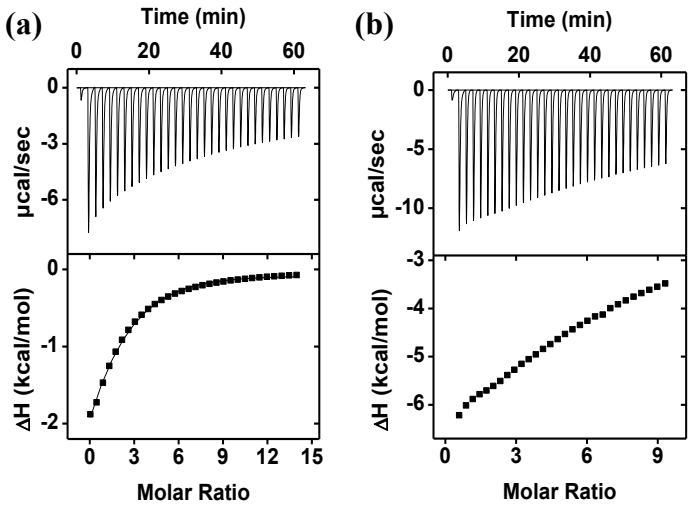

Figure 7. ITC titration curves obtained at 298 K for the binding of (a) **5** (6 mM) by CER **3** (0.1 mM) in D.I. water (pH = 7.0) and (b) **6** (4 mM) by CER **3** (0.1 mM) in D.I. water (pH = 7.0). The data correspond to entries 8 and 9 respectively, in Table 1. The top panel shows the raw calorimetric data. The area under each peak represents the amount of heat generated at each ejection and is plotted against the molar ratio of CER to the substrate. The solid line is the best fit of the experimental data to the sequential binding of N equal and independent binding sites on the CER. The heat of dilution for the substrate, obtained by adding the substrate to D.I. water (pH = 7.0), was subtracted from the heat released during the binding. Binding parameters were auto-generated after curve fitting using Microcal Origin 7.

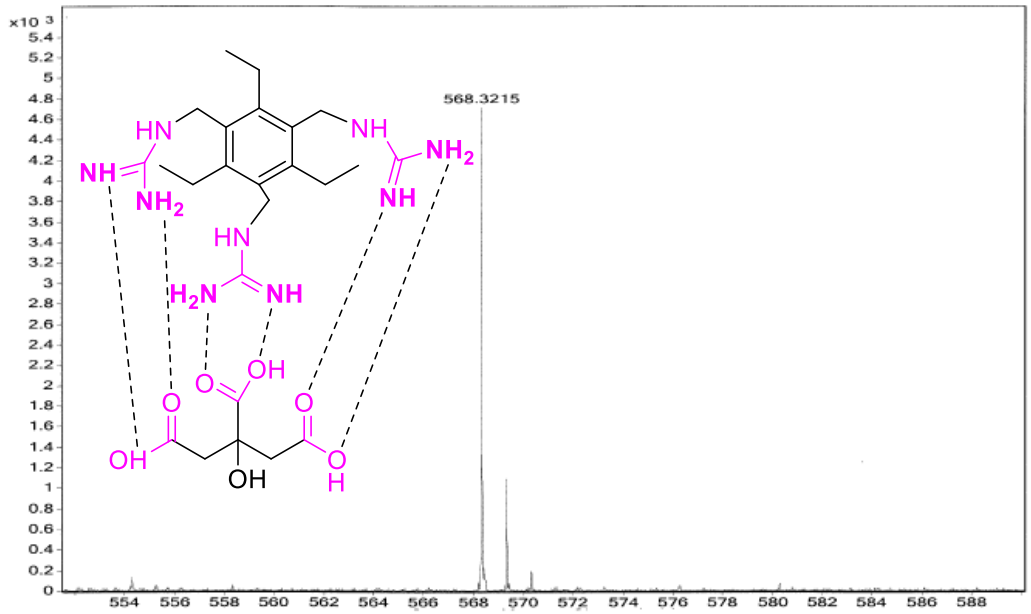

Figure 8. ESI-MS (*m/z*) for CER **3** with compound **4**: $[M+H]^+$ cacld for $C_{24}H_{42}N_9O_7$, 568.3142; found, 568.3215.

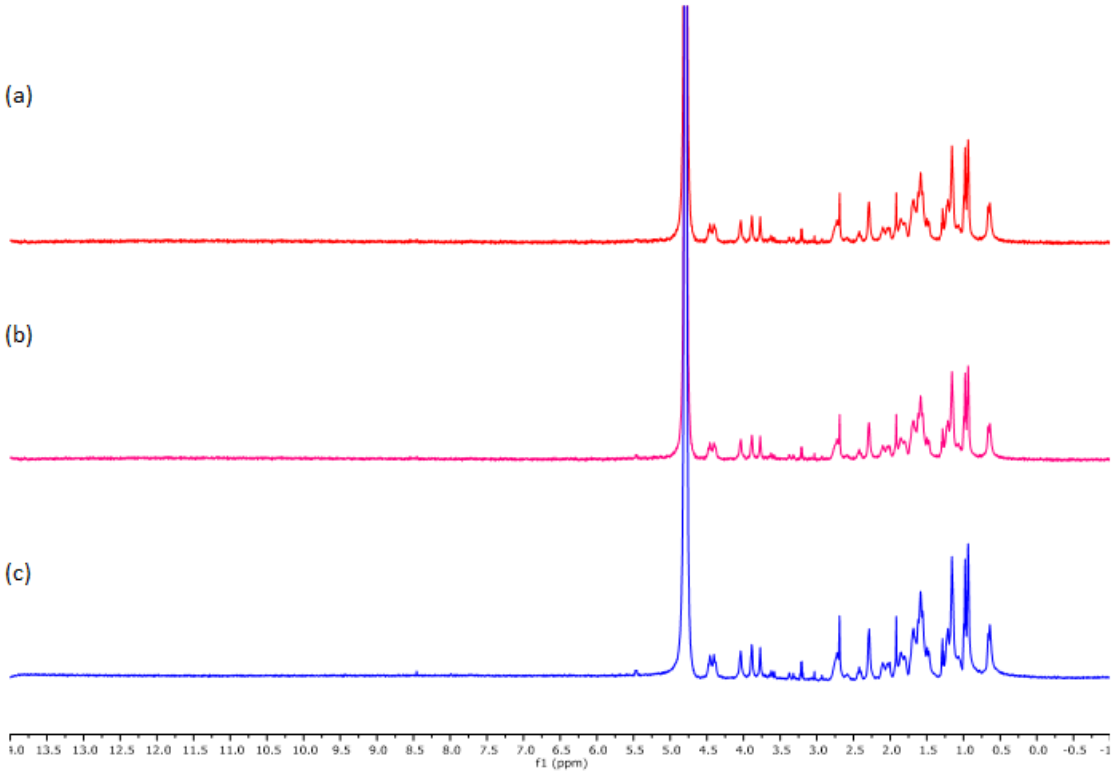

Figure 9. NMR dilution experiment (a) 0.2 mM, (b) 0.4 mM, and (c) 0.6 mM CER **2** concentration at 298 K.

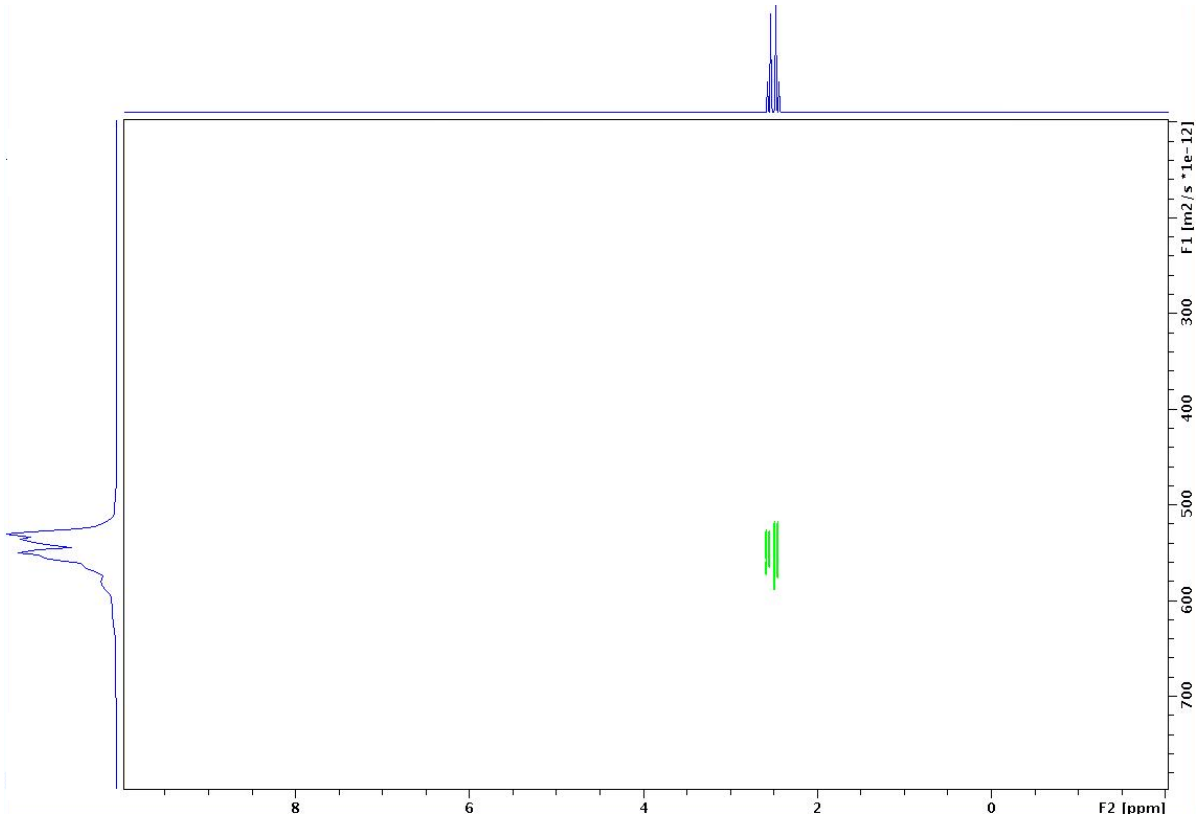

Figure 10. 400 MHz 2D DOSY NMR spectra obtained at 298 K in D_2O solution of **4**. (D_4 = 5.570×10^{-10} m^2S^{-1}, 1.5 mM)

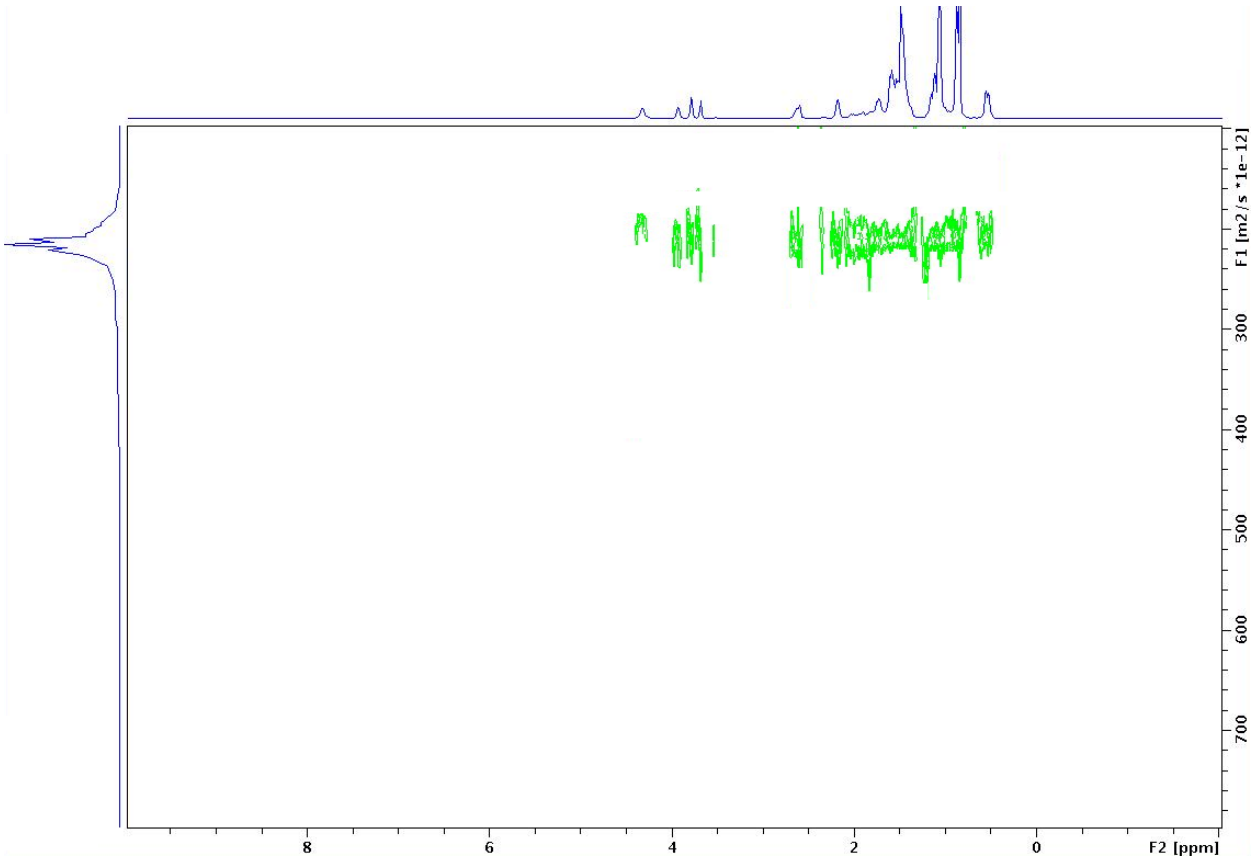

Figure 11. 400 MHz 2D DOSY NMR spectra obtained at 298 K in D_2O solution of CER **2**. ($D_{\mathbf{CER\ 2}} = 2.434 \times 10^{-10}\ m^2S^{-1}$, 1.5 mM)

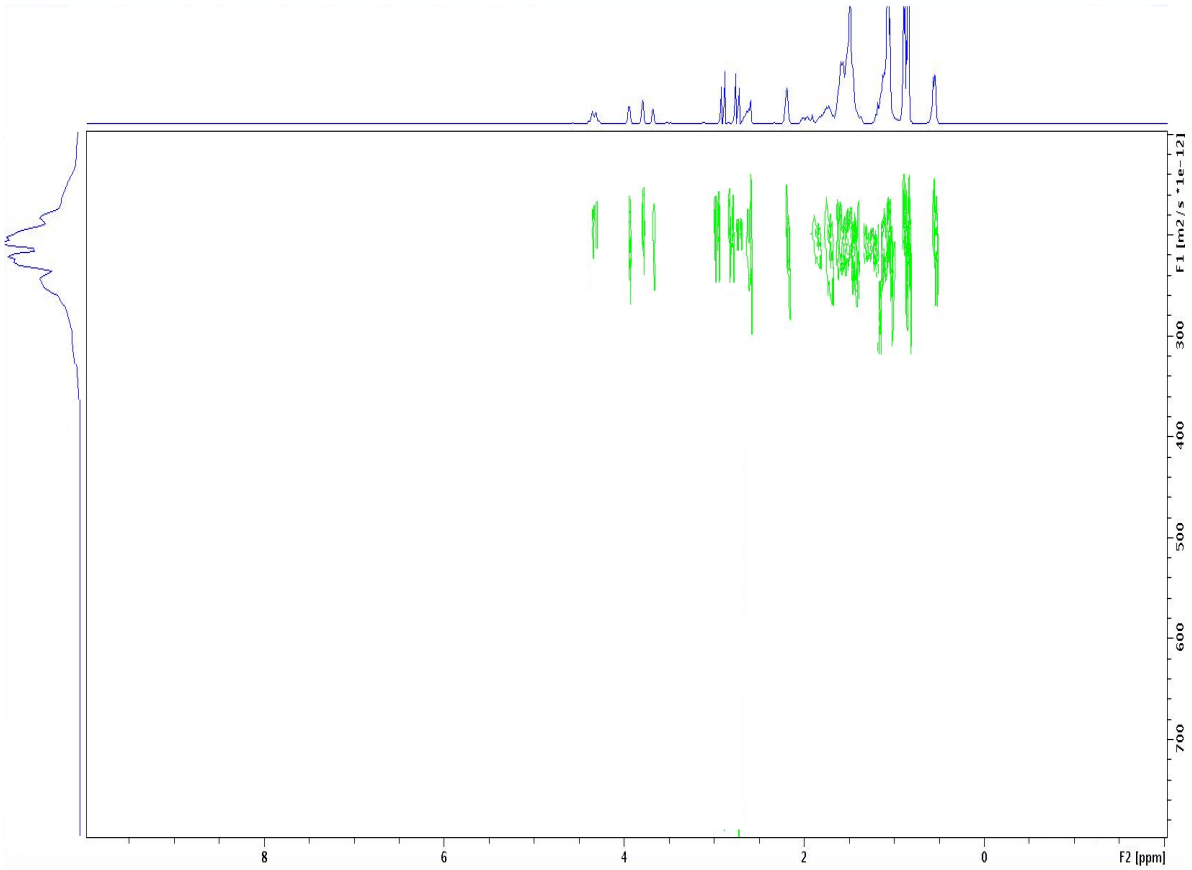

Figure 12. 400 MHz 2D DOSY NMR spectra obtained at 298 K in D_2O solution of 1:1 mixture of CER **2** and Compound **4**. ($D_{Complex}$ = 2.164 $\times 10^{-10}$ m^2S^{-1}, 1.5 mM)

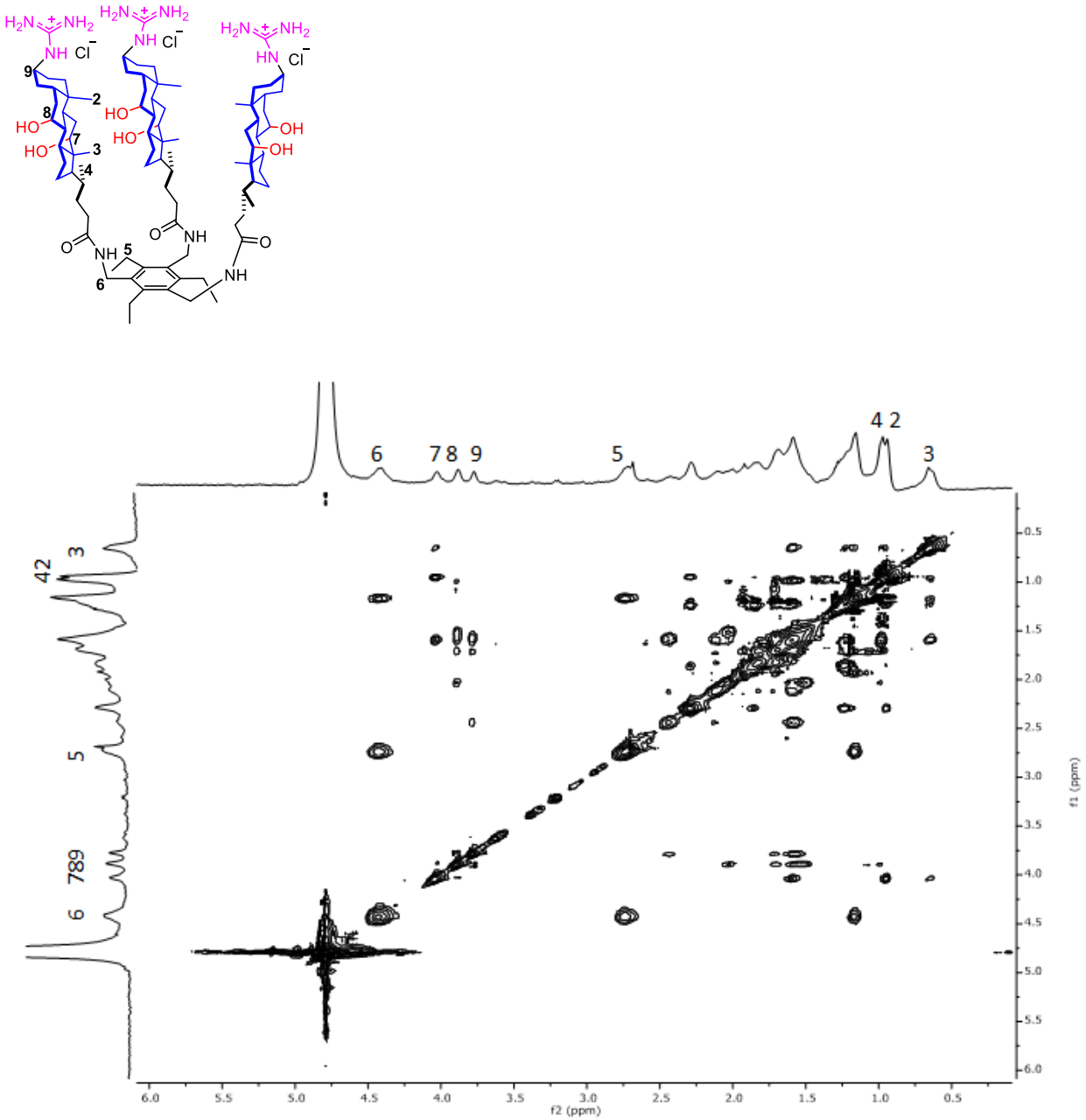

Figure 13. The 2D NOESY spectrum of CER **2** in D_2O at 298 K.

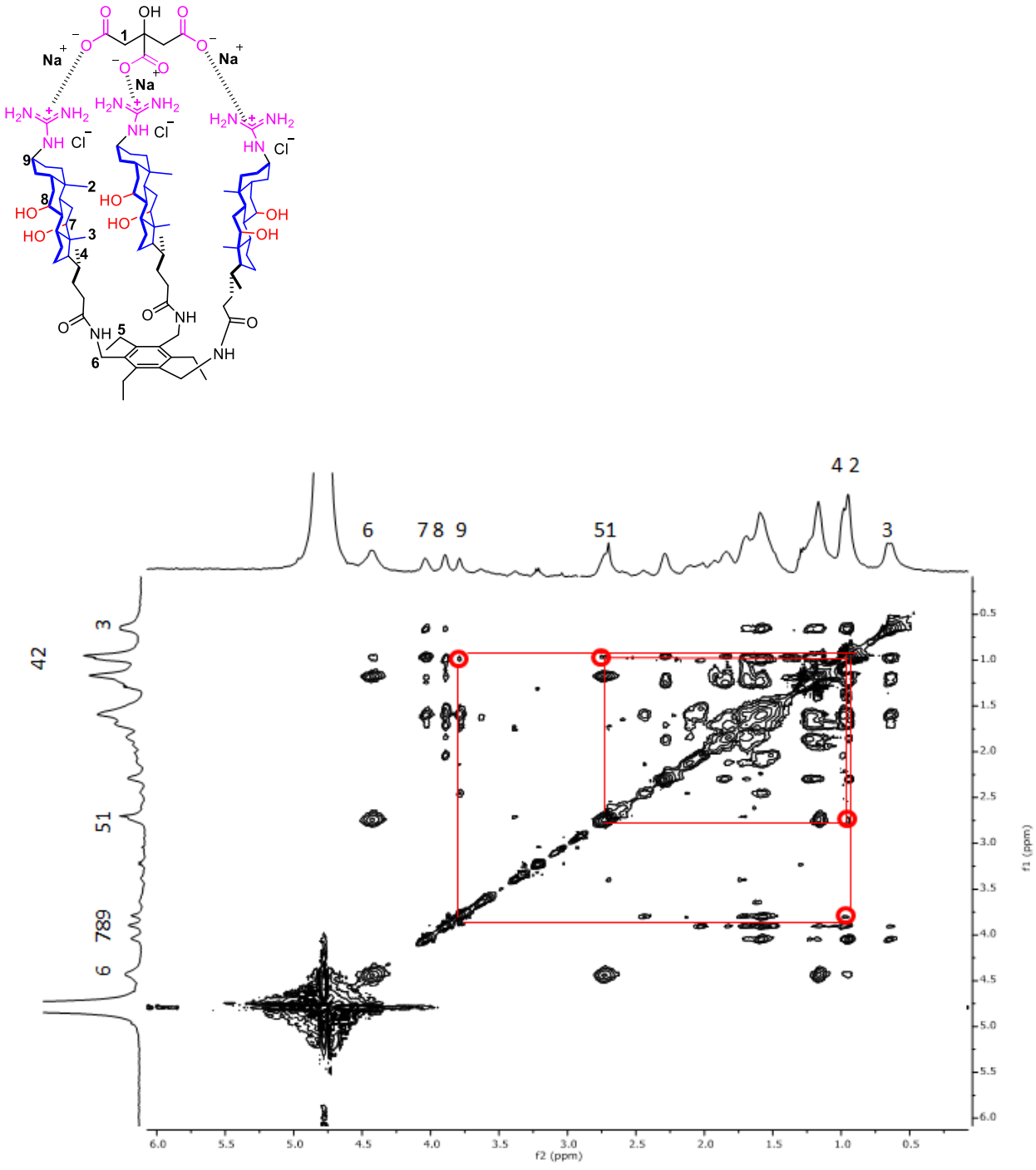

Figure 14. The 2D NOESY spectrum of 1:1 mixture of CER **2** and Compound **4** in D_2O at 298 K. The cross-peaks circled in red were absent in receptor **2** (**Figure 13**) and indicated the close contact between the cholate β faces and between citrate and the receptor.

^{1}H and ^{13}C NMR spectra

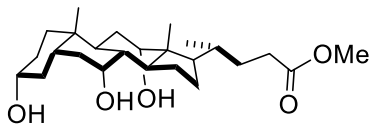

7

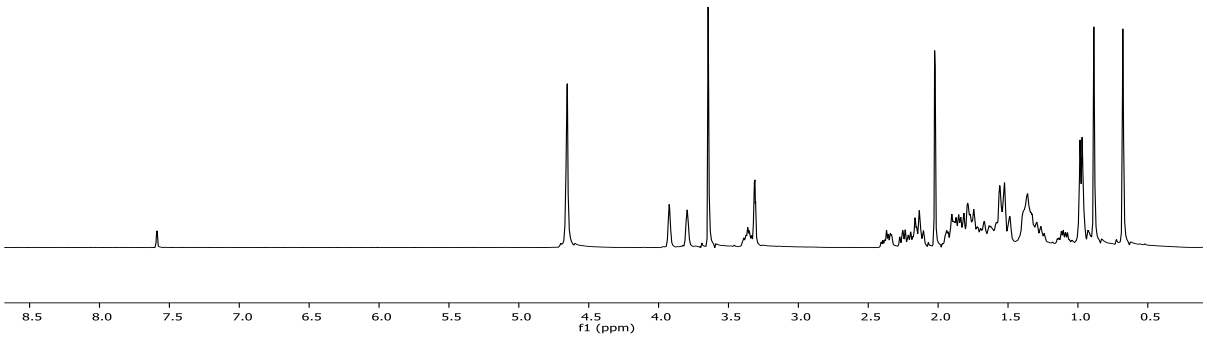

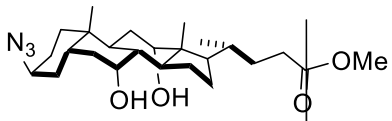

9

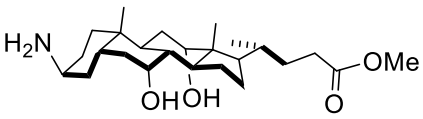

10

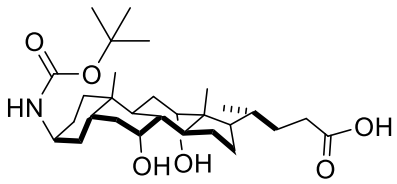

11

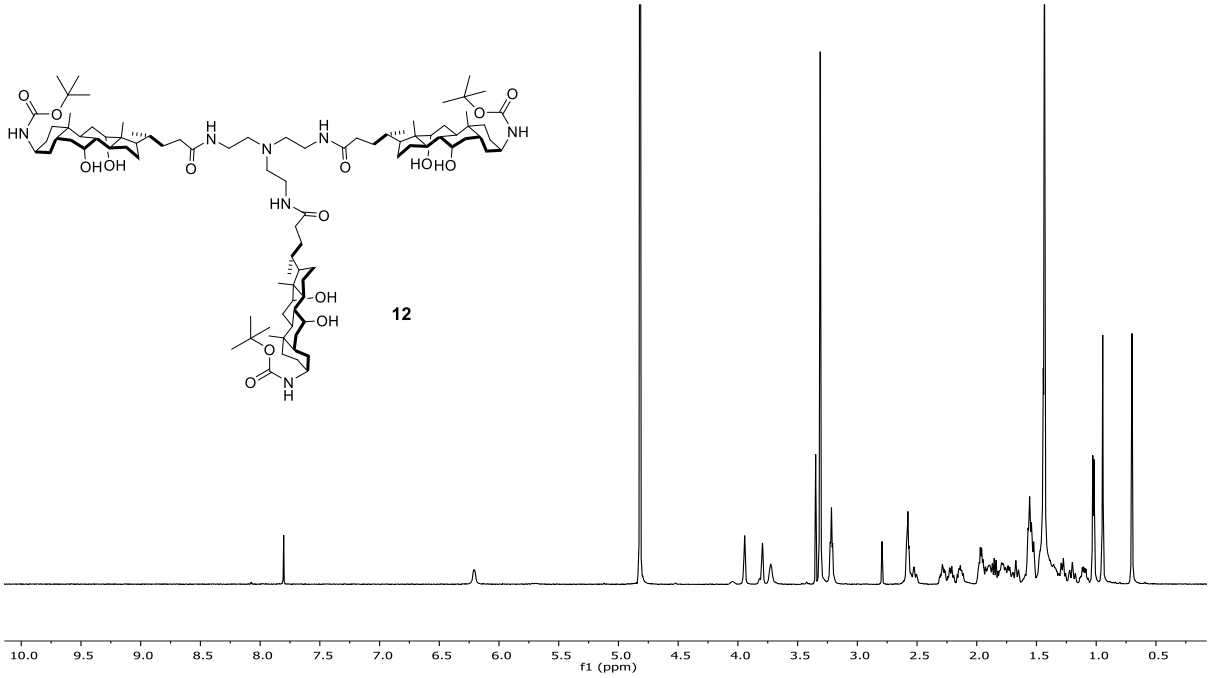

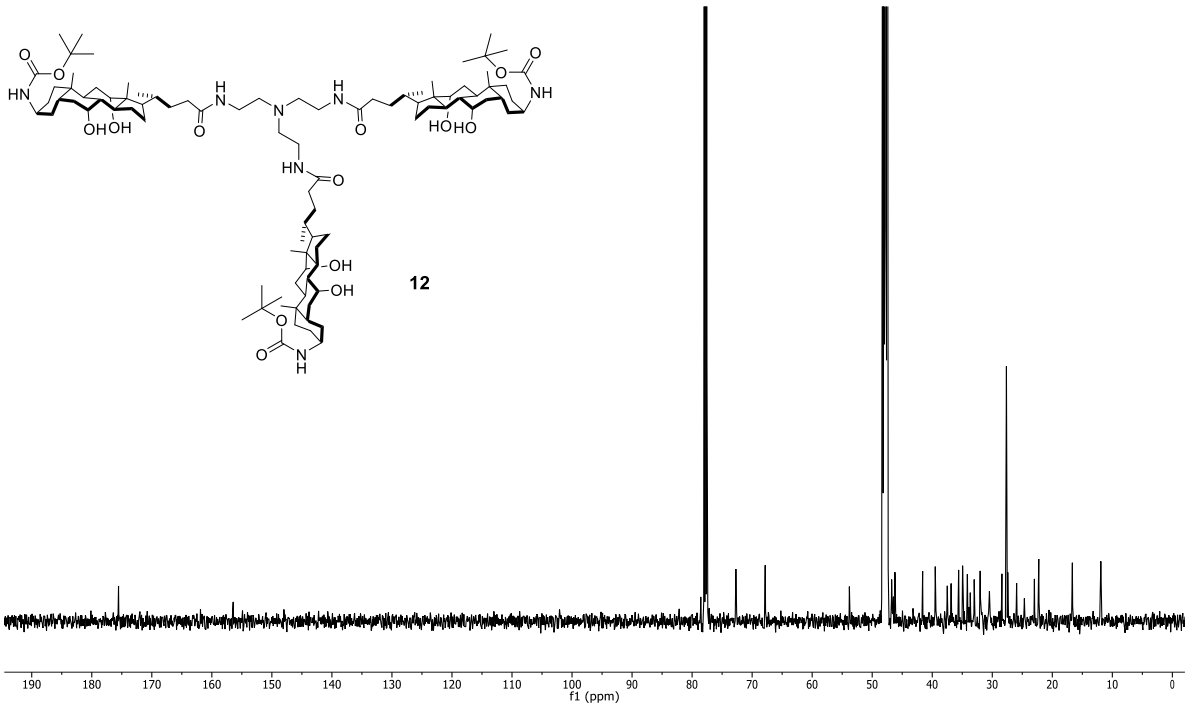

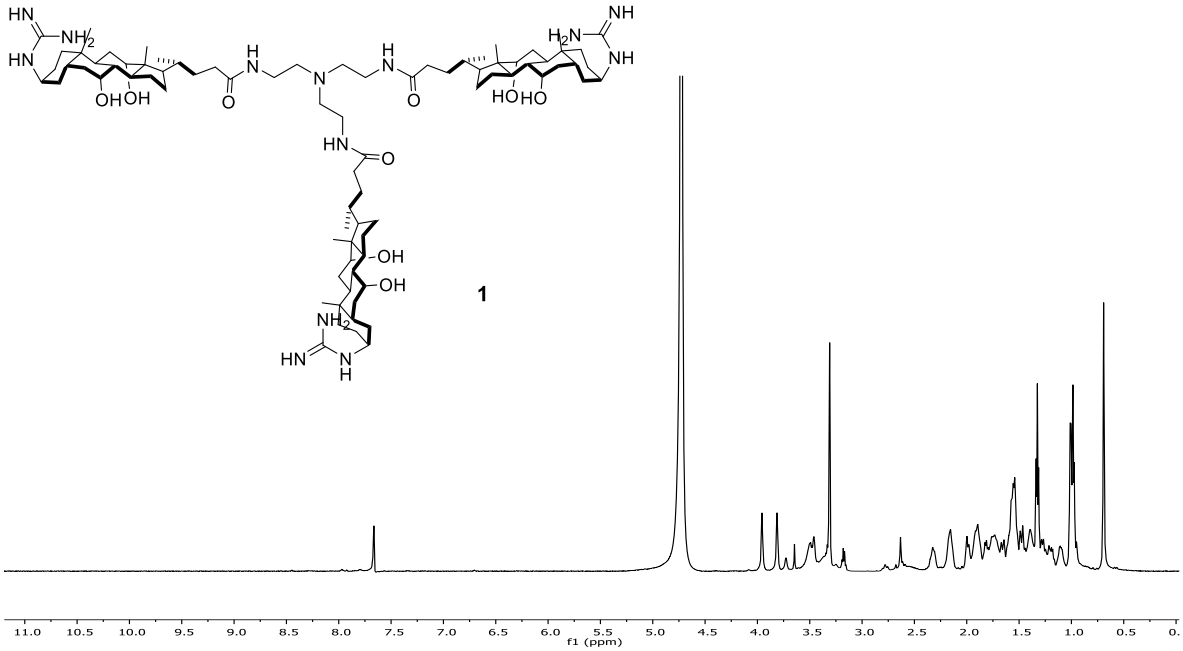

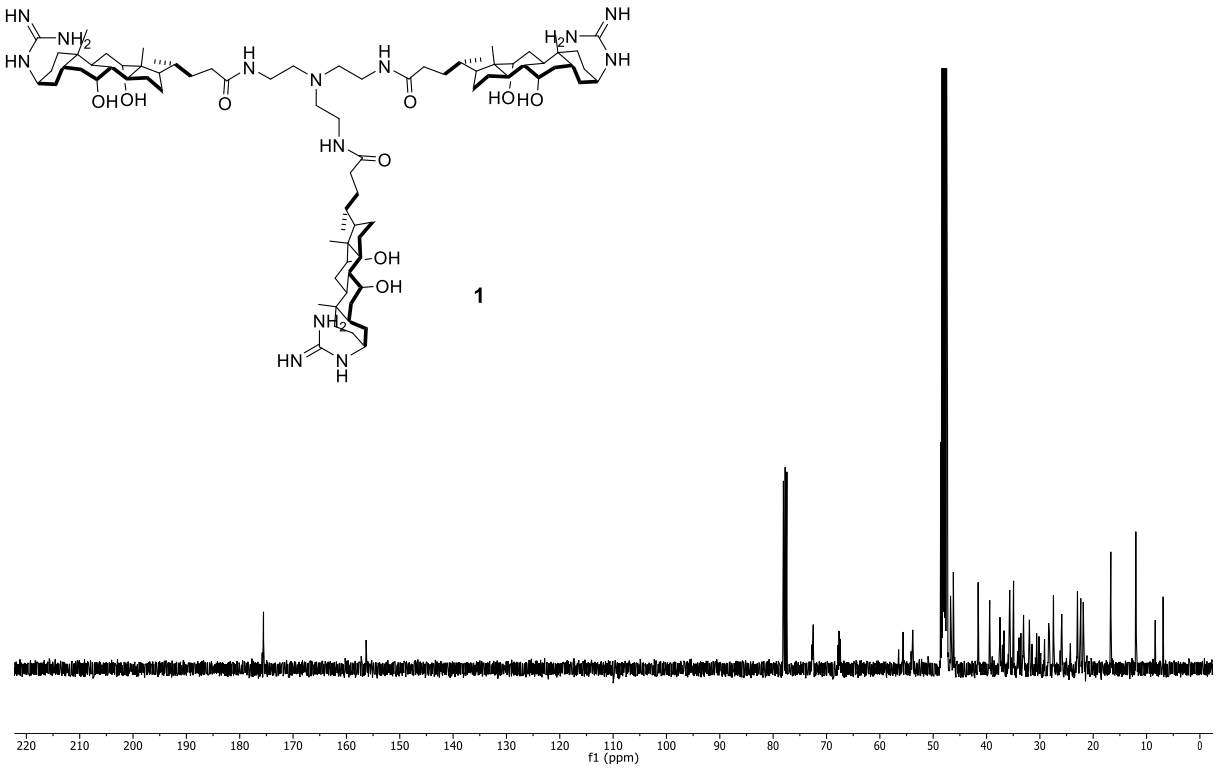

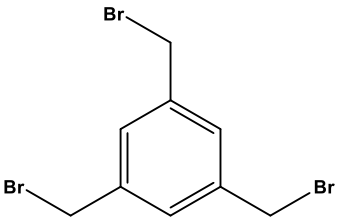

16

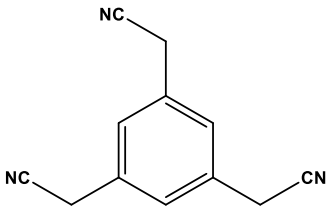

17

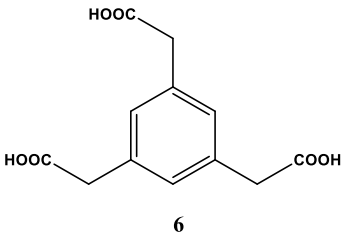

6

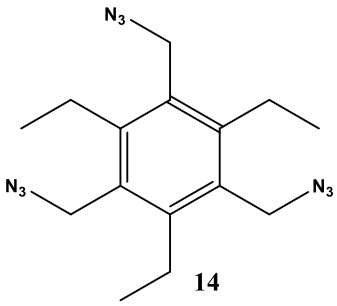

14

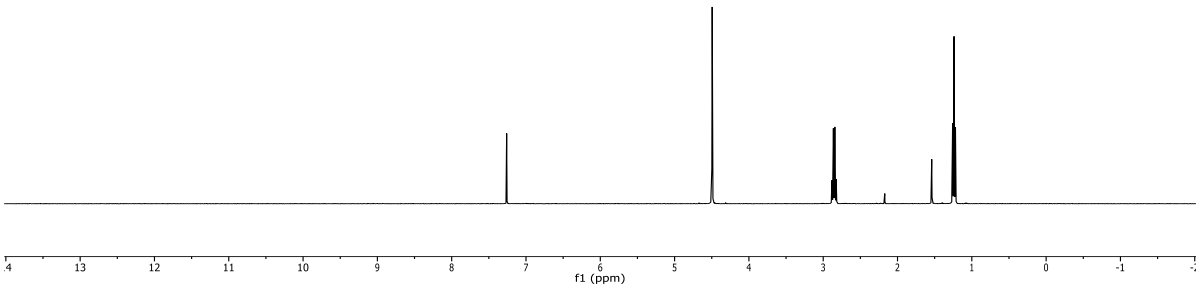

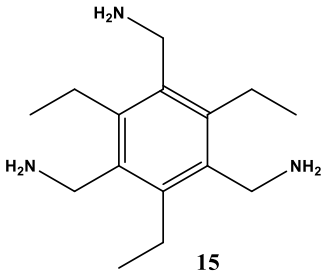

15

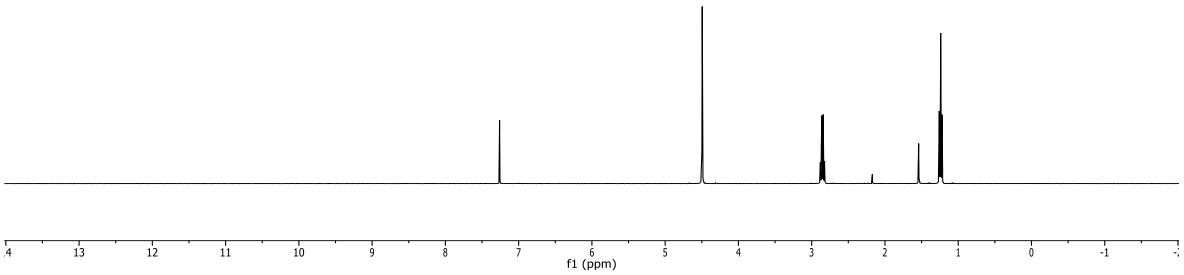

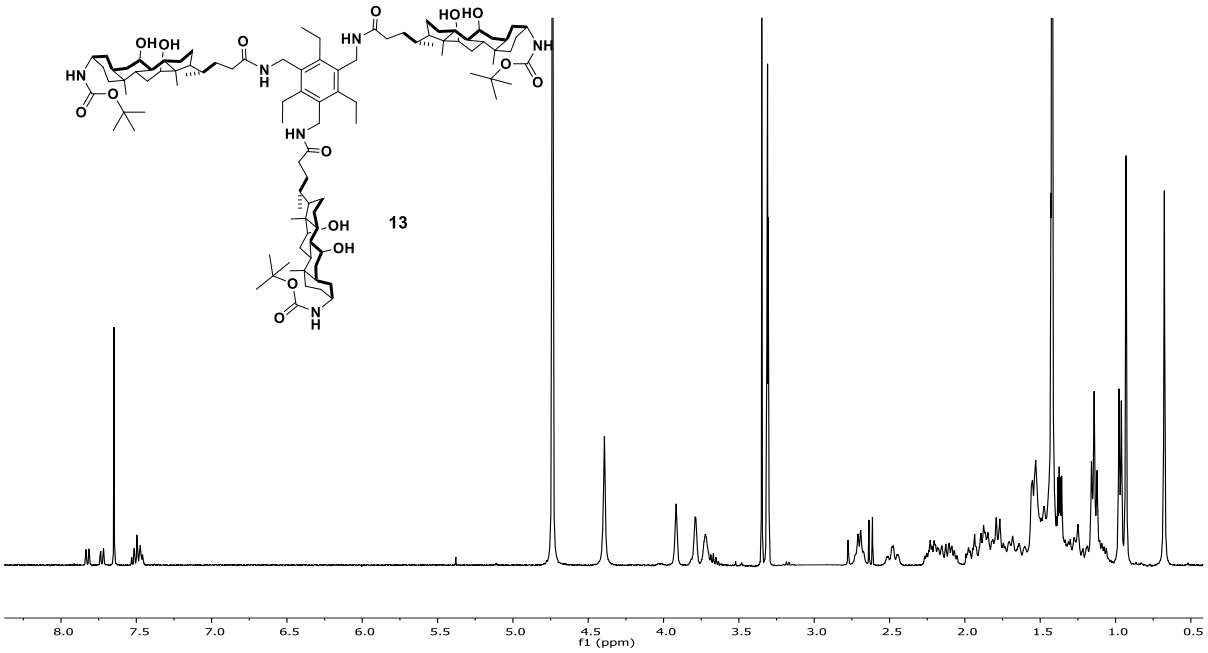

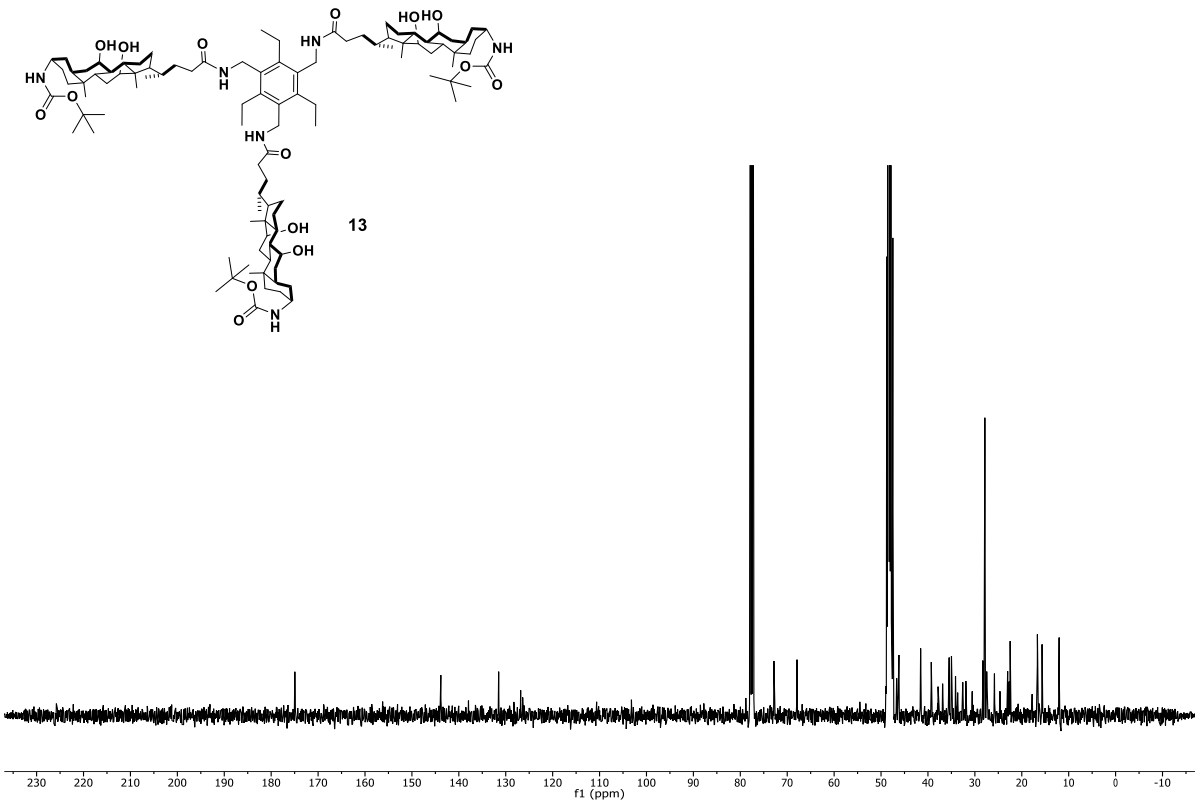

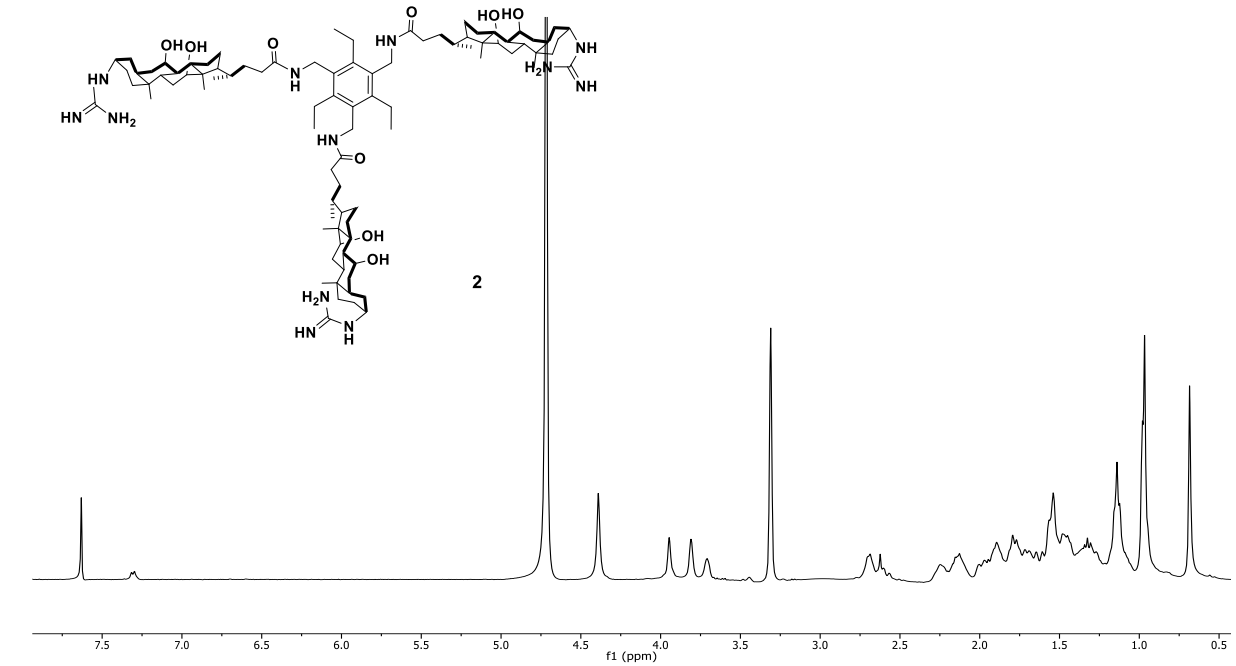

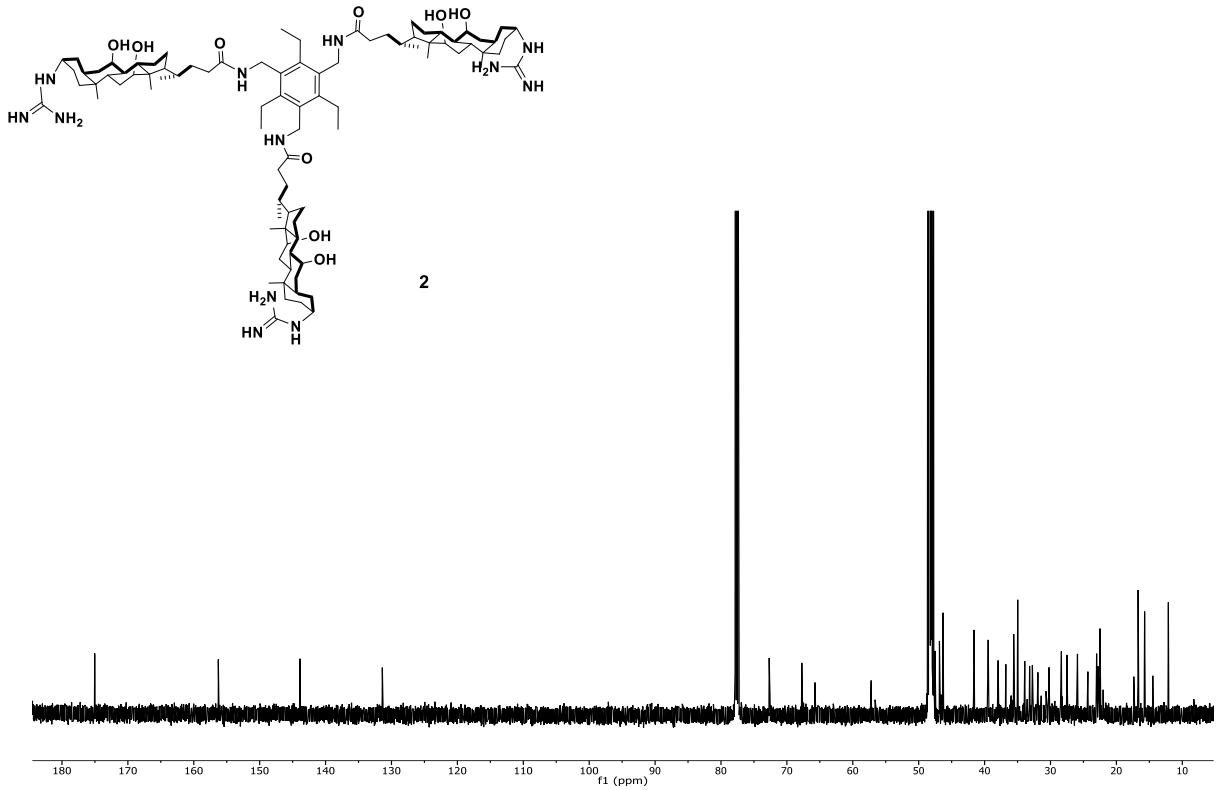

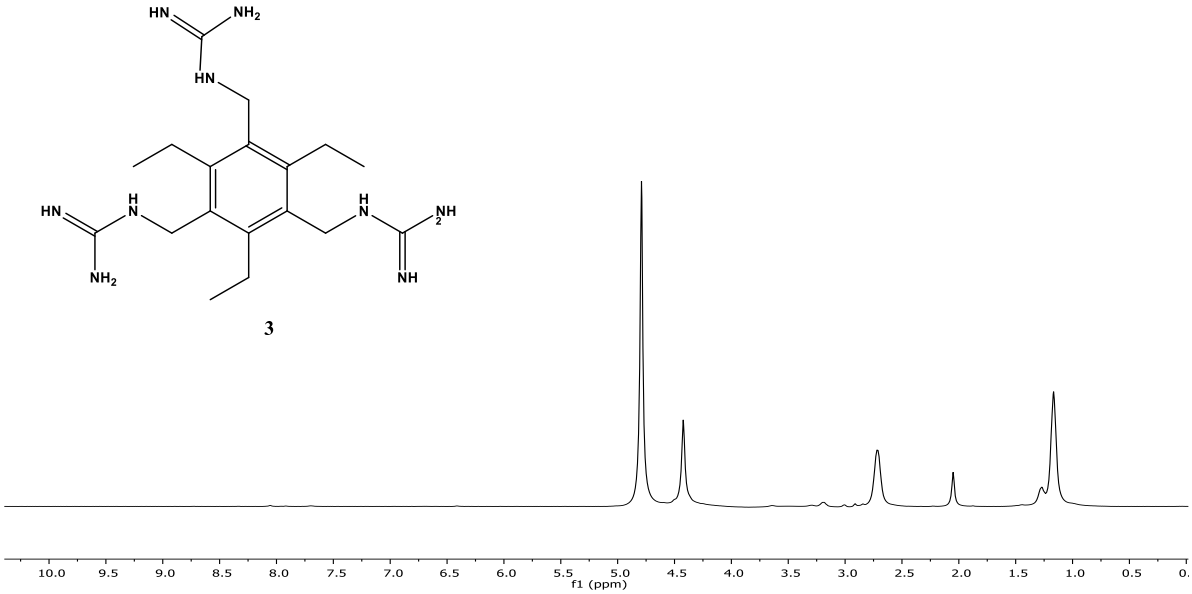

3

3

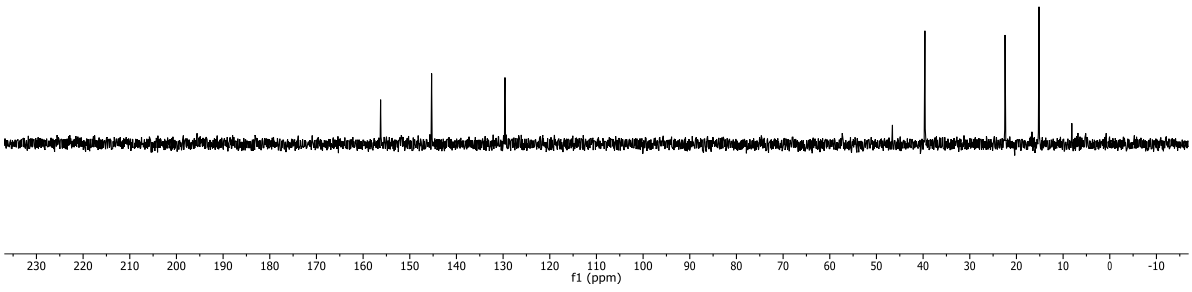

Notes and References

(1) J. L. Atwood and J. M. Lehn, *Comprehensive Supramolecular Chemistry*, Pergamon, New York, 1996.

(2) J. W. Steed and P. A. Gale, *Supramolecular Chemistry: From Molecules to Nanomaterials*, Wiley, Weinheim, 2012.

(3) G. V. Oshovsky, D. N. Reinhoudt and W. Verboom, *Angew. Chem. Int. Ed.*, 2007, **46**, 2366-2393.

(4) E. A. Kataev and C. Müller, *Tetrahedron*, 2014, **70**, 137-167.

(5) J. K. Awino and Y. Zhao, *J. Am. Chem. Soc.*, 2013, **135**, 12552-12555.

(6) J. K. Awino and Y. Zhao, *Chem. Commun.*, 2014, **50**, 5752-5755.

(7) J. K. Awino and Y. Zhao, *Chem.-Eur. J.*, 2015, **21**, 655-661.

(8) J. K. Awino and Y. Zhao, *ACS Biomater. Sci. Eng.*, 2015, **1**, 425-430.

(9) M. Rekharsky, Y. Inoue, S. Tobey, A. Metzger and E. Anslyn, *J. Am. Chem. Soc.*, 2002, **124**, 14959-14967.

(10) M. Mammen, S. K. Choi and G. M. Whitesides, *Angew. Chem. Int. Ed.*, 1998, **37**, 2755-2794.

(11) J. D. Badjic, A. Nelson, S. J. Cantrill, W. B. Turnbull and J. F. Stoddart, *Acc. Chem. Res.*, 2005, **38**, 723-732.

(12) A. Metzger, V. M. Lynch and E. V. Anslyn, *Angew. Chem. Int. Ed.*, 1997, **36**, 862-865.

(13) L. A. Cabell, M. D. Best, J. J. Lavigne, S. E. Schneider, D. M. Perreault, M.-K. Monahan and E. V. Anslyn, *J. Chem. Soc., Perkin Trans. 2*, 2001, 315-323.

(14) L. Fabbrizzi, F. Foti and A. Taglietti, *Org. Lett.*, 2005, **7**, 2603-2606.

(15) M. P. Clares, C. Lodeiro, D. Fernandez, A. J. Parola, F. Pina, E. Garcia-Espana, C. Soriano and R. Tejero, *Chem. Commun.*, 2006, 3824-3826.

(16) M. H. Filby and J. W. Steed, *Coord. Chem. Rev.*, 2006, **250**, 3200-3218.

(17) D. R. Turner, M. J. Paterson and J. W. Steed, *J. Org. Chem.*, 2006, **71**, 1598-1608.

(18) K. Ghosh and S. Adhikari, *Tetrahedron Lett*, 2008, **49**, 658-663.

(19) V. Vajpayee, Y. H. Song, M. H. Lee, H. Kim, M. Wang, P. J. Stang and K. W. Chi, *Chem.-Eur. J.*, 2011, **17**, 7837-7844.

(20) M. d. C. Gonzalez, F. Oton, A. Espinosa, A. Tarraga and P. Molina, *Org. Biomol. Chem.*, 2015, **13**, 1429-1438.

(21) A. Akdeniz, M. G. Caglayan and P. Anzenbacher, *Chem. Commun.*, 2016, **52**, 1827-1830.

(22) N. Chandramouli, Y. Ferrand, B. Kauffmann and I. Huc, *Chem. Commun.*, 2016, **DOI:** 10.1039/C6CC00190D.

(23) D. H. Williams, E. Stephens, D. P. O'Brien and M. Zhou, *Angew. Chem. Int. Ed.*, 2004, **43**, 6596-6616.

(24) Y. Zhao, *ChemPhysChem*, 2013, **14**, 3878-3885.

(25) Z. Rodriguez-Docampo, S. I. Pascu, S. Kubik and S. Otto, *J. Am. Chem. Soc.*, 2006, **128**, 11206-11210.

(26) R. Carrillo, E. Q. Morales, V. S. Martín and T. Martín, *J. Org. Chem.*, 2013, **78**, 7785-7795.

(27) R. Carrillo, A. Feher-Voelger and T. Martín, *Angew. Chem. Int. Ed.*, 2011, **50**, 10616-10620.

(28) R. Carrillo, E. Q. Morales, V. S. Martín and T. Martín, *Chem. -Eur. J.*, 2013, **19**, 7042-7048.

(29) Z. Zhong, X. Li and Y. Zhao, *J. Am. Chem. Soc.*, 2011, **133**, 8862-8865.

(30) R. W. Gunasekara and Y. Zhao, *J. Am. Chem. Soc.*, 2015, **137**, 843-849.

(31) E.-H. Ryu and Y. Zhao, *Org. Lett.*, 2004, **6**, 3187-3189.

(32) E.-H. Ryu, J. Yan, Z. Zhong and Y. Zhao, *J. Org. Chem.*, 2006, **71**, 7205-7213.

(33) M. Berger and F. P. Schmidtchen, *Angew. Chem. Int. Ed.*, 1998, **37**, 2694-2696.

(34) B. R. Linton, M. S. Goodman, E. Fan, S. A. van Arman and A. D. Hamilton, *J. Org. Chem.*, 2001, **66**, 7313-7319.

(35) S. L. Tobey and E. V. Anslyn, *J. Am. Chem. Soc.*, 2003, **125**, 14807-14815.

(36) S. Chen, Y. Ruan, J. D. Brown, C. M. Hadad and J. D. Badjić, *J. Am. Chem. Soc.*, 2014, **136**, 17337-17342.

(37) C. Schmuck and M. Schwegmann, *J. Am. Chem. Soc.*, 2005, **127**, 3373-3379.

(38) K. Kalyanasundaram and J. K. Thomas, *J. Am. Chem. Soc.*, 1977, **99**, 2039-2044.

(39) Young, D. G. In *Encyclopedia of Reagents for Organic Synthesis*; John Wiley & Sons, Ltd: 2001.

(40) Ryu, E.-H.; Ellern, A.; Zhao, Y. *Tetrahedron* **2006**, *62*, 6808-6813.

(41) Moorthy, J. N.; Saha, S. *Eur. J. Org. Chem.* **2010**, *2010*, 6359-6365.

(42) Hermann, K.; Turner, D. A.; Hadad, C. M.; Badjić, J. D. *Chem. Eur. J.* **2012**, *18*, 8301-8305.

(43) Aakeroy, C. B.; Smith, M. M.; Desper, J. *CrystEngComm* **2012**, *14*, 71-74.

CHAPTER 4

A GENERAL METHOD FOR SELECTIVE RECOGNITION OF MONOSACCHARIDES AND OLIGOSACCHARIDES IN WATER

Manuscript submitted.

Roshan W. Gunasekara and Yan Zhao

Abstract

Molecularly imprinted nanoparticle (MINP) receptors were created for a wide variety of mono- and oligosaccharides through double cross-linking of surfactant micelles in aqueous solution. The boroxole functional monomer bound the sugar templates through *cis*-1,2-diol, *cis*-3,4-diol, and *trans*-4,6-diol. The protein-sized MINPs showed excellent selectivity for D-aldohexoses in water with submillimolar binding affinities and completely distinguished the three biologically important hexoses (glucose, mannose, and galactose). Glycosides with nonpolar aglycon showed stronger binding due to enhanced hydrophobic interactions. Oligosaccharides were distinguished based on their monosaccharide building blocks, glycosidic linkages, chain length, as well as additional functional groups that could interact with the MINPs.

Introduction

Lectins are carbohydrate-binding proteins essential to numerous biological processes including fertilization, cell–cell interactions, immune response, and viral and bacterial infection.[1-3] Synthetic materials with similar binding properties are powerful tools in the study and intervention of these carbohydrate-triggered bioprocesses and functions. Selective binding of carbohydrates in water, however, is extremely difficult. Due to strong interactions between water and carbohydrates, a supramolecular host in aqueous solution has to pay a tremendous amount of desolvation energy to bind its sugar guest. Unlike proteins and DNAs, carbohydrates do not adopt well-defined three-dimensional conformations, making the design of their complementary hosts difficult. Monosaccharides, the building blocks of more complex carbohydrates, differ minutely in structure, often by the stereochemistry of a single hydroxyl. Even with the same building block, slightly different connections between the monomers lead to oligo- and polysaccharides with completely different physical, chemical, and biological properties.

During the last several decades, chemists have devoted great efforts towards developing synthetic carbohydrate receptors and, as a result, molecular recognition of carbohydrates progressed steadily from organic to aqueous solution, and from simple monosaccharides to functionalized oligosaccharides.[1-6] Chemists now are able to distinguish glucosides from their isomeric sugars by their unique all equatorial substitutions.[7,8] Binding affinities for monosaccharides by synthetic receptors in water could approach those by natural lectins (binding constant K_a = 10^3-10^4 M^{-1}).[1,2] Despite these impressive accomplishments, however, a general method for molecular recognition of carbohydrates in water is still not available, due to the many challenges involved.

Synthetic carbohydrate receptors can be classified in two groups depending on whether noncovalent[6-10] or covalent[5,11-14] bonds are used for binding. For the latter, the most common binding group is boronic acid that forms boronate esters fast and reversibly with diols prevalent on carbohydrates. Wulff and co-workers in as early as the 1970s employed boronic acid-functionalized molecularly imprinted polymers as the stationary phase to separate sugar derivatives.[15] In the following decades, boronic acids became one of the most popular tools in the construction of synthetic receptors and sensors for carbohydrates.[5]

Herein, we report a general method for constructing carbohydrate-binding receptors, by installing boroxole groups on a nanoparticle scaffold to match the appropriate diols on the sugar guest precisely. These receptors are soluble in water, resemble proteins in size, and displayed selectivity for monosaccharides and oligosaccharides that has not been achieved by previous synthetic materials.

Results and Discussion

Design and Synthesis of MINPs

Synthesis of the nanoparticle receptors was adapted from our recently developed molecular imprinting in cross-linked micelles (Scheme 1).[16,17] Mixed micelles of **1a** and **1b** were used to solubilize DVB (a free radical cross-linker) and DMPA (a photoinitiator) in water. The micellar solution also contained a 1:2 mixture of glucose and polymerizable functional monomer (FM) **3**, which formed FM•template complex **2** under the reaction condition. The structure of **2** was inferred from the binding property of boroxole,[18,19] as well as our own binding studies (vide infra).

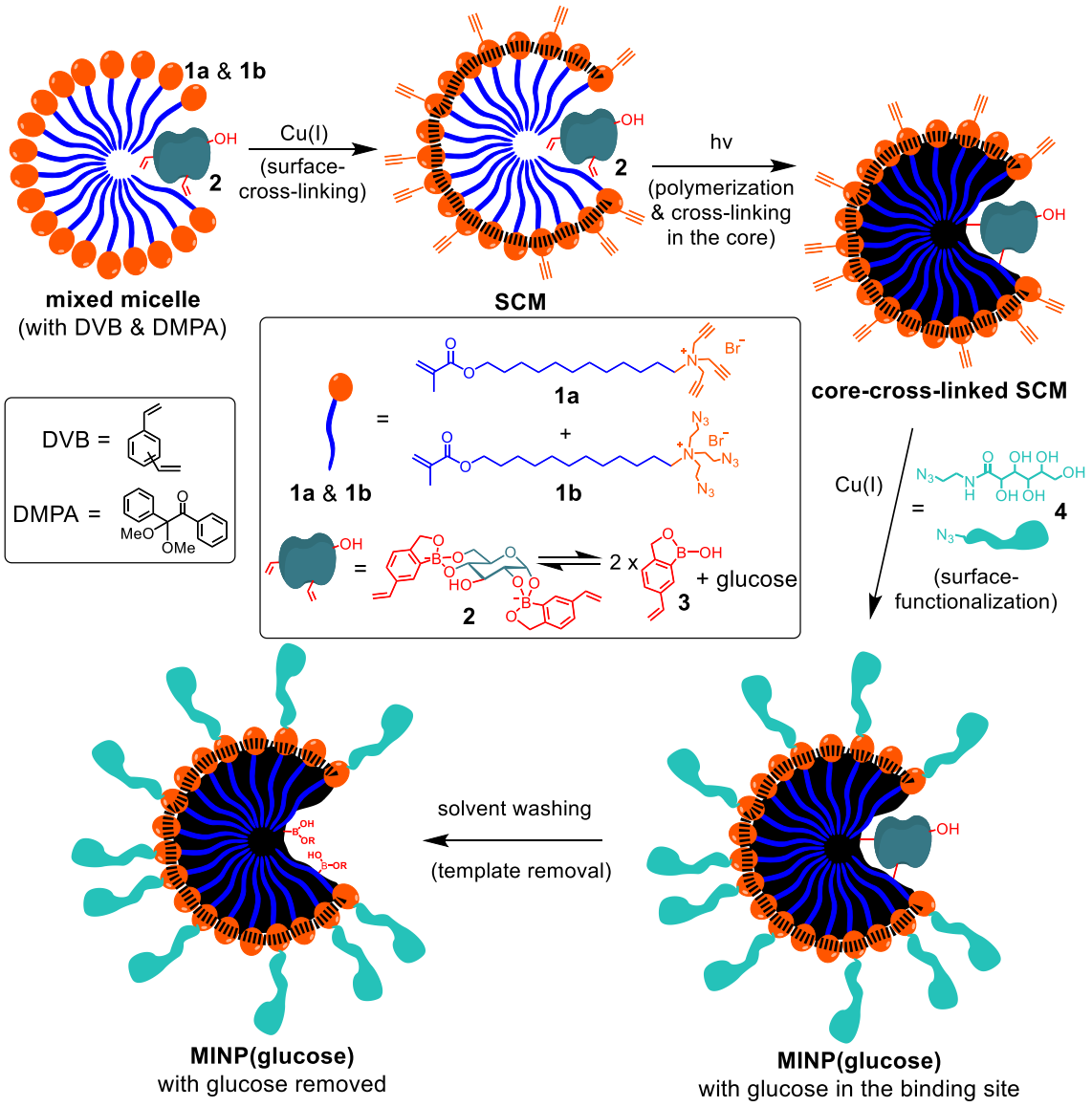

Scheme 1. Preparation of boroxole-functionalized MINP(glucose).

The intimately mixed **1a** and **1b** allowed the micelles to be readily cross-linked on the surface by the click reaction.[20,21] The 3:2 ratio of **1a** and **1b** left the surface-cross-linked micelle (SCM)[20-22] with a layer of alkynyl groups. Subsequent UV irradiation initiated free radical polymerization/cross-linking in the micellar core among **1a**, **1b**, **2**, and DVB. The core-cross-linked SCM was surface-functionalized with **4** by another round of click reaction,

affording MINP(glucose) with the template still bound. The MINP was then precipitated from acetone, and the template was removed by repeated washing using acetone/water, methanol/acetic acid, and acetone.

The reaction progress was generally monitored by ^{1}H NMR spectroscopy as in our previous studies.[16,17] Dynamic light scattering (DLS) afforded the size and molecular weight of the MINP. The nanoparticles were typically 4–5 nm in diameter. The DLS size in general showed good agreement with the size obtained from transmission electron microscopy (TEM) for similarly cross-linked micelles.[20]

We examined the binding of the MINP by isothermal by isothermal titration calorimetry (ITC), a method of choice for studying intermolecular interactions.[23] In addition to its accuracy, the method could afford the number of binding sites per particle (N), as well as other thermodynamic binding parameters. We have demonstrated in several studies that (for fluorescently labeled guests) ITC afforded very similar binding constants for MINPs as other spectroscopic methods.[16,17,24]

As shown in Table 1, MINP(glucose) prepared with template/FM = 1:2 bound glucose with $K_a = 2.30 \times 10^3$ M^{-1} in 10 mM HEPES buffer at pH 7.4 (entry 1). Reducing the template/FM ratio to 1:1 lowered the binding constant (entry 2). Having an excess of FM (thee equiv to the template) did not improve the binding (entry 3). Binding was negligible by the nonimprinted materials prepared without FM **3** and the glucose template (entry 4) or with FM **3** but without glucose (entry 5). These results demonstrated that molecular imprinting was clearly in operation and the optimal binding stoichiometry was 1:2 between the template and the boroxole.

MINP(glucose) displayed excellent selectivity: among the seven isomeric sugars, only allose showed noticeable binding with $K_a = 0.37 \times 10^3$ M^{-1}, while all the rest were not bound at all. Similar selectivity was found for MINP(mannose), which only bound altrose among the remaining seven D-aldohexoses.

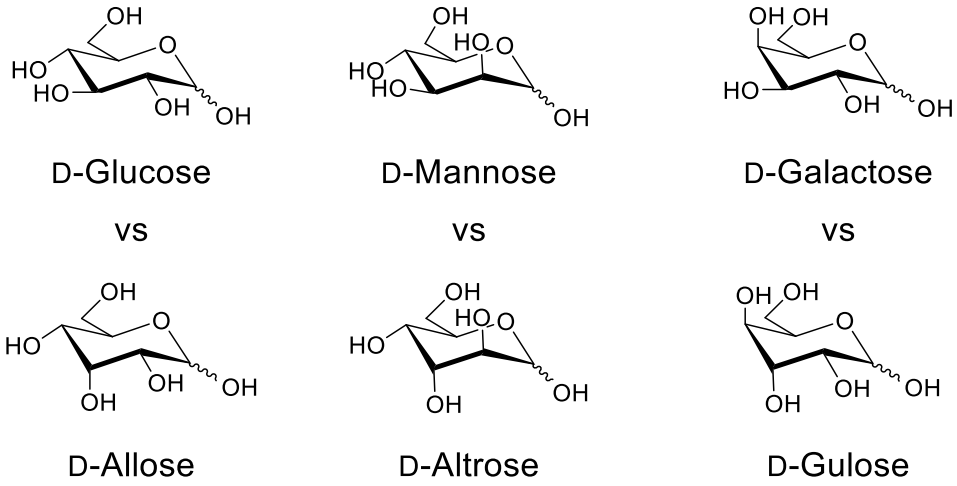

Chart 1. Structures of selected D-aldohexoses.

The boroxole-functionalized MINP(glucose) and MINP(mannose) showed higher binding selectivity than our recently reported MINP prepared using 4-vinylphenyl boronate esters of these sugars as the templates, even though the overall trend was the same.[25] The selectivity suggests that the C2 and C4 hydroxyls were critical to the molecular recognition because their inversion shuts off the binding. The C6 hydroxyl was also essential, as xylose, lacking this hydroxyl, showed no binding. The C3 hydroxyl played a secondary role in the binding, with its inversion lowering K_a by 74–86% from the template sugar.

MINP(galactose) behaved distinctively differently from the first two MINPs. Among the eight D-aldohexoses, it bound only its template and achieved a higher binding constant (K_a = 3.37 × 10^3 M^{-1}) than MINP(glucose) and MINP(mannose) (Table 1).

Table 1. ITC binding data for monosaccharide guests.[a]

Entry	Host	Guest	K_a (10^3 M^{-1})	-ΔG (kcal/mol)	N
1	MINP(glucose)	glucose	2.30 ± 0.11	4.58	1.1 ± 0.1
2	MINP(glucose)[b]	glucose	0.95 ± 0.01	4.06	1.2 ± 0.1
3	MINP(glucose)[c]	glucose	2.33 ± 0.38	4.59	1.0 ± 0.1
4	NINP[d]	glucose	<0.05[e]	-	-
5	NINP[f]	glucose	<0.05[e]	-	-
6	MINP(glucose)	glucose[g]	1.30 ± 0.16	4.24	1.0 ± 0.1
7	MINP(glucose)	glucose[h]	0.52 ± 0.09	3.70	1.1 ± 0.1
8	MINP(glucose)	allose[I]	0.37 ± 0.09	3.51	0.8 ± 0.1
9	MINP(mannose)	mannose	1.90 ± 0.34	4.47	1.0 ± 0.3
10	MINP(mannose)	altrose[j]	0.50 ± 0.01	3.68	1.0 ± 0.1
11	MINP(galactose)	galactose[k]	3.37 ± 0.30	4.81	1.0 ± 0.1
12	MINP(**5**)	5	65.3 ± 8.8	6.56	1.1 ± 0.1
13	MINP(**5**)	6	11.0 ± 1.2	5.51	1.0 ± 0.1
14	MINP(**5**)	7	4.66 ± 0.39	5.00	1.1 ± 0.1

[a] The FM/template ratio in the MINP synthesis was 1:2 unless otherwise indicated. The titrations were performed in 10 mM HEPES buffer at pH 7.4. The ITC titration curves are reported in the Experimental Section, including the binding enthalpy and entropy. [b] The template/FM ratio was 1:1. [c] The template/FM ratio was 1:3. [d] Prepared without FM **3** and the glucose template. [e] Binding was extremely weak. Because the binding constant was estimated from ITC, -ΔG and N are not listed in the table (Figure 62 in Experimental Section). [f] Prepared with FM **3** but without the glucose template. [g] The binding was in 10 mM HEPES buffer at pH 8.5. [h] The binding was in 10 mM HEPES buffer at pH 6.5. [I] The binding for other D-aldohexoses including mannose, galactose, altrose, gulose, talose, idose, and xylose was extremely weak, with estimated K_a <0.02 × 10^3 M^{-1} (Figure 66 and 67). [j] The binding for other D-aldohexoses including glucose, allose, galactose, gulose, talose, and idose was extremely weak, with estimated K_a <0.02 × 10^3 M^{-1} (Figure 68). [k] The binding for other D-

aldohexoses including glucose, mannose, allose, altrose, gulose, talose, and idose was extremely weak, with estimated K_a <0.05 × 10^3 M^{-1} (Figure 69 and 70).

Hall and co-workers reported that benzoboroxole binds glucose in a 1:1 ratio in water, with K_a = 17 M^{-1}.[18,19] It is possible that the 2nd binding observed in our MINPs was weaker than the first one in bulk aqueous solution and simply not observed in Hall's study. The hydrophobic and positive environment of the cationic micelle conceivably could stabilize the negatively charged boronate and enable the second, less stable adduct to form under our imprinting and binding conditions.

Benzoboroxole binds the methyl pyranosides of glucose, mannose, and galactose with K_a = 10–30 M^{-1},[18,19] thus lacking intrinsic selectivity for these sugars. The much higher selectivity and binding affinity displayed by our MINPs must come from the microenvironment of the cross-linked micelle and the two-point binding as revealed in the binding studies. It is known that that benzoboroxole has a strong preference for *trans*-4,6-diol over *trans*-3,4-diol in glucosides, suggesting the C3 hydroxyl would not be involved in binding in glucose and mannose.[26] Hall's work also demonstrated that, for galatopyranosides, *cis*-3,4-diol is preferred by boroxole over *cis*-4,6-diol. This preference was also maintained by MINP(galactose), because gulose, which differs from galactose only by the C3 hydroxyl, was not bound.[27]

For MINP(**5**) prepared with 4-nitrophenyl α-D-mannopyranoside **5** as the template, the aromatic aglycon was expected to create a complementary hydrophobic binding pocket in the MINP, as we have demonstrated amply in recent studies.[16,17,24] Indeed, a much stronger binding of K_a = 65.3 × 10^3 M^{-1} was obtained. Gratifyingly, excellent binding selectivity was

observed. The K_a values for the corresponding glucoside **6** and mannoside **7** were ~1/6 and 1/14, respectively. Thus, inversion of one or two hydroxyl groups was easily distinguished in the glycosides as well.

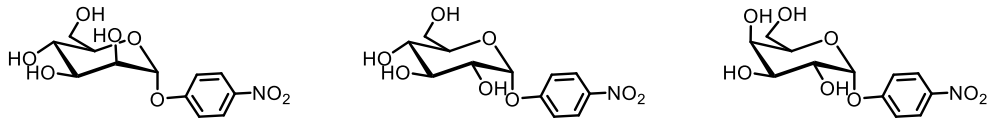

5
4-nitrophenyl-
α-D-mannopyranoside

6
4-nitrophenyl-
α-D-glucopyranoside

7
4-nitrophenyl-
α-D-galactopyranoside

Chart 2. Structures of 4-nitrophenyl aldohexoses.

Molecular imprinting is a tremendously useful technique for creating guest-complementary binding sites in polymers on surface.[28-32] However, conventional imprinting often affords intractable highly cross-linked polymers, hindering their usage in biology. In our case, by confining the polymerization/cross-linking largely within micelles, we not only made our materials water-soluble but also were able to control the number of binding sites on the nanosized MINP. Our previous studies indicate that the SCM of **1** has roughly 50 cross-linked surfactants. With surfactant/template = 50/1 in the synthesis, the MINPs on average contained one binding site per nanoparticle (Table 1).[33] As demonstrated in a previous work, this number is fully tunable if so desired.[16]

FM **3** not only afforded MINPs with higher binding affinity and selectivity than 4-vinylphenylboronuc acid but also enabled us to imprint oligosaccharides. The sugar templates of 4-vinylphenylboronate esters have to be synthesized in a separate step prior to MINP preparation,[25] through azeotropic removal of water in dioxane at 88 °C.[34] The low solubility of oligosaccharides in the solvent makes such a synthesis impractical. Furthermore, if we want to imprint more sensitive sugar derivatives such as glycoproteins in a longer term,

organic solvents and high temperatures clearly have to be avoided. In situ imprinting is certainly preferred for the ease of synthesis.

Maltose was the first oligosaccharide template used in our study and expected to form FM•template complex **8** based on the binding data of the aldohexoses. Because numerous hydrogen-bonding groups exist in the complex, we hypothesized that the micelle/MINP should contain hydrogen-bonding groups that interact with **8** through hydrogen bonds, in addition to hydrophobic and electrostatic interactions present in the normal micelle/MINP. Amide-functionalized cross-linkable surfactant **9** was recently found to enhance the binding of guest through hydrogen bonds.[35] To our delight, MINP(maltose) prepared with **9** as the cross-linkable surfactant bound maltose with $K_a = 20.5 \times 10^3$ M^{-1}, much higher than the value obtained ($K_a = 3.50 \times 10^3$ M^{-1}) with surfactant **1a** (Table 2, entries 1 and 2). When the template/FM ratio was varied (1:1, 1:2, and 1:3), 1:2 gave the highest K_a, supporting the hypothesized 1:2 binding model.

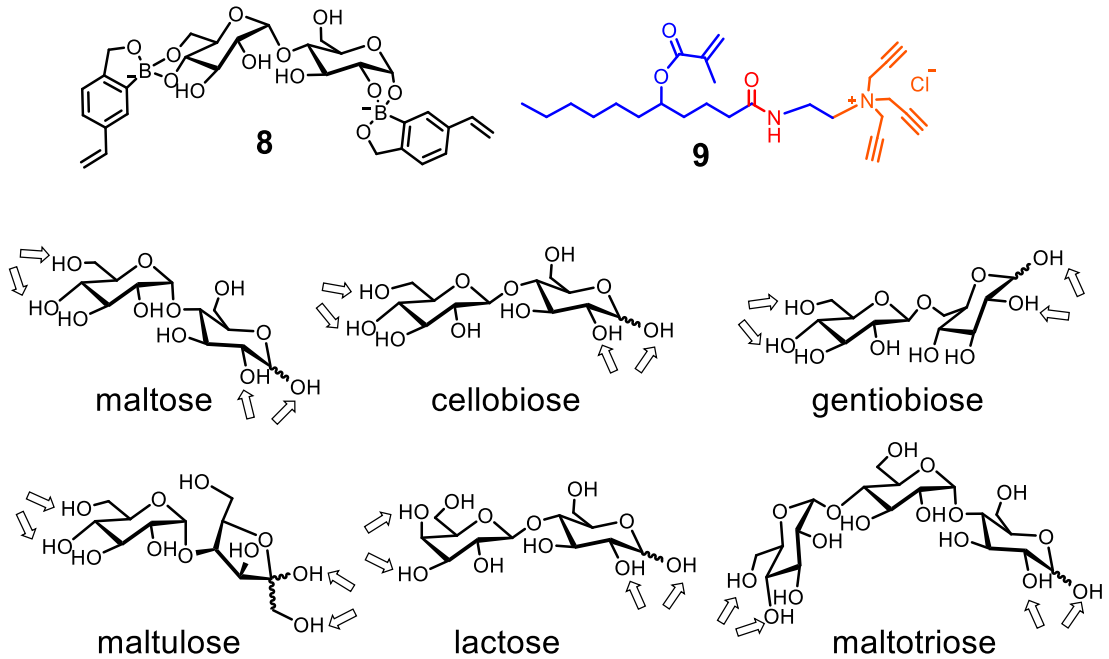

Chart 3. Structures of FM•template complex **8**, surfactant **9**, and oligosaccharides.

Table 2. ITC binding data for oligosaccharide guests.[a]

Entry	Host	Guest	K_a (10^3 M^{-1})	K_{rel}	-ΔG (kcal/mol)	N
1	MINP(maltose)	maltose	20.5 ± 3.2	1	5.88	1.0 ± 0.1
2	MINP(maltose)[b]	maltose	3.50 ± 0.23	-	4.83	1.2 ± 0.1
3	MINP(maltose)[c]	maltose	5.72 ± 0.61	-	5.12	1.2 ± 0.1
4	MINP(maltose)[d]	maltose	19.7 ± 2.5	-	5.85	1.0 ± 0.1
5	MINP(maltose)	cellobiose	7.99 ± 0.12	0.39	5.32	1.2 ± 0.1
6	MINP(maltose)	gentiobiose	4.37 ± 0.53	0.21	4.96	1.2 ± 0.1
7	MINP(maltose)	maltulose	<0.05	<0.002	-	-
8	MINP(maltose)	lactose	0.79 ± 0.16	0.04	3.95	0.8 ± 0.1
9	MINP(maltose)	maltotriose	<0.05	<0.002	-	-
10	MINP(maltose)	glucose	1.81 ± 0.22	0.09	4.44	0.9 ± 0.1
11	MINP(cellobiose)	maltose	9.45 ± 0.14	0.29	5.42	1.1 ± 0.1
12	MINP(cellobiose)	cellobiose	32.9 ± 5.9	1	6.16	1.1 ± 0.1
13	MINP(cellobiose)	gentiobiose	4.77 ± 0.67	0.14	5.01	1.1 ± 0.1
14	MINP(cellobiose)	maltulose	<0.05	<0.002	-	-
15	MINP(cellobiose)	lactose	1.29 ± 0.09	0.04	4.24	0.8 ± 0.1
16	MINP(lactose)	maltose	3.24 ± 0.42	0.06	4.79	1.0 ± 0.1
17	MINP(lactose)	cellobiose	6.83 ± 0.92	0.13	5.23	0.8 ± 0.1
18	MINP(lactose)	gentiobiose	11.6 ± 1.7	0.22	5.54	0.9 ± 0.1
19	MINP(lactose)	maltulose	0.50 ± 0.13	0.01	3.67	1.0 ± 0.1
20	MINP(lactose)	lactose	52.2± 9.5	1	6.43	1.3 ± 0.1
21	MINP(maltotriose)	maltotriose	52.8 ± 8.6	1	6.44	1.1 ± 0.1
22	MINP(maltotriose)	maltose	14.1 ± 2.0	0.27	5.66	1.0 ± 0.1
23	MINP(maltotriose)	glucose	0.56 ± 0.02	0.01	3.75	1.0 ± 0.1

[a] The template/FM ratio in the MINP synthesis was 1:2 unless otherwise indicated. The cross-linkable surfactants were a 3:2 mixture of **9** and **1b** unless otherwise indicated. The titrations were performed in 10 mM HEPES buffer at pH 7.4. K_{rel} is the binding constant of a guest relative to that of the template sugar for a particular MINP. The ITC titration curves are reported in the Experimental Section, including the binding enthalpy and entropy. [b] The cross-linkable surfactants were a 3:2 mixture of **1a** and **1b**. [c]The template/FM ratio was 1:1. [d]The template/FM ratio was 1:3.

Binding of the oligosaccharides worked fully as expected (Table 2). The selectivity of MINP is indicated by K_{rel}, which is the binding constant of a sugar guest relative to that of the template. Cellobiose and gentiobiose had a K_{rel} value of 0.39 and 0.21 toward

MINP(maltose), indicating that changing the α 1,4-glycosidic linkage to the β 1,4 or α 1,6 weakened the binding significantly. Replacing one of the two glucoses in maltose with fructose and galactose was even less tolerated, yielding K_{rel} of <0.002 and 0.04, respectively. Interestingly, shortening the chain length was better tolerated than lengthening the chain length: glucose was bound with K_{rel} = 0.09 but maltotriose with K_{rel} <0.002. The result is reasonable because maltotriose should not fit into the binding pocket generated from the smaller maltose but glucose should be able to fit it, although only expected to bind one of the two boroxoles. Note that K_a (= 1.81×10^3 M^{-1}) for glucose by MINP(maltose) was close to that (= 2.30×10^3 M^{-1}) by MINP(glucose) in Table 1. Apparently, the hydrogen-bonding interactions between the bound glucose and the amide-functionalized MINP nearly compensated for the loss of one boronate binding interaction.

We then created MINPs for all the other oligosaccharides and studied their binding. Good selectivity was generally obtained and each MINP always bound its own template sugar better than other sugars (Table 2 and Table 6). As far as the absolute binding strength is concerned, gentiobiose, lactose, and maltotriose gave somewhat higher K_a values than the other sugars. The stronger binding for maltotriose could result from the additional hydroxyls on the template that interacted with the amide-functionalized MINP by hydrogen bonds. Expectedly, as the guest became smaller (i.e., from maltotriose to maltose to glucose), binding became progressively weaker toward MINP(maltotriose) (Table 2, entries 21–23).

To test whether these boroxole-functionalized MINPs could distinguish more challenging targets, we prepared receptors for the three sugars that determine the human blood type: type O has sugar H on the surface of its blood cells, type A has A, type B has B, and type AB has both A and B. As shown in Table 3, MINP(H), generated from sugar H,

bound its template with K_a = 35.6 × 10^3 M^{-1} and showed no binding for the other two sugars. The difference between sugar A and B was extremely subtle: among the numerous functional groups, the only difference is a single acetoamido group in sugar A versus a hydroxyl in B. Impressively, MINP(A) was found to bind sugar A twice as strongly as sugar B and MINP(B) displayed slightly higher selectivity. Meantime, sugar H displayed weak binding to MINP(A) and MINP(B), with K_{rel} = 0.13 in both cases.

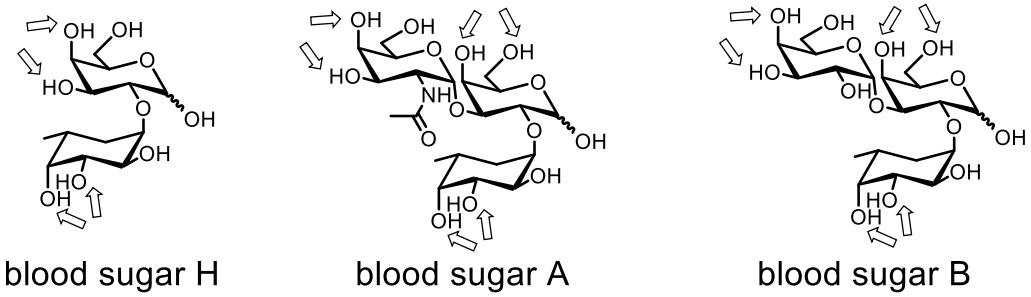

Chart 4. Structures of blood sugars.

Table 3. ITC binding data for blood sugars.[a]

Entry	Host	Guest	K_a (10^3 M^{-1})	K_{rel}	-ΔG (kcal/mol)	N
1	MINP(H)	Sugar H	35.6 ± 5.2	1	6.2	1.0 ± 0.1
2	MINP(H)	Sugar A	<0.02	<0.001	-	-
3	MINP(H)	Sugar B	<0.02	<0.001	-	-
4	MINP(A)	Sugar H	9.9 ± 0.1	0.13	5.45	1.0 ± 0.1
5	MINP(A)	Sugar A	76.7 ± 1.2	1	6.66	1.0 ± 0.1
6	MINP(A)	Sugar B	39.0 ± 4.8	0.51	6.26	1.1 ± 0.1
7	MINP(B)	Sugar H	7.6 ± 0.8	0.13	5.29	1.1 ± 0.1
8	MINP(B)	Sugar A	21.8 ± 4.3	0.38	5.91	1.0 ± 0.1
9	MINP(B)	Sugar B	57.1 ± 7.5	1	6.48	1.1 ± 0.1

[a] The template/FM ratio in the MINP synthesis was 1:2 for MINP(H) and 1:3 for MINP(A) and MINP(B). The cross-linkable surfactants were a 3:2 mixture of **9** and **1b**. The titrations were performed in 10 mM HEPES buffer at pH 7.4. The ITC titration curves are reported in the Experimental Section, including the binding enthalpy and entropy.

Conclusion

In summary, we have reported a facile method to create protein-sized water-soluble nanoparticle receptors for a wide range of mono- and oligosaccharides. The generality of the method is the highlight of the covalent imprinting-based approach. The in situ imprinting was enabled by the strong interactions between FM **3** and the appropriate diol functionalities on the sugar in the micellar environment. The preparation and purification took about 2 days and required no special techniques, and thus could be potentially adopted by researchers without substantial training in chemistry. The number of binding sites on these "synthetic lectins" could be controlled easily. Importantly, the binding sites on the sugar can be identified prior to imprinting (namely, *cis*-1,2-diol, *cis*-3,4-diol, and *trans*-4,6-diol), making the molecular recognition highly predictable. Among the eight D-aldohexoses, glucose, mannose, and galactose are the most biologically relevant and can be distinguished completely. With the ability to differentiate oligosaccharides by their building blocks, chain length, and glycosidic linkages, we expect these MINP receptors could become highly useful in biology and chemistry in the future.

Acknowledgement

We thank the National Institute of General Medical Sciences of the National Institutes of Health (R01GM113883) for financial support of the research.

Experimental Section

General Method

Routine ^{1}H and ^{13}C NMR spectra were recorded on a Bruker DRX-400, on a Bruker AV II 600 or on a Varian VXR-400 spectrometer. ESI-MS mass was recorded on Shimadzu

LCMS-2010 mass spectrometer. Dynamic light scattering (DLS) data were recorded at 25 °C using PDDLS/ CoolBatch 90T with PD2000DLS instrument. Isothermal titration calorimetry (ITC) was performed using a MicroCal VP-ITC Microcalorimeter with Origin 7 software and VPViewer2000 (GE Healthcare, Northampton, MA).

Syntheses of compounds **1a**,[16] **10**,[16] **11a**,[16] **12**,[36] **13**,[37] **14**,[38] **15**,[37] **16**,[37] **17**,[37] **18**,[35] **19**,[35] and **9**[35] were previously reported.

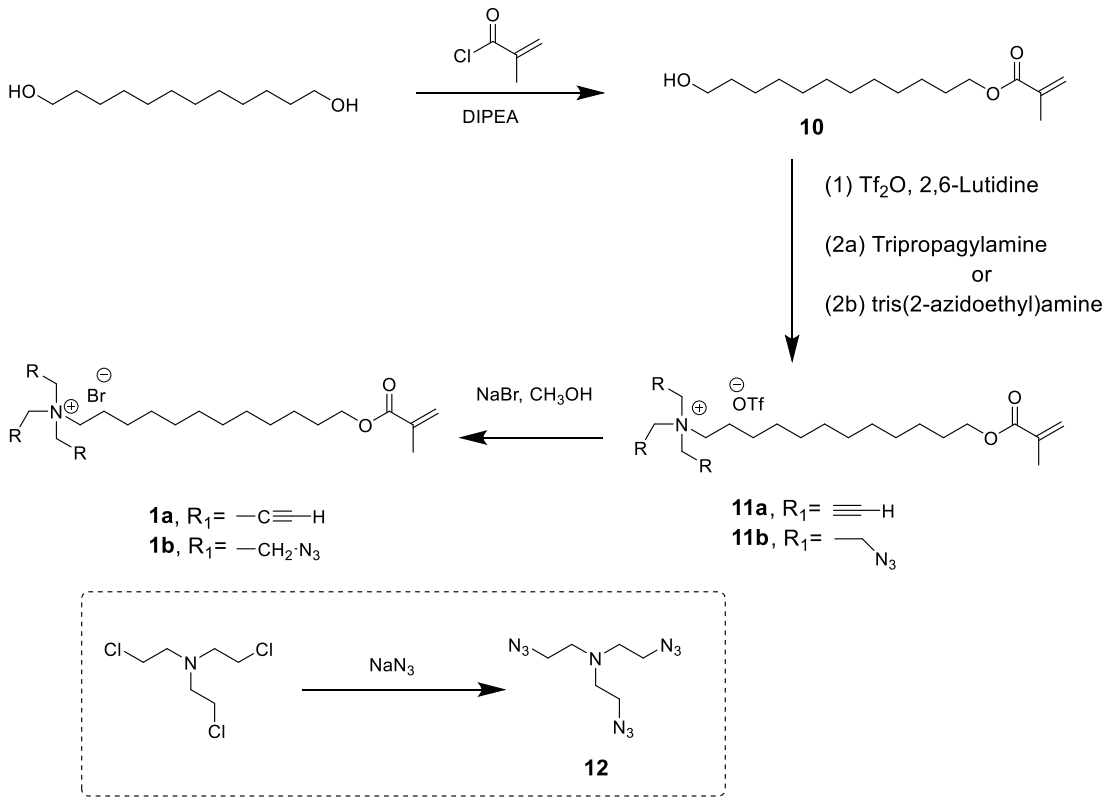

Scheme 2. Synthesis of compound **1a, 1b,** and **12.**

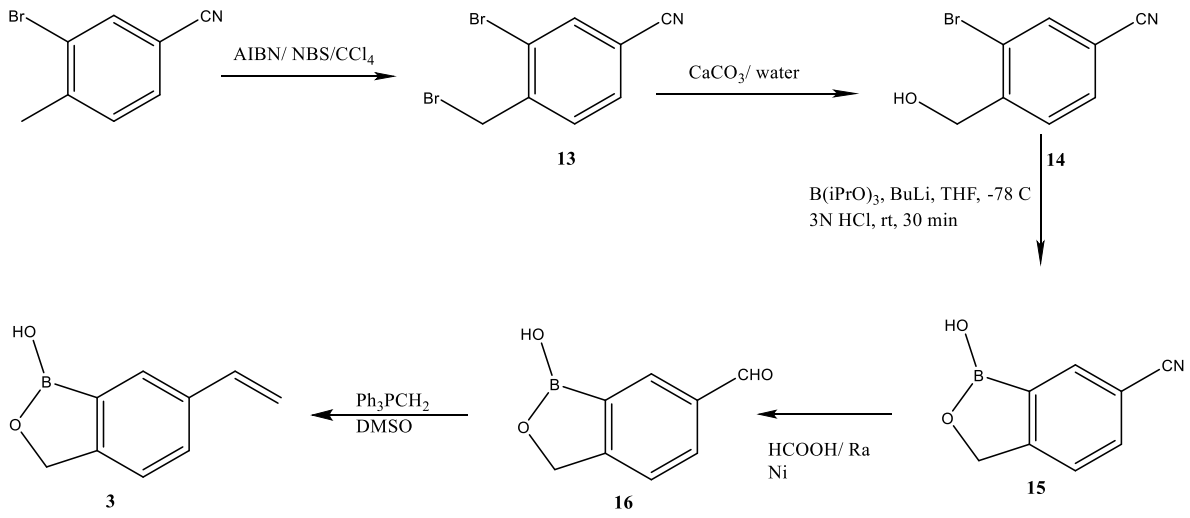

Scheme 3. Synthesis of compound **3.**

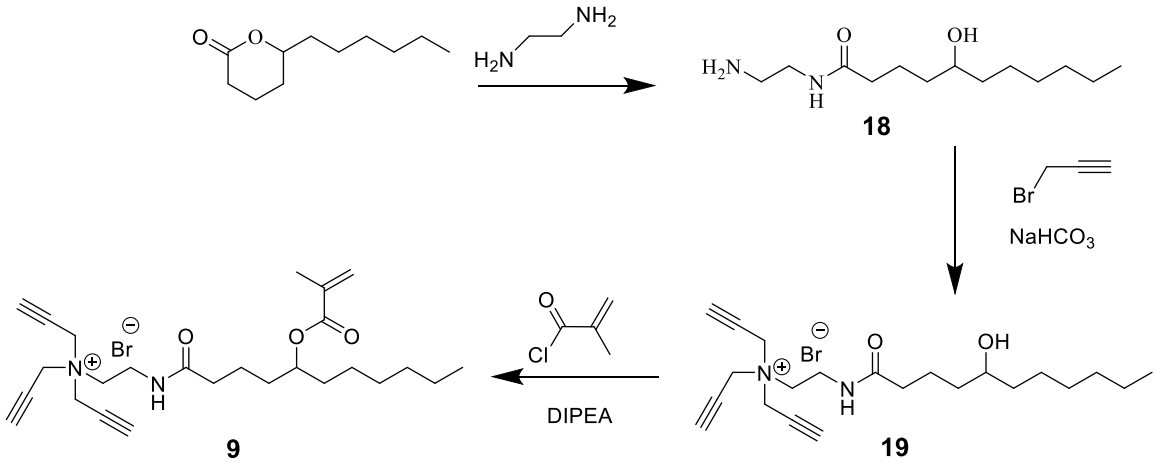

Scheme 4. Synthesis of compound **9**.

Compound 1b. Triflic anhydride (0.40 mL, 2.4 mmol) and 2,6-lutidine (0.26 mL, 2.4 mmol) were added to 7 mL of dry dichloromethane, which was cooled at -20 °C. The cooling bath was removed and compound **10** (0.50 g, 1.8 mmol) in CH_2Cl_2 (3 mL) was added dropwise to the stirred solution. After being stirred at room temperature for 90 min, the reaction mixture was diluted with CH_2Cl_2 (5 mL). The organic layer was washed with 1 M HCl (10 mL) and water (2 × 10 mL), dried with magnesium sulfate, filtered, and concentrated by rotary

evaporation to give the triflate as a yellowish oil (680 mg, 94 %). The oil was dissolved in dry THF (5 mL) and compound **12** (0.88 mL, 2.2 mmol) was added dropwise. After being stirred at room temperature overnight, the reaction mixture was concentrated by rotary evaporation and the residue was purified by column chromatography over silica gel using 1:10 methanol/ CH_2Cl_2 as eluent to afford a yellowish oil (869 mg, 77 %). This oil was dissolved in methanol (5 mL), followed by the addition of excess sodium bromide solution in 5 mL of water (3.86 g, 37.5 mmol). After being stirred for 6 h, the reaction mixture was diluted with CH_2Cl_2 (10 mL). The organic layer was washed with water (2 × 30 mL), dried with sodium sulfate, and concentrated by rotary evaporation. The process was repeated once to afford a yellowish oil (770, 100 %). ^{1}H NMR (400 MHz, $CDCl_3$, δ): 6.09 (s, 1H), 5.54 (s, 1H), 4.13 (t, J = 6.7 Hz, 2H), 3.40 (d, J = 5.3 Hz, 14H), 1.94 (s, 3H), 1.42 – 1.15 (m, 20H). ^{13}C NMR (100 MHz, $CDCl_3$, δ): 167.4, 136.4, 125.1, 77.2, 77.1, 70.6, 70.5, 70.5, 70.5, 70.5, 70.5, 70.5, 70.5, 70.5, 64.7, 53.8, 53.8, 29.4, 29.4, 29.4, 29.4, 29.4, 28.5, 26.4, 26.4, 26.4, 26.4, 26.4, 26.4, 26.4, 26.4, 26.4, 26.4, 26.4, 26.4, 26.3, 26.3, 26.3, 26.3, 18.2. ESI-HRMS (m/z): $[M\text{-}Br]^+$ calcd for $C_{22}H_{41}N_{10}O_2$, 477.3408; found, 477.3402.

Compound 13. 3-bromo-4-methylbenzonitrile (1.00 g, 5.1 mmol) was added to 2,2′-azobis(2-methylpropionitrile) (AIBN, 42 mg, 0.25 mmol) and N-bromosuccinimide (NBS, 1.00 g, 5.61 mmol) in CCl_4 (40 mL). The mixture was refluxed for 18 h and cooled to room temperature. The residue was mixed with water (10 mL) and extracted with DCM (3×15 mL), dried with anhydrous Na_2SO4, and concentrated *in vacuo* to obtain white powder (1.10 g, 80%). ^{1}H NMR (600 MHz, $CDCl_3$, δ): 7.87 (d, J = 1.5 Hz, 1H), 7.58 (m, 2H), 4.58 (s, J = 1.7 Hz, 2H).

Compound 14. 3-bromo-4-bromomethylbenzonitrile (1.50 g, 5.45 mmol) was added to a suspension of $CaCO_3$ (2.5 g, 25 mmol) in dioxane/water (2:3 v/v, 60 mL). This mixture was stirred at 100 °C for 28 h. After cooling to room temperature, the reaction mixture was extracted with diethyl ether (3×20 mL). The combined organic phase was washed with brine (15 mL), water (20 mL), dried over anhydrous $MgSO_4$, and concentrated *in vacuo*. The resulting solid was recrystallized with CH_2Cl_2/MeOH (80:10, v/v) to obtained white powder (0.89 g, 77%). ^{1}H NMR (600 MHz, CD_3OD, δ): 7.94 (s, 1H), 7.74 (m, 2H), 4.69 (s, 2H).

Compound 15. Compound **14** (422 mg, 2.0 mmol) and triisopropyl borate (0.92 mL, 4.0 mmol) in anhydrous THF (10 mL) at N_2 atmosphere was cooled at -78 °C for 20 min. 2M n-BuLi in hexane (2.25 mL, 4.50 mmol) was added dropwise at-78° C. Then the mixture was allowed to warm to room temperature and stirred at room temperature for overnight under N_2 atmosphere. The mixture was quenched with IN HCl and extracted with ethyl acetate (3×10 mL). The combined organic layers were washed with brine (20 mL), dried over anhydrous $MgSO_4$, concentrated *in vacuo*. The residue was purified by a flash column chromatograph over silica gel with 4:1 dichloromethane/methanol as the eluent to give a yellow powder (0.22, 69%). ^{1}H NMR (600 MHz, CD_3OD, δ): 7.99 (s, 1H), 7.81 (dt, J = 7.9, 1.5 Hz, 1H), 7.59 (d, J = 7.9 Hz, 1H), 5.17 (s, 2H).

Compound 16. Compound **15** (0.1 g, 0.63 mmol) in HCOOH/water/THF (16:2:12 v/v/v, 30 mL) was added to Raney-Ni (0.85 g) and refluxed for 3 h. The reaction mixture was cooled and filtered through Celite and concentrated *in vacuo*. The filtrate was extracted with ethyl acetate (3×5 mL), washed with brine (5 mL), dried with anhydrous $MgSO_4$ and concentrated *in vacuo*. The residue was purified by a flash column chromatograph over silica gel with 20:1 dichloromethane/methanol as the eluent to give a white powder (81 mg, 80%). ^{1}H NMR (600

MHz, CD_3OD, δ): 10.01 (s, 1H), 8.25 (s, 1H), 8.01 (dt, *J* = 7.9, 1.5 Hz, 1H), 7.59 (d, *J* = 7.9 Hz, 1H), 5.11 (s, 2H).

Compound 3. Methyltriphenyl-phosphonium bromide (1.0 g, 2.8 mmol) and potassium t-butoxide (0.38 g, 3.30 mmol) was mixed in DMSO (4 mL) and stirred 4 h before adding Compound **16** (0.3 g, 1.85 mmol) in THF (6 mL). The reaction was stirred 14 h and quenched with aqueous HCl and extracted with ethyl acetate (3×10 mL), washed with brine (5 mL), dried with anhydrous $MgSO_4$ and concentrated in *vacuo*. The residue was purified by a flash column chromatograph over silica gel with 20:1 dichloromethane/methanol as the eluent to give a white powder (0.21, 72%). ^{1}H NMR (400 MHz, $DMSO_4$-D_6, δ): 9.17 (s, 1H), 7.75 (d, *J* = 1.5 Hz, 1H), 7.56 (d, *J* = 8.0 Hz, 1H), 7.35 (d, *J* = 7.9 Hz, 1H), 6.76 (dd, *J* = 17.6, 10.9 Hz, 1H), 5.78 (d, *J* = 17.7 Hz, 1H), 5.22 (d, *J* = 11.0 Hz, 1H), 4.94 (s, 2H).

Synthesis of monosaccharide MINPs. A solution of 6-vinylbenzoxaborole (**2**) in methanol (10 μL of a 6.4 mg/mL, 0.0004 mmol) was added to glucose in methanol (10 μL of 7.20 mg/mL, 0.0004 mmol). After the mixture was stirred for 6 h at room temperature, methanol was removed *in vacuo*. A micellar solution of **1a** (0.03 mmol), **1b** (0.02 mmol), divinylbenzene (DVB, 2.8 μL, 0.02 mmol), and 2,2-dimethoxy-2-phenylacetophenone (DMPA,10 μL of a 12.8 mg/mL solution in DMSO, 0.0005 mmol) in D_2O (2.0 mL) was added to the sugar–boronate complex. (D_2O instead of H_2O was used to allow the reaction progress to be monitored by ^{1}H NMR spectroscopy.) The mixture was subjected to ultrasonication for 10 min before $CuCl_2$ (10 μL of a 6.7 mg/mL solution in D_2O, 0.0005 mmol) and sodium ascorbate (10 μL of a 99 mg/mL solution in D_2O, 0.005 mmol) were added. After the reaction mixture was stirred slowly at room temperature for 12 h, the reaction mixture was transferred into a glass vial, purged with nitrogen for 15 min, sealed

with a rubber stopper, and irradiated in a Rayonet reactor for 8 h. Compound **4** (10.6 mg, 0.04 mmol), $CuCl_2$ (10 μL of a 6.7 mg/mL solution in D_2O, 0.0005 mmol), and sodium ascorbate (10 μL of a 99 mg/mL solution in D_2O, 0.005 mmol) were added. After being stirred for another 6 h at room temperature, the reaction mixture was poured into acetone (8 mL). The precipitate collected by centrifugation was washed with a mixture of acetone/water (5 mL/1 mL), and methanol/acetic acid (5 mL/0.1 mL) for three times and finally with acetone (1×5 mL) to neutral before being dried in air to afford the final MINPs.

Table 4. Monosaccharide formulation.

Entry	MINP	Amount of 0.04 M Sugar / μL	Amount of 0.04 M 6-vinylbenzoxoborole / μL	Ratio (Sugar: benzoxoborole)
1	MINP(glucose)	10	10	1:1
2	MINP(glucose)	10	20	1:2
3	MINP(glucose)	10	30	1:3
4	NINP[a]	-	-	-
5	NINP[b]	-	20	-
6	MINP(mannose)	10	20	1:2
7	MINP(galactose)	10	20	1:2
8	MINP(**5**)	10	10	1:1

[a] The nonimprinted nanoparticles were prepared without functional monomer **3** and sugar. [b] The nonimprinted nanoparticles were prepared with functional monomer **3** but without sugar.

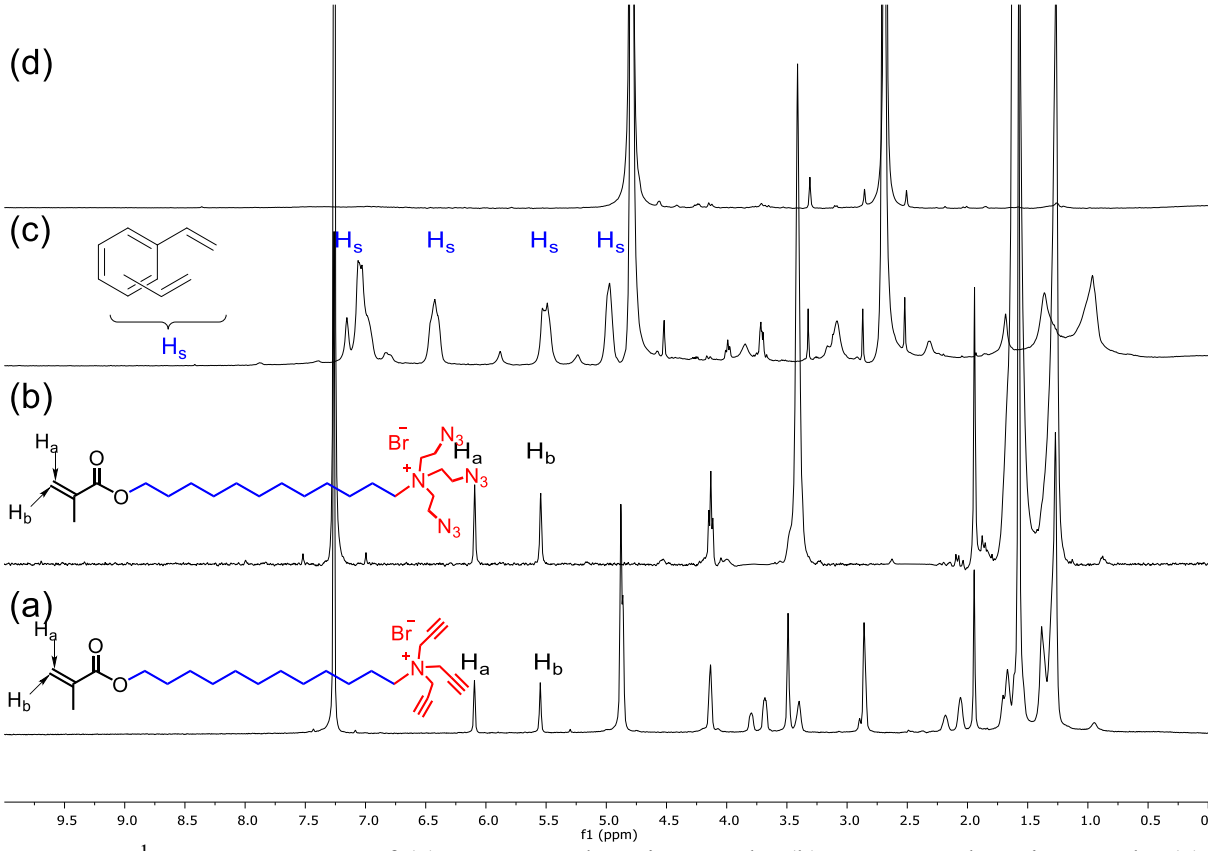

Figure 1. ^{1}H NMR spectra of (a) Compound **1a** in $CDCl_3$, (b) Compound **1b** in $CDCl_3$, (c) alkynyl-SCM in D_2O, and (d) MINP(glucose) in D_2O at 298 K. The data correspond to entry 1 in Table 4.

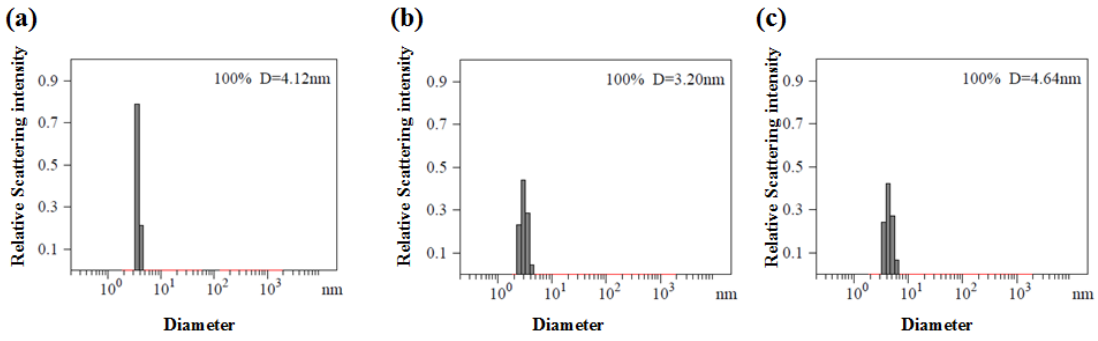

Figure 2. Distribution of the hydrodynamic diameters of the nanoparticles in water as determined by DLS for the synthesis of MINP(glucose) (a) alkynyl-SCM, (b) core-cross-linked SCM, and (c) surface-functionalized MINP(glucose) after purification. The data correspond to entry 1 in Table 4.

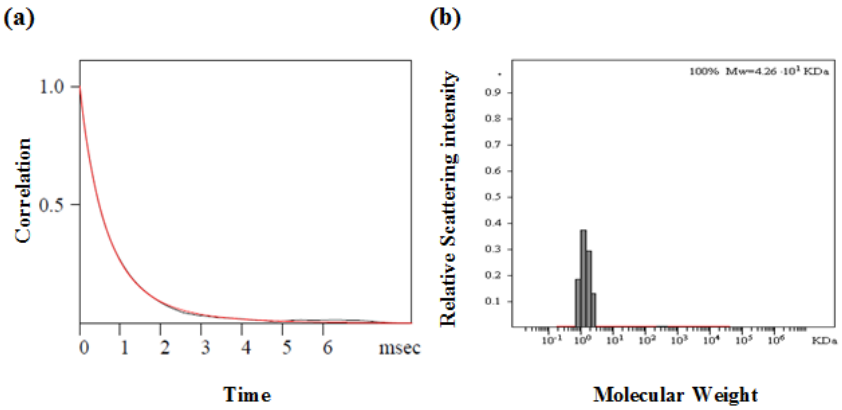

Figure 3. The correlation curve and the distribution of the molecular weight for MINP(glucose) from the DLS. The data correspond to entry 1 in Table 4. The PRECISION DECONVOLVE program assumes the intensity of scattering is proportional to the mass of the particle squared. If each unit of building block for the MINP(glucose) is assumed to contain 0.6 molecules of compound **1a** (MW = 465 g/mol), 0.4 molecules of compound **1b** (MW = 558 g/mol), 0.6 molecules of compound **4** (MW = 264 g/mol), one molecule of DVB (MW = 130 g/mol), and 0.02 molecules of 6-vinylbenzoxaborole (MW = 160 g/mol), the molecular weight of MINP(glucose) translates to 54 [= 42600 / (0.6×465 +0.4×558 +0.6×264 +130 +0.02×160)] of such units.

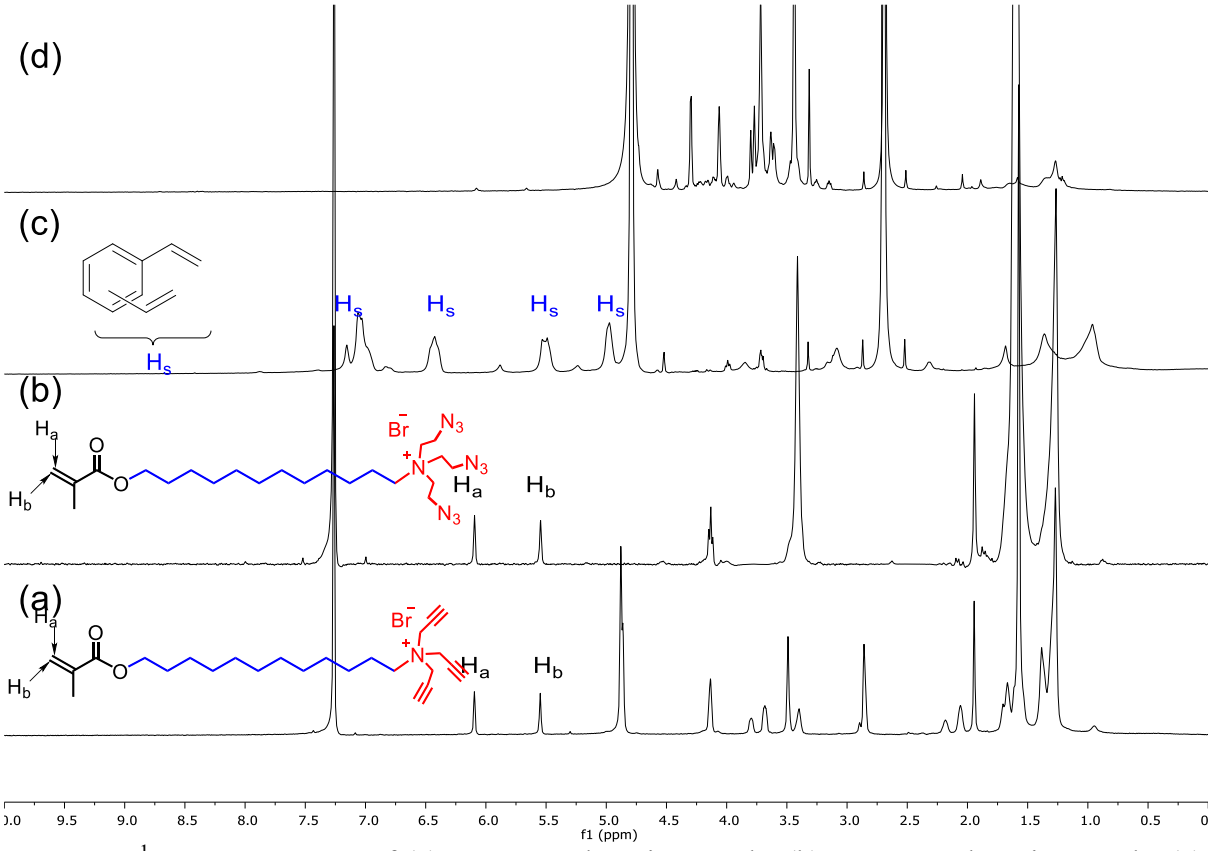

Figure 4. ^{1}H NMR spectra of (a) Compound **1a** in $CDCl_3$, (b) Compound **1b** in $CDCl_3$, (c) alkynyl-SCM in D_2O, and (d) MINP(glucose) in D_2O at 298 K. The data correspond to entry 2 in Table 4.

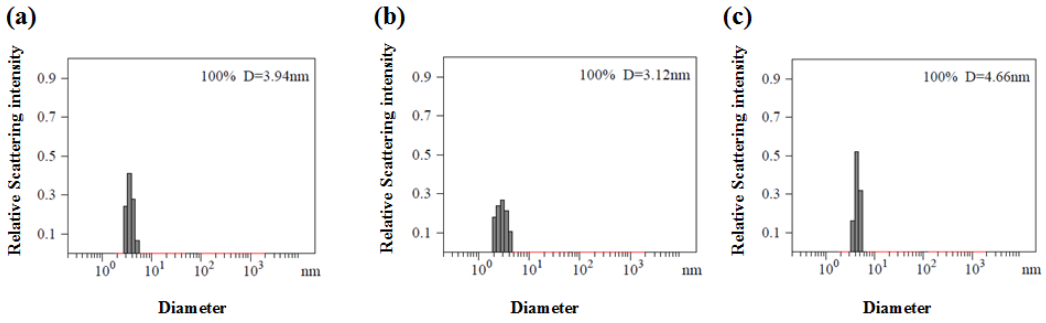

Figure 5. Distribution of the hydrodynamic diameters of the nanoparticles in water as determined by DLS for the synthesis of MINP(glucose) (a) alkynyl-SCM, (b) core-cross-linked-SCM, and (c) surface-functionalized MINP(glucose) after purification. The data correspond to entry 2 in Table 4.

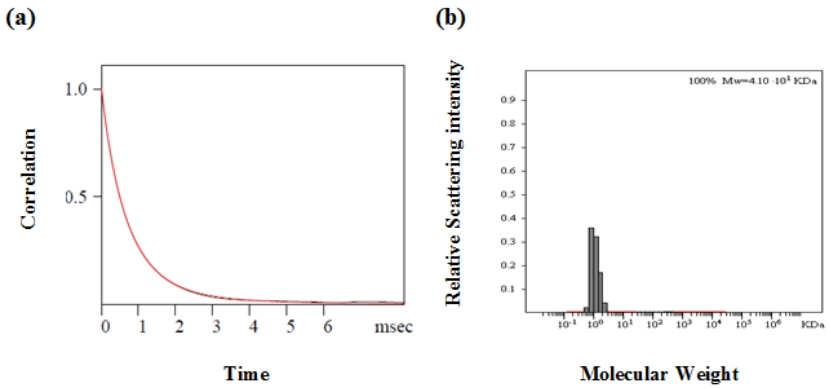

Figure 6. The correlation curve and the distribution of the molecular weight for MINP(glucose) from the DLS. The data correspond to entry 2 in Table 4. The PRECISION DECONVOLVE program assumes the intensity of scattering is proportional to the mass of the particle squared. If each unit of building block for the MINP(glucose) is assumed to contain 0.6 molecules of compound **1a** (MW = 465 g/mol), 0.4 molecules of compound **1b** (MW = 558 g/mol), 0.6 molecules of compound **4** (MW = 264 g/mol), one molecule of DVB (MW = 130 g/mol), and 0.04 molecules of 6-vinylbenzoxaborole (MW = 160 g/mol), the molecular weight of MINP(glucose) translates to 51 [= 41000 / (0.6×465 +0.4×558 +0.6×264 +130 +0.04×160)] of such units.

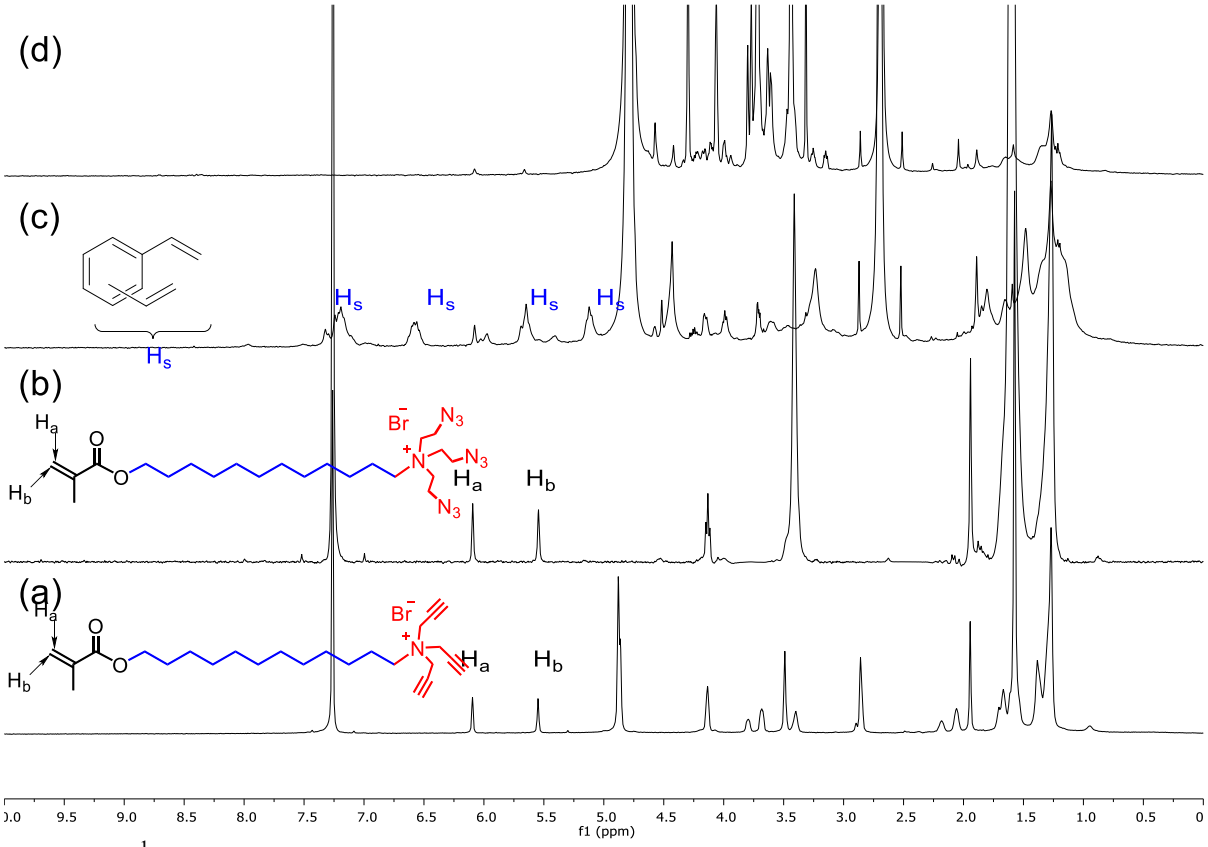

Figure 7. ^{1}H NMR spectra of (a) Compound **1a** in $CDCl_3$, (b) Compound **1b** in $CDCl_3$, (c) alkynyl-SCM in D_2O, and (d) MINP(glucose) in D_2O at 298 K. The data correspond to entry 3 in Table 4.

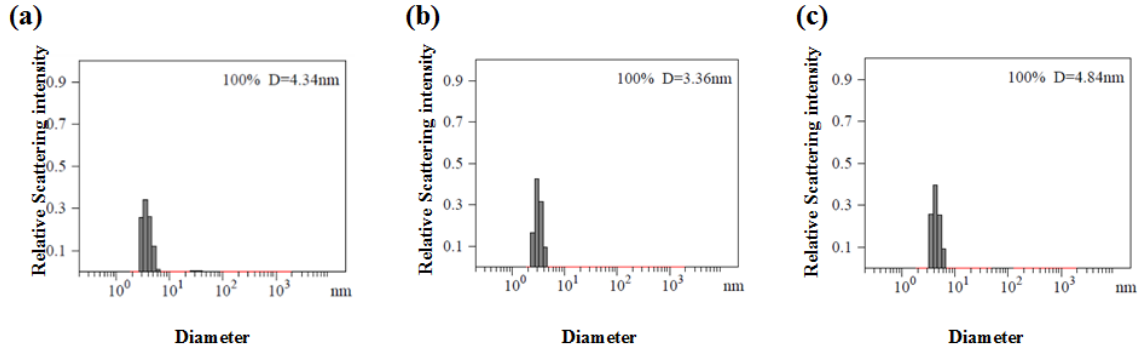

Figure 8. Distribution of the hydrodynamic diameters of the nanoparticles in water as determined by DLS for the synthesis of MINP(glucose) (a) alkynyl-SCM, (b) core-cross-linked-SCM, and (c) surface-functionalized MINP(glucose) after purification. The data correspond to entry 3 in Table 4.

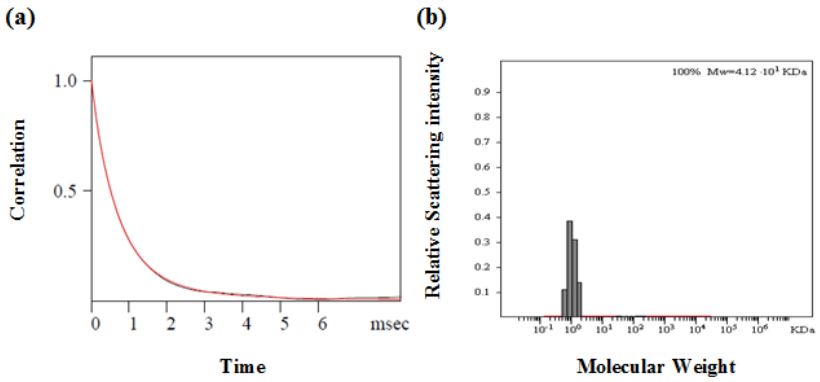

Figure 9. The correlation curve and the distribution of the molecular weight for MINP(glucose) from the DLS. The data correspond to entry 3 in Table 4. The PRECISION DECONVOLVE program assumes the intensity of scattering is proportional to the mass of the particle squared. If each unit of building block for the MINP(glucose) is assumed to contain 0.6 molecules of compound **1a** (MW = 465 g/mol), 0.4 molecules of compound **1b** (MW = 558 g/mol), 0.6 molecules of compound **4** (MW = 264 g/mol), one molecule of DVB (MW = 130 g/mol), and 0.06 molecules of 6-vinylbenzoxaborole (MW = 160 g/mol), the molecular weight of MINP(glucose) translates to 51 [= 41200 / (0.6×465 +0.4×558 +0.6×264 +130 +0.06×160)] of such units.

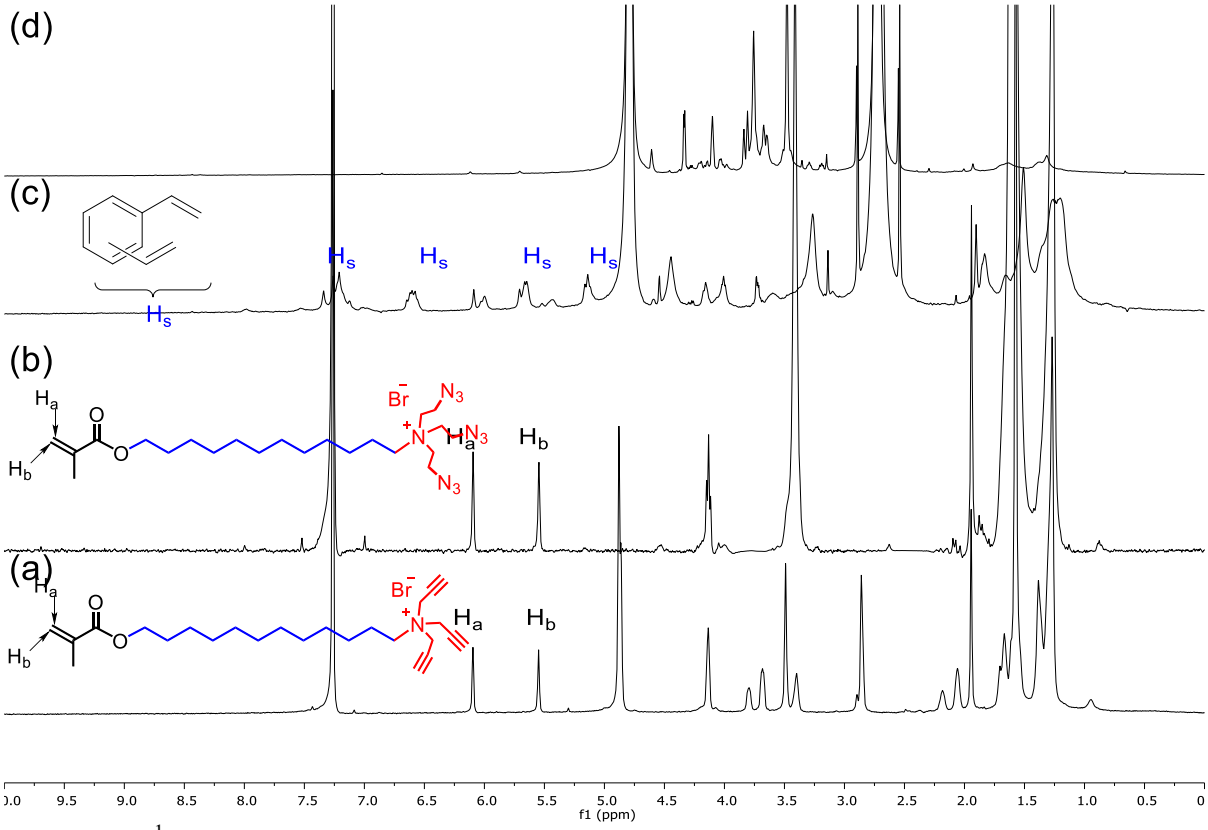

Figure 10. ^{1}H NMR spectra of (a) Compound **1a** in $CDCl_3$, (b) Compound **1b** in $CDCl_3$, (c) alkynyl-SCM in D_2O, and (d) NINP in D_2O at 298 K. The data correspond to entry 4 in Table 4.

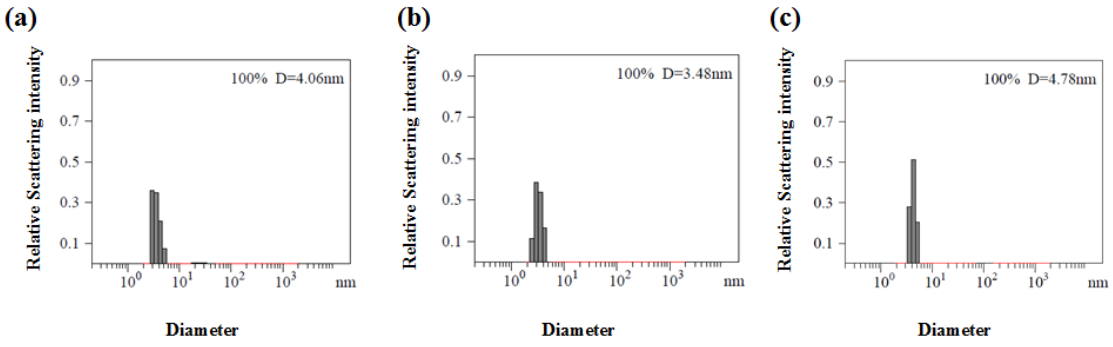

Figure 11. Distribution of the hydrodynamic diameters of the nanoparticles in water as determined by DLS for the synthesis of NINP (a) alkynyl-SCM, (b) core-cross-linked-SCM, and (c) surface-functionalized NINP after purification. The data correspond to entry 4 in Table 4.

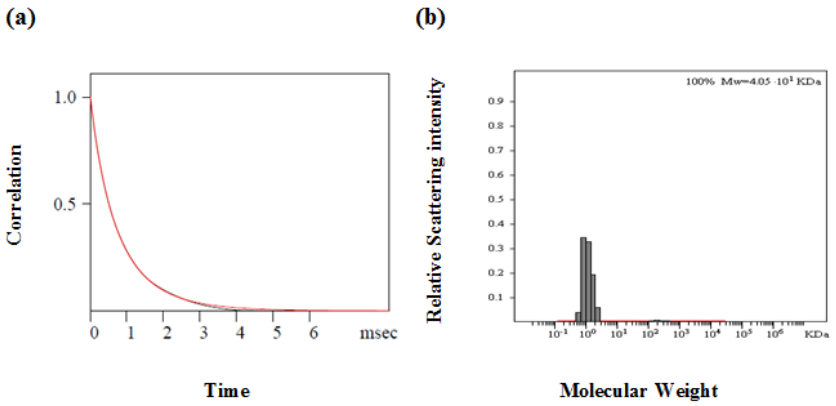

Figure 12. The correlation curve and the distribution of the molecular weight for NINP from the DLS. The data correspond to entry 4 in Table 4. The PRECISION DECONVOLVE program assumes the intensity of scattering is proportional to the mass of the particle squared. If each unit of building block for the NINP is assumed to contain 0.6 molecules of compound **1a** (MW = 465 g/mol), 0.4 molecules of compound **1b** (MW = 558 g/mol), 0.6 molecules of compound **4** (MW = 264 g/mol), and one molecule of DVB (MW = 130 g/mol), the molecular weight of NINP translates to 51 [= 40500 / (0.6×465 +0.4×558 +0.6×264 +130)] of such units.

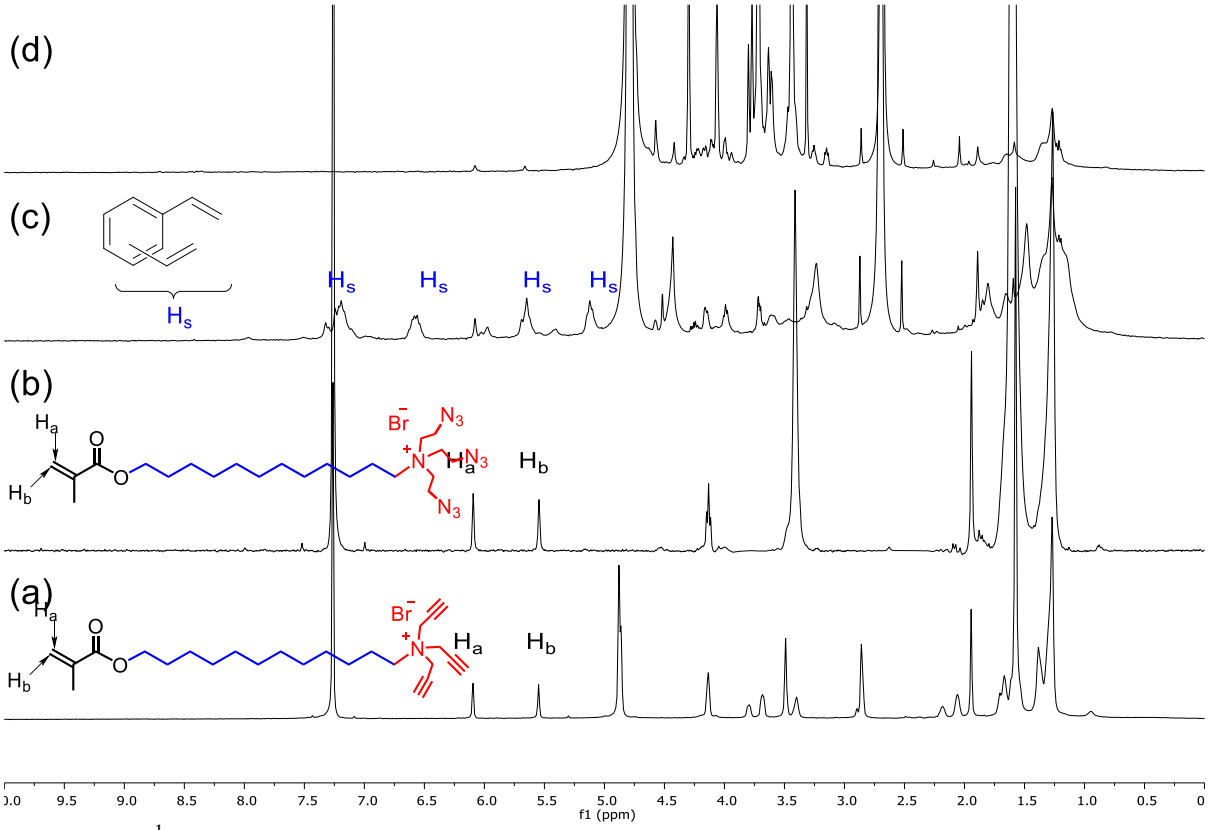

Figure 13. ^{1}H NMR spectra of (a) Compound **1a** in $CDCl_3$, (b) Compound **1b** in $CDCl_3$, (c) alkynyl-SCM in D_2O, and (d) NINP in D_2O at 298 K. The data correspond to entry 5 in Table 4.

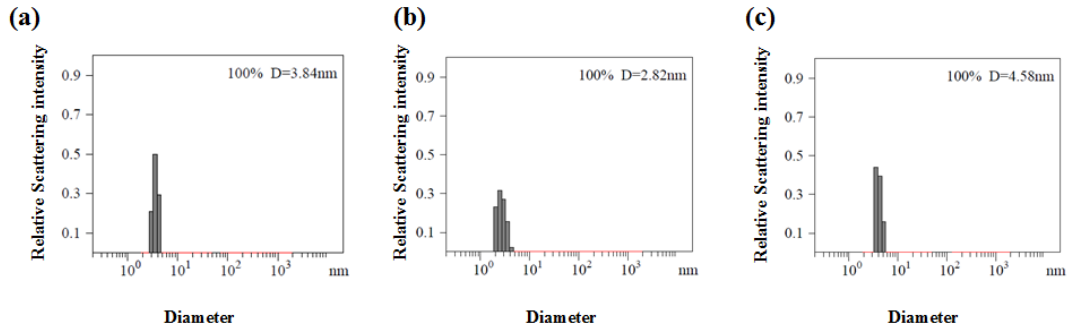

Figure 14. Distribution of the hydrodynamic diameters of the nanoparticles in water as determined by DLS for the synthesis of NINP (a) alkynyl-SCM, (b) core-cross-linked-SCM, and (c) surface-functionalized NINP after purification. The data correspond to entry 5 in Table 4.

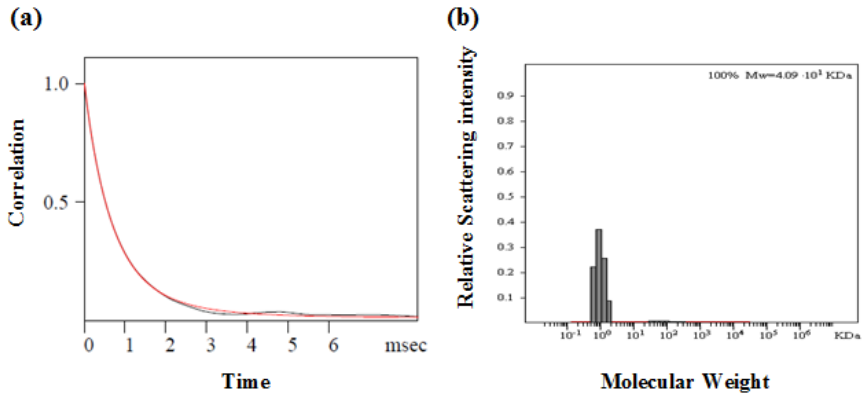

Figure 15. The correlation curve and the distribution of the molecular weight for NINP from the DLS. The data correspond to entry 5 in Table 4. The PRECISION DECONVOLVE program assumes the intensity of scattering is proportional to the mass of the particle squared. If each unit of building block for the NINP is assumed to contain 0.6 molecules of compound **1a** (MW = 465 g/mol), 0.4 molecules of compound **1b** (MW = 558 g/mol), 0.6 molecules of compound **4** (MW = 264 g/mol), one molecule of DVB (MW = 130 g/mol), and 0.04 molecules of 6-vinylbenzoxaborole (MW = 160 g/mol), the molecular weight of NINP translates to 51 [= 40900 / (0.6×465 +0.4×558 +0.6×264 +130 +0.04×160)] of such units.

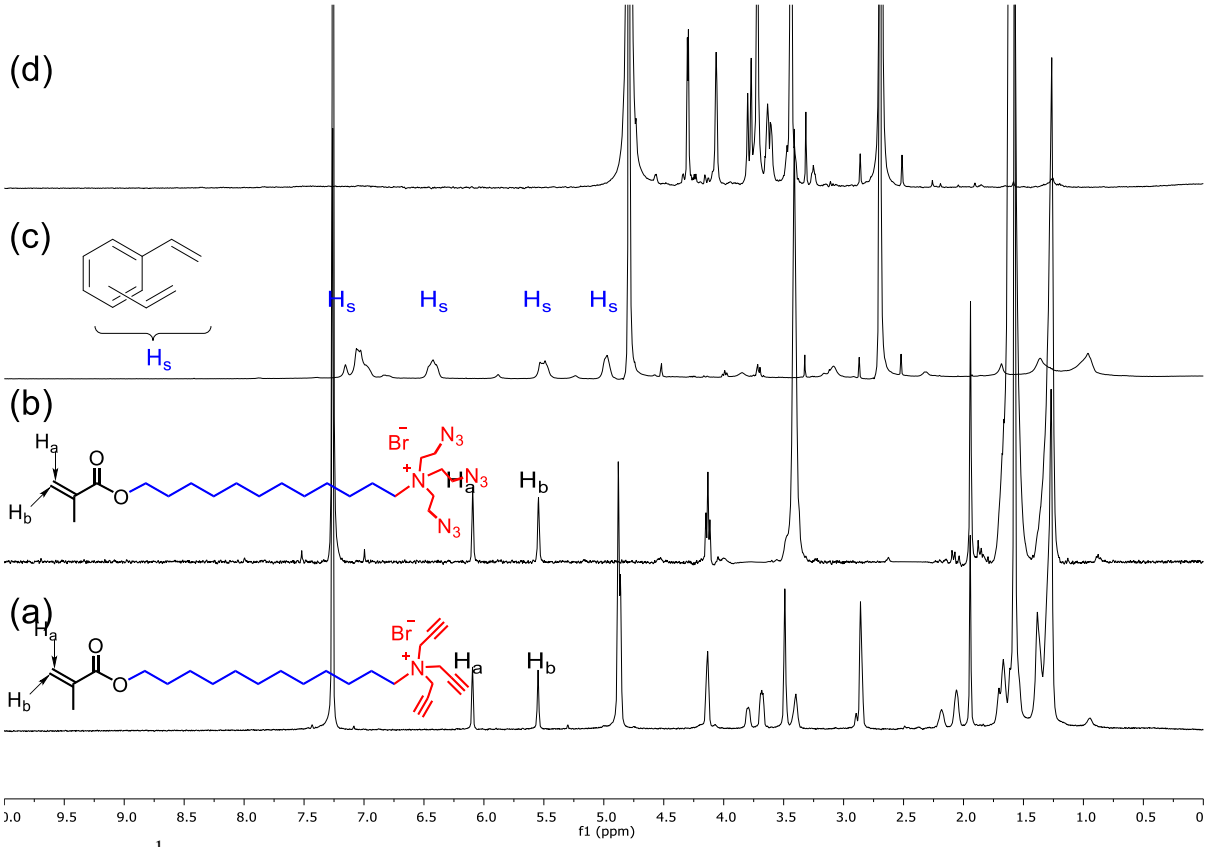

Figure 16. ^{1}H NMR spectra of (a) Compound **1a** in $CDCl_3$, (b) Compound **1b** in $CDCl_3$, (c) alkynyl-SCM in D_2O, and (d) MINP(mannose) in D_2O at 298 K. The data correspond to entry 6 in Table 4.

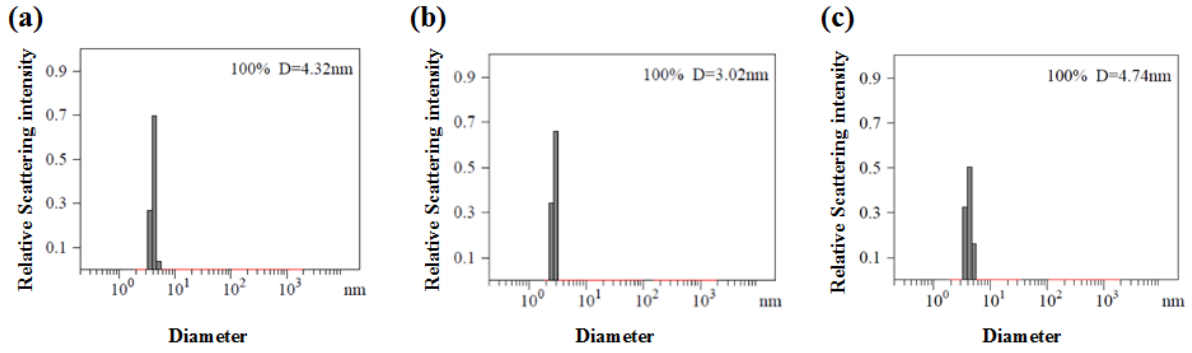

Figure 17. Distribution of the hydrodynamic diameters of the nanoparticles in water as determined by DLS for the synthesis of MINP(mannose) (a) alkynyl-SCM, (b) core-cross-linked-SCM, and (c) surface-functionalized MINP(mannose) after purification. The data correspond to entry 6 in Table 4.

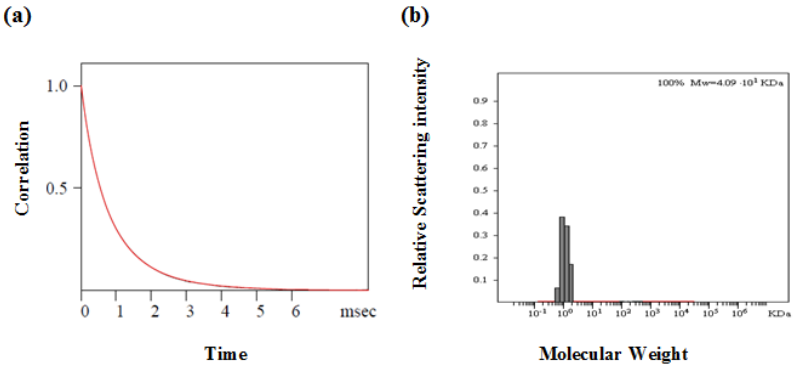

Figure 18. The correlation curve and the distribution of the molecular weight for MINP(mannose) from the DLS. The data correspond to entry 6 in Table 4. The PRECISION DECONVOLVE program assumes the intensity of scattering is proportional to the mass of the particle squared. If each unit of building block for the MINP(mannose) is assumed to contain 0.6 molecules of compound **1a** (MW = 465 g/mol), 0.4 molecules of compound **1b** (MW = 558 g/mol), 0.6 molecules of compound **4** (MW = 264 g/mol), one molecule of DVB (MW = 130 g/mol), and 0.04 molecules of 6-vinylbenzoxaborole (MW = 160 g/mol), the molecular weight of MINP(mannose) translates to 51 [= 40900 / (0.6×465 +0.4×558 +0.6×264 +130 +0.04×160)] of such units.

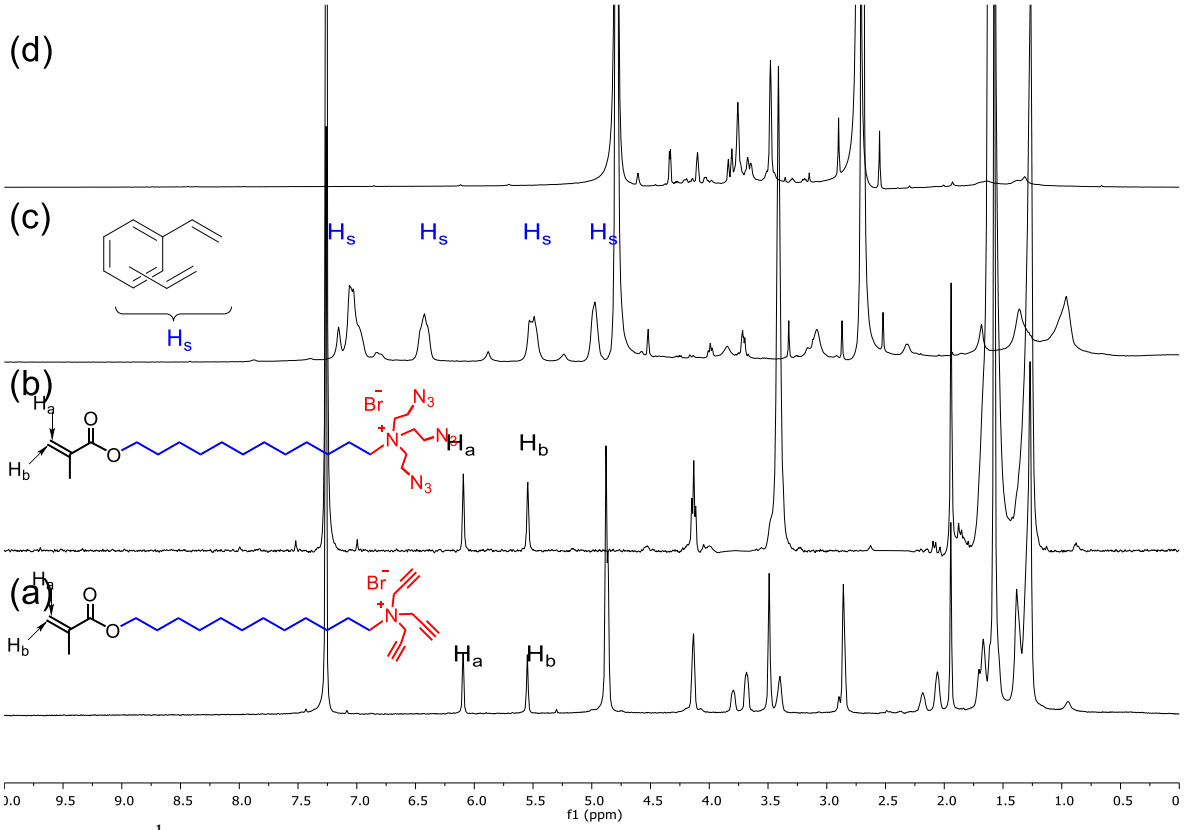

Figure 19. ^{1}H NMR spectra of (a) Compound **1a** in $CDCl_3$, (b) Compound **1b** in $CDCl_3$, (c) alkynyl-SCM in D_2O, and (d) MINP(galactose) in D_2O at 298 K. The data correspond to entry 7 in Table 4.

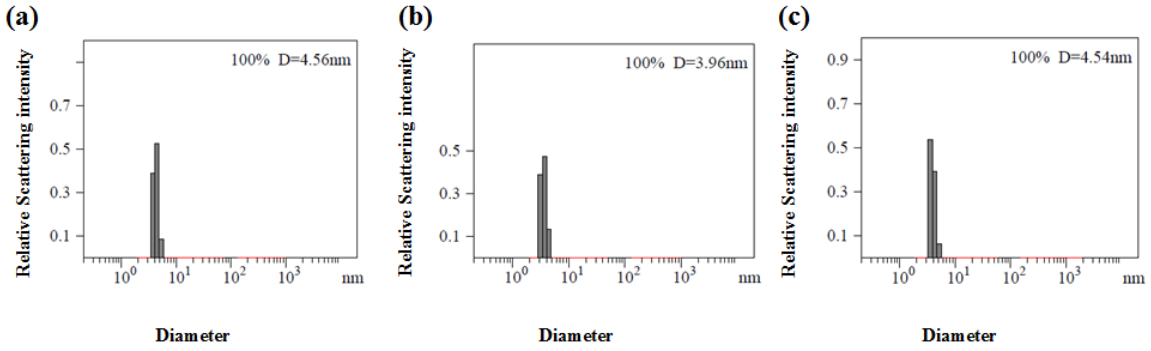

Figure 20. Distribution of the hydrodynamic diameters of the nanoparticles in water as determined by DLS for the synthesis of MINP(galactose) (a) alkynyl-SCM, (b) core-cross-linked-SCM, and (c) surface-functionalized MINP(galactose) after purification. The data correspond to entry 7 in Table 4.

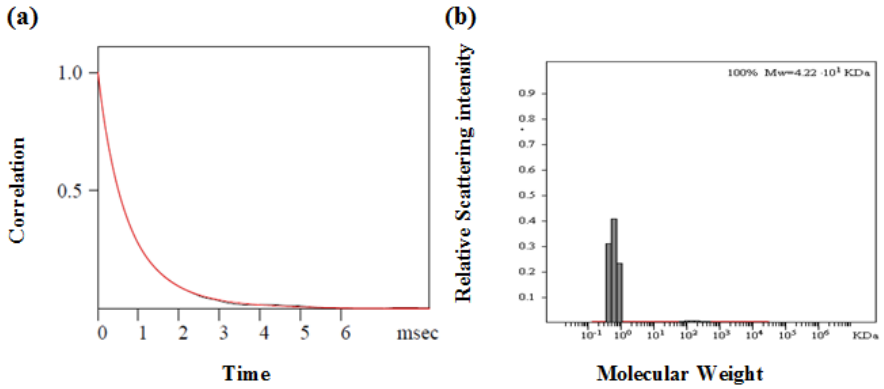

Figure 21. The correlation curve and the distribution of the molecular weight for MINP(galactose) from the DLS. The data correspond to entry 7 in Table 4. The PRECISION DECONVOLVE program assumes the intensity of scattering is proportional to the mass of the particle squared. If each unit of building block for the MINP(galactose) is assumed to contain 0.6 molecules of compound **1a** (MW = 465 g/mol), 0.4 molecules of compound **1b** (MW = 558 g/mol), 0.6 molecules of compound **4** (MW = 264 g/mol), one molecule of DVB (MW = 130 g/mol), and 0.04 molecules of 6-vinylbenzoxaborole (MW = 160 g/mol), the molecular weight of MINP(galactose) translates to 53 [= 42200 / (0.6×465 +0.4×558 +0.6×264 +130 +0.04×160)] of such units.

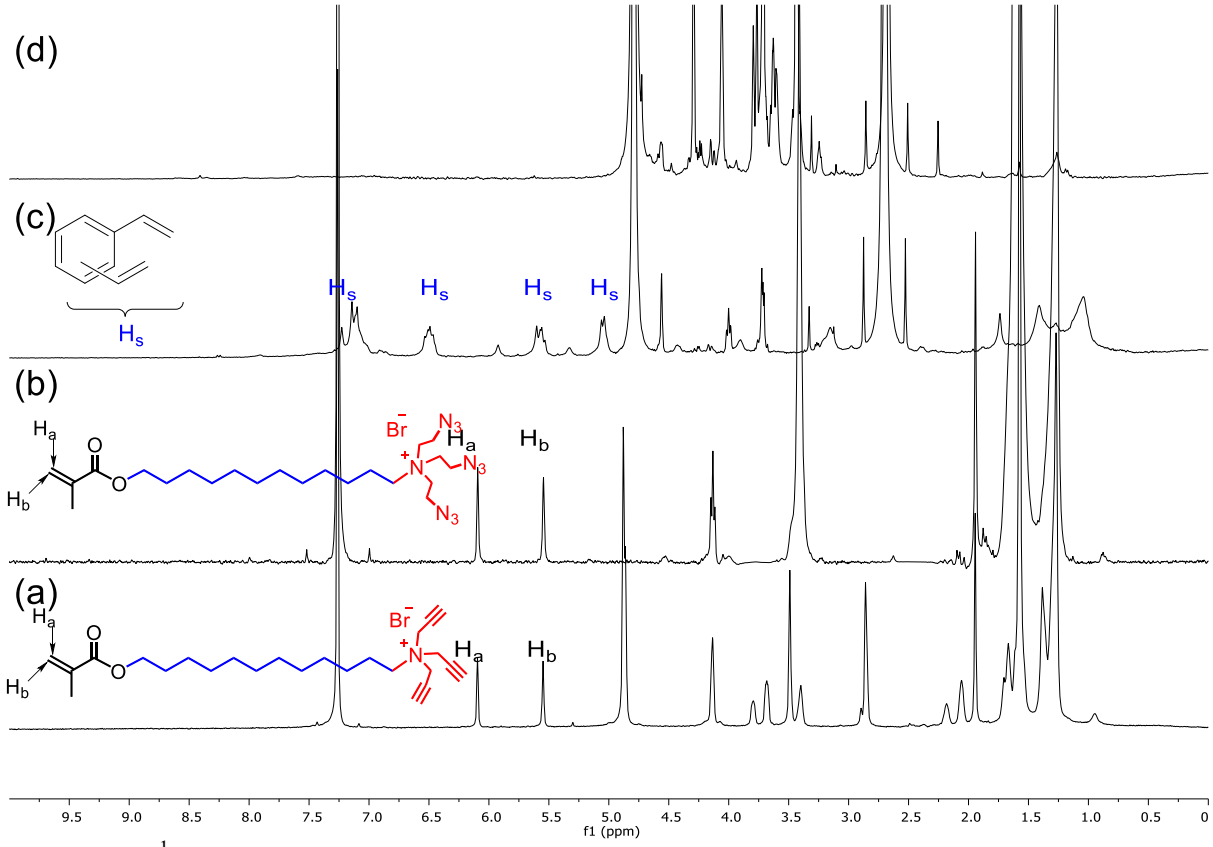

Figure 22. ^{1}H NMR spectra of (a) Compound **1a** in $CDCl_3$, (b) Compound **1b** in $CDCl_3$, (c) alkynyl-SCM in D_2O, and (d) MINP(**5**) in D_2O at 298 K. The data correspond to entry 8 in Table 4.

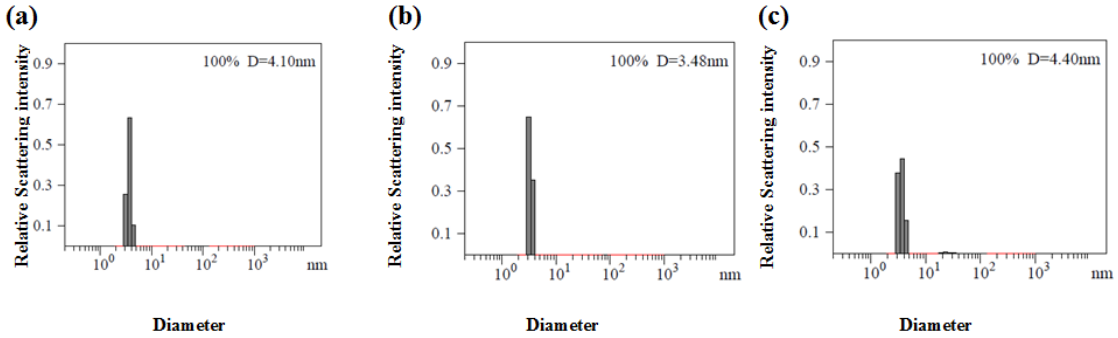

Figure 23. Distribution of the hydrodynamic diameters of the nanoparticles in water as determined by DLS for the synthesis of MINP(**5**) (a) alkynyl-SCM, (b) core-cross-linked-SCM, and (c) surface-functionalized MINP(**5**) after purification. The data correspond to entry 8 in Table 4.

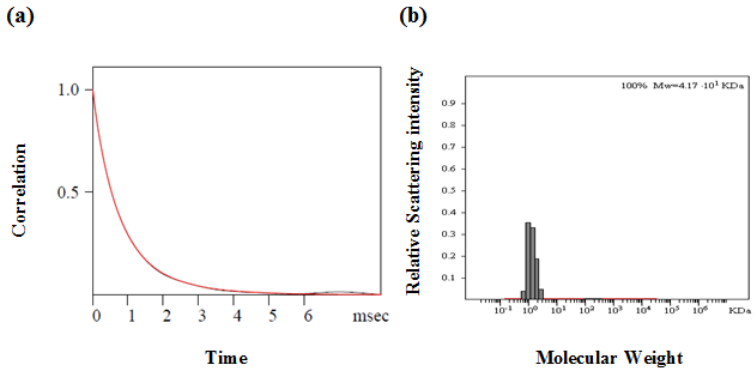

Figure 24. The correlation curve and the distribution of the molecular weight for MINP(**5**) from the DLS. The data correspond to entry 8 in Table 4. The PRECISION DECONVOLVE program assumes the intensity of scattering is proportional to the mass of the particle squared. If each unit of building block for the MINP(**5**) is assumed to contain 0.6 molecules of compound **1a** (MW = 465 g/mol), 0.4 molecules of compound **1b** (MW = 558 g/mol), 0.6 molecules of compound **4** (MW = 264 g/mol), one molecule of DVB (MW = 130 g/mol), and 0.04 molecules of 6-vinylbenzoxaborole (MW = 160 g/mol), the molecular weight of MINP(**5**) translates to 52 [= 41700 / (0.6×465 +0.4×558 +0.6×264 +130 +0.02×160)] of such units.

Synthesis of oligosaccharide MINPs. A solution of 6-vinylbenzoxaborole (**2**) in methanol (20 μL of a 6.4 mg/mL, 0.0008 mmol) was added to maltose in methanol (10 μL of 13.68 mg/mL, 0.0004 mmol). After the mixture was stirred for 6 h at room temperature. methanol was removed *in vacuo*. A micellar solution of **9** (0.03 mmol), **1b** (0.02 mmol), divinylbenzene (DVB, 2.8 μL, 0.02 mmol), and 2,2-dimethoxy-2-phenylacetophenone (DMPA,10 μL of a 12.8 mg/mL solution in DMSO, 0.0005 mmol) in D_2O (2.0 mL) was added to the sugar–boronate complex. (D_2O instead of H_2O was used to allow the reaction progress to be monitored by ^1H NMR spectroscopy.) The mixture was subjected to ultrasonication for 10 min before $CuCl_2$ (10 μL of a 6.7 mg/mL solution in D_2O, 0.0005 mmol) and sodium ascorbate (10 μL of a 99 mg/mL solution in D_2O, 0.005 mmol) were added. After the reaction mixture was stirred slowly at room temperature for 12 h, the reaction mixture was transferred into a glass vial, purged with nitrogen for 15 min, sealed with a rubber stopper, and irradiated in a Rayonet reactor for 8 h. Compound **4** (10.6 mg, 0.04 mmol), $CuCl_2$ (10 μL of a 6.7 mg/mL solution in D_2O, 0.0005 mmol), and sodium ascorbate (10 μL of a 99 mg/mL solution in D_2O, 0.005 mmol) were added. After being stirred for another 6 h at room temperature, the reaction mixture was poured into acetone (8 mL). The precipitate collected by centrifugation was washed with a mixture of acetone/water (5 mL/1 mL), and methanol/acetic acid (5 mL/0.1 mL) for three times and finally with acetone (1×5 mL) to neutral before being dried in air to afford the final MINPs.

Table 5. Oligosaccharide formulation.

Entry	MINP	Amount of 0.04 M Sugar / µL	Amount of 0.04 M 6-vinylBenzoxoborole / µL	Ratio (Sugar:benzoxoborole)
1	MINP(maltose)[a]	10	10	1:1
2	MINP(maltose)[a]	10	20	1:2
3	MINP(maltose)[a]	10	30	1:3
4	MINP(maltose)[b]	10	20	1:2
5	MINP(cellobiose)[a]	10	20	1:2
6	MINP(gentiobiose)[a]	10	20	1:2
7	MINP(maltulose)[a]	10	20	1:2
8	MINP(lactose)[a]	10	20	1:2
9	MINP(maltotriose)[a]	10	20	1:2
10	MINP(H)[a]	10	30	1:3
11	MINP(A)[a]	10	30	1:3
12	MINP(B)[a]	10	30	1:3

[a] The micellar solution was prepared with compound **9**/compound **1b**. [b] The micellar solution was prepared with compound **1a**/compound **1b**.

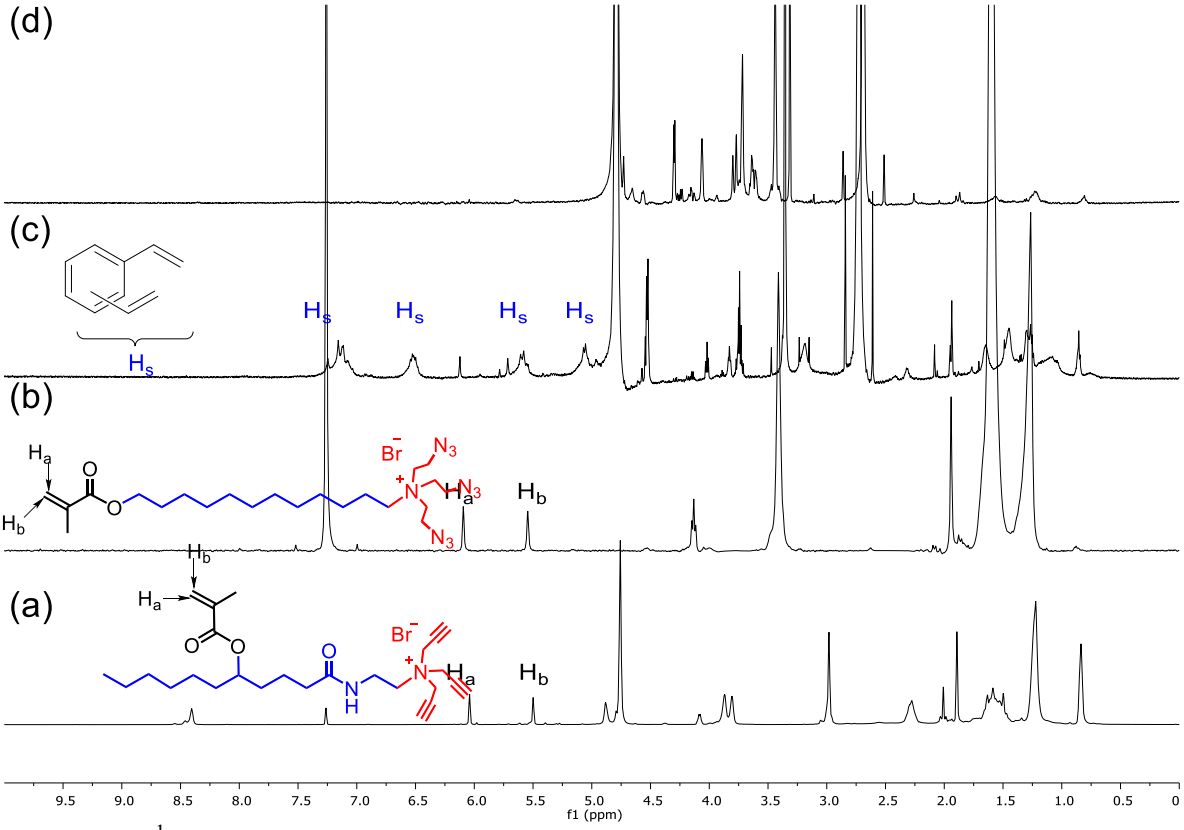

Figure 25. ^{1}H NMR spectra of (a) Compound **9** in $CDCl_3$, (b) Compound **1b** in $CDCl_3$, (c) alkynyl-SCM in D_2O, and (d) MINP(maltose) in D_2O at 298 K. The data correspond to entry 1 in Table 5.

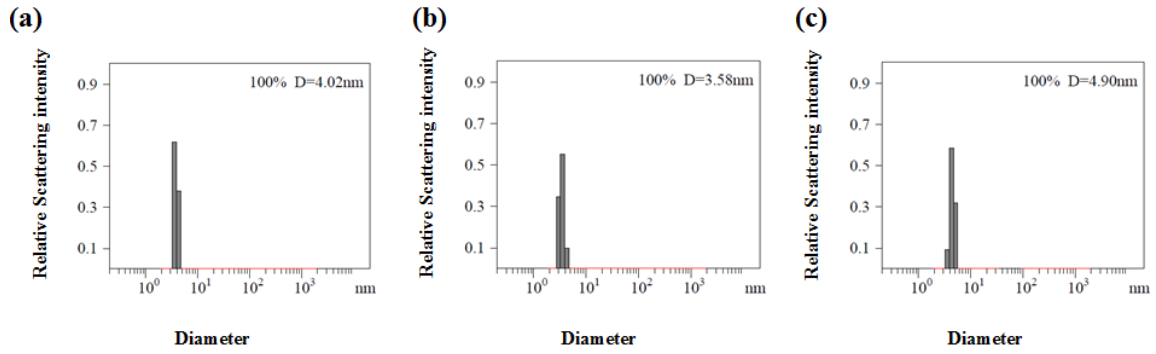

Figure 26. Distribution of the hydrodynamic diameters of the nanoparticles in water as determined by DLS for the synthesis of MINP(maltose) (a) alkynyl-SCM, (b) core-cross-linked-SCM, and (c) surface-functionalized MINP(maltose) after purification. The data correspond to entry 1 in Table 5.

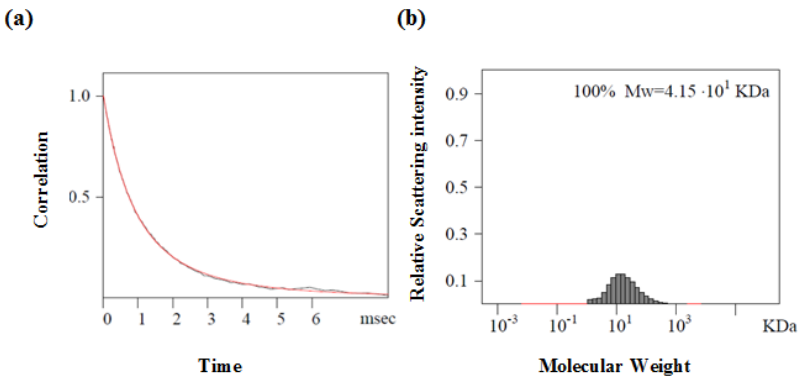

Figure 27. The correlation curve and the distribution of the molecular weight for MINP(maltose) from the DLS. The data correspond to entry 1 in Table 5. The PRECISION DECONVOLVE program assumes the intensity of scattering is proportional to the mass of the particle squared. If each unit of building block for the MINP(maltose) is assumed to contain 0.4 molecules of compound **1b** (MW = 558 g/mol), 0.6 molecules of compound **9** (MW = 508 g/mol), 0.6 molecules of compound **4** (MW = 264 g/mol), one molecule of DVB (MW = 130 g/mol), and 0.02 molecules of 6-vinylbenzoxaborole (MW = 160 g/mol), the molecular weight of MINP(maltose) translates to 51 [= 41500 / (0.4×558 +0.6×508 +0.6×264 +130 +0.02×160)] of such units.

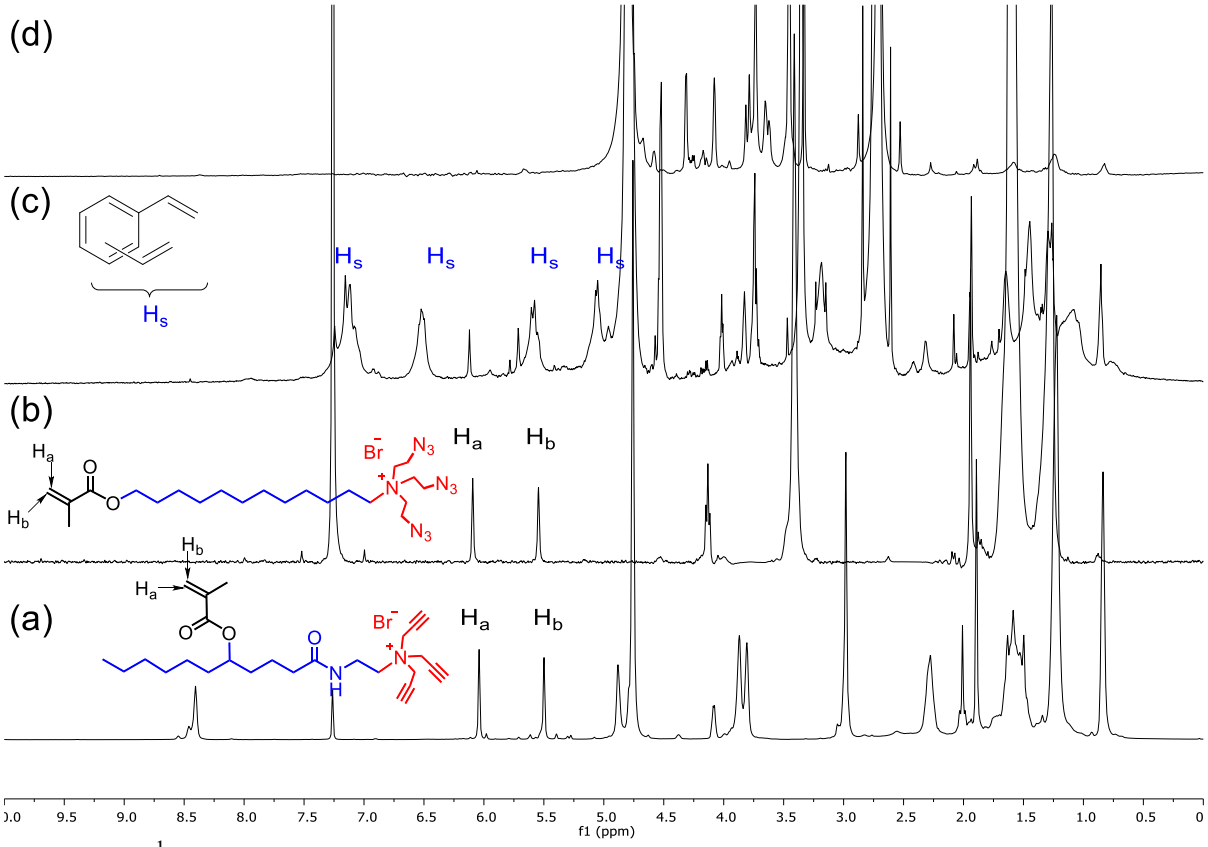

Figure 28. ^{1}H NMR spectra of (a) Compound **9** in $CDCl_3$, (b) Compound **1b** in $CDCl_3$, (c) alkynyl-SCM in D_2O, and (d) MINP(maltose) in D_2O at 298 K. The data correspond to entry 2 in Table 5.

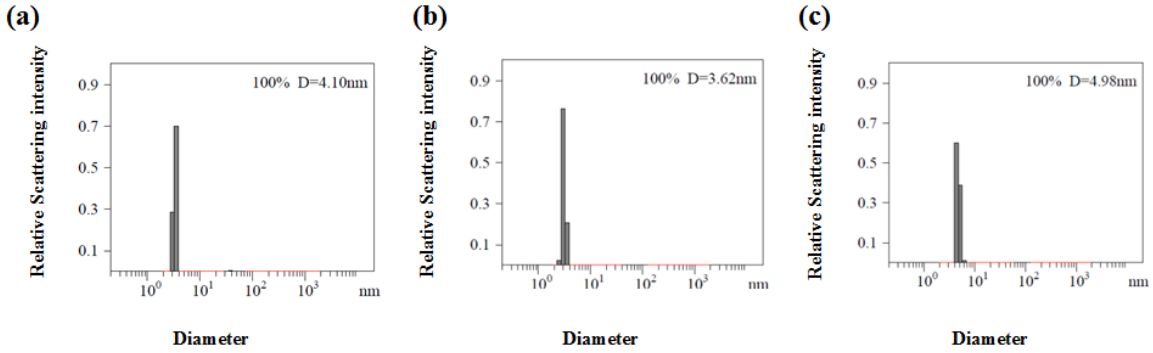

Figure 29. Distribution of the hydrodynamic diameters of the nanoparticles in water as determined by DLS for the synthesis of MINP(maltose) (a) alkynyl-SCM, (b) core-cross-linked-SCM, and (c) surface-functionalized MINP(maltose) after purification. The data correspond to entry 2 in Table 5.

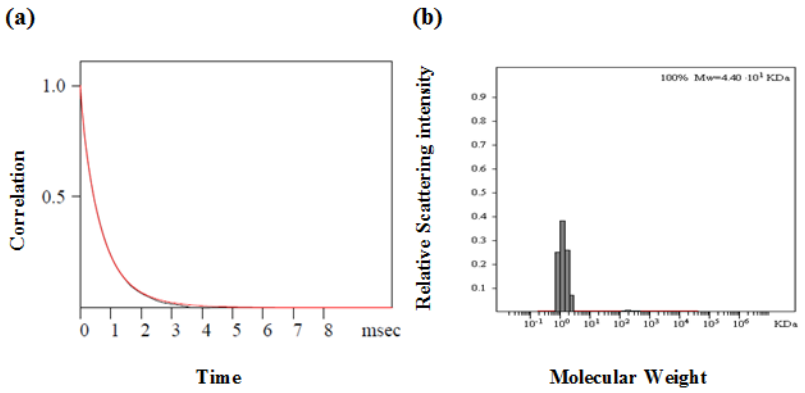

Figure 30. The correlation curve and the distribution of the molecular weight for MINP(maltose) from the DLS. The data correspond to entry 2 in Table 5. The PRECISION DECONVOLVE program assumes the intensity of scattering is proportional to the mass of the particle squared. If each unit of building block for the MINP(maltose) is assumed to contain 0.6 molecules of compound **9** (MW = 508 g/mol), 0.4 molecules of compound **1b** (MW = 558 g/mol), 0.6 molecules of compound **4** (MW = 264 g/mol), one molecule of DVB (MW = 130 g/mol), and 0.04 molecules of 6-vinylbenzoxaborole (MW = 160 g/mol), the molecular weight of MINP(maltose) translates to 53 [= 44000 / (0.6×508 +0.4×558 +0.6×264 +130 +0.04×160)] of such units.

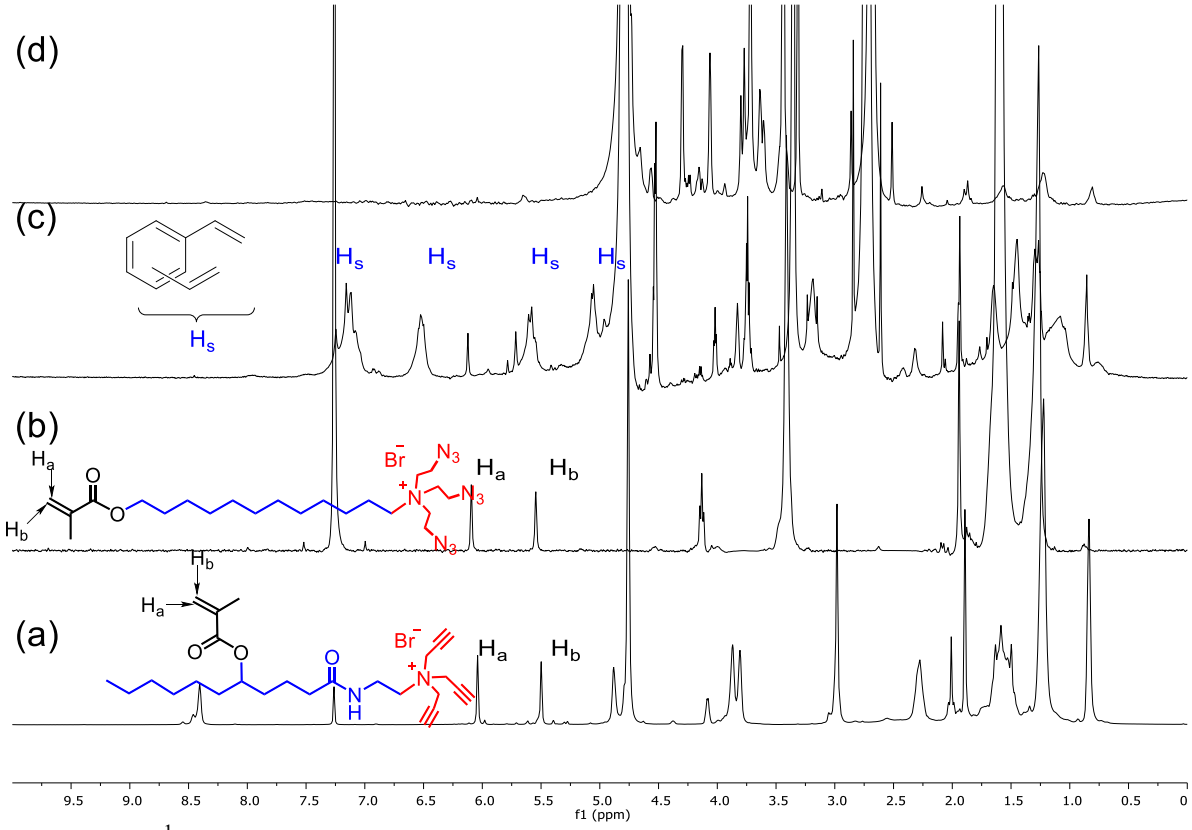

Figure 31. ^{1}H NMR spectra of (a) Compound **9** in $CDCl_3$, (b) Compound **1b** in $CDCl_3$, (c) alkynyl-SCM in D_2O, and (d) MINP(maltose) in D_2O at 298 K. The data correspond to entry 3 in Table 5.

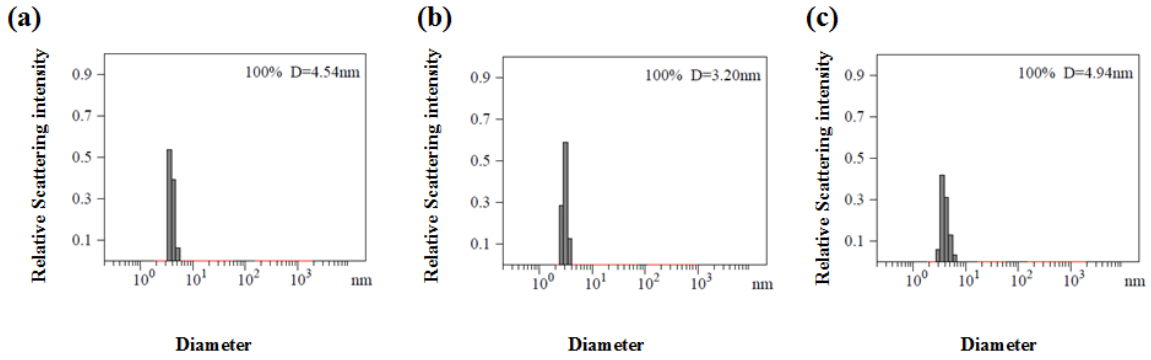

Figure 32. Distribution of the hydrodynamic diameters of the nanoparticles in water as determined by DLS for the synthesis of MINP(maltose) (a) alkynyl-SCM, (b) core-cross-linked-SCM, and (c) surface-functionalized MINP(maltose) after purification. The data correspond to entry 3 in Table 5.

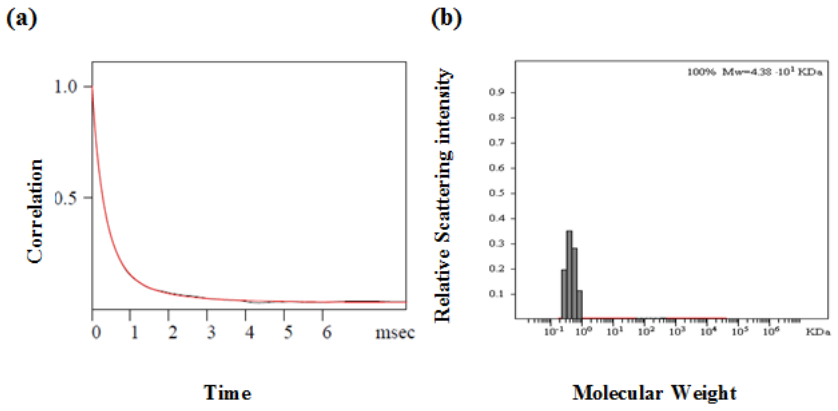

Figure 33. The correlation curve and the distribution of the molecular weight for MINP(maltose) from the DLS The data correspond to entry 3 in Table 5. The PRECISION DECONVOLVE program assumes the intensity of scattering is proportional to the mass of the particle squared. If each unit of building block for the MINP(maltose) is assumed to contain 0.4 molecules of compound **1b** (MW = 558 g/mol), 0.6 molecules of compound **9** (MW = 508 g/mol), 0.6 molecules of compound **4** (MW = 264 g/mol), one molecule of DVB (MW = 130 g/mol), and 0.06 molecules of 6-vinylbenzoxaborole (MW = 160 g/mol), the molecular weight of MINP(maltose) translates to 53 [= 43800 / (0.4×558 +0.6×508 +0.6×264 +130 +0.06×160)] of such units.

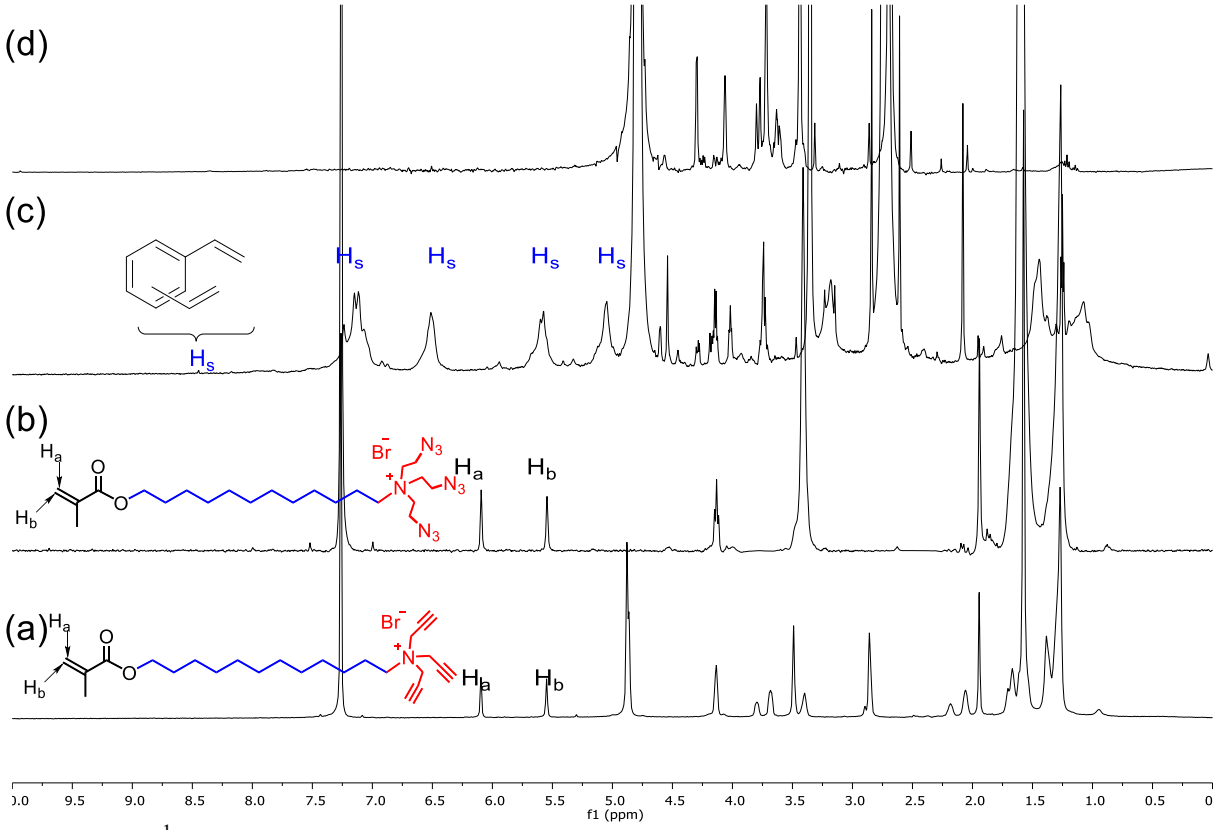

Figure 34. ^{1}H NMR spectra of (a) Compound **1a** in $CDCl_3$, (b) Compound **1b** in $CDCl_3$, (c) alkynyl-SCM in D_2O, and (d) MINP(maltose) in D_2O at 298 K. The data correspond to entry 4 in Table 5.

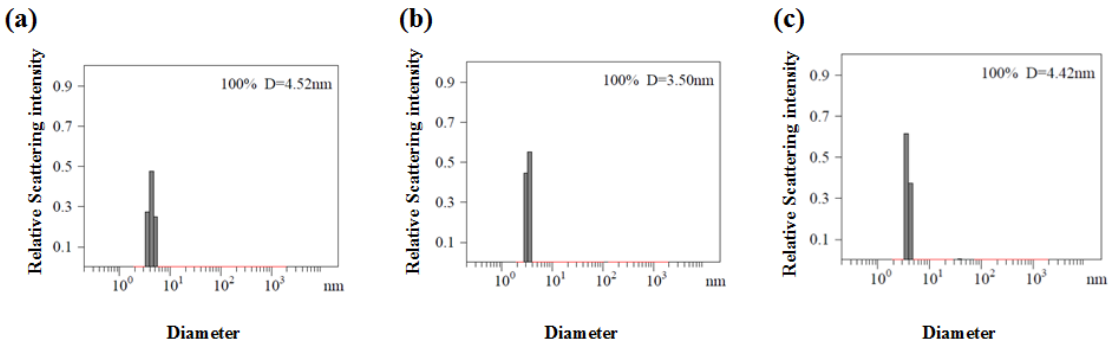

Figure 35. Distribution of the hydrodynamic diameters of the nanoparticles in water as determined by DLS for the synthesis of MINP(maltose) (a) alkynyl-SCM, (b) core-cross-linked-SCM, and (c) surface-functionalized MINP(maltose) after purification. The data correspond to entry 4 in Table 5.

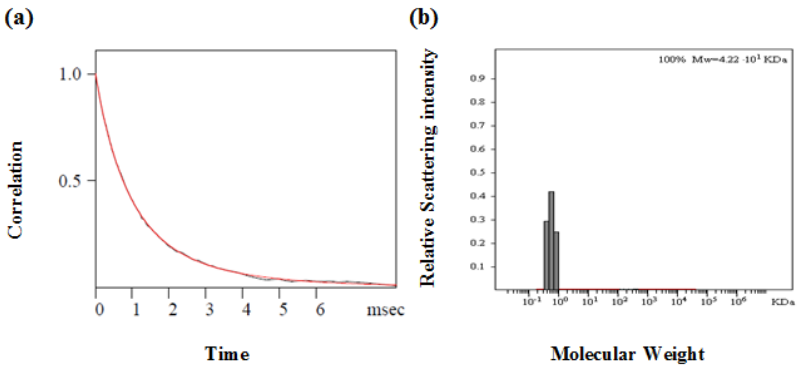

Figure 36. The correlation curve and the distribution of the molecular weight for MINP(maltose) from the DLS. The data correspond to entry 4 in Table 5. The PRECISION DECONVOLVE program assumes the intensity of scattering is proportional to the mass of the particle squared. If each unit of building block for the MINP(maltose) is assumed to contain 0.6 molecules of compound **1a** (MW = 465 g/mol), 0.4 molecules of compound **1b** (MW = 558 g/mol), 0.6 molecules of compound **4** (MW = 264 g/mol), one molecule of DVB (MW = 130 g/mol), and 0.04 molecules of 6-vinylbenzoxaborole (MW = 160 g/mol), the molecular weight of MINP(maltose) translates to 53 [= 42200 / (0.6×465 +0.4×558 +0.6×264 +130 +0.04×160)] of such units.

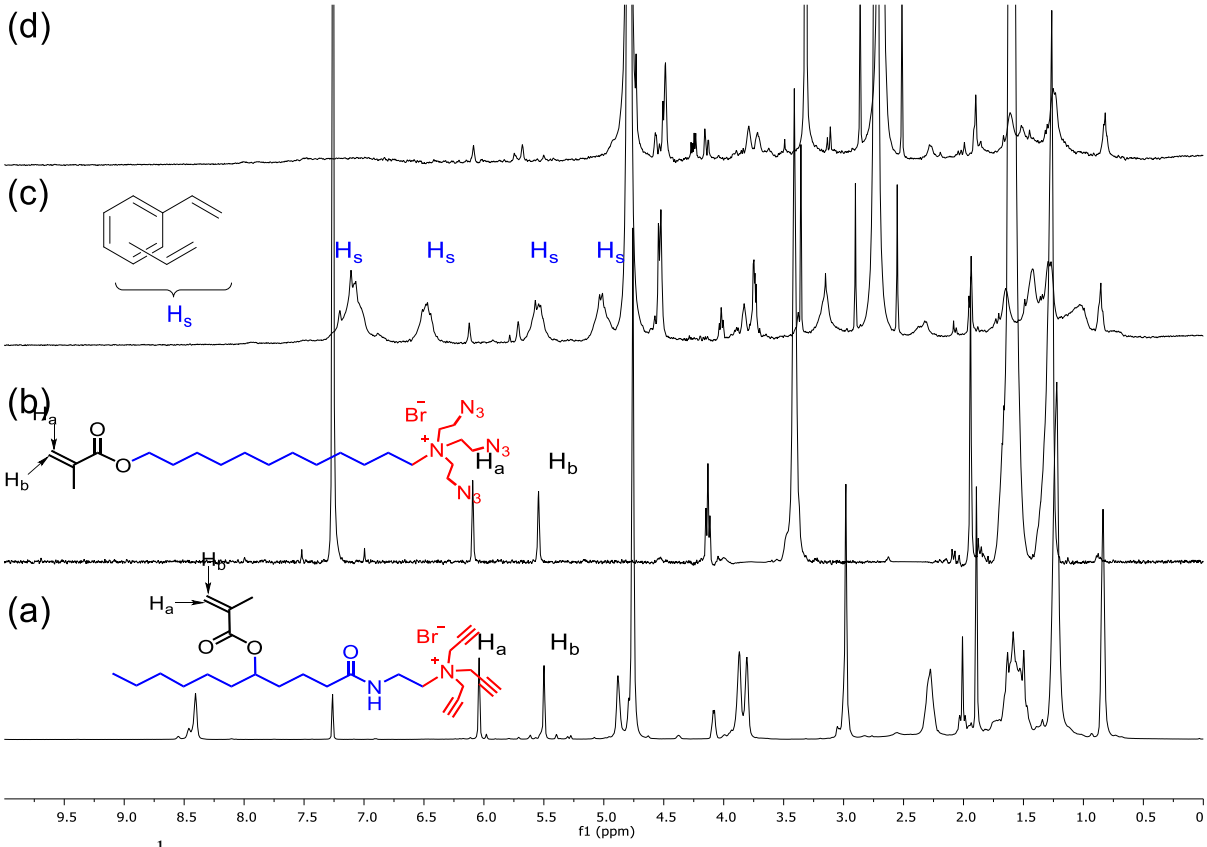

Figure 37. ^{1}H NMR spectra of (a) Compound **9** in $CDCl_3$, (b) Compound **1b** in $CDCl_3$, (c) alkynyl-SCM in D_2O, and (d) MINP(cellobiose) in D_2O at 298 K. The data correspond to entry 5 in Table 5.

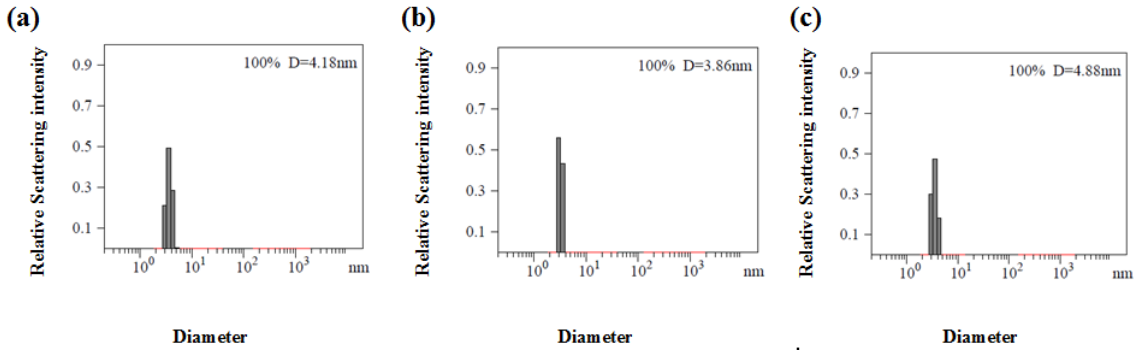

Figure 38. Distribution of the hydrodynamic diameters of the nanoparticles in water as determined by DLS for the synthesis of MINP(cellobiose) (a) alkynyl-SCM, (b) core-cross-linked-SCM, and (c) surface-functionalized MINP(cellobiose) after purification. The data correspond to entry 5 in Table 5.

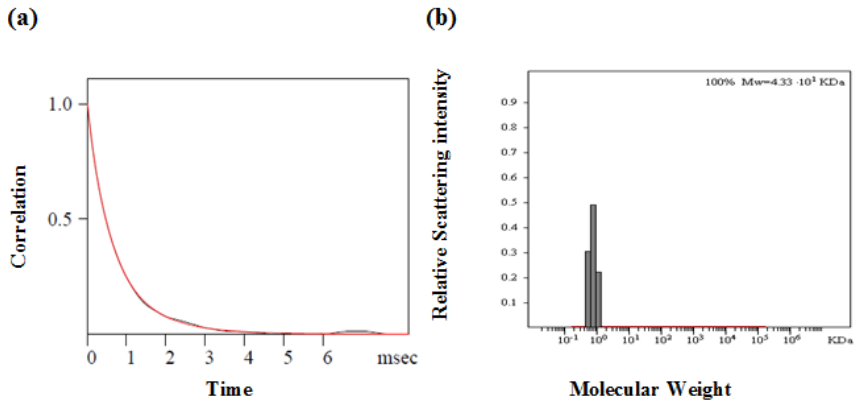

Figure 39. The correlation curve and the distribution of the molecular weight for MINP(cellobiose) from the DLS The data correspond to entry 5 in Table 5. The PRECISION DECONVOLVE program assumes the intensity of scattering is proportional to the mass of the particle squared. If each unit of building block for the MINP(cellobiose) is assumed to contain 0.4 molecules of compound **1b** (MW = 558 g/mol), 0.6 molecules of compound **9** (MW = 508 g/mol), 0.6 molecules of compound **4** (MW = 264 g/mol), one molecule of DVB (MW = 130 g/mol), and 0.04 molecules of 6-vinylbenzoxaborole (MW = 160 g/mol), the molecular weight of MINP(cellobiose) translates to 53 [= 43300 / (0.4×558 +0.6×508 +0.6×264 +130 +0.04×160)] of such units.

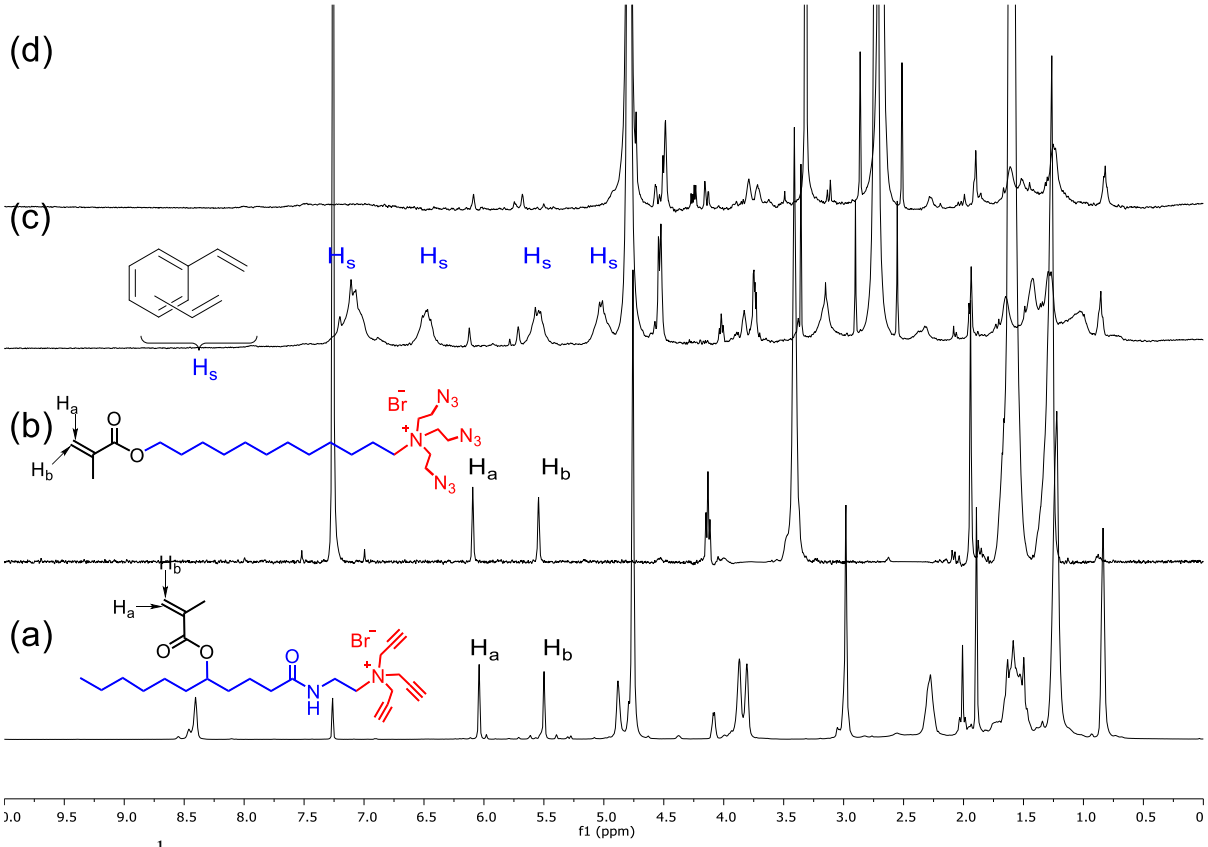

Figure 40. ^{1}H NMR spectra of (a) Compound **9** in $CDCl_3$, (b) Compound **1b** in $CDCl_3$, (c) alkynyl-SCM in D_2O, and (d) MINP(gentiobiose) in D_2O at 298 K. The data correspond to entry 6 in Table 5.

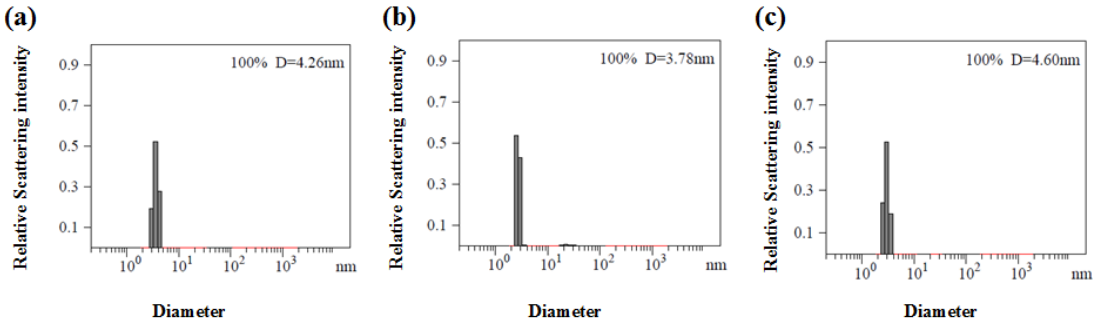

Figure 41. Distribution of the hydrodynamic diameters of the nanoparticles in water as determined by DLS for the synthesis of MINP(gentiobiose) (a) alkynyl-SCM, (b) core-cross-linked-SCM, and (c) surface-functionalized MINP(gentiobiose) after purification. The data correspond to entry 6 in Table 5.

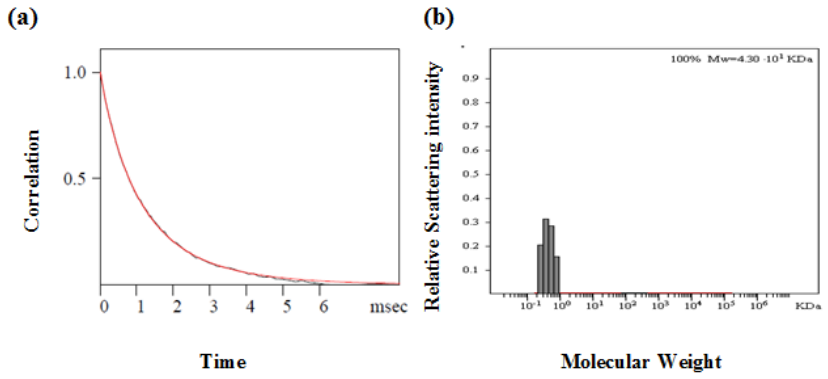

Figure 42. The correlation curve and the distribution of the molecular weight for MINP(gentiobiose) from the DLS The data correspond to entry 6 in Table 5. The PRECISION DECONVOLVE program assumes the intensity of scattering is proportional to the mass of the particle squared. If each unit of building block for the MINP(gentiobiose) is assumed to contain 0.4 molecules of compound **1b** (MW = 558 g/mol), 0.6 molecules of compound **9** (MW = 508 g/mol), 0.6 molecules of compound **4** (MW = 264 g/mol), one molecule of DVB (MW = 130 g/mol), and 0.04 molecules of 6-vinylbenzoxaborole (MW = 160 g/mol), the molecular weight of MINP(gentiobiose) translates to 52 [= 43000 / (0.4×558 +0.6×508 +0.6×264 +130 +0.04×160)] of such units.

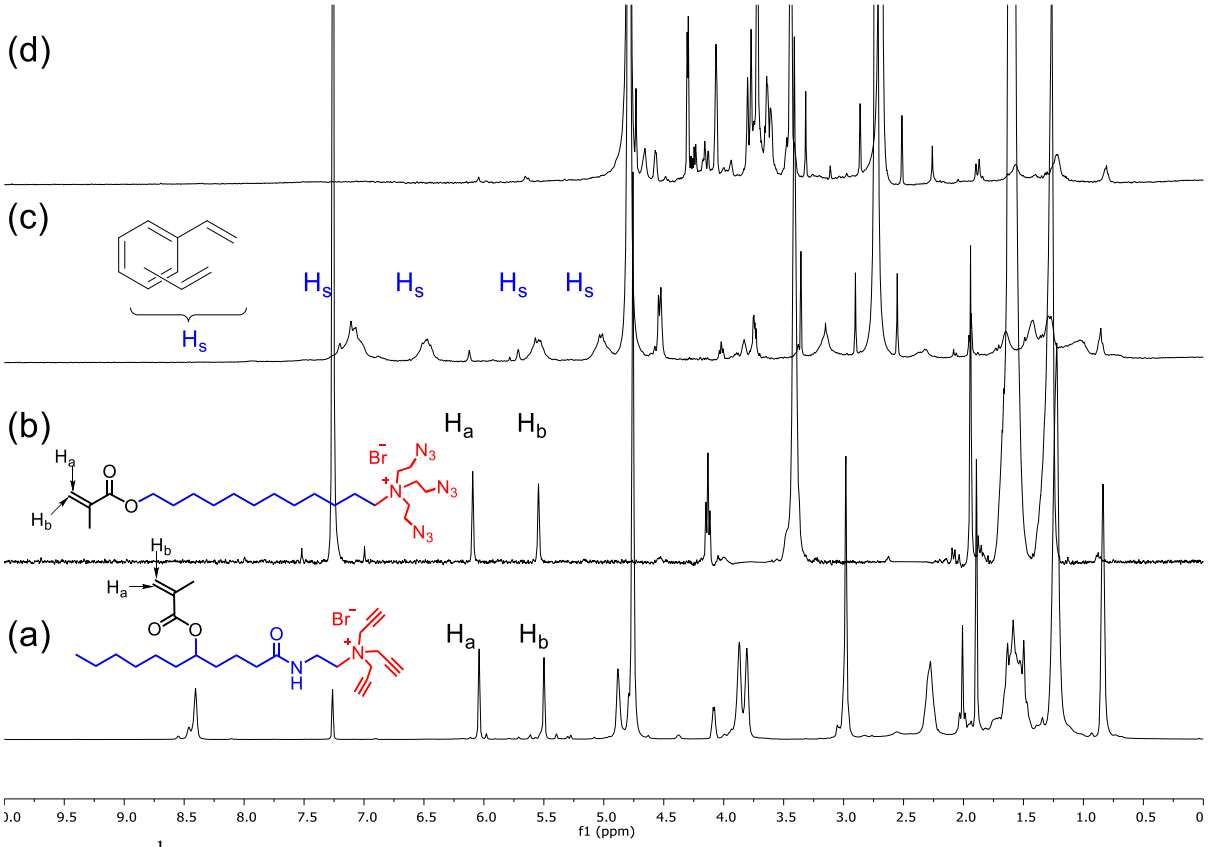

Figure 43. ^{1}H NMR spectra of (a) Compound **9** in $CDCl_3$, (b) Compound **1b** in $CDCl_3$, (c) alkynyl-SCM in D_2O, and (d) MINP(maltulose) in D_2O at 298 K. The data correspond to entry 7 in Table 5.

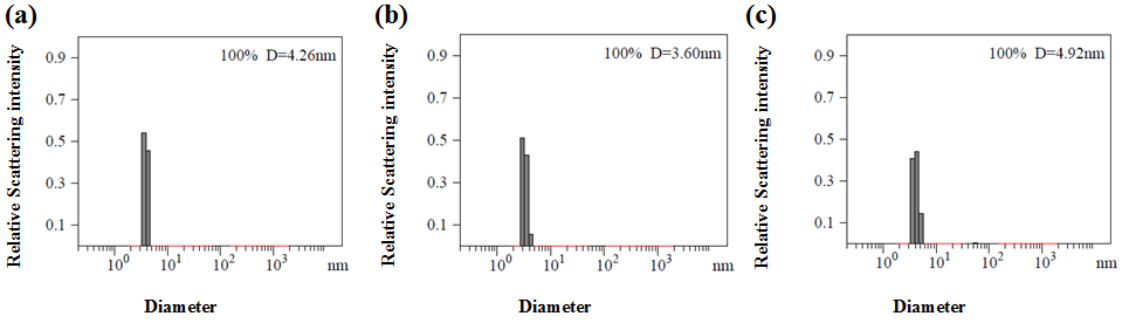

Figure 44. Distribution of the hydrodynamic diameters of the nanoparticles in water as determined by DLS for the synthesis of MINP(maltulose) (a) alkynyl-SCM, (b) core-cross-linked-SCM, and (c) surface-functionalized MINP(maltulose) after purification. The data correspond to entry 7 in Table 5.

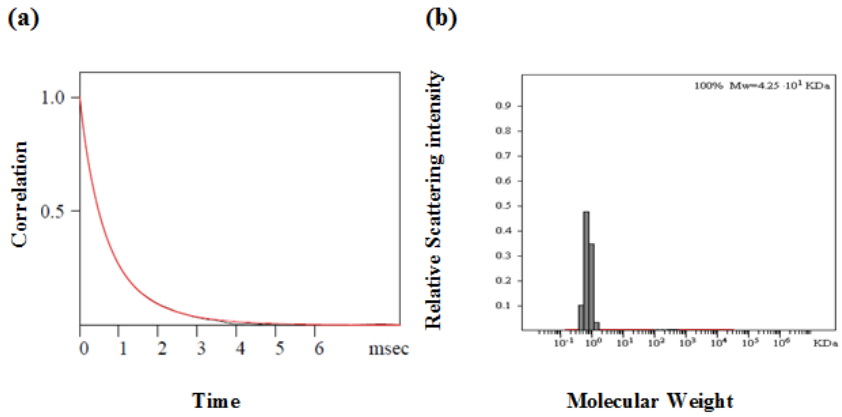

Figure 45. The correlation curve and the distribution of the molecular weight for MINP(maltulose) from the DLS The data correspond to entry 7 in Table 5. The PRECISION DECONVOLVE program assumes the intensity of scattering is proportional to the mass of the particle squared. If each unit of building block for the MINP(maltulose) is assumed to contain 0.4 molecules of compound **1b** (MW = 558 g/mol), 0.6 molecules of compound **9** (MW = 508 g/mol), 0.6 molecules of compound **4** (MW = 264 g/mol), one molecule of DVB (MW = 130 g/mol), and 0.04 molecules of 6-vinylbenzoxaborole (MW = 160 g/mol), the molecular weight of MINP(maltulose) translates to 52 [= 42500 / (0.4×558 +0.6×508 +0.6×264 +130 +0.04×160)] of such units.

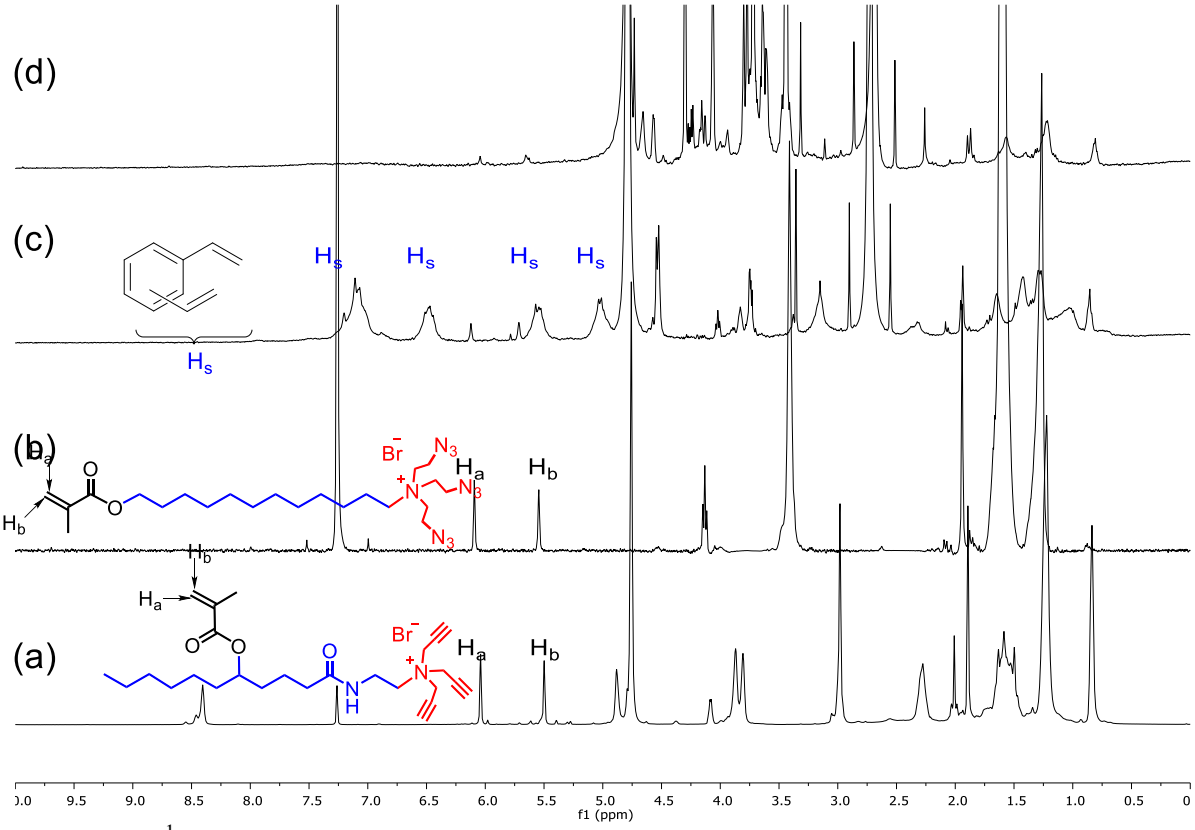

Figure 46. ^{1}H NMR spectra of (a) Compound **9** in $CDCl_3$, (b) Compound **1b** in $CDCl_3$, (c) alkynyl-SCM in D_2O, and (d) MINP(lactose) in D_2O at 298 K. The data correspond to entry 8 in Table 5.

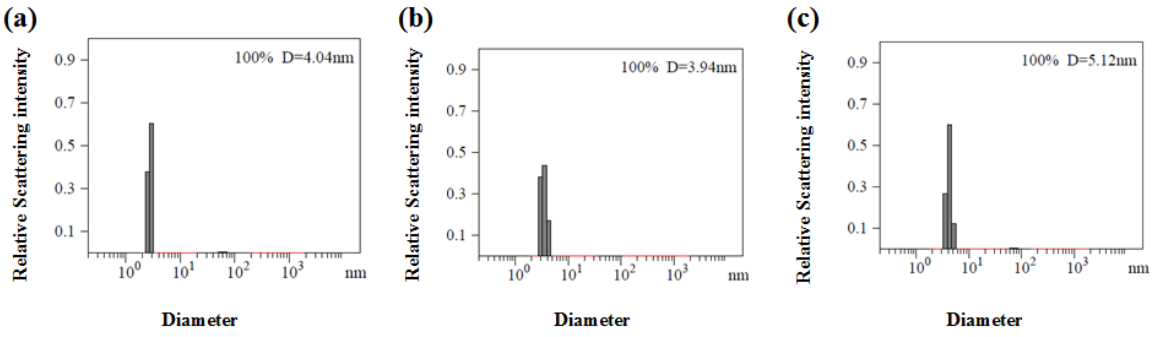

Figure 47. Distribution of the hydrodynamic diameters of the nanoparticles in water as determined by DLS for the synthesis of MINP(lactose) (a) alkynyl-SCM, (b) core-cross-linked-SCM, and (c) surface-functionalized MINP(lactose) after purification. The data correspond to entry 8 in Table 5.

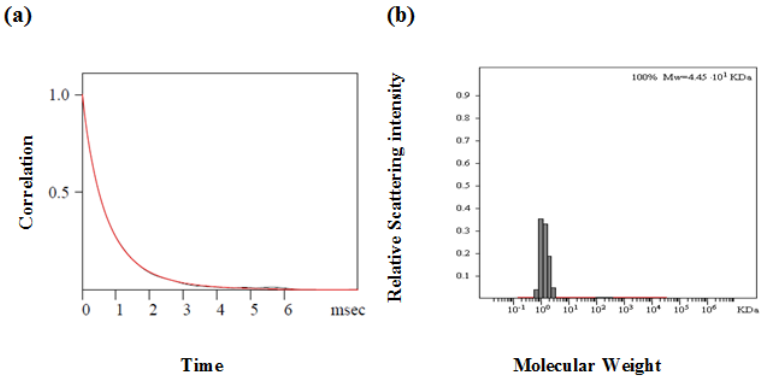

Figure 48. The correlation curve and the distribution of the molecular weight for MINP(lactose) from the DLS The data correspond to entry 8 in Table 5. The PRECISION DECONVOLVE program assumes the intensity of scattering is proportional to the mass of the particle squared. If each unit of building block for the MINP(lactose) is assumed to contain 0.4 molecules of compound **1b** (MW = 558 g/mol), 0.6 molecules of compound **9** (MW = 508 g/mol), 0.6 molecules of compound **4** (MW = 264 g/mol), one molecule of DVB (MW = 130 g/mol), and 0.04 molecules of 6-vinylbenzoxaborole (MW = 160 g/mol), the molecular weight of MINP(lactose) translates to 54 [= 44500 / (0.4×558 +0.6×508 +0.6×264 +130 +0.04×160)] of such units.

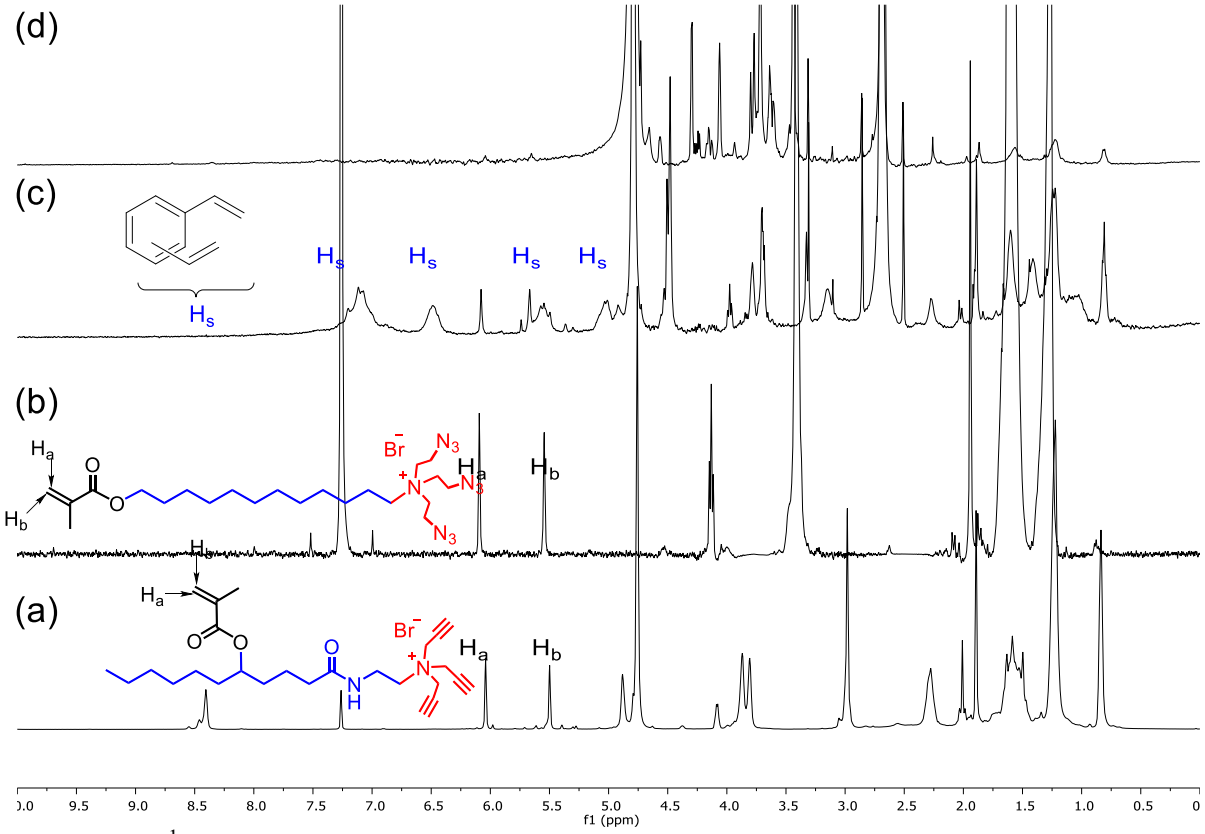

Figure 49. ^{1}H NMR spectra of (a) Compound **9** in $CDCl_3$, (b) Compound **1b** in $CDCl_3$, (c) alkynyl-SCM in D_2O, and (d) MINP(maltotriose) in D_2O at 298 K. The data correspond to entry 9 in Table 5.

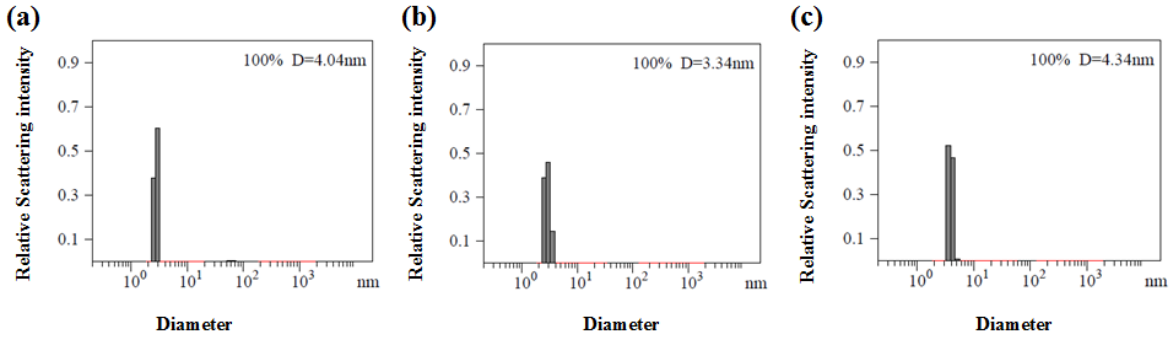

Figure 50. Distribution of the hydrodynamic diameters of the nanoparticles in water as determined by DLS for the synthesis of MINP(maltotriose) (a) alkynyl-SCM, (b) core-cross-linked-SCM, and (c) surface-functionalized MINP(maltotriose) after purification. The data correspond to entry 9 in Table 5.

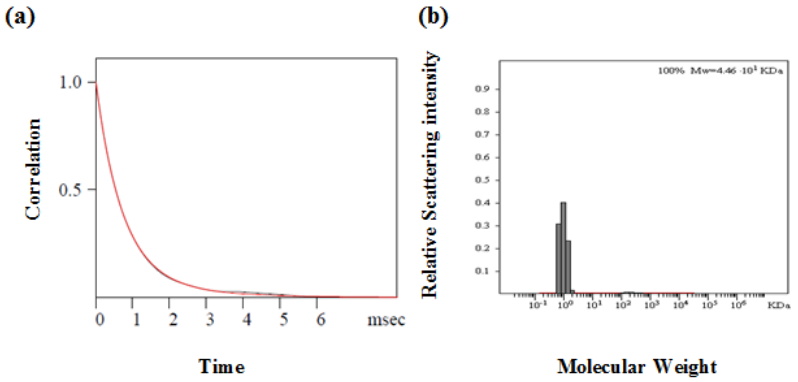

Figure 51. The correlation curve and the distribution of the molecular weight for MINP(maltotriose) from the DLS The data correspond to entry 9 in Table 5. The PRECISION DECONVOLVE program assumes the intensity of scattering is proportional to the mass of the particle squared. If each unit of building block for the MINP(maltotriose) is assumed to contain 0.4 molecules of compound **1b** (MW = 558 g/mol), 0.6 molecules of compound **9** (MW = 508 g/mol), 0.6 molecules of compound **4** (MW = 264 g/mol), one molecule of DVB (MW = 130 g/mol), and 0.04 molecules of 6-vinylbenzoxaborole (MW = 160 g/mol), the molecular weight of MINP(maltotriose) translates to 54 [= 44600 / (0.4×558 +0.6×508 +0.6×264 +130 +0.04×160)] of such units.

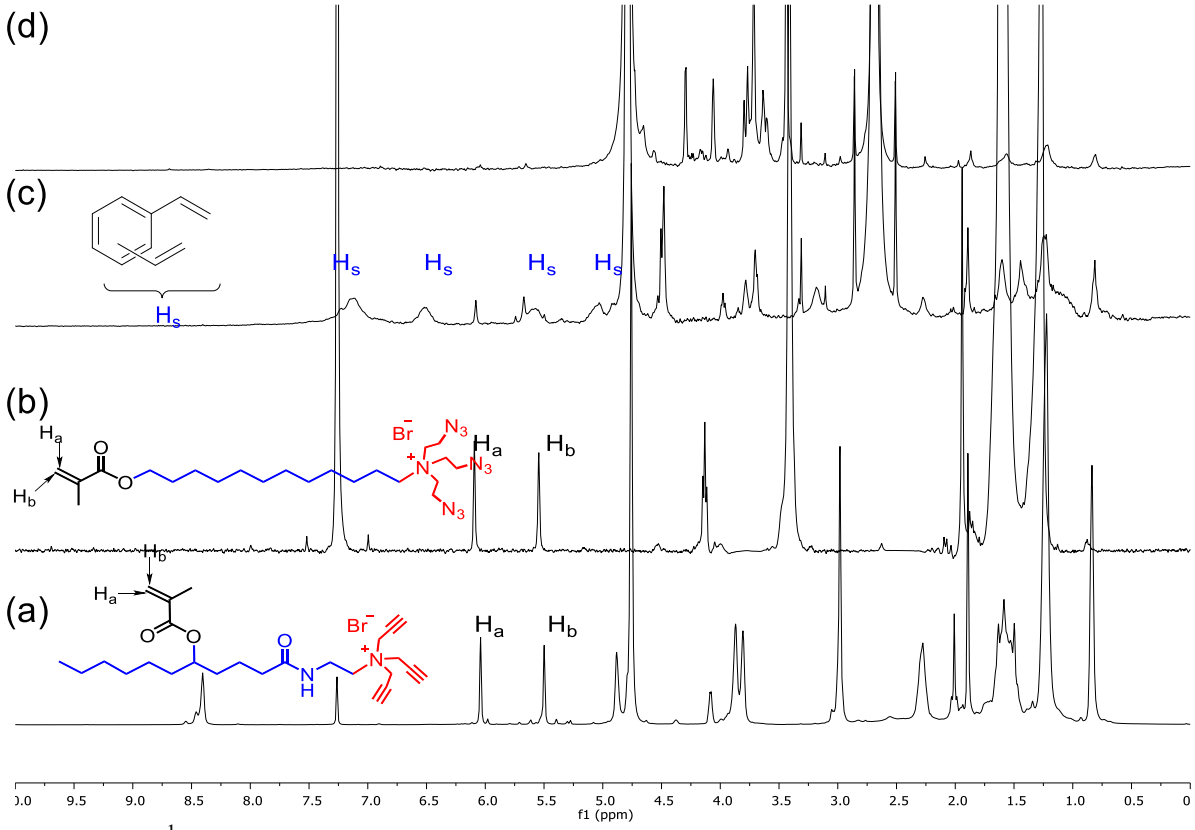

Figure 52. ^{1}H NMR spectra of (a) Compound **9** in $CDCl_3$, (b) Compound **1b** in $CDCl_3$, (c) alkynyl-SCM in D_2O, and (d) MINP(sugar H) in D_2O at 298 K. The data correspond to entry 10 in Table 5.

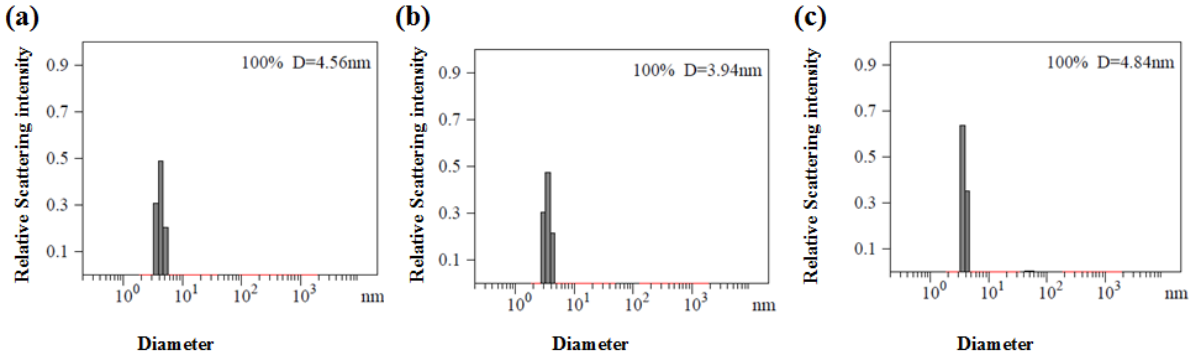

Figure 53. Distribution of the hydrodynamic diameters of the nanoparticles in water as determined by DLS for the synthesis of MINP(sugar H) (a) alkynyl-SCM, (b) core-cross-linked-SCM, and (c) surface-functionalized MINP(sugar H) after purification. The data correspond to entry 10 in Table 5.

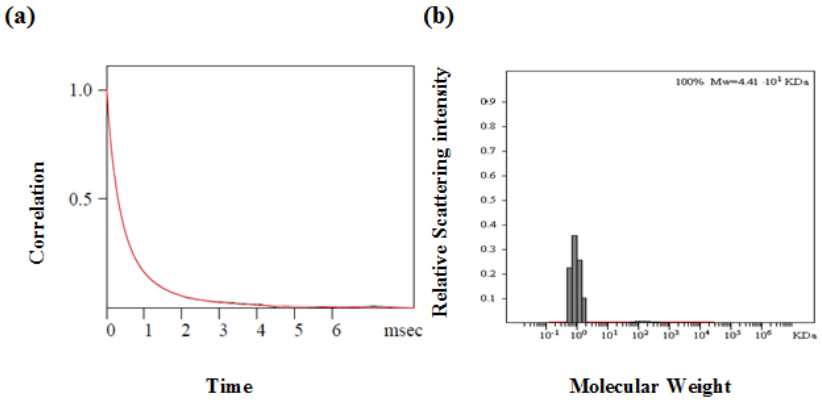

Figure 54. The correlation curve and the distribution of the molecular weight for MINP(sugar H) from the DLS. The data correspond to entry 10 in Table 5. The PRECISION DECONVOLVE program assumes the intensity of scattering is proportional to the mass of the particle squared. If each unit of building block for the MINP(sugar H) is assumed to contain 0.4 molecules of compound **1b** (MW = 558 g/mol), 0.6 molecules of compound **9** (MW = 508 g/mol), 0.6 molecules of compound **4** (MW = 264 g/mol), one molecule of DVB (MW = 130 g/mol), and 0.06 molecules of 6-vinylbenzoxaborole (MW = 160 g/mol), the molecular weight of MINP(sugar H) translates to 53 [= 44100 / (0.4×558 +0.6×508 +0.6×264 +130 +0.06×160)] of such units.

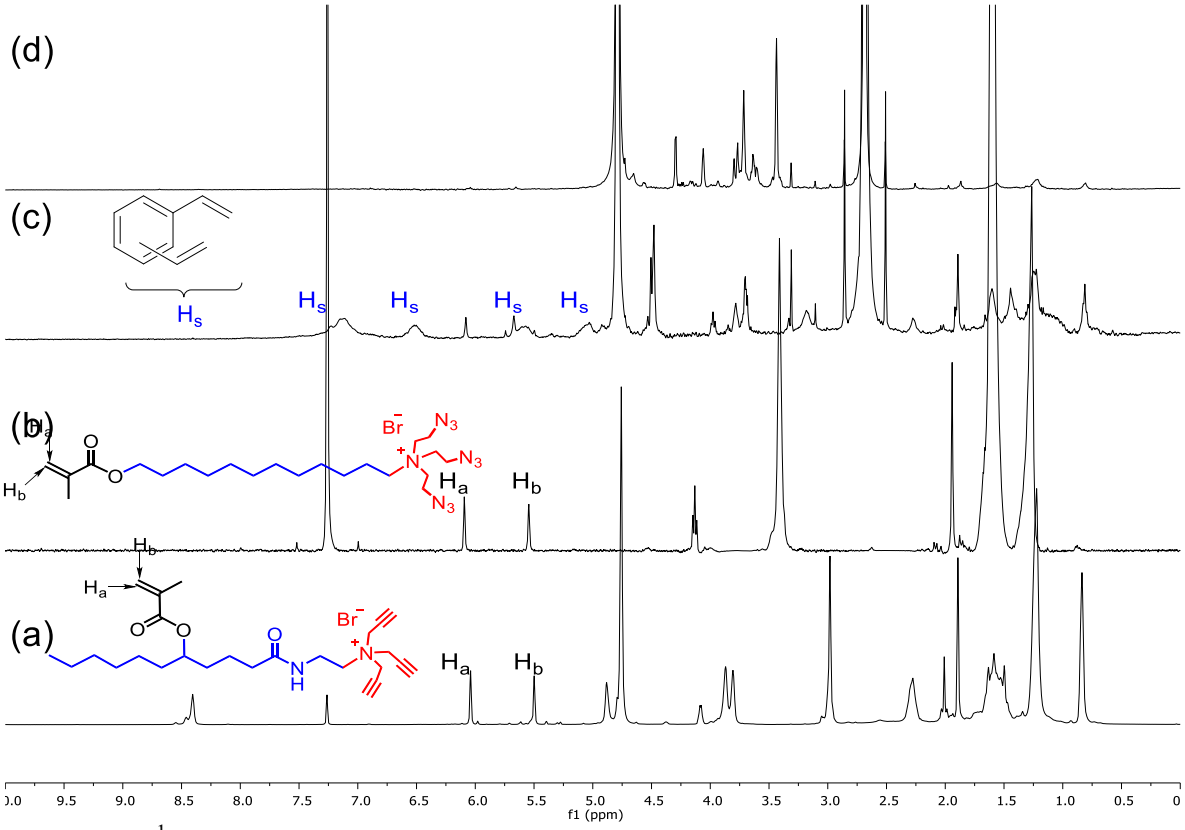

Figure 55. ^{1}H NMR spectra of (a) Compound **9** in $CDCl_3$, (b) Compound **1b** in $CDCl_3$, (c) alkynyl-SCM in D_2O, and (d) MINP(sugar A) in D_2O at 298 K. The data correspond to entry 11 in Table 5.

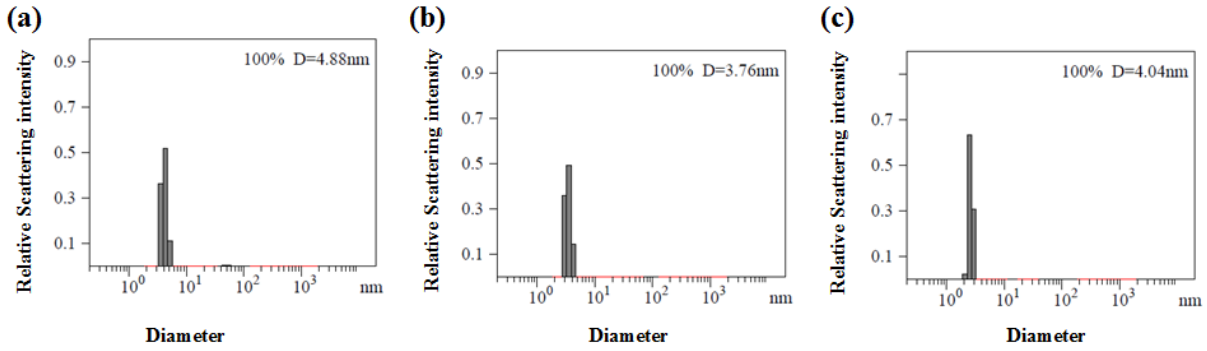

Figure 56. Distribution of the hydrodynamic diameters of the nanoparticles in water as determined by DLS for the synthesis of MINP(sugar A) (a) alkynyl-SCM, (b) core-cross-linked-SCM, and (c) surface-functionalized MINP(sugar A) after purification. The data correspond to entry 11 in Table 5.

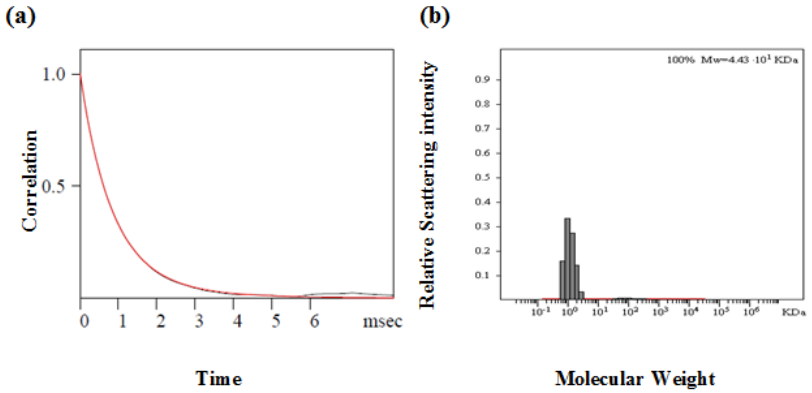

Figure 57. The correlation curve and the distribution of the molecular weight for MINP(sugar A) from the DLS. The data correspond to entry 11 in Table 5. The PRECISION DECONVOLVE program assumes the intensity of scattering is proportional to the mass of the particle squared. If each unit of building block for the MINP(sugar A) is assumed to contain 0.4 molecules of compound **1b** (MW = 558 g/mol), 0.6 molecules of compound **9** (MW = 508 g/mol), 0.6 molecules of compound **4** (MW = 264 g/mol), one molecule of DVB (MW = 130 g/mol), and 0.06 molecules of 6-vinylbenzoxaborole (MW = 160 g/mol), the molecular weight of MINP(sugar A) translates to 54 [= 44300 / (0.4×558 +0.6×508 +0.6×264 +130 +0.06×160)] of such units.

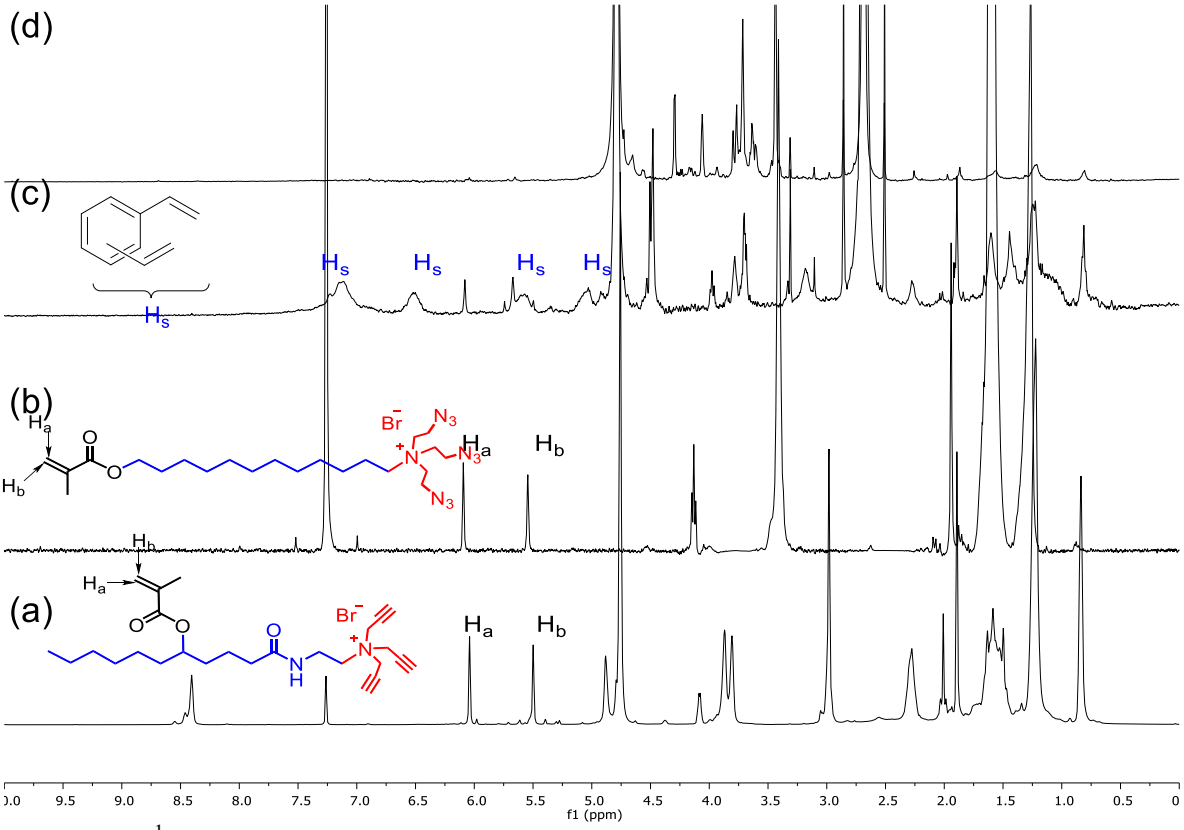

Figure 58. ^{1}H NMR spectra of (a) Compound **9** in $CDCl_3$, (b) Compound **1b** in $CDCl_3$, (c) alkynyl-SCM in D_2O, and (d) MINP(sugar B) in D_2O at 298 K. The data correspond to entry 12 in Table 5.

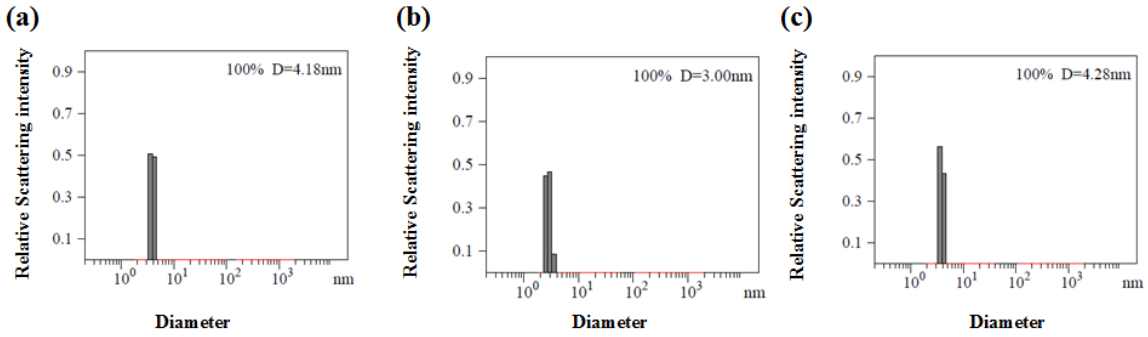

Figure 59. Distribution of the hydrodynamic diameters of the nanoparticles in water as determined by DLS for the synthesis of MINP(sugar B) (a) alkynyl-SCM, (b) core-cross-linked-SCM, and (c) surface-functionalized MINP(sugar B) after purification. The data correspond to entry 12 in Table 5.

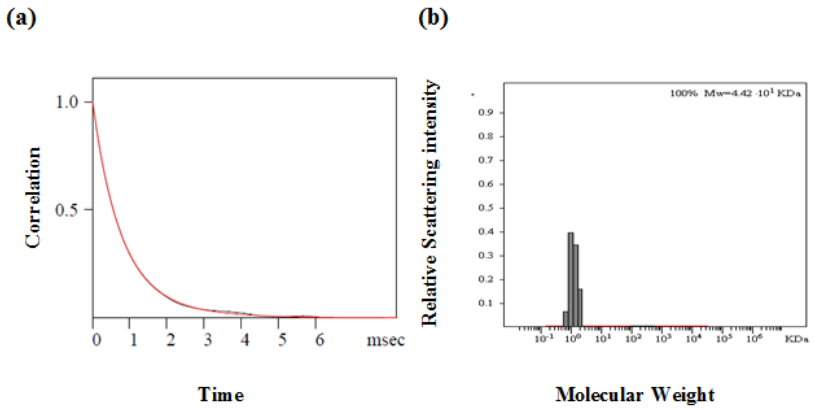

Figure 60. The correlation curve and the distribution of the molecular weight for MINP(sugar B) from the DLS. The data correspond to entry 12 in Table 5. The PRECISION DECONVOLVE program assumes the intensity of scattering is proportional to the mass of the particle squared. If each unit of building block for the MINP(sugar B) is assumed to contain 0.4 molecules of compound **1b** (MW = 558 g/mol), 0.6 molecules of compound **9** (MW = 508 g/mol), 0.6 molecules of compound **4** (MW = 264 g/mol), one molecule of DVB (MW = 130 g/mol), and 0.06 molecules of 6-vinylbenzoxaborole (MW = 160 g/mol), the molecular weight of MINP(sugar B) translates to 53 [= 44200 / (0.4×558 +0.6×508 +0.6×264 +130 +0.06×160)] of such units.

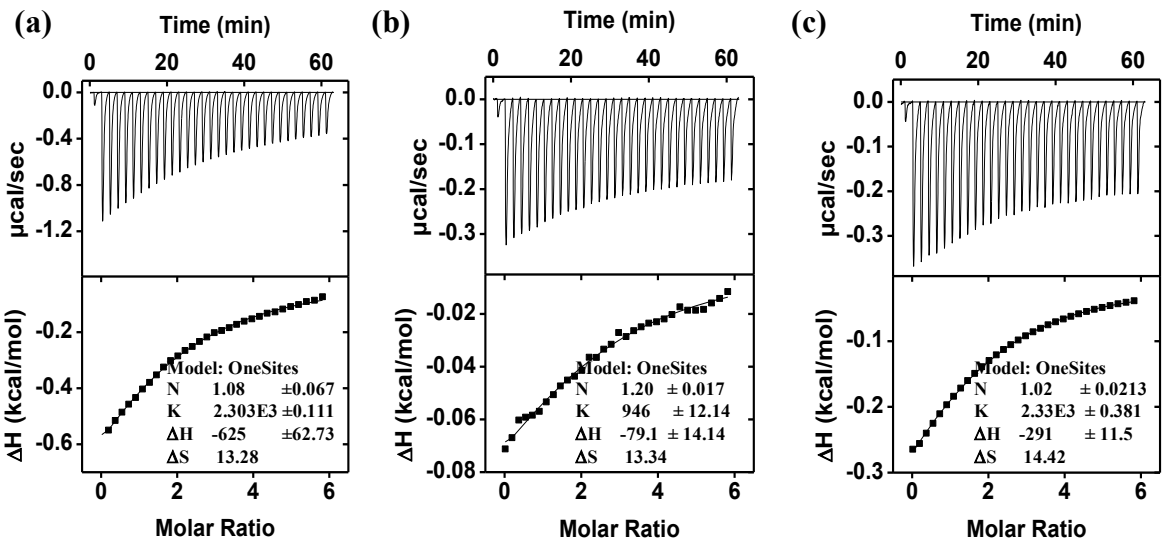

Figure 61. ITC titration curves obtained at 298 K for the titration of MINP(glucose) with (a) glucose/FM **3** = 1:2, (b) glucose/FM **3** = 1:1, and (c) glucose/FM **3** = 1:3 in 10 mM HEPES buffer (pH 7.4). The data correspond to entries 1–3, respectively, in Table 1. The top panel shows the raw calorimetric data. The area under each peak represents the amount of heat generated at each ejection and is plotted against the molar ratio of MINP to the substrate. The solid line is the best fit of the experimental data to the sequential binding of N equal and independent binding sites on the MINP. The heat of dilution for the substrate, obtained by adding the substrate to the buffer, was subtracted from the heat released during the binding. Binding parameters were auto-generated after curve fitting using Microcal Origin 7.

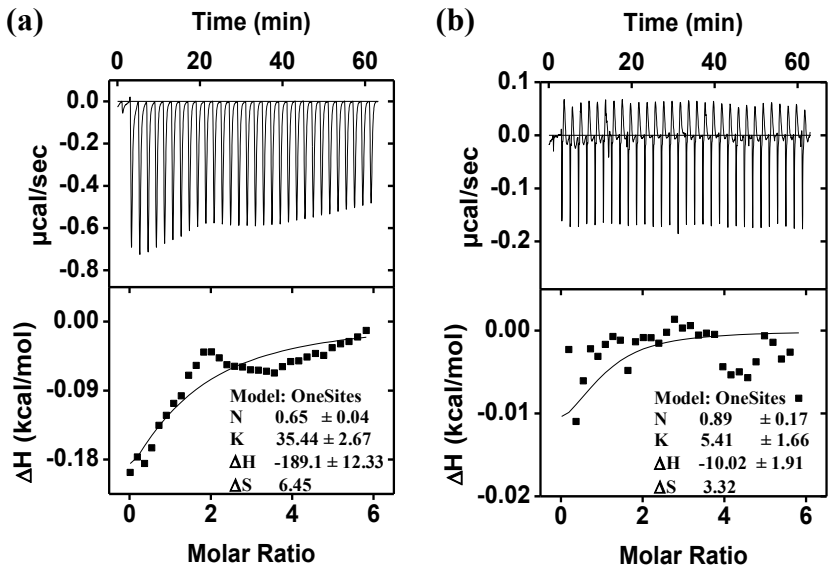

Figure 62. ITC titration curves obtained at 298 K for the titration of (a) NINP without FM **3** and the glucose template and (b) NINP with FM **3** but without the glucose template in 10 mM HEPES buffer (pH 7.4). The data correspond to entries 4–5, respectively, in Table 1. The top panel shows the raw calorimetric data. The area under each peak represents the amount of heat generated at each ejection and is plotted against the molar ratio of MINP to the substrate. The solid line is the best fit of the experimental data to the sequential binding of N equal and independent binding sites on the MINP. The heat of dilution for the substrate, obtained by adding the substrate to the buffer, was subtracted from the heat released during the binding. Binding parameters were auto-generated after curve fitting using Microcal Origin 7.

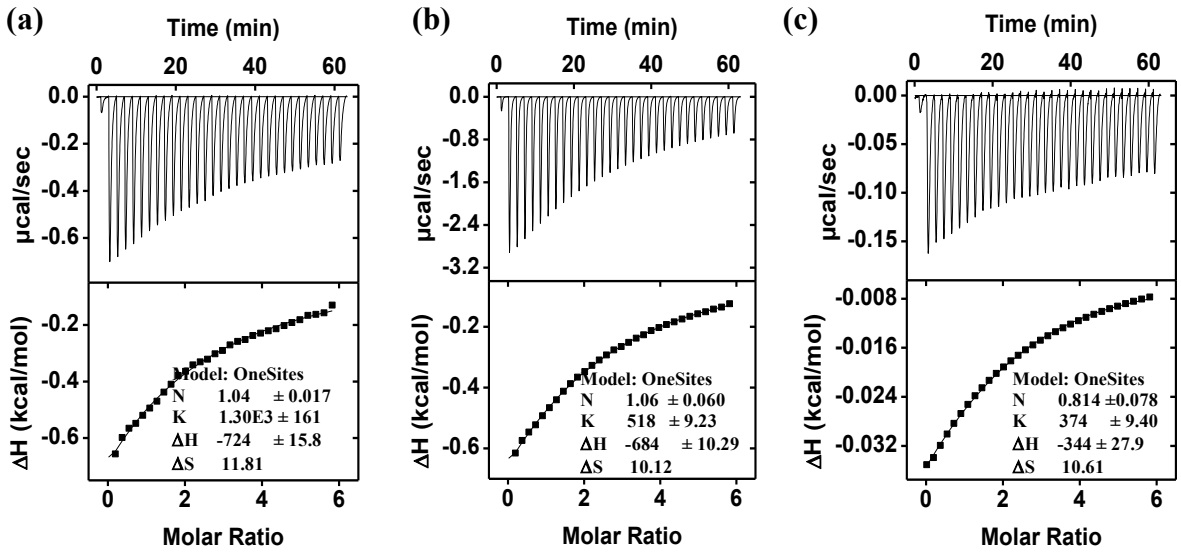

Figure 63. ITC titration curves obtained at 298 K for the titration of MINP(glucose) with glucose at pH 8.5 (a), glucose at pH 6.5 (b), and allose at pH 7.4 (c) in 10 mM HEPES buffer (template/FM **3** = 1:2). The data correspond to entries 6–8, respectively, in Table 1. The top panel shows the raw calorimetric data. The area under each peak represents the amount of heat generated at each ejection and is plotted against the molar ratio of MINP to the substrate. The solid line is the best fit of the experimental data to the sequential binding of N equal and independent binding sites on the MINP. The heat of dilution for the substrate, obtained by adding the substrate to the buffer, was subtracted from the heat released during the binding. Binding parameters were auto-generated after curve fitting using Microcal Origin 7.

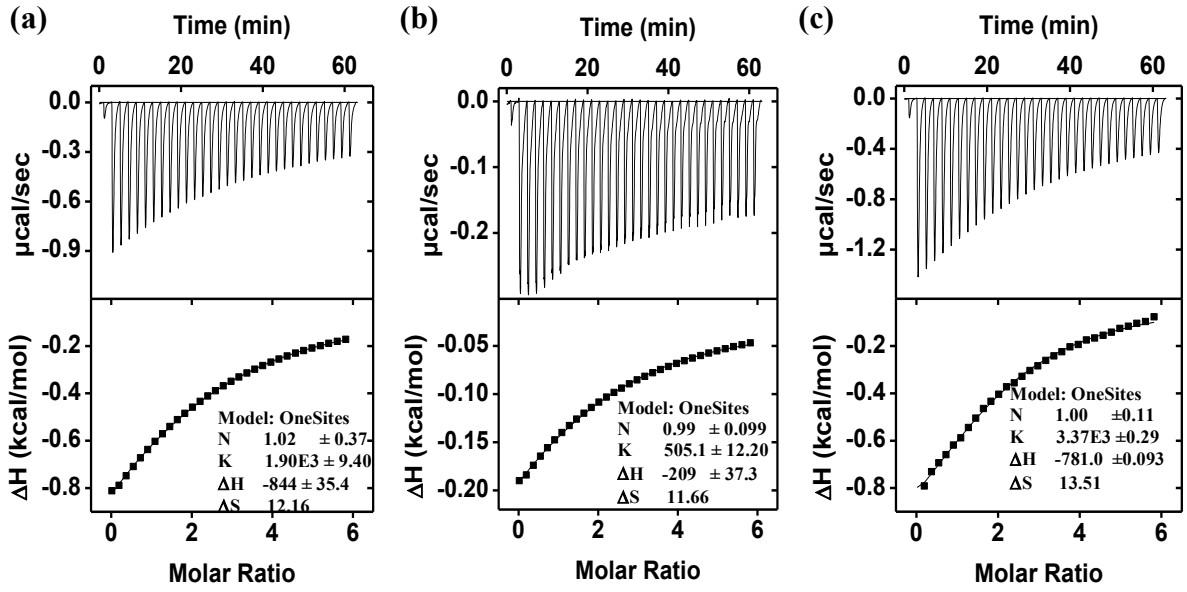

Figure 64. ITC titration curves obtained at 298 K for the titration of (a) MINP(mannose) with mannose, (b) MINP(mannose) with altrose, and (c) MINP(galactose) with galactose in 10 mM HEPES buffer (pH 7.4, template/FM **3** = 1:2). The data correspond to entries 9–11, respectively, in Table 1. The top panel shows the raw calorimetric data. The area under each peak represents the amount of heat generated at each ejection and is plotted against the molar ratio of MINP to the substrate. The solid line is the best fit of the experimental data to the sequential binding of N equal and independent binding sites on the MINP. The heat of dilution for the substrate, obtained by adding the substrate to the buffer, was subtracted from the heat released during the binding. Binding parameters were auto-generated after curve fitting using Microcal Origin 7.

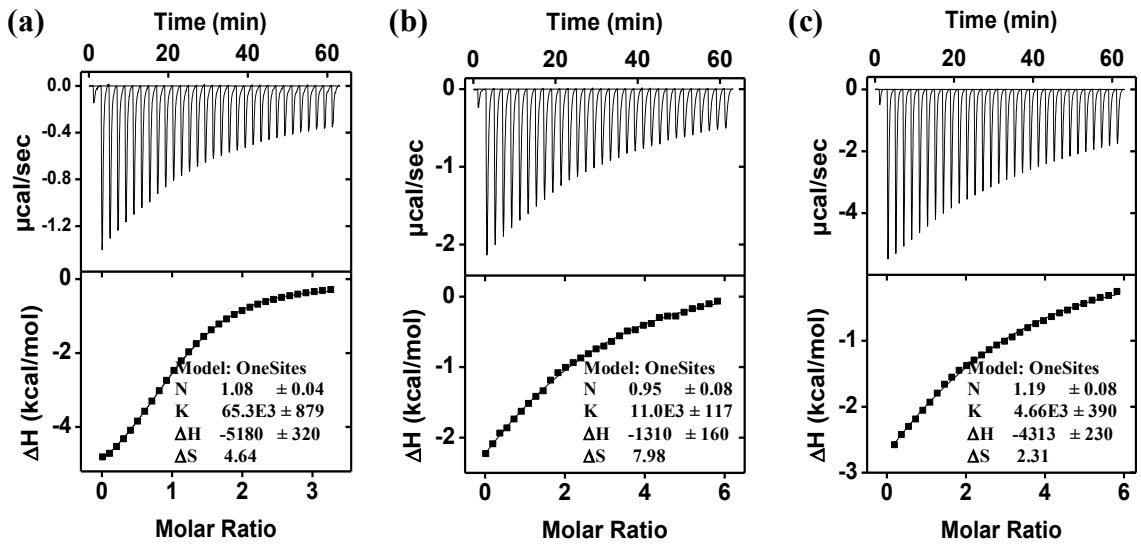

Figure 65. ITC titration curves obtained at 298 K for the titration of MINP(**5**) with **5** (a), **6** (b), and **7** (c) in 10 mM HEPES buffer (pH 7.4, template/FM **3** = 1:1). The data correspond to entries 12–14, respectively, in Table 1. The top panel shows the raw calorimetric data. The area under each peak represents the amount of heat generated at each ejection and is plotted against the molar ratio of MINP to the substrate. The solid line is the best fit of the experimental data to the sequential binding of N equal and independent binding sites on the MINP. The heat of dilution for the substrate, obtained by adding the substrate to the buffer, was subtracted from the heat released during the binding. Binding parameters were auto-generated after curve fitting using Microcal Origin 7.

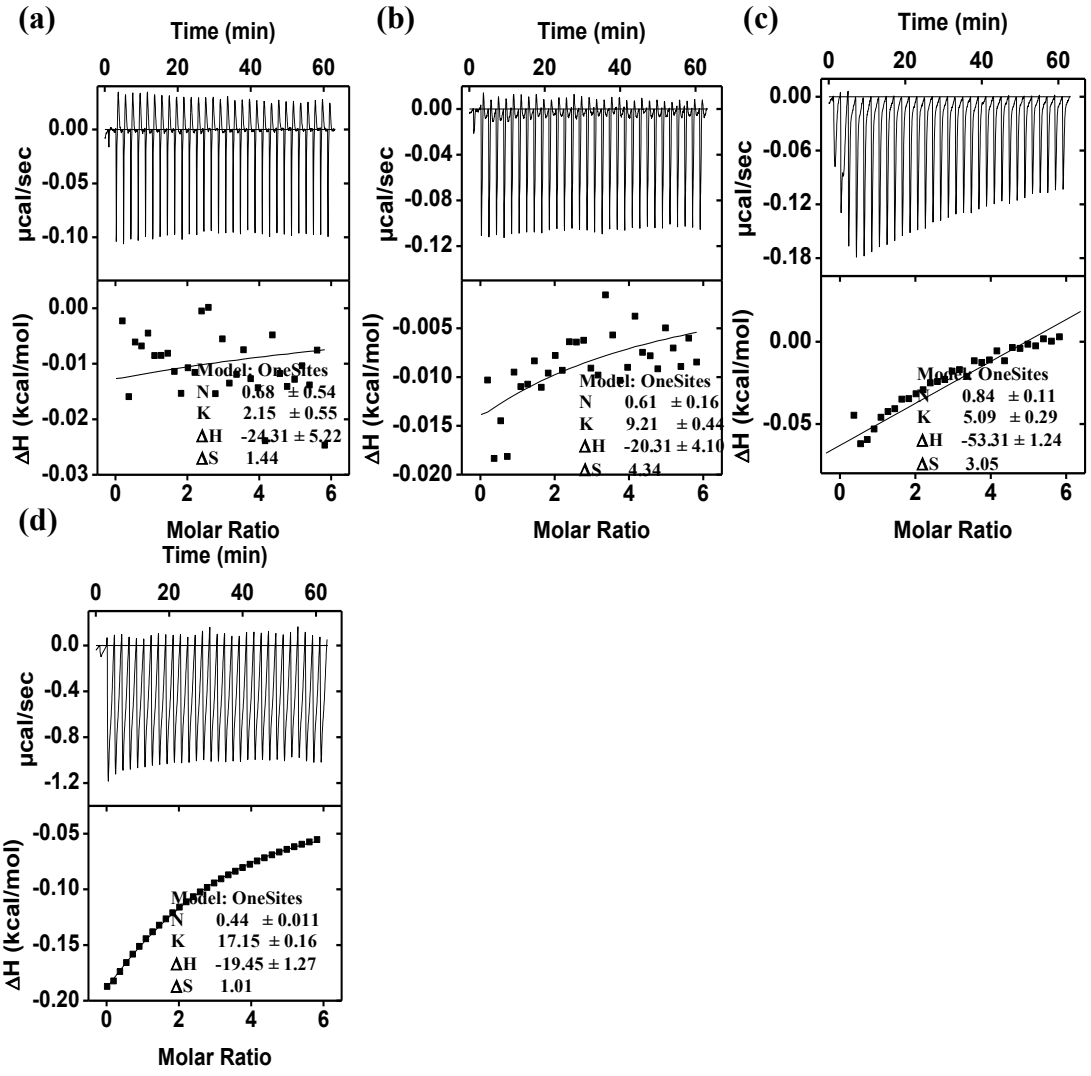

Figure 66. ITC titration curves obtained at 298 K for the titration of MINP(glucose) with mannose (a), galactose (b), altrose (c), and gulose (d) in 10 mM HEPES buffer (pH 7.4, glucose/FM **3** = 1:2). The top panel shows the raw calorimetric data. The area under each peak represents the amount of heat generated at each ejection and is plotted against the molar ratio of MINP to the substrate. The solid line is the best fit of the experimental data to the sequential binding of N equal and independent binding sites on the MINP. The heat of dilution for the substrate, obtained by adding the substrate to the buffer, was subtracted from the heat released during the binding. Binding parameters were auto-generated after curve fitting using Microcal Origin 7.

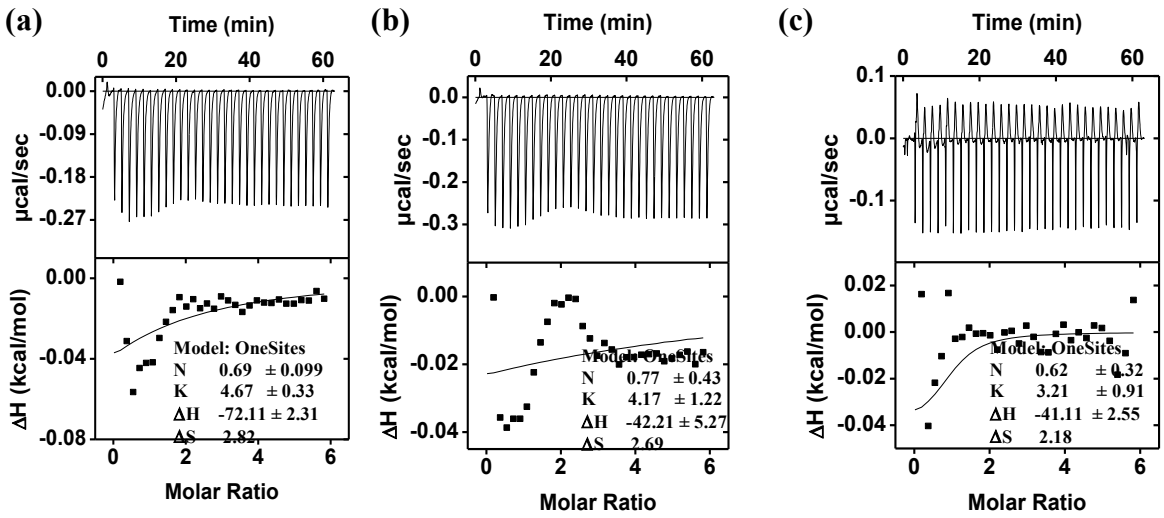

Figure 67. ITC titration curves obtained at 298 K for the titration of MINP(glucose) with talose (a), idose (b), and xylose (c) in 10 mM HEPES buffer (pH 7.4, glucose/FM **3** = 1:2). The top panel shows the raw calorimetric data. The area under each peak represents the amount of heat generated at each ejection and is plotted against the molar ratio of MINP to the substrate. The solid line is the best fit of the experimental data to the sequential binding of N equal and independent binding sites on the MINP. The heat of dilution for the substrate, obtained by adding the substrate to the buffer, was subtracted from the heat released during the binding. Binding parameters were auto-generated after curve fitting using Microcal Origin 7.

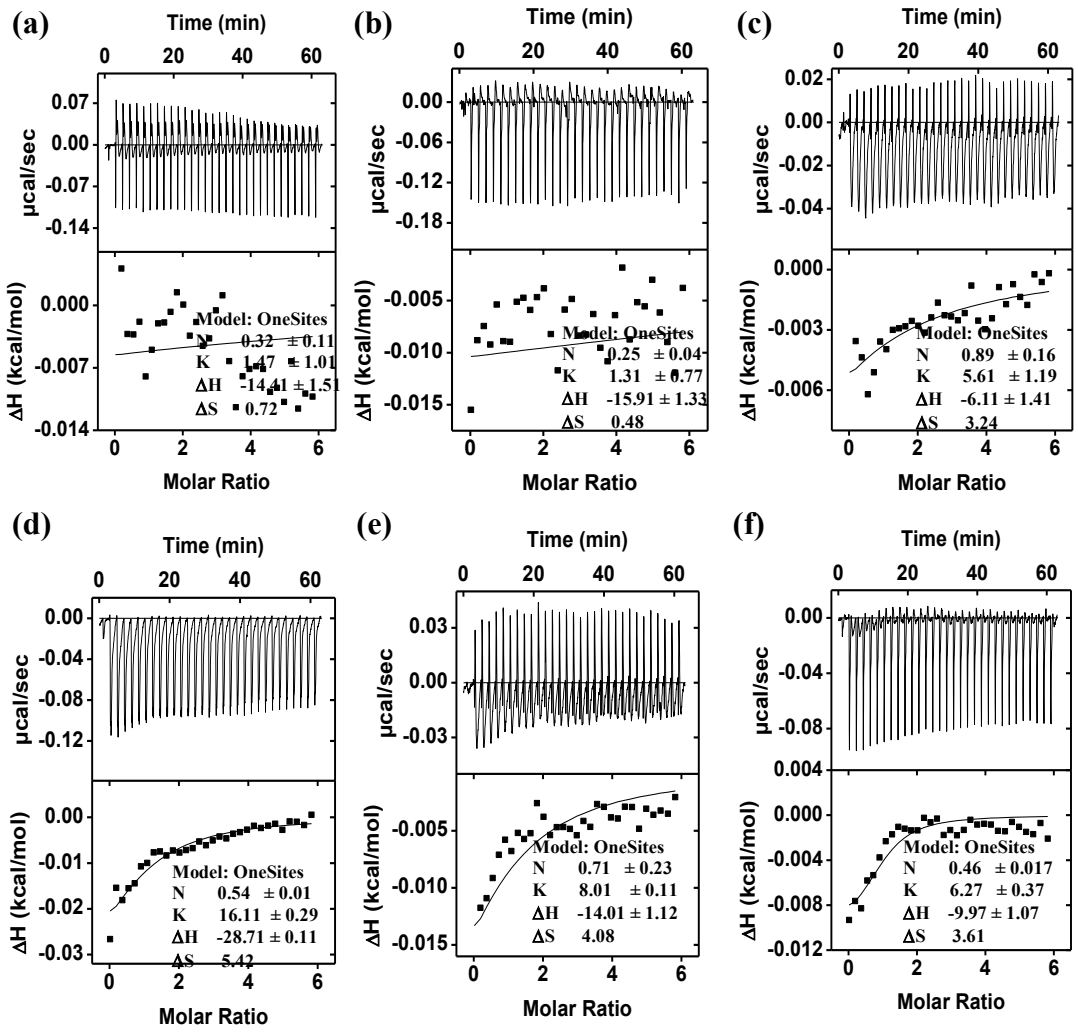

Figure 68. ITC titration curves obtained at 298 K for the titration of MINP(mannose) with glucose (a), allose (b), galactose (c), gulose (d), talose (e), and idose (f) in 10 mM HEPES buffer (pH 7.4, mannose/FM **3** =1:2). The top panel shows the raw calorimetric data. The area under each peak represents the amount of heat generated at each ejection and is plotted against the molar ratio of MINP to the substrate. The solid line is the best fit of the experimental data to the sequential binding of N equal and independent binding sites on the MINP. The heat of dilution for the substrate, obtained by adding the substrate to the buffer, was subtracted from the heat released during the binding. Binding parameters were auto-generated after curve fitting using Microcal Origin 7.

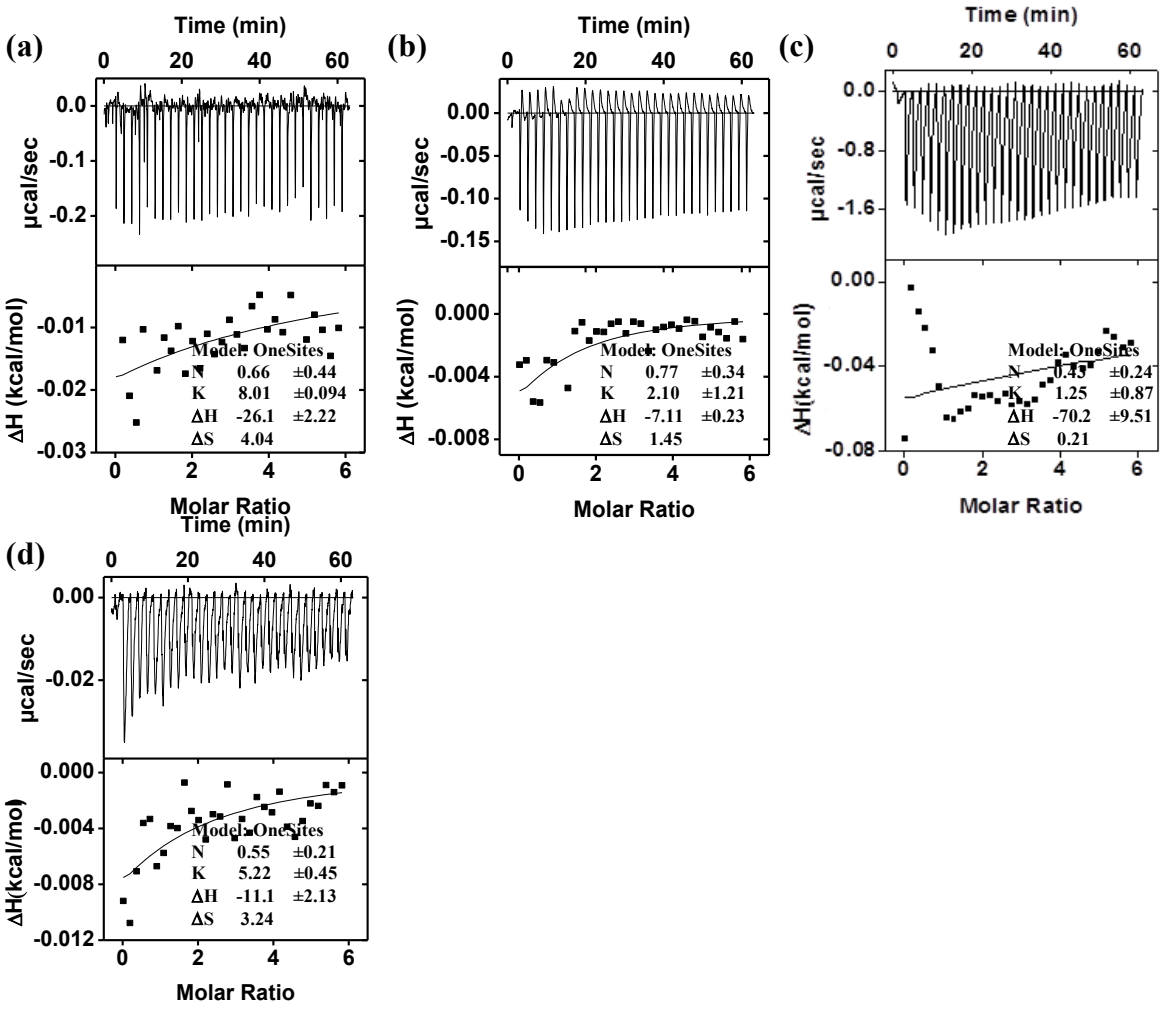

Figure 69. ITC titration curves obtained at 298 K for the titration of MINP(galactose) with glucose (a), mannose (b), allose (c), and altrose (d) in 10 mM HEPES buffer (pH 7.4, galactose/FM **3** = 1:2). The top panel shows the raw calorimetric data. The area under each peak represents the amount of heat generated at each ejection and is plotted against the molar ratio of MINP to the substrate. The solid line is the best fit of the experimental data to the sequential binding of N equal and independent binding sites on the MINP. The heat of dilution for the substrate, obtained by adding the substrate to the buffer, was subtracted from the heat released during the binding. Binding parameters were auto-generated after curve fitting using Microcal Origin 7.

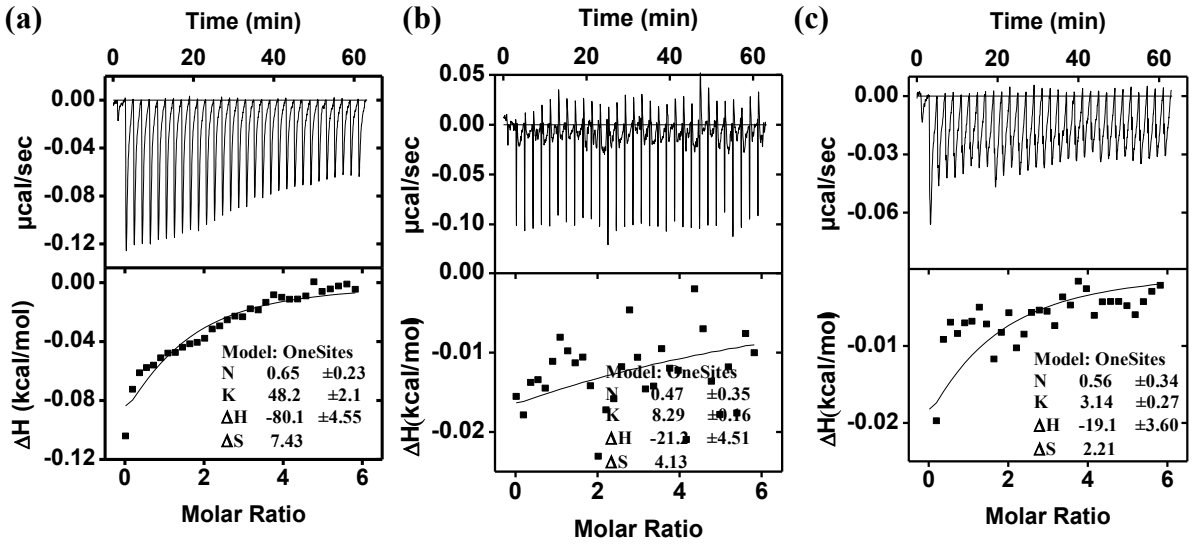

Figure 70. ITC titration curves obtained at 298 K for the titration of MINP(galactose) with gulose (a), talose (b), and idose (c) in 10 mM HEPES buffer (pH 7.4, galactose/FM **3** = 1:2). The top panel shows the raw calorimetric data. The area under each peak represents the amount of heat generated at each ejection and is plotted against the molar ratio of MINP to the substrate. The solid line is the best fit of the experimental data to the sequential binding of N equal and independent binding sites on the MINP. The heat of dilution for the substrate, obtained by adding the substrate to the buffer, was subtracted from the heat released during the binding. Binding parameters were auto-generated after curve fitting using Microcal Origin 7.

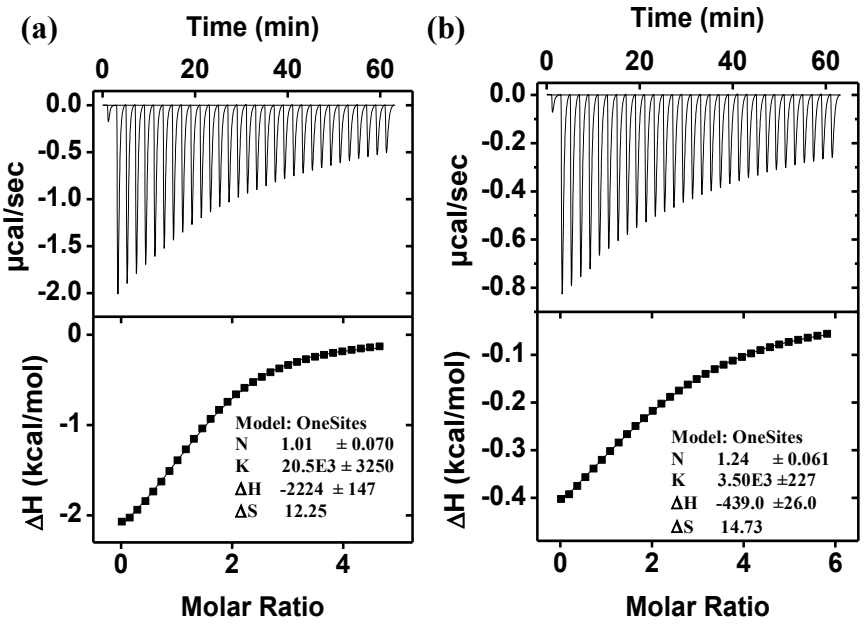

Figure 71. ITC titration curves obtained at 298 K for the titration of (a) MINP(maltose) prepared with cross-linkable surfactants compound **9**/compound **1b** and (b) MINP(maltose) prepared with cross-linkable surfactants compound **1a**/compound **1b** by maltose in 10 mM HEPES buffer (pH 7.4, maltose/FM **3** = 1:2). The data correspond to entries 1–2, respectively, in Table 2. The top panel shows the raw calorimetric data. The area under each peak represents the amount of heat generated at each ejection and is plotted against the molar ratio of MINP to the substrate. The solid line is the best fit of the experimental data to the sequential binding of N equal and independent binding sites on the MINP. The heat of dilution for the substrate, obtained by adding the substrate to the buffer, was subtracted from the heat released during the binding. Binding parameters were auto-generated after curve fitting using Microcal Origin 7.

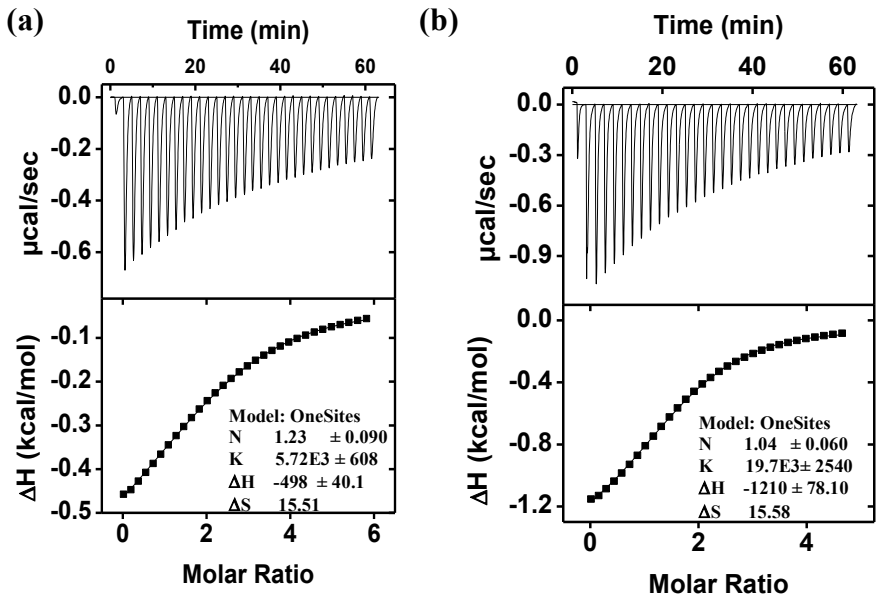

Figure 72. ITC titration curves obtained at 298 K for the titration of MINP(maltose) with (a) maltose/FM **3** = 1:1 and (b) maltose/FM **3** = 1:3 in 10 mM HEPES buffer (pH 7.4). The data correspond to entries 3–4, respectively, in Table 2. The top panel shows the raw calorimetric data. The area under each peak represents the amount of heat generated at each ejection and is plotted against the molar ratio of MINP to the substrate. The solid line is the best fit of the experimental data to the sequential binding of N equal and independent binding sites on the MINP. The heat of dilution for the substrate, obtained by adding the substrate to the buffer, was subtracted from the heat released during the binding. Binding parameters were auto-generated after curve fitting using Microcal Origin 7.

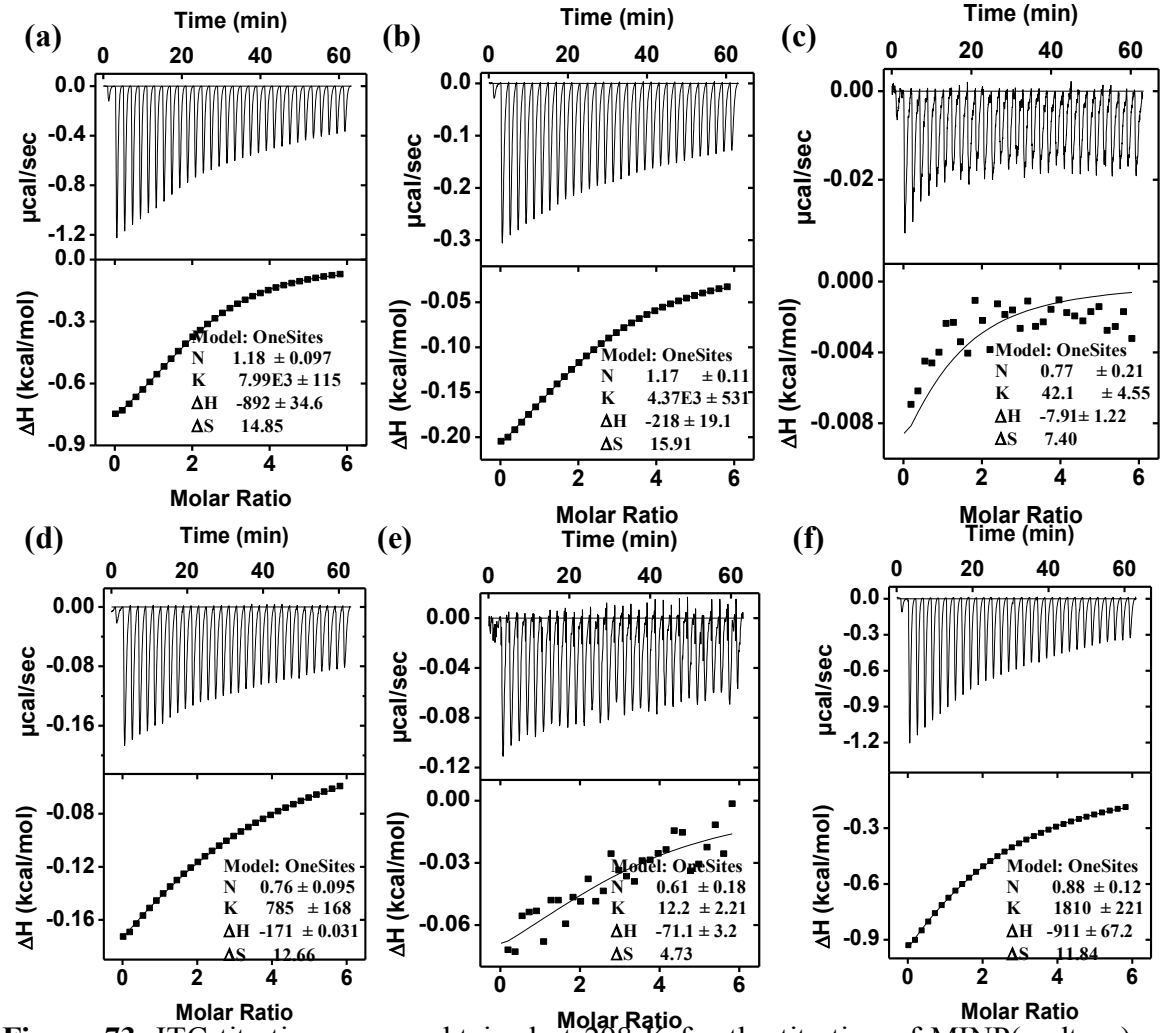

Figure 73. ITC titration curves obtained at 298 K for the titration of MINP(maltose) with cellobiose (a), gentiobiose (b), maltulose (c), lactose (d), maltotriose (e), and glucose (f) in 10 mM HEPES buffer (pH 7.4, maltose/FM **3** = 1:2). The data correspond to entries 5–10, respectively, in Table 2. The top panel shows the raw calorimetric data. The area under each peak represents the amount of heat generated at each ejection and is plotted against the molar ratio of MINP to the substrate. The solid line is the best fit of the experimental data to the sequential binding of N equal and independent binding sites on the MINP. The heat of dilution for the substrate, obtained by adding the substrate to the buffer, was subtracted from the heat released during the binding. Binding parameters were auto-generated after curve fitting using Microcal Origin 7.

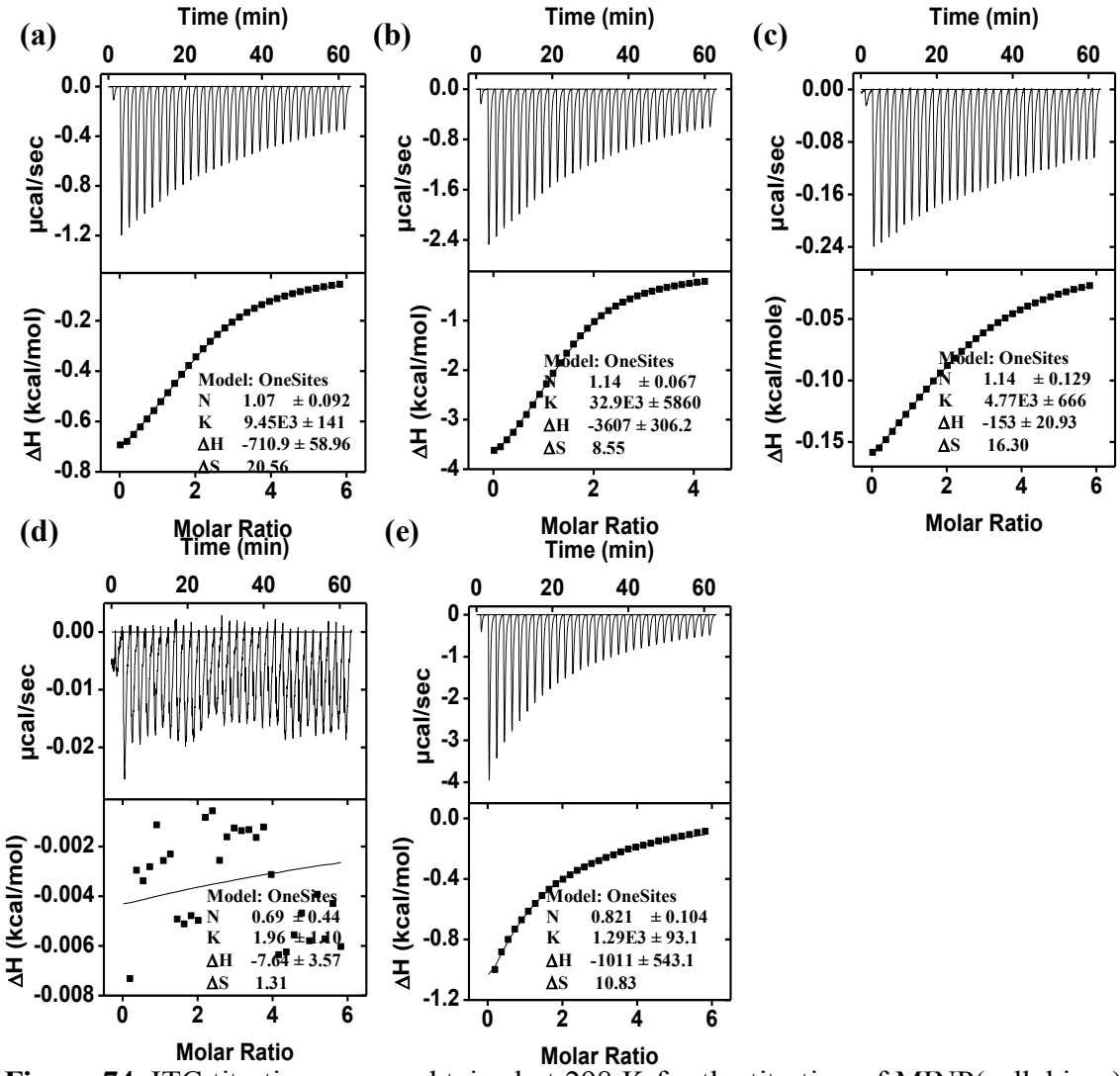

Figure 74. ITC titration curves obtained at 298 K for the titration of MINP(cellobiose) with maltose (a), cellobiose (b), gentiobiose (c), maltulose (d), and lactose (e) in 10 mM HEPES buffer (pH 7.4, cellobiose/FM **3** = 1:2). The data correspond to entries 11–15, respectively, in Table 2. The top panel shows the raw calorimetric data. The area under each peak represents the amount of heat generated at each ejection and is plotted against the molar ratio of MINP to the substrate. The solid line is the best fit of the experimental data to the sequential binding of N equal and independent binding sites on the MINP. The heat of dilution for the substrate, obtained by adding the substrate to the buffer, was subtracted from the heat released during the binding.

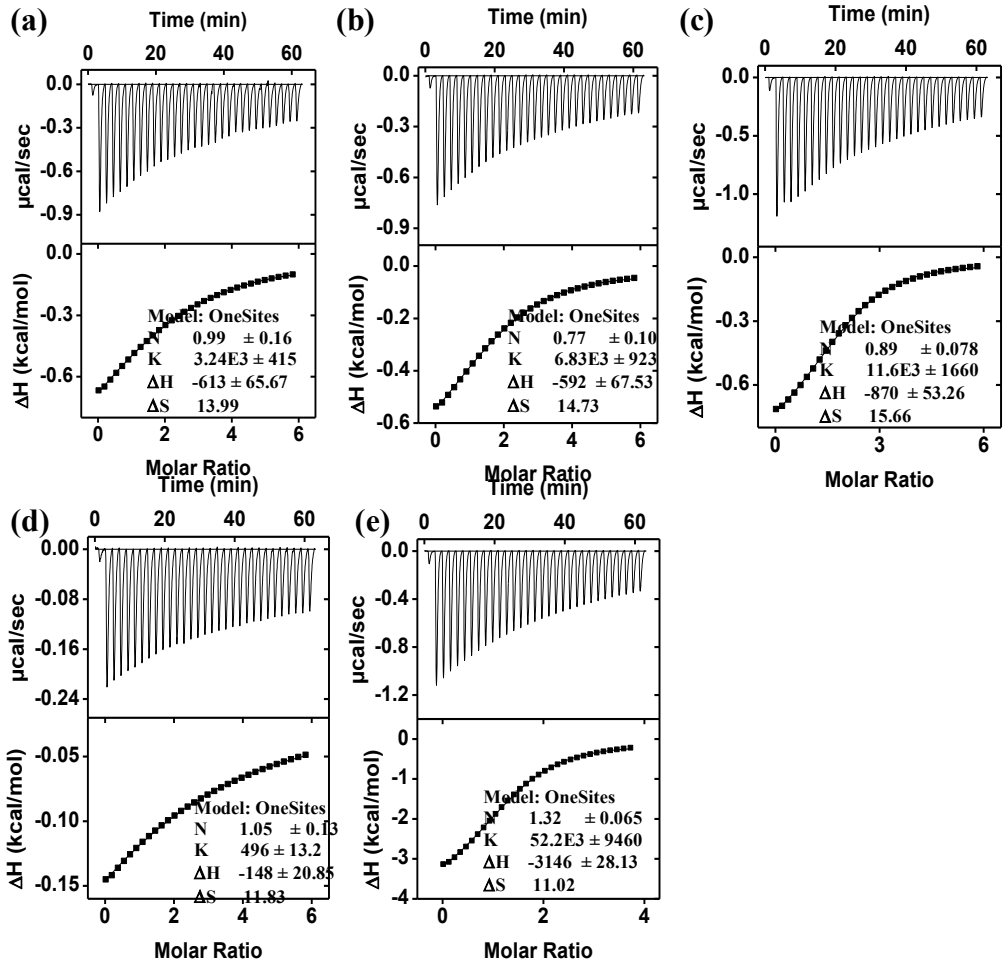

Figure 75. ITC titration curves obtained at 298 K for the titration of MINP(lactose) with maltose (a), cellobiose (b), gentiobiose (c), maltulose (d), and lactose (e) in 10 mM HEPES buffer (pH 7.4, lactose/FM **3** = 1:2). The data correspond to entries 16–20, respectively, in Table 2. The top panel shows the raw calorimetric data. The area under each peak represents the amount of heat generated at each ejection and is plotted against the molar ratio of MINP to the substrate. The solid line is the best fit of the experimental data to the sequential binding of N equal and independent binding sites on the MINP. The heat of dilution for the substrate, obtained by adding the substrate to the buffer, was subtracted from the heat released during the binding. Binding parameters were auto-generated after curve fitting using Microcal Origin 7.

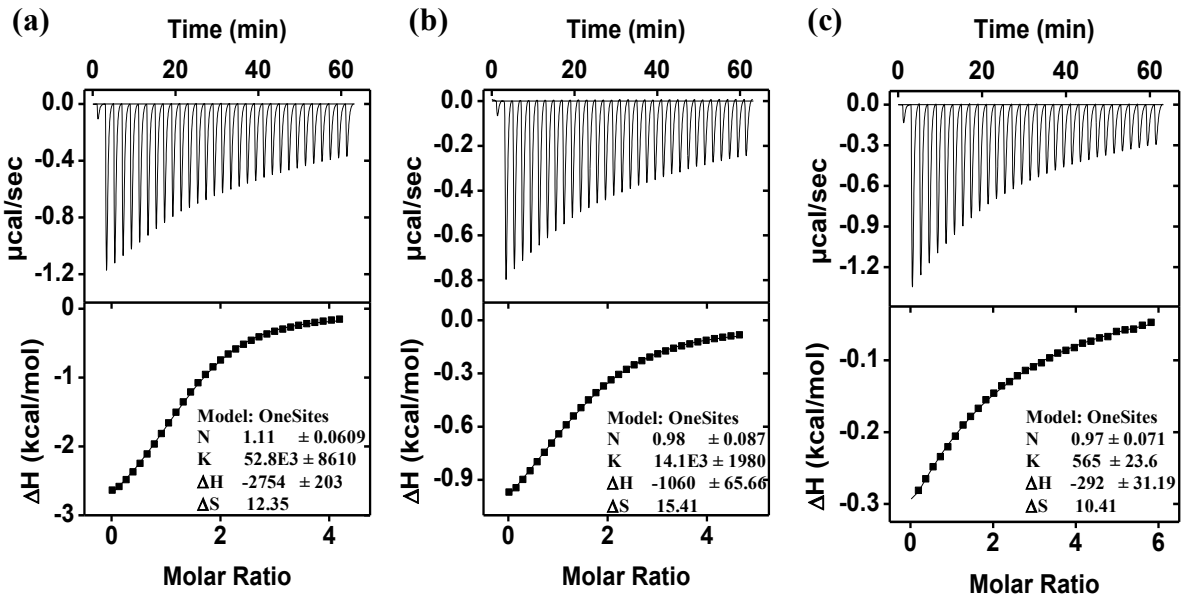

Figure 76. ITC titration curves obtained at 298 K for the titration of MINP(maltotriose) with maltotriose (a), maltose (b), and glucose (c) in 10 mM HEPES buffer (pH 7.4, maltotriose/FM **3** = 1:2). The data correspond to entries 21–23, respectively, in Table 2. The top panel shows the raw calorimetric data. The area under each peak represents the amount of heat generated at each ejection and is plotted against the molar ratio of MINP to the substrate. The solid line is the best fit of the experimental data to the sequential binding of N equal and independent binding sites on the MINP. The heat of dilution for the substrate, obtained by adding the substrate to the buffer, was subtracted from the heat released during the binding. Binding parameters were auto-generated after curve fitting using Microcal Origin 7.

Table 6. ITC binding data for oligosaccharide guests.[a]

Entry	Host	Guest	K_a (10^3 M^{-1})	K_{rel}	-ΔG (kcal/mol)	N
1	MINP(maltose)[b]	maltose	9.20 ± 0.11	-	-5.40	1.2±0.1
2	MINP(maltose)[c]	maltose	4.03 ± 0.51	-	-4.91	1.0±0.1
3	MINP(maltulose)	maltose	0.005±0.001	0.005	--[d]	--[d]
4	MINP(maltulose)	cellobiose	0.002±0.001	0.0002	--[d]	--[d]
5	MINP(maltulose)	gentiobiose	5.46 ± 0.63	0.57	-5.09	1.1±0.1
6	MINP(maltulose)	maltulose	9.56 ± 0.14	1	-5.43	0.9±0.1
7	MINP(maltulose)	lactose	1.79 ± 0.22	0.19	-4.43	1.0±0.1
8	MINP(gentiobiose)	maltose	2.95 ± 0.56	0.04	-4.73	1.1±0.1
9	MINP(gentiobiose)	cellobiose	6.31 ± 0.61	0.09	-5.18	1.0 ± 0.1
10	MINP(gentiobiose)	gentiobiose	73.2 ± 1.7	1	-6.63	1.1 ± 0.1
11	MINP(gentiobiose)	maltulose	0.55 ± 0.01	0.008	-3.73	1.0 ± 0.1
12	MINP(gentiobiose)	lactose	10.1 ± 1.6	0.14	-5.46	0.9 ± 0.1

[a]The titrations were performed in 10 mM HEPES buffer at pH 7.4 with template/FM **3** = 1:2. [b] pH 8.5. [c] pH 6.5. [d] Binding was extremely weak. Because the binding constant was estimated from ITC, -ΔG and N are not listed.

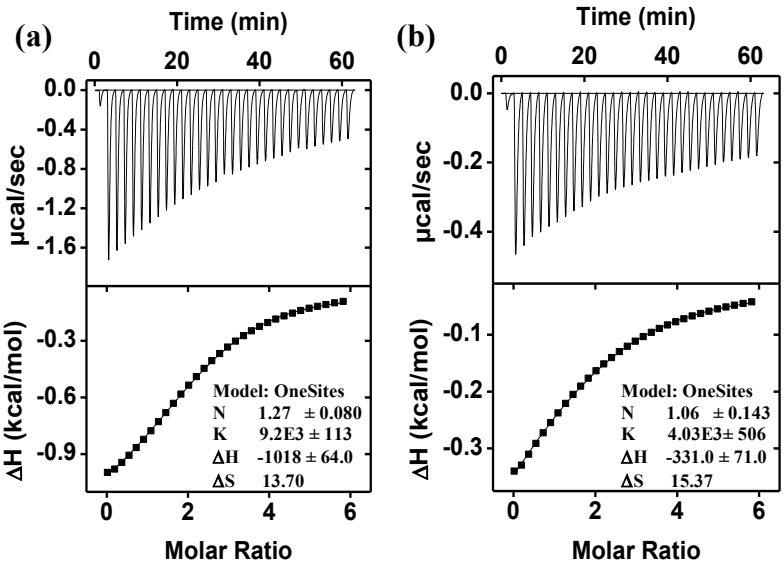

Figure 77. ITC titration curves obtained at 298 K for the titration of MINP(maltose) with maltose at pH 8.5 (a), and pH 6.5 (b) in 10 mM HEPES buffer (maltose/FM **3** = 1:2). The data correspond to entries 1–2, respectively, in Table 6. The top panel shows the raw calorimetric data. The area under each peak represents the amount of heat generated at each ejection and is plotted against the molar ratio of MINP to the substrate. The solid line is the best fit of the experimental data to the sequential binding of N equal and independent binding sites on the MINP. The heat of dilution for the substrate, obtained by adding the substrate to the buffer, was subtracted from the heat released during the binding. Binding parameters were auto-generated after curve fitting using Microcal Origin 7.

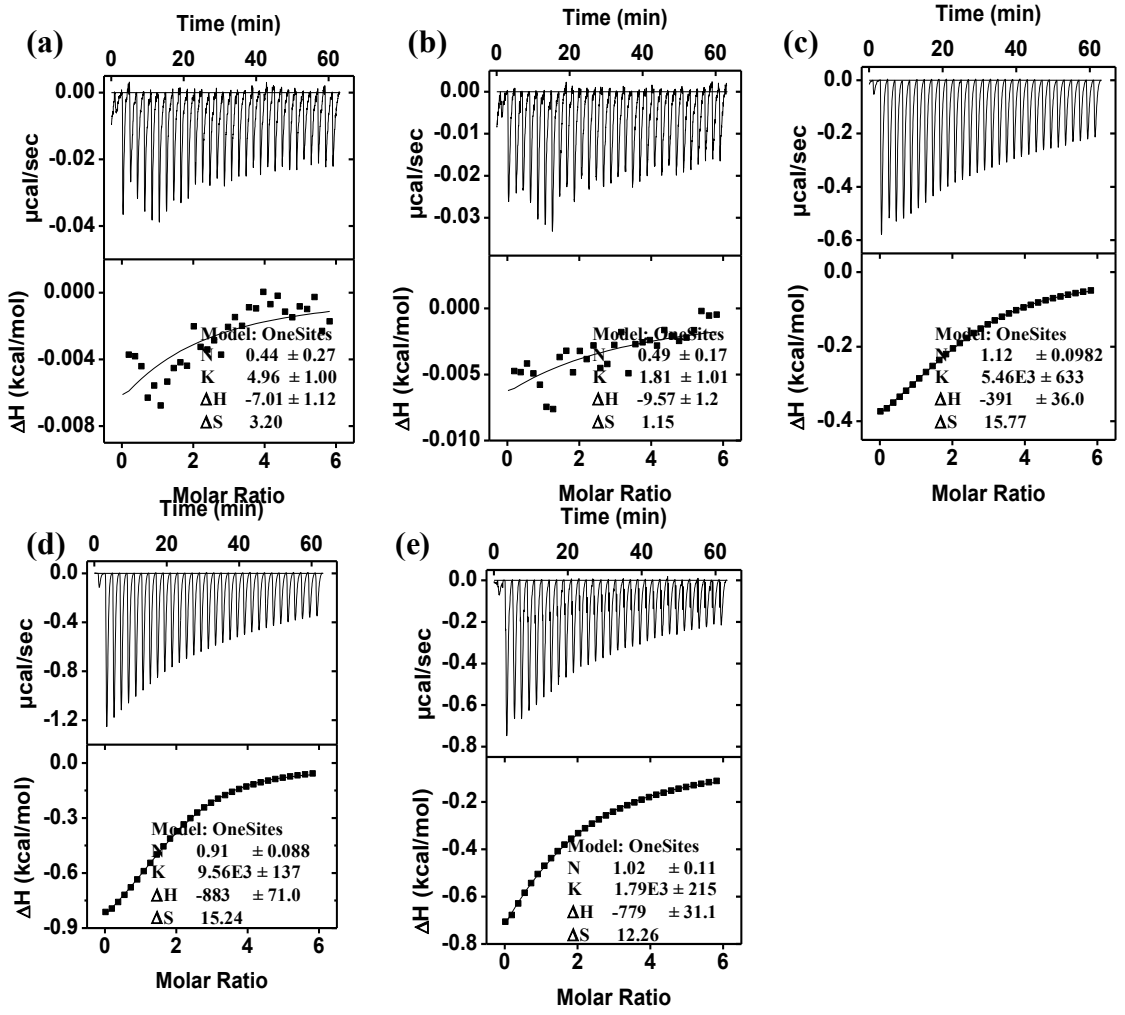

Figure 78. ITC titration curves obtained at 298 K for the titration of MINP(maltulose) with maltose (a), cellobiose (b), gentiobiose (c), maltulose (d), and lactose (e) in 10 mM HEPES buffer (pH 7.4, maltulose/FM **3** = 1:2). The data correspond to entries 3–7, respectively, in Table 6. The top panel shows the raw calorimetric data. The area under each peak represents the amount of heat generated at each ejection and is plotted against the molar ratio of MINP to the substrate. The solid line is the best fit of the experimental data to the sequential binding of N equal and independent binding sites on the MINP. The heat of dilution for the substrate, obtained by adding the substrate to the buffer, was subtracted from the heat released during the binding. Binding parameters were auto-generated after curve fitting using Microcal Origin 7.

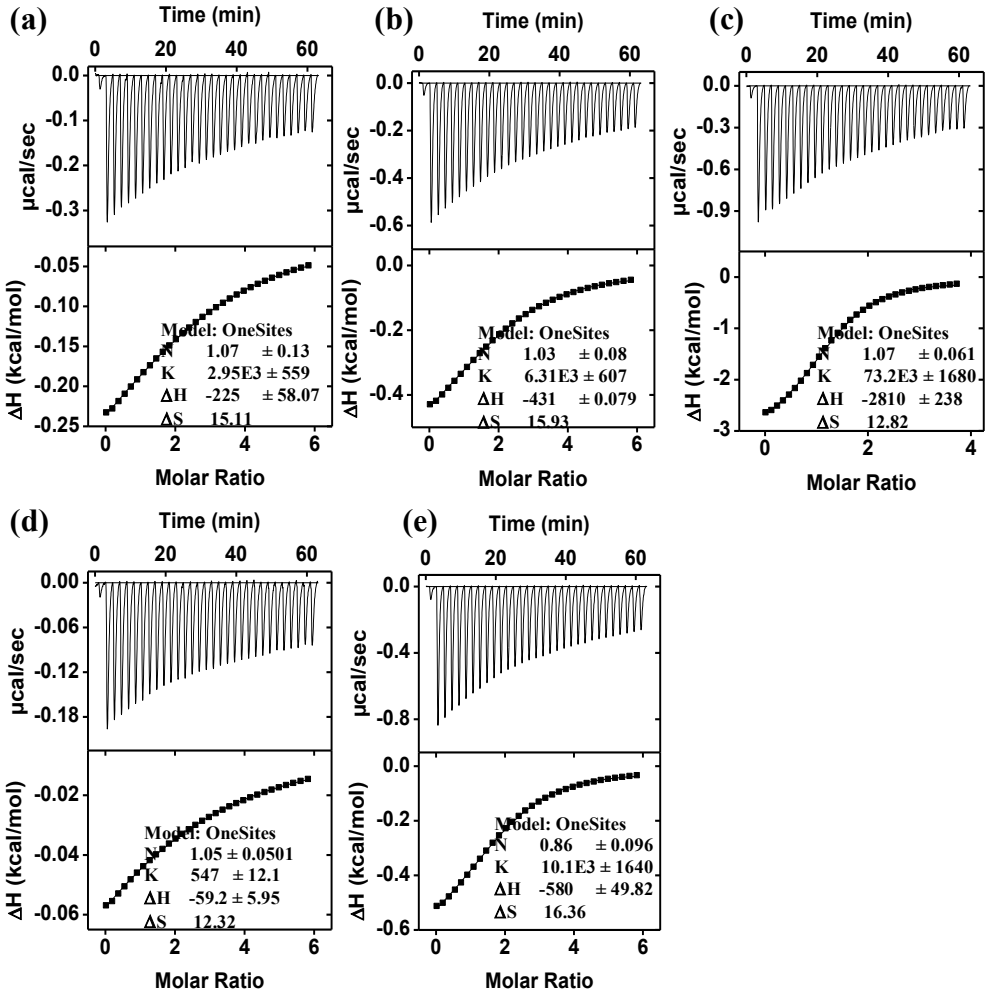

Figure 79. ITC titration curves obtained at 298 K for the titration of MINP(gentiobiose) with maltose (a), cellobiose (b), gentiobiose (c), maltulose (d), and lactose (e) in 10 mM HEPES buffer (pH 7.4, gentiobiose/FM **3** = 1:2). The data correspond to entries 8–12, respectively, in Table 6. The top panel shows the raw calorimetric data. Area under each peak represents amount of heat generated at each ejection and is plotted against the molar ratio of MINP to the substrate. The solid line is the best fit of the experimental data to the sequential binding of N equal and independent binding sites on the MINP. The heat of dilution for the substrate, obtained by adding the substrate to the buffer, was subtracted from the heat released during the binding. Binding parameters were auto-generated after curve fitting using Microcal Origin 7.

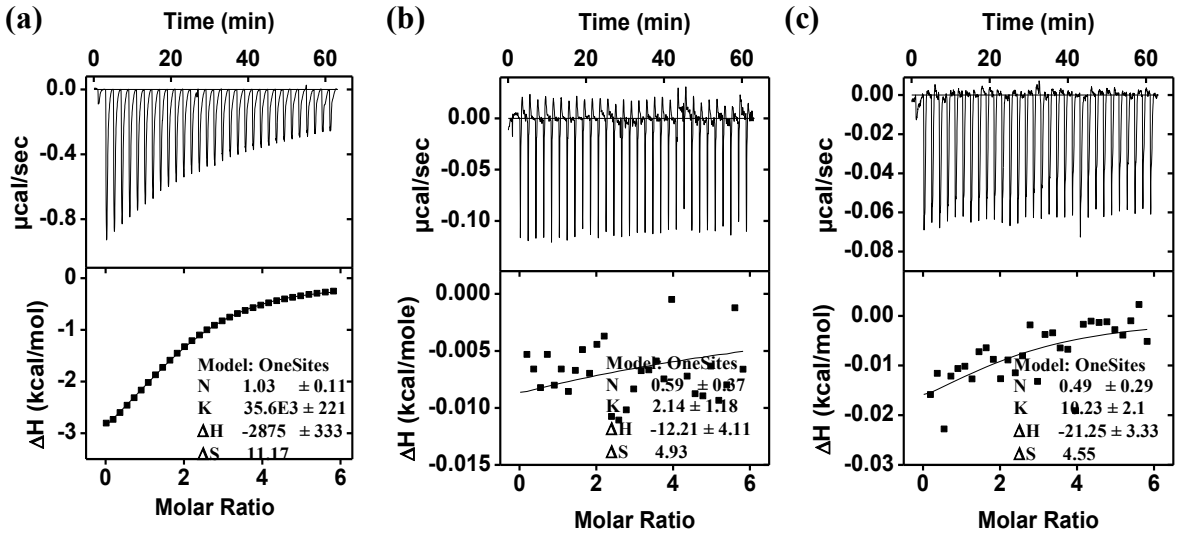

Figure 80. ITC titration curves obtained at 298 K for the titration of MINP(H) with sugar H (a), sugar A (b), and sugar B (c) in 10 mM HEPES buffer (pH 7.4, sugar H/FM **3** = 1:2). The data correspond to entries 1–3, respectively, in Table 3. The top panel shows the raw calorimetric data. The area under each peak represents the amount of heat generated at each ejection and is plotted against the molar ratio of MINP to the substrate. The solid line is the best fit of the experimental data to the sequential binding of N equal and independent binding sites on the MINP. The heat of dilution for the substrate, obtained by adding the substrate to the buffer, was subtracted from the heat released during the binding. Binding parameters were auto-generated after curve fitting using Microcal Origin 7.

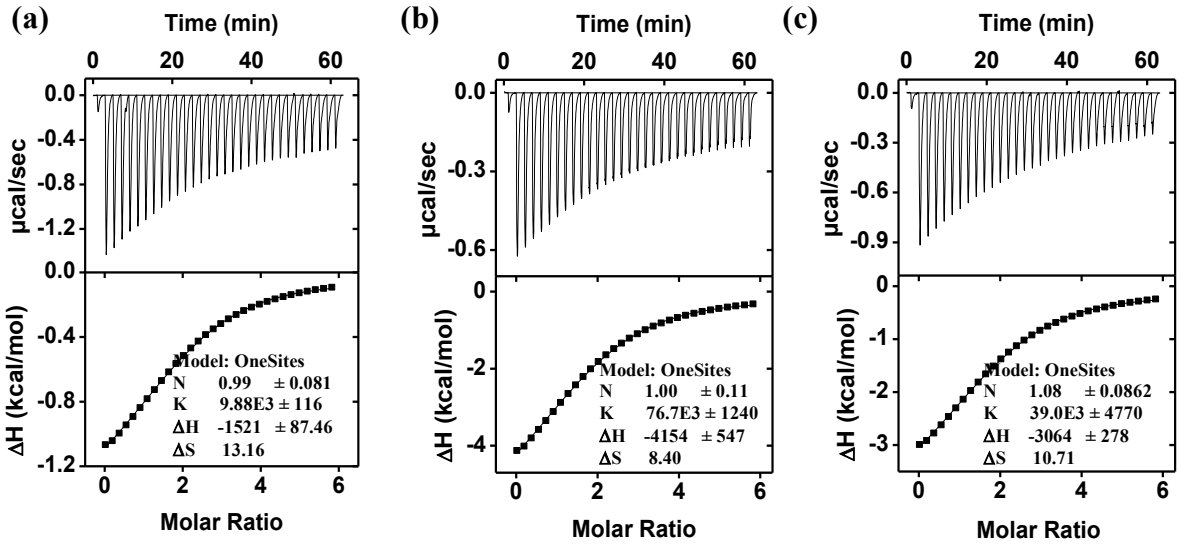

Figure 81. ITC titration curves obtained at 298 K for the titration of MINP(A) with sugar H (a), sugar A (b), and sugar B (c) in 10 mM HEPES buffer (pH 7.4, sugar A/FM **3** = 1:3). The data correspond to entries 4–6, respectively, in Table 3. The top panel shows the raw calorimetric data. The area under each peak represents the amount of heat generated at each ejection and is plotted against the molar ratio of MINP to the substrate. The solid line is the best fit of the experimental data to the sequential binding of N equal and independent binding sites on the MINP. The heat of dilution for the substrate, obtained by adding the substrate to the buffer, was subtracted from the heat released during the binding. Binding parameters were auto-generated after curve fitting using Microcal Origin 7.

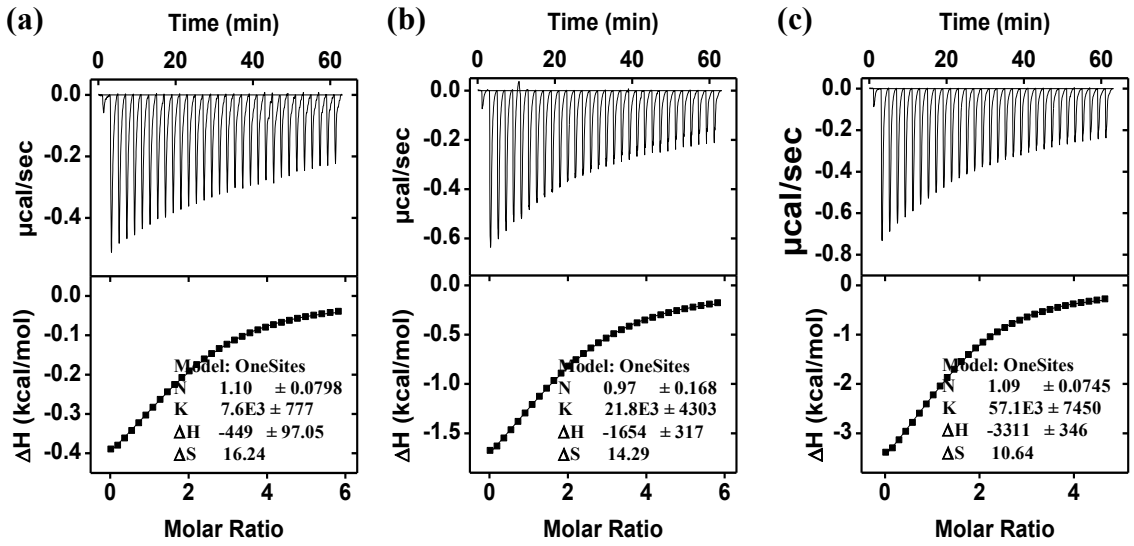

Figure 82. ITC titration curves obtained at 298 K for the titration of MINP(B) with sugar H (a), sugar A (b), and sugar B (c) in 10 mM HEPES buffer (pH 7.4, sugar B/FM **3** = 1:3). The data correspond to entries 7–9, respectively, in Table 3. The top panel shows the raw calorimetric data. The area under each peak represents the amount of heat generated at each ejection and is plotted against the molar ratio of MINP to the substrate. The solid line is the best fit of the experimental data to the sequential binding of N equal and independent binding sites on the MINP. The heat of dilution for the substrate, obtained by adding the substrate to the buffer, was subtracted from the heat released during the binding. Binding parameters were auto-generated after curve fitting using Microcal Origin 7.

^{1}H and ^{13}C NMR spectra

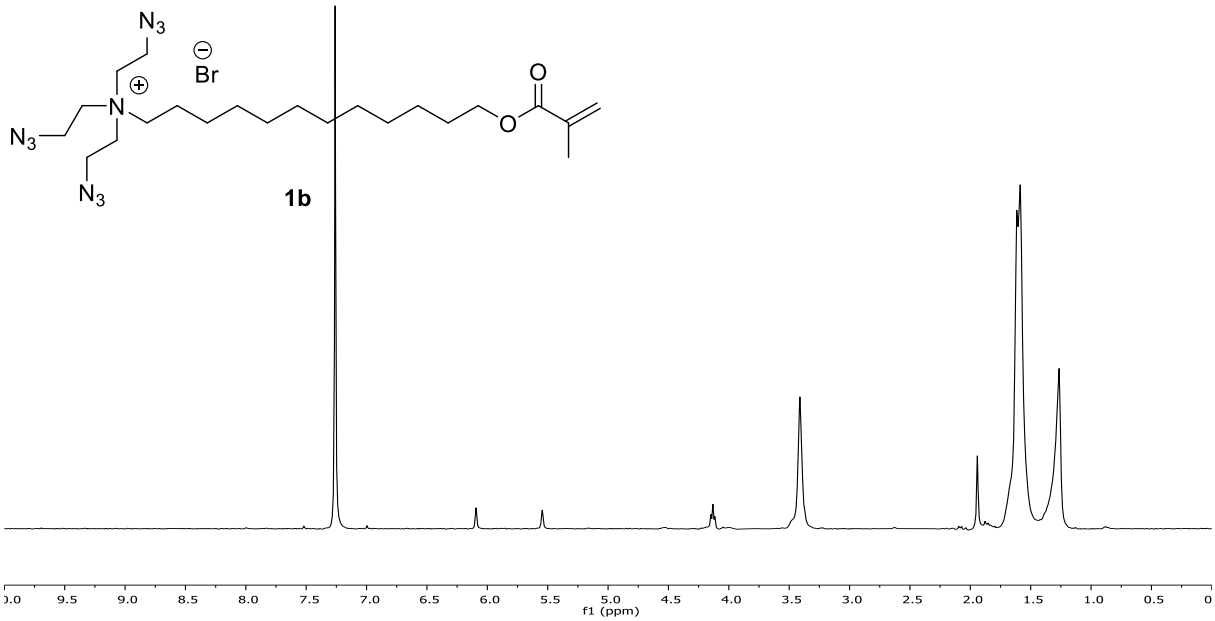

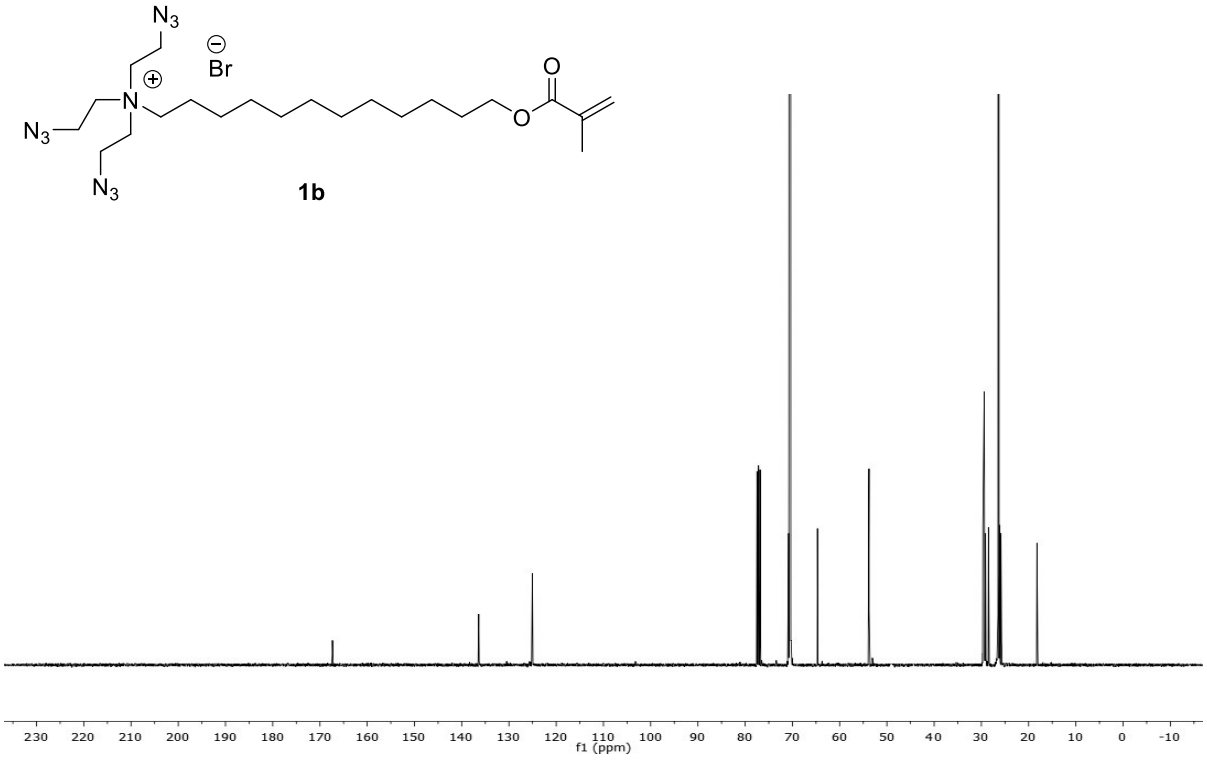

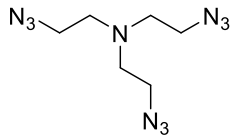

12

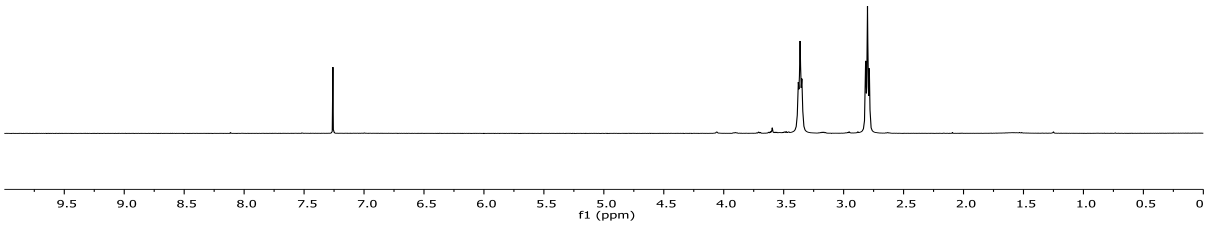

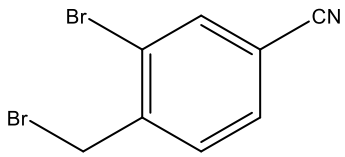

13

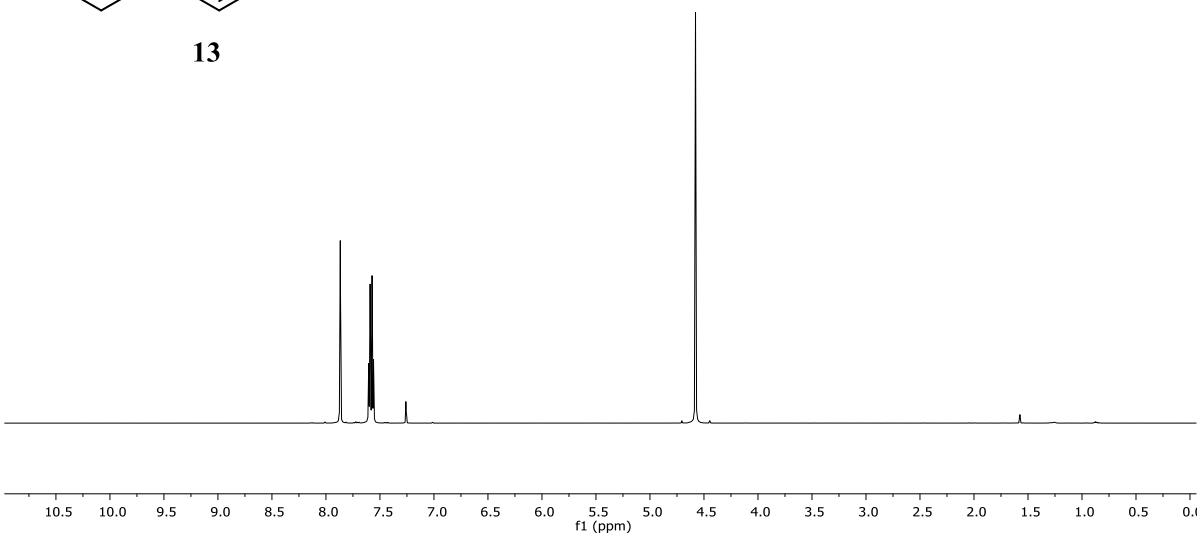

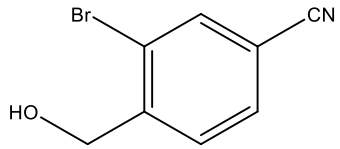

14

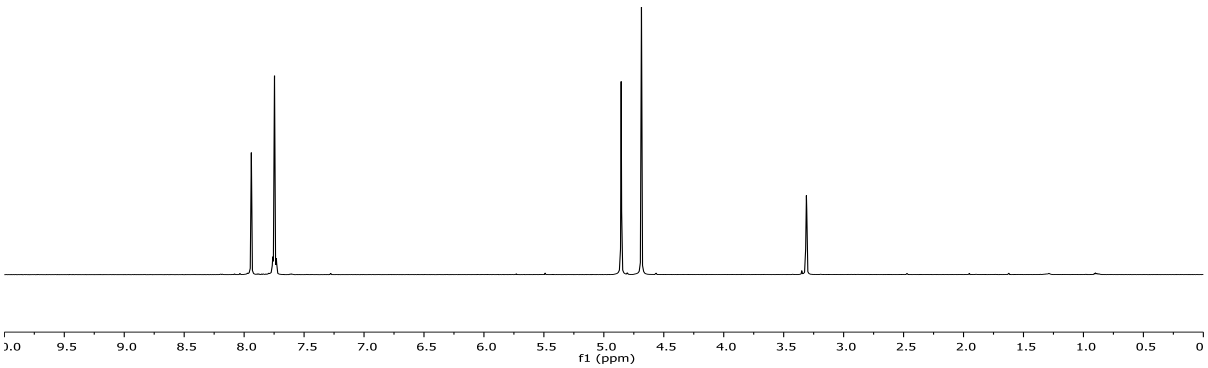

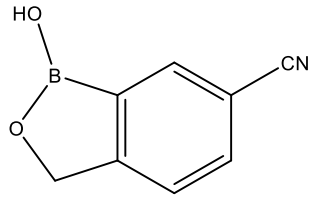

15

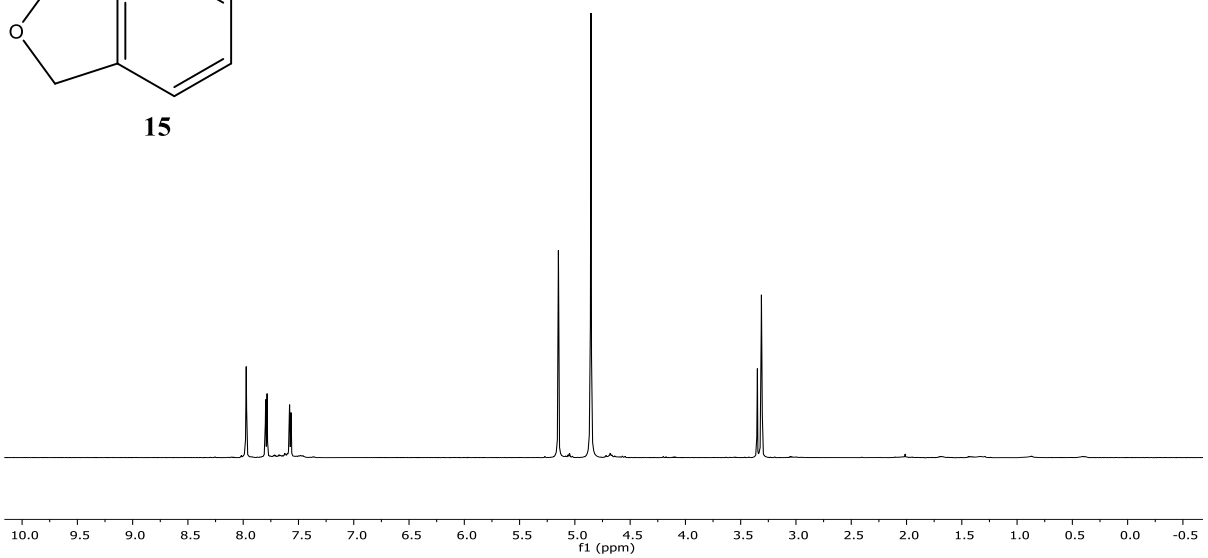

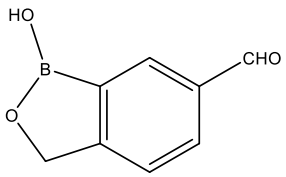

16

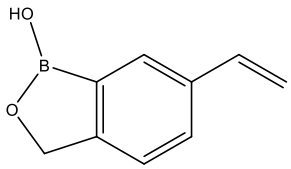

3

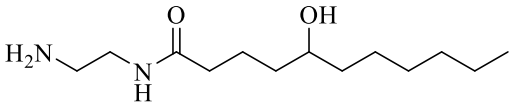

18

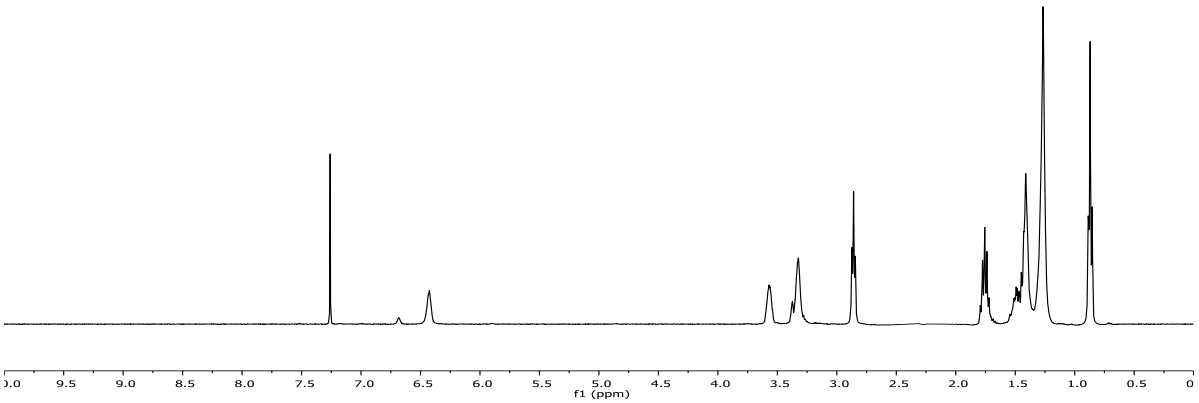

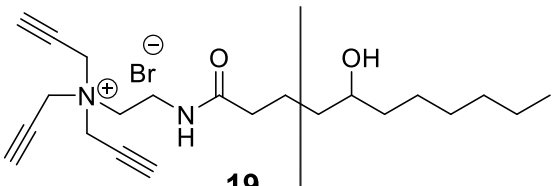

19

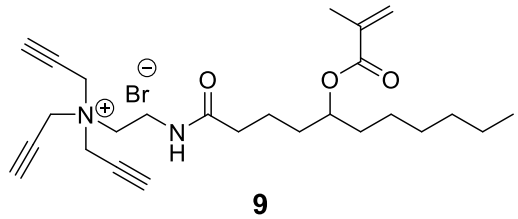

9

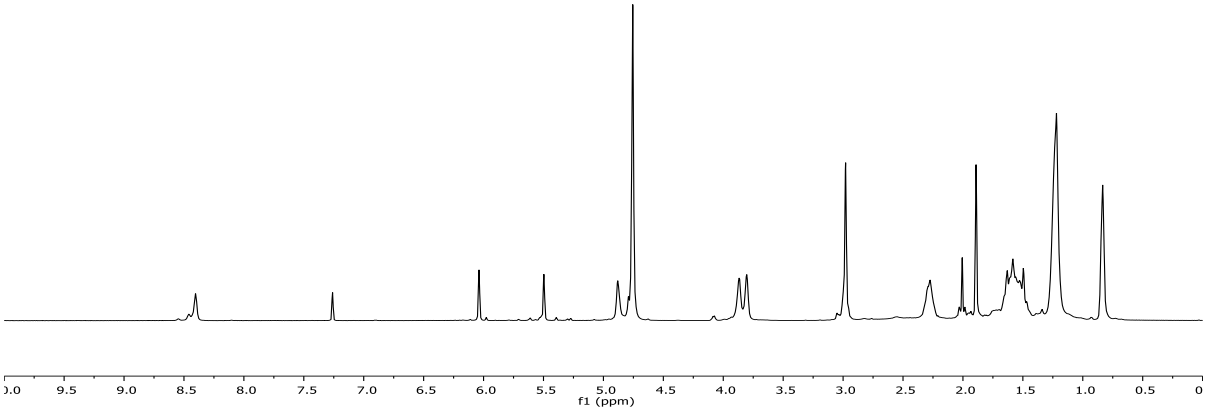

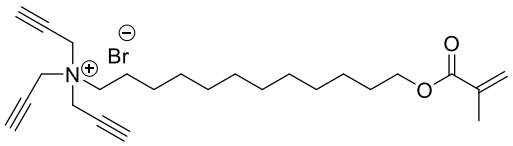

1a

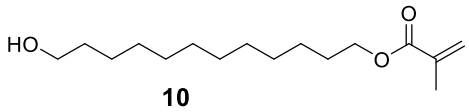

10

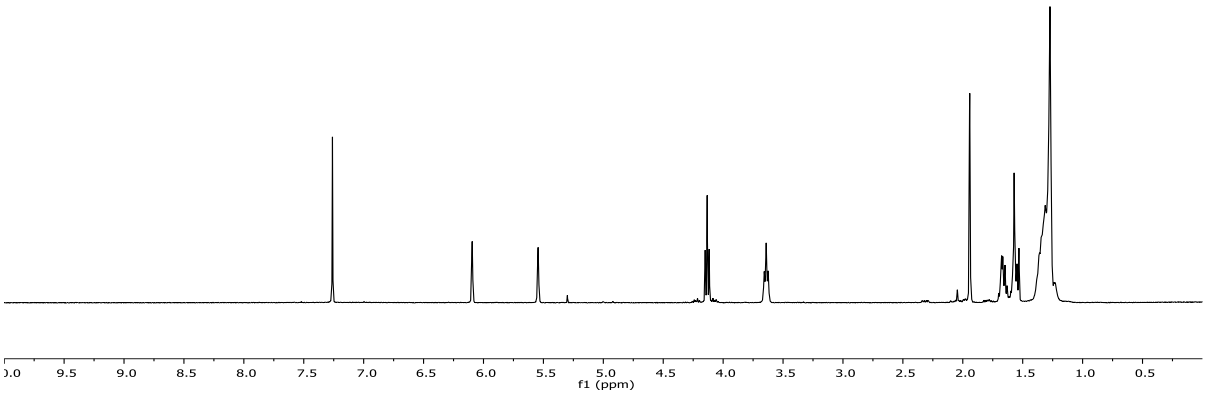

Notes and References

(1) Kamerling, J. P.; Boons, G.-J. *Comprehensive glycoscience : from chemistry to systems biology*; 1st ed.; Elsevier: Amsterdam ; Boston, 2007.

(2) Wang, B.; Boons, G.-J. *Carbohydrate recognition: biological problems, methods, and applications*; Wiley: Hoboken, N.J., 2011.

(3) Jin, S.; Cheng, Y.; Reid, S.; Li, M.; Wang, B. *Med. Res. Rev.* **2010**, *30*, 171.

(4) Davis, A. P.; James, T. D. *Carbohydrate Receptors*; Wiley-VCH Verlag GmbH & Co. KGaA, 2005.

(5) James, T. D.; Phillips, M. D.; Shinkai, S. *Boronic acids in saccharide recognition*; RSC Publishing: Cambridge, 2006.

(6) Ferrand, Y.; Crump, M. P.; Davis, A. P. *Science* **2007**, *318*, 619.

(7) Barwell, N. P.; Crump, M. P.; Davis, A. P. *Angew. Chem. Int. Ed.* **2009**, *48*, 7673.

(8) Ke, C.; Destecroix, H.; Crump, M. P.; Davis, A. P. *Nat. Chem.* **2012**, *4*, 718.

(9) Rauschenberg, M.; Bomke, S.; Karst, U.; Ravoo, B. J. *Angew. Chem. Int. Ed.* **2010**, *49*, 7340.

(10) Kobayashi, K.; Asakawa, Y.; Kato, Y.; Aoyama, Y. *J. Am. Chem. Soc.* **1992**, *114*, 10307.

(11) Kim, K. T.; Cornelissen, J. J. L. M.; Nolte, R. J. M.; van Hest, J. C. M. *J. Am. Chem. Soc.* **2009**, *131*, 13908.

(12) Pal, A.; Bérubé, M.; Hall, D. G. *Angew. Chem. Int. Ed.* **2010**, *49*, 1492.

(13) Wu, X.; Li, Z.; Chen, X.-X.; Fossey, J. S.; James, T. D.; Jiang, Y.-B. *Chem. Soc. Rev.* **2013**, *42*, 8032.

(14) Bull, S. D.; Davidson, M. G.; Van den Elsen, J. M. H.; Fossey, J. S.; Jenkins, A. T. A.; Jiang, Y. B.; Kubo, Y.; Marken, F.; Sakurai, K.; Zhao, J. Z.; James, T. D. *Acc. Chem. Res.* **2013**, *46*, 312.

(15) Wulff, G.; Vesper, W. *J. Chromatogr.* **1978**, *167*, 171.

(16) Awino, J. K.; Zhao, Y. *J. Am. Chem. Soc.* **2013**, *135*, 12552.

(17) Awino, J. K.; Zhao, Y. *Chem.-Eur. J.* **2015**, *21*, 655.

(18) Dowlut, M.; Hall, D. G. *J. Am. Chem. Soc.* **2006**, *128*, 4226.

(19) Bérubé, M.; Dowlut, M.; Hall, D. G. *J. Org. Chem.* **2008**, *73*, 6471.

(20) Zhang, S.; Zhao, Y. *Macromolecules* **2010**, *43*, 4020.

(21) Zhao, Y. *Langmuir* **2016**, *32*, 5703.

(22) Zhang, S.; Zhao, Y. *J. Am. Chem. Soc.* **2010**, *132*, 10642.

(23) Schmidtchen, F. P. In *Supramol Chem*; John Wiley & Sons, Ltd: 2012.

(24) Awino, J. K.; Zhao, Y. *Chem. Commun.* **2014**, *50*, 5752.

(25) Awino, J. K.; Gunasekara, R. W.; Zhao, Y. *J. Am. Chem. Soc.* **2016**, *138*, 9759.

(26) Since the binding selectivity for MINP(mannose) suggests that the cis-1,2-diol was invovled in the binding, the C3 hydroxyl could not have participated in in the binding with the (cis) C2 hydroxyl.

(27) If the 4,6-diol had been involved in the binding, gulose should have displayed weaker but significant binding as allose and altrose did toward MINP(glucose) and MINP(mannose), respectively.

(28) Wulff, G. *Angew. Chem. Int. Ed. Engl.* **1995**, *34*, 1812.

(29) Haupt, K.; Mosbach, K. *Chem. Rev.* **2000**, *100*, 2495.

(30) Sellergren, B. *Molecularly imprinted polymers: man-made mimics of antibodies and their applications in analytical chemistry*; Elsevier: Amsterdam, 2001.

(31) Alexander, C.; Andersson, H. S.; Andersson, L. I.; Ansell, R. J.; Kirsch, N.; Nicholls, I. A.; O'Mahony, J.; Whitcombe, M. J. *J. Mol. Recognit.* **2006**, *19*, 106.

(32) Sellergren, B.; Hall, A. J. In *Supramol Chem*; John Wiley & Sons, Ltd: 2012.

(33) Single-sited receptors have been obtained by molecular imprinting within dendrimers, see: (a) Zimmerman, S. C.; Wendland, M. S.; Rakow, N. A.; Zharov, I.; Suslick, K. S. *Nature* **2002**, *418*, 399. (b) Zimmerman, S. C.; Zharov, I.; Wendland, M. S.; Rakow, N. A.; Suslick, K. S. *J. Am. Chem. Soc.* **2003**, *125*, 13504.

(34) Wulff, G.; Schauhoff, S. *J. Org. Chem.* **1991**, *56*, 395.

(35) Arifuzzaman, M.; Zhao, Y. *J. Org. Chem.* **2016**, DOI: 10.1021/acs.joc.6b01191.

(36) Michaels, H. A.; Zhu, L. *Chem. Asian J.* **2011**, *6*, 2825.

(37) Zhou, H.; Ding, D.; Zhou, Y.; Zhang, Y. K.; Plattner, J. J.; WO2011022337 A1: 2011.

(38) Kim, H.; Kang, Y. J.; Kang, S.; Kim, K. T. *J. Am. Chem. Soc.* **2012**, *134*, 4030.

CHAPTER 5

CONFORMATIONALLY SWITCHABLE WATER-SOLUBLE FLUORESCENT BISCHOLATE FOLDAMERS AS MEMBRANE-CURVATURE SENSORS

A paper published in *Langmuir* **2015**, *31*, 3919−3925.

Roshan W. Gunasekara and Yan Zhao

Abstract

Membrane curvature is an important parameter in biological processes such as cellular movement, division, and vesicle fusion and budding. Traditionally, only proteins and protein-derived peptides have been used as sensors for membrane curvature. Three water-soluble bischolate foldamers were synthesized, all labelled with an environmentally sensitive fluorophore to report their binding with lipid membranes. The orientation and ionic nature of the fluorescent label were found to be particularly important in their performance as membrane-curvature sensors. The bischolate with an NBD group in the hydrophilic α-face of the cholate outperformed the other two analogues as a membrane-curvature sensor and responded additionally to the lipid composition including the amounts of cholesterol and anionic lipids in the membranes.

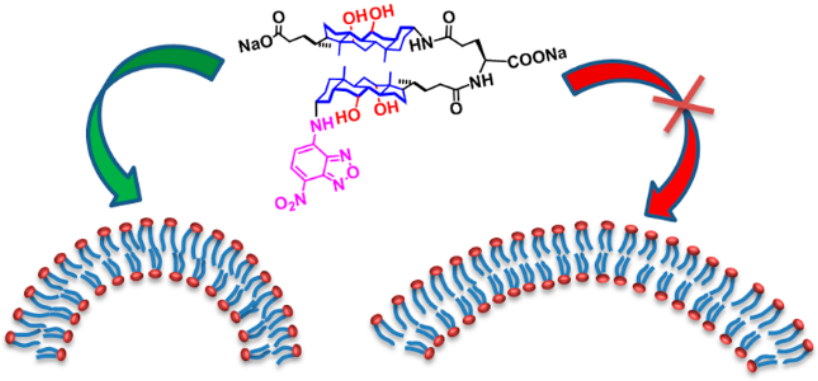

Scheme 1. Bischolate foldamer **4** in different sizes of lipid membranes.

Introduction

Lipids are the main ingredients of biological membranes, whether plasma membranes that define the boundary of a cell or membranes of intracellular organelles that isolate them form the cytoplasm.[1] In comparison to proteins, nucleic acids, and polysaccharides, these small-molecule amphiphiles seem to lack the usual biological sophistication. However, continued studies in recent decades revealed that lipids have their unique way of complexity that in some ways rival or even surpass what is found in the other more complex biomacromolecules.[2] For example, biological membranes are made of complex mixtures of lipids, whose composition is subject to change at different stages of the cell life and even in response to biological conditions of the cell.[3] Membranes are not homogeneous mixtures of lipid molecules either. Heterogeneity is found both horizontally within the same leaflet of a bilayer membrane and vertically across the two leaflets.[4,5] Phase-separated lipid domains play important roles in biological processes such as membrane protein assembly and signal transduction. Thus, even without secondary and tertiary structures, lipid molecules communally could change their chemical composition and dynamic structures, similar to what proteins do at the primary and secondary structural levels. Because these changes and the dynamics of lipids occur in a self-assembled ensemble, the complexity is no smaller than the individual complexity displayed by the other seemingly more sophisticated biomacromolecules.

Another level of complexity in lipid assemblies comes from membrane curvature.[6] Larger plasma membranes are, as a result of simple geometry, flatter or have smaller curvature than membranes of intracellular organelles. Certain organelles have notably highly curved membranes including endoplasmic reticulum and golgi apparatus. However,

membrane curvature is a not a static property of biological membranes. In processes such as cellular movement, division, and vesicle fusion and budding, membrane curvature is actively modulated by proteins to enable these processes. Curvature modulation is an extremely important and intriguing process, as it translates molecular interactions between lipids and proteins into mechanical movement/rearrangement of cells and vesicles.[7]

For these reasons, there is strong interest in developing tools that can sense membrane curvature, particularly under dynamic conditions.[8,9] In nature, certain proteins are known to be specific membrane-curvature sensors. BAR domains are coiled-coil bundles of proteins; these arc-shaped structures can associate with membranes with matching curvatures.[10,11] Other membrane sensors such as ALPS do not have specific secondary/tertiary structures on their own but recognize the hydrophobic defects in highly curved membranes. The most interesting feature of this class of membrane sensors is that they stay soluble in water in the presence of low-curvature membranes (e.g., liposomes with $R > 100$ nm) but selectively bind high-curvature membranes (e.g., liposomes with $R < 50$ nm), meanwhile switching from a random conformation to an α-helix on the surface of the membrane.[12,13]

Because of the complexity of the natural protein-based curvature sensors, scientists in recent years became interested in developing small-molecule-based sensors, for their ease of synthesis and more straightforward structure–activity correlation. A cyclic peptide derived from Synaptotagmin-I (a protein possibly involved in calcium-dependent membrane-trafficking and fusion)[14,15] and a 25-mer peptide (MARCKS-ED) were both shown recently to be effective curvature sensors.[16]

In this work, we report that simple bischolate foldamers could be used as effective membrane-curvature sensors. The location and the nature of the fluorescent probe on the foldamer turned out particularly important in their ability to act as membrane-curvature sensors. Our most effective foldamer sensor not only responded to membrane curvature, but also to the cholesterol content and the amount of negatively charged lipids in predictable fashions.

Experimental Section

The general methods and the syntheses of the compounds are reported in the Experimental Section.

Liposome preparation.

A chloroform solution of POPC (1-palmitoyl-2-oleoyl-*sn*-glycero-3-phosphocholine) and POPG (1-palmitoyl-2-oleoyl-*sn*-glycero-3-phospho-1'-*rac*-glycerol sodium salt) was placed in a 10 mL test tube and dried under a stream of nitrogen for 10 min. The residue was dried further under high vacuum overnight to obtain a thin lipid film. A solution of PBS buffer (1.0 mL, pH = 7.4) was added to the test tube containing thin lipid film. Rehydration of the lipid was allowed to continue for 90 min with frequent vortexing at 4 °C. The lipid suspensions of the resulting multilamellar vesicles were subjected to ten freeze–thaw cycles. The resulting mixture was then extruded twenty-nine times through a polycarbonate filter (diameter = 19 mm, pore diameters of 30, 100, and 400 nm) at room temperature using an Avanti Mini-Extruder to produce the desired LUVs. Each LUV was diluted in PBS to a lipid concentration of 15–25 μM and their size was analyzed by DLS. Intensity data from each sample were collected in five replicates and analyzed by the Precision Deconvolve software.

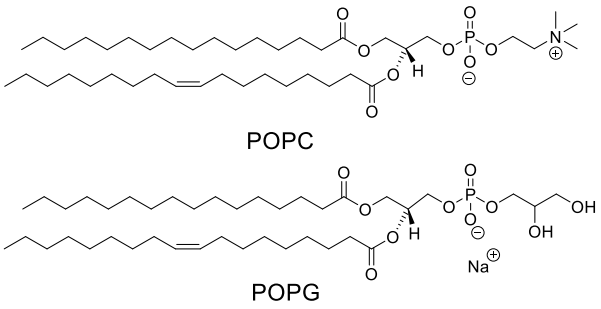

Scheme 2. Structures of POPC and POPG.

Fluorescence enhancement assay.

Different bischolates were mixed with the above prepared LUV solutions to afford a solution with [bischolate] = 0.10 μM and [total lipids] = 300 μM in PBS buffer. The samples were transferred to 10 mm cuvettes and fluorescence spectra were recorded on a Varian Cary Eclipse spectrofluorometer. Fluorescence spectra were also obtained without liposomes in the solution. The excitation wavelength (λ_{ex}) was 340, 470, and 470 nm for bischolate **1**, **3** and **4**, respectively. The excitation slit width was 10 nm and the emission slit width was 20 nm. The fluorescence enhancement was obtained by averaging two scans and normalizing the emission intensity of the probe in the presence of the LUVs to the intensity in the absence of the LUVs.

Fluorescence titration.

A series of LUV solutions (2.5–1200 μM) containing the appropriate bischolate probe (0.10 μM) were prepared in PBS buffer (2.0 mL, pH = 7.4). After the samples were allowed to sit for 5 min at room temperature, fluorescence spectra were recorded on a Varian Cary Eclipse spectrofluorometer. The excitation wavelength (λ_{ex}) was 340, 470, and 470 nm for bischolate **1**, **3** and **4**, respectively. The excitation slit width was 10 nm and the emission slit width was 20 nm.

Results and Discussion

Design and Synthesis of Bischolate Membrane-Curvature Sensors

Foldamers are synthetic mimics of biomacromolecules with controlled conformations.[17-19] Our group has been interested in foldamers made of cholic acid, a natural facial amphiphile.[20-22] The amphiphilicity of the building block and the resultant foldamers allows these compounds to interact with lipid membranes in tunable fashions.[23-25] Since amphipathic peptides act as membrane-curvature sensors[8,12-16,26,27] and facially amphiphilic cholate derivatives have been used by researchers as amphiphilic peptide-mimics,[28,29] we reasoned that appropriate cholate foldamers might be able to bind membranes in a curvature-dependent fashion.

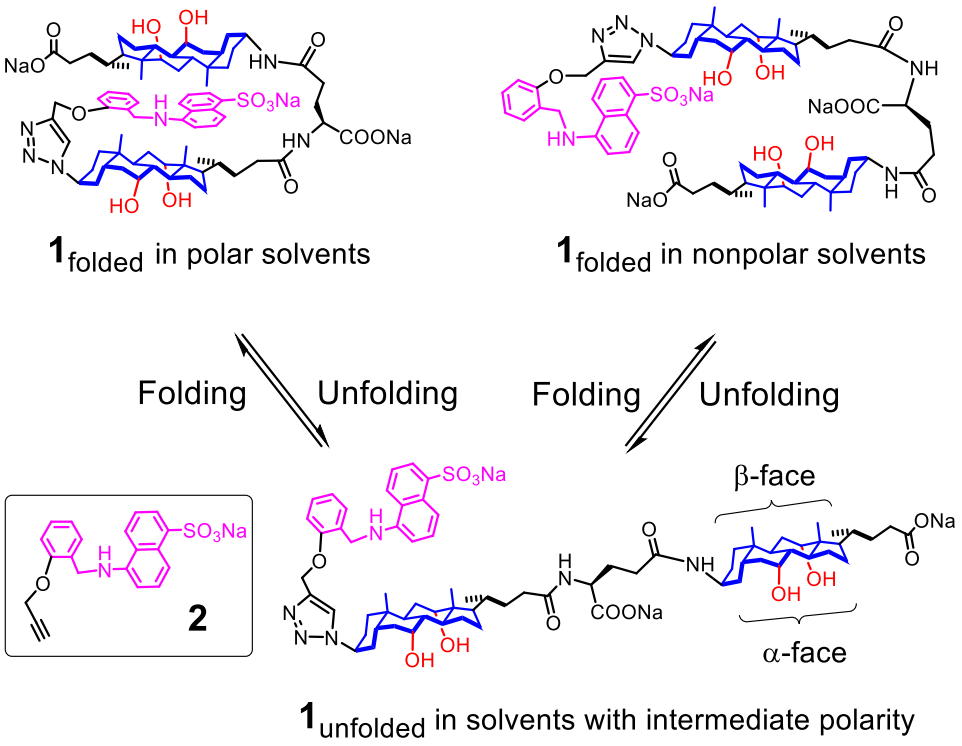

Scheme 3. Folding and unfolding of bischolate foldamer **1**.

Bischolate **1** was recently synthesized in our group.[30] The molecule has two cholates connected head-to-tail with a glutamic acid tether in between. The glutamic acid was introduced to facilitate the cholate–cholate interactions. Our previous work suggests that a C4 tether allows the facial amphiphiles to interact with each other readily.[31] The molecule contains two carboxylates, one from one of the cholates and the other from the glutamate tether. These ionic groups (including the sulfonate on the fluorophore) make the molecule soluble in water, a feature important to aqueous-based applications such as membrane-curvature sensing. Natural cholic acid has a hydrophilic α-face with three hydroxyl groups and a hydrophobic β-face made of hydrocarbon. Bischolate **1** has the terminal hydroxyl inverted and replaced with an amido and a triazoloyl group, respectively. The triazoloyl was used to introduce the aminonaphthalene sulfonate group, which is analogous to the more common environmentally sensitive fluorophore dansyl.[32] Its environment-dependent emission allowed us to characterize its conformation in different solvents (Scheme 3).

Our previous work shows that, in polar solvents (i.e., >50% water in methanol), bischolate **1** folds hydrophobically, with the polar groups exposed to the solvents. In nonpolar solvents (i.e., >30% THF in methanol), the molecule adopts a conformation with the polar groups point inward, solvated by polar solvents concentrated in the center of the molecule.[30] At intermediate polarity (namely, in between 30% THF/methanol and 50% methanol/water), the molecule adopts an unfolded, random conformation, with both the hydrophilic and hydrophobic faces exposed. The solvent-induced conformational change between a micelle-like conformation with exposed hydrophilic groups and a reverse-micelle-like conformation with buried hydrophilic groups has been observed multiple times for both cholate foldamers[20,33] and nonfoldamers[33-36] under similar conditions.

The above conformational change was established through the solvent-sensitive emission and its comparison with the control compound **2** (Scheme 3).[30] The environmentally dependent switachable conformaitons seem to be perfect for a membrane-curvature sensor and resemble ALPS in its transition from a random conformation in water to the amphipathic α-helix upon binding with a highly curved membrane.[12,13] The environmentally-sensitive aminonaphthalene sulfonate is also important, as it could serve as a spectroscopic reporter to indicate its migration from an aqueous phase to a more hydrophobic membrane.[30,32]

In this work, we synthesized two additional bischolates, **3** and **4**. Molecule **3** is identical to **1** in every aspect except that the ionic aminonaphthalene sulfonate was replaced by another environmentally sensitive NBD fluorophore. NBD absorbs and emits at a longer wavelength than aminonaphthalene sulfonate derivatives.[37] As will be shown in our discussion below, the (ionic or nonionic) nature of the fluorophore turns out to be a key parameter to the compound's performance as a membrane curvature-sensor. Molecule **4** is similar to **3**, having the nonionic NBD fluorescent label, except that the label is located on the α-face of the attached cholate.

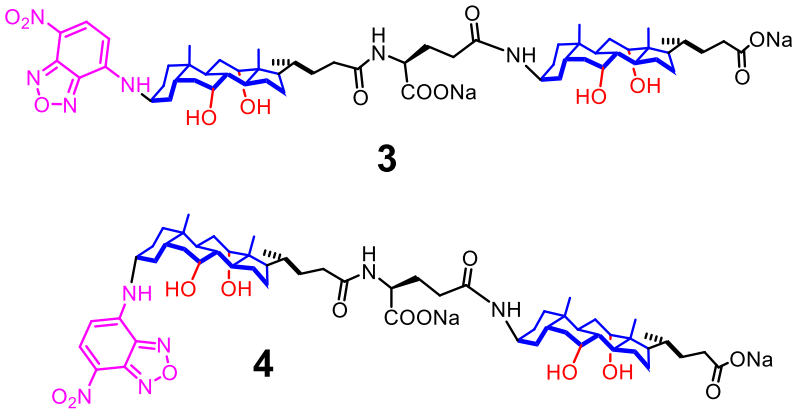

Scheme 4. Structures of bischolate foldamers.

Evaluation of Bischolate Membrane-Curvature Sensors

The performance of these bischolates as membrane-curvature sensors was evaluated by a fluorescence enhancement assay used by many researchers.[13,14,16,26,27] Briefly, a given concentration of liposomes of a certain size was added to an aqueous solution of the membrane-curvature sensor. Association of the sensor with the hydrophobic membranes enhances the emission of the sensor. In general, the effectiveness of the sensor is measured by the extent of fluorescence enhancement and its response to liposome sizes (i.e., membrane curvatures).

We prepared three different batches of liposomes using the membrane extrusion method.[38] The hydrated liposomes made of 10:1 POPC/POPG were extruded through polycarbonate membranes with pore size of 30, 100, and 400 nm. The liposomes obtained, according to our DLS studies, had average diameters of 58, 83, and 141 nm. These numbers were consistent with literature reports for similarly prepared liposomes.[27]

As shown in Figure 1, although the emission intensity of all three probes increased in the presence of the liposomes, the three probes displayed dramatically different responses. Among the three bischolates, compound **1** showed the smallest enhancement in emission. We believe the main reason for the small enhancement might derive from its ionic state of the fluorophore. After the probe goes from a water-soluble state to a membrane-bound state, a nonionic fluorophore can easily enter the hydrophobic region of a membrane, thus experiencing a large change in environmental polarity. In contrast, an ionic fluorophore such as aminonaphthalene sulfonate may still have significant water-contact in the membrane-bound state, due to its poor solvation by the lipids and strong solvation by water. In this way,

an ionic fluorophore may not experience as clear a change in environmental polarity as a nonionic one. However, regardless of the magnitude of fluorescence enhancement, it is clear that bischolate **1** was not a good membrane-curvature sensor, as its emission enhancement did not display a monotonous trend as a function of the liposome size (Figure 1, △).

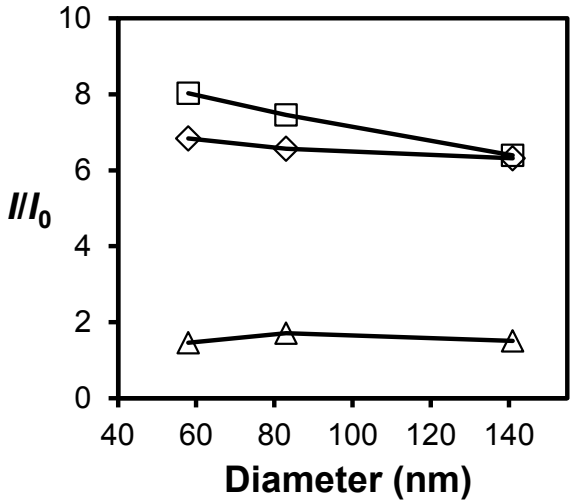

Figure 1. Enhancement in the fluorescence emission of bischolate foldamer **1** (△), **3** (◇), and **4** (□) induced by LUVs of different sizes. I and I_0 represent the maximum emission intensity of the probe in the presence of LUVs and in PBS buffer (pH 7.4), respectively. The experiments were typically run in duplicates and the errors in the two runs were generally <5%. [bischolate] = 0.10 μM. [lipids] = 300 μM. [POPC]/[POPG] = 10/1. The excitation wavelength (λ_{ex}) was 340, 470, and 470 nm for bischolate **1**, **3**, and **4**, respectively.

The NBD-functionalized bischolate **3** experienced a stronger enhancement of emission in the presence of the liposomes (Figure 1, ◇), possibly due to the nonionic nature of its fluorophore. Nonetheless, despite its stronger emission enhancement, this compound is

not a good membrane-curvature sensor either, as its emission intensity displayed a very small response to the membrane curvature.

The largest emission enhancement was observed for compound **4**, which has the same fluorophore as **3** but the opposite stereochemistry for the NBD group. This bischolate was clearly the best curvature sensor among the three, not only because of its strongest emission enhancement but, more importantly, a clear increase of emission intensity with increasing membrane curvature or decreasing liposome size (Figure 1, □). The results suggest that the location of the fluorescent label is highly important to the curvature sensing and having the NBD group on the hydrophilic α-face of the cholate is critical. According to our previous studies, bischolate **1** folds hydrophobically in water through the interactions of the β-faces of the cholates.[30] Although **3** and **4** have some significant differences from **1** (in terms of the orientation and nonionic nature of the fluorescent label), they are expected to fold in water similarly through the hydrophobic interactions of the cholate β-faces. This is because, for any hydrophobic molecules to be soluble in water, they need to minimize unfavorable solvent contact for their hydrophobic surfaces and the largest and most hydrophobic surfaces are the cholate β-faces.

The emission wavelength of the NBD group of **3** and **4** in aqueous buffer was quite similar (545–550 nm). There was no significant difference between the two over half of dozen measurements in our hands. The results suggest that the water exposure of the NBD groups in **3** and **4** was similar when the two compounds were dissolved in water. The conclusion is reasonable, as the two compounds are expected to fold in water through the hydrophobic association of the β-faces. In compound **4**, the NBD group was on the water-exposed α-face; folding is thus not expected to bury the fluorophore. In compound **3**,

although the NBD group was on the hydrophobic β-face of the cholate, its large size suggests that it is unlikely to be shielded from water contact either, at least not completely.

As the molecules (**3** and **4**) enter the membrane, totally different situations occurred. The maximum emission wavelength (λ_{em}) of the NBD of **3** occurred at 521 nm, regardless of the liposome sizes. In contrast, probe **4** emitted at 538 nm, also independent of the liposome sizes. Since these wavelengths are both blue-shifted in comparison to their emission wavelength in water (545–550 nm), the probes were undoubtedly interacting with the hydrophobic membranes after the addition of the liposomes. This conclusion is also consistent with the large increase of their emission intensity caused by the addition of the liposomes (Figure 1). The fact that the NBD of **3** emitted at a significantly lower wavelength that the NBD of **4** suggests that the former was located in a more hydrophobic microenvironment than the latter.[37] Given the location of the NBD on the hydrophobic β-face of the cholate in **4**, this is an extremely likely situation: as **3** enters the membrane, it has to hide its hydrophilic groups from the lipid hydrocarbon (Scheme 5, left), similar to the folded **1** in nonpolar solvents (Scheme 3). Since the NBD group is on the opposite site of the hydrophilic α-face, it should be in a fairly hydrophobic microenvironment. For compound **4**, the small change in λ_{em} upon binding with the membranes suggest that its NBD group was in a fairly polar environment, in agreement with the schematic representation of the folded bischolate in the membrane (Scheme 5, right).

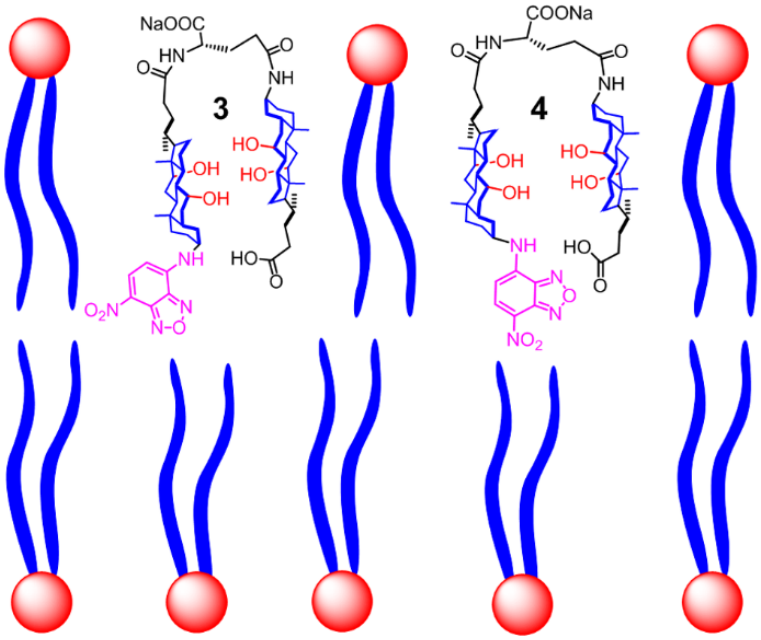

Scheme 5. Schematic representation of possible conformations of the folded **3** and **4** in the lipid bilayer. The carboxylic acid in the hydrophobic membrane is shown to be protonated whereas that in the aqueous environment to be deprotonated.

The emission wavelengths (λ_{em}) of **3** and **4** were reasonable from the location of the NBD group and the presumed reverse-micelle-like conformation of these molecules in a nonpolar membrane environment. What remains puzzling was the fact that bischolate **4** enjoyed a much stronger emission enhancement than **3** under similar conditions (Figure 1). Normally, one expects a fluorophore entering a more hydrophobic environment should emit more strongly. However, it has been reported that that for primary amine-derived NBD derivatives such as **3** and **4**, the quantum yield of the compounds were also influenced by other factors.[37] Although the general trend is that such compounds emit more strongly in less polar solvents, *n*-propylamino-NBD was found to emit very weakly in highly nonpolar solvents such as hexane and cyclohexane but much more strongly in solvents of intermediate polarity including ethyl acetate, THF, dioxane, acetone, and chloroform. Since the NBD

group of **3** was on the β-face of the cholate, it would be expected to be in a more hydrocarbon-like environment than that of **4**. Thus, the stronger emission of **4** than **3** in the membrane-bound state is consistent with the behavior of *n*-propylamino-NBD in different solvents.

Our study so far indicates that bischolate **4** was the best membrane-curvature sensor for its high sensitivity and direct correlation between the emission enhancement and membrane curvature. We wondered whether the sensitivity was a result of a stronger binding with higher-curvature membranes or some other factors. The binding affinity of a membrane-curvature sensor to the membrane can be determined by fluorescence titration, in which the concentration effect of the liposomes on the emission intensity of the sensor is measured.[27,39] The affinity is defined as the apparent molar partition coefficient (K_p) of the probe between lipid membranes and the aqueous solution and is described by the following two equations:

$$\% \text{ bound} = (F - F_0)/(F_{100} - F_0) \times 100\% \quad (1)$$

$$\% \text{ bound} = (C_a K_p)/(1 + C_a K_p) \times 100\% \quad (2)$$

in which F is the maximum NBD emission intensity at a given lipid concentration, F_0 is the NBD emission intensity in the buffer in the absence of lipids, F_{100} is the emission intensity at lipid saturation, and C_a is the concentration of the accessible lipids in the sample. For large unilamellar vesicles (LUVs) as we have, the accessible lipids amount to 50% of the total lipid concentration.[27]

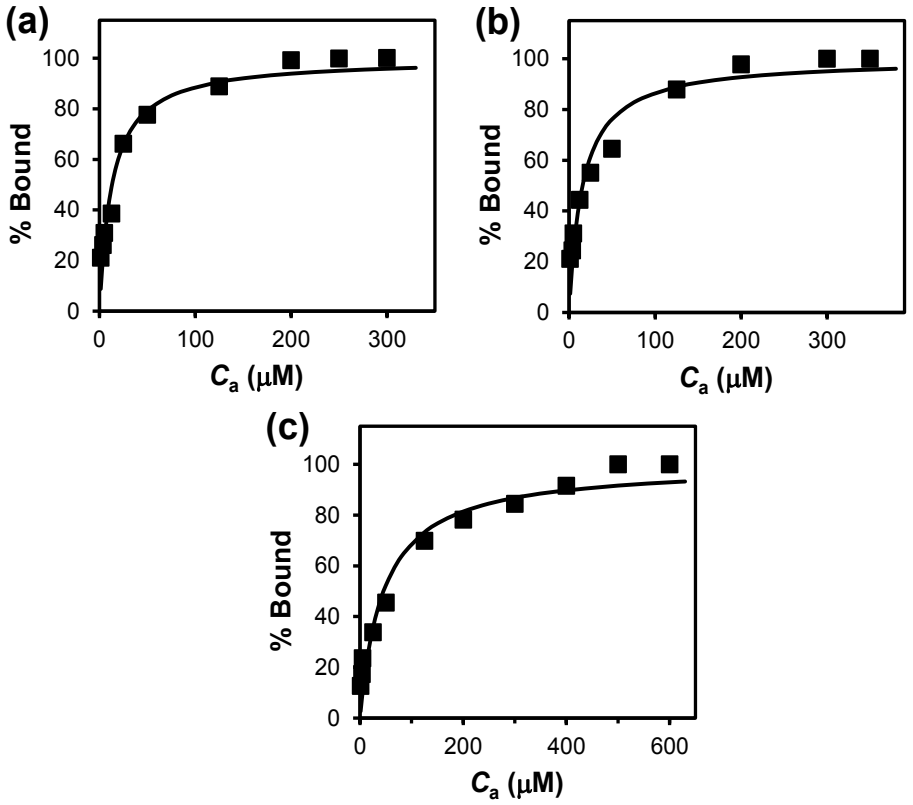

Figure 2. Binding of bischolate **4** in PBS buffer (pH 7.4) by LUVs with the average diameter of (a) 58, (b) 83, and (c) 141 nm. The smooth curves are nonlinear least squares curving fitting of the binding data to eq 2. [bischolate] = 0.10 μM. C_a is the concentration of the accessible lipid and is 50% of the total lipid in the sample.

Figure 2 shows the fluorescence titration of probe **4**, our best membrane-curvature sensor, by liposomes of different sizes. The data fit quite nicely to equation 2 and allowed us to understand the binding affinities of the probe to the membranes. The binding data are summarized in Table 1, which also contains the data for probes **1** and **3**.

For biologically derived membrane-curvature sensors such as amphipathic α-helices, it has been found that their preferential binding to highly curvature membranes is mainly caused by a higher number of hydrophobic binding sites (i.e., packing defects) rather than a stronger binding affinity.[26] For liposomes ranging from 75 to 500 nm in size, for example, the binding affinity displayed a mere 2- to 2.5-fold increase with decreasing liposome sizes. Our binding data in general showed the same trend. For all three probes, the apparent molar partition coefficient (K_p) increased with decreasing liposome sizes. The largest increase was almost 4-fold. Thus, the binding affinity of these bischolate probes was somewhat more sensitive to the membrane curvature than that of the naturally occurring amphipathic α-helices. One possibility for the more sensitive binding affinity could originate from the size of the hydrophobic groups in our bischolates. Amphipathic α-helices rely on their hydrophobic amino acid side chains to bind the hydrophobic packing defects in the membrane. Since these groups are much smaller than the cholate groups in our probes, they might be able fit into many smaller binding sites that our probes simply cannot bind. If this is indeed the case, our probe could be sensing preferentially the larger hydrophobic packing defects in comparison to natural α-helical membrane-curvature sensors. Such a feature makes our probe complementary to the natural sensors and may be useful in certain settings.

Table 1. Apparent partition coefficients (K_p) for the oligocholate foldamers in PBS buffer (pH 7.4)[a]

entry	Liposome size (nm)	Probe	K_p (10^3 M^{-1})
1	58	**1**	41 ± 7
2	83	**1**	33 ± 4
3	141	**1**	15 ± 3
4	58	**3**	50 ± 8
5	83	**3**	39 ± 7
6	141	**3**	13 ± 2
7	58	**4**	77 ± 10
8	83	**4**	64 ± 10
9	141	**4**	22 ± 4

[a] [bischolate] = 0.10 μM. [POPC]/[POPG] = 10/1. The binding data were obtained by nonlinear least squares curving fitting of the binding data to eq 2.

There are two other important conclusions we can draw from the binding data. First, although the binding affinity of all our probes displayed a monotonous increase with decreasing liposome sizes and thus increasing membrane curvatures (Table 1), only probe **4** showed monotonous changes in emission enhancement as a function of the liposome size (Figure 1). Clearly, in addition to binding affinity, other factors such as the location of the fluorophore in the probe (and in turn the location in the membrane) and the ionic nature of the fluorophore are all important to the emission intensity. Since measuring the binding affinity involves a substantially larger amount of work, probe **4** remains the sensor of choice

in our study. Second, the binding affinity of the probe to lipid membranes overall correlates with the fluorescence enhancement for the three probes, particularly for the smaller liposomes. The binding affinity, for example, followed the order of **4** > **3** > **1** for liposomes 58 and 83 nm in size.[40] The binding affinity seemed to make sense from the viewpoint of hydrophobic driving force in the binding. Probe **1** has a total of three ionic groups (two carboxylates and one sulfonate); its strong hydrophilicity is expected to lower the hydrophobic driving force for the binding. In addition, our membranes were overall negatively charged, with a ratio of [POPG]/[POPC] = 10/1. A larger number of anionic groups in **1** also translates to a stronger repulsion by the liposomes. The stronger binding of **4** over **3** by the liposomes also seems to be reasonable. The NBD group of **4** is on the hydrophilic α-face of the cholate and thus is completely exposed to water in the water-soluble state. The unfavorable water-contact for the NBD probably provided a stronger hydrophobic driving force for the probe to enter the membrane. For probe **3**, although the NBD group must also have significant water-exposure (as discussed above in terms of its emission wavelength), its location on the hydrophobic β-face of the cholate suggests that it should be in partial contact with the other folded hydrophobic cholate. Undoubtedly, more hydrophobic contact *prior to* binding to the membranes means that part of the hydrophobic surface is already buried and thus is equivalent to a lower hydrophobic driving force for the binding.

All the data so far suggest that probe **4** is the best membrane-curvature sensor among the three, displaying the strongest emission enhancement (Figure 1), a monotonous response to lipid curvatures (Figure 1), and the strongest binding for lipid membranes (Table 1). It is known that the composition of lipids also have an impact on the number of hydrophobic

binding sites in the membranes. Cholesterol, for example, is able to reduce the number of hydrophobic defects in a membrane.[41] Figure 3a shows the emission enhancement of the three probes as a function of liposome sizes for POPC/POPG membranes consisting of 30 mol % cholesterol. Probe **4** clearly remained as the most sensitive membrane-curvature sensor in the high cholesterol membranes. Overall, the inclusion of cholesterol in the lipids lowered the fluorescence enhancement, especially for probes **3** (◇) and **4** (□). The trend could be seen more clearly in Figure 3b, showing the I/I_0 curve with 30 mol % (▲) cholesterol significantly lower than those with 0 (■) and 10 (◆) mol % cholesterol.

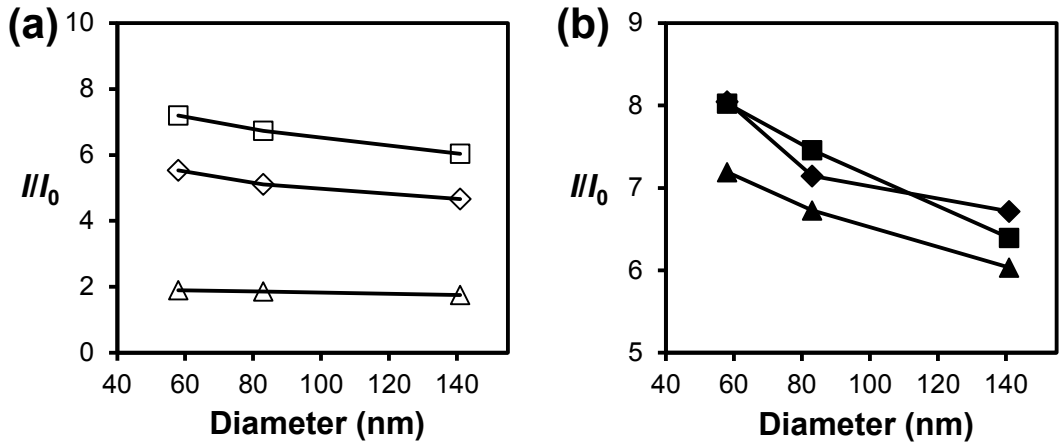

Figure 3. (a) Enhancement in the fluorescence emission of bischolate foldamer **1** (△), **3** (◇), and **4** (□) induced by LUVs of different sizes made of 10:1 POPC/POPG consisting of 30 mol % cholesterol. (b) Enhancement in the fluorescence emission of oligocholate foldamer **4** induced by LUVs made of 10:1 POPC/POPG consisting of 0 (■), 10 (◆), and 30 mol % (▲) cholesterol. I and I_0 represent the maximum emission intensity of the probe in the presence of LUVs and in PBS buffer (pH 7.4), respectively. [bischolate] = 0.10 μM. [lipids] = 300 μM.

Our membrane-curvature sensor (i.e., **4**) is an anionic foldamer. Since its binding with the membrane is driven by hydrophobic interactions and electrostatic repulsion exists between the anionic foldamer and the negatively charged POPC/POPG membranes, we wanted to see whether the electric potential of the liposomes will influence the performance of the sensor. Figure 4a shows the fluorescence enhancement of **4** in the presence of the same concentrations of 50:1 (□), 10:1 (◇), and 0:1 (△) POPC/POPG liposomes. Overall, the membranes consisting the least amount of anionic lipids (i.e., POPG) showed the largest enhancement, while those with the highest amount of POPG showed the smallest enhancement. Thus, electrostatic repulsion between the membranes and the sensor indeed impacted the binding negatively. As shown in Figure 4b, increasing POPG in the lipid formulation consistently lowers the emission of the probe, most likely due to weaker binding between the more negatively charged membranes and the anionic sensor.

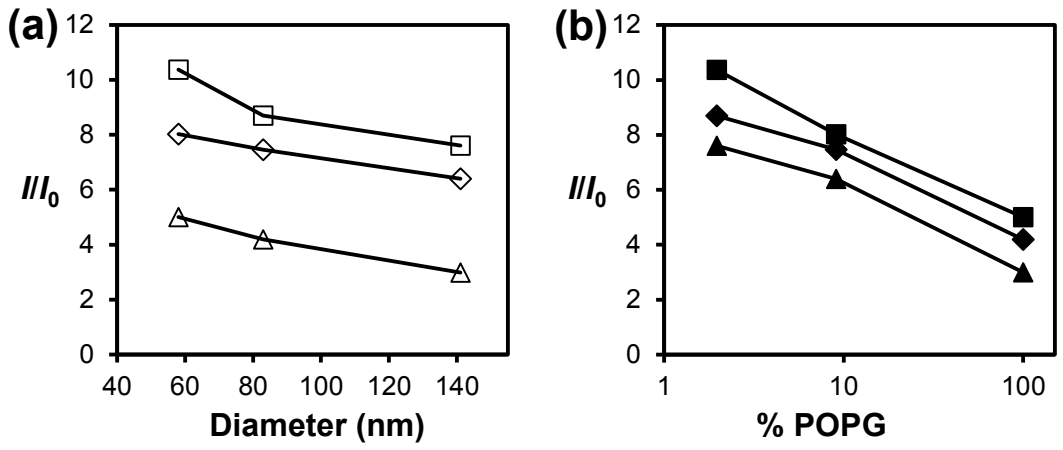

Figure 4. (a) Enhancement in the fluorescence emission of oligocholate foldamer **4** induced by LUVs made of 50:1 (□), 10:1 (◇), and 0:1 (△) POPC/POPG. (b) Enhancement in the fluorescence emission of oligocholate foldamer **4** induced by 58 (■), 83 (◆), and 141 nm (▲) LUVs with different lipid formations. I and I_0 represent the maximum emission intensity

of the probe in the presence of LUVs and in PBS buffer (pH 7.4), respectively. [bischolate] = 0.10 μM. [lipids] = 300 μM.

Conclusion

In comparison to the membrane curvature-sensors found in nature (mainly proteins and amphipathic α-helices), the bischolates reported in this work is much easier to synthesize. Importantly, their ability to act as curvature-sensors can be tuned rationally as shown by this study. Their design is highly modular and each component in the structure has specific functions: the amphiphilic β-cholates interacting with water and membranes in a predictable fashion; the glutamic acid tether provides the flexibility for the two cholates to interact intramolecularly; the anionic carboxylates on the cholate and the glutamic acid make the probe water-soluble; the environmentally sensitive fluorophore reports the transition from the water-soluble state to the membrane-bound state in a curvature-dependent fashion. It is significant that the ionic nature and the orientation of the fluorescent label are critical to the performance of the bischolates as the sensor. Their simple synthesis as compared to the natural membrane-curvature sensors makes them potentially useful tools in biophysics and biochemistry.

Acknowledgement

We thank NSF (CHE-1303764) for financial support of the research.

Experimental Section

General Method

For spectroscopic purpose, methanol, tetrahydrofuran, hexanes, and ethyl acetate were of HPLC grade. All other reagents and solvents were of ACS-certified grade or higher,

and were used as received from commercial suppliers. Routine ^{1}H and ^{13}C NMR spectra were recorded on a Bruker DRX-400, on a Bruker AV II 600 or on a Varian VXR-400 spectrometer. MALDI-TOF mass was recorded on a Thermobioanalysis Dynamo mass spectrometer. UV-vis spectra were recorded at ambient temperature on a Cary 100 Bio UV-visible spectrophotometer. Fluorescence spectra were recorded at ambient temperature on a Varian Cary Eclipse Fluorescence spectrophotometer. Dynamic Light Scattering (DLS) data were recorded at 25 °C using PDDLS/ CoolBatch 90T with PD2000DLS instrument.

Abbreviations

POPC: 1-palmitoyl-2-oleoyl-sn-glycero-3-phosphocholine; POPG: 1-palmitoyl-2-oleoyl-sn-glycero-3-[phospho-rac-(1-glycerol)] sodium salt; PBS: Phosphate buffered saline.

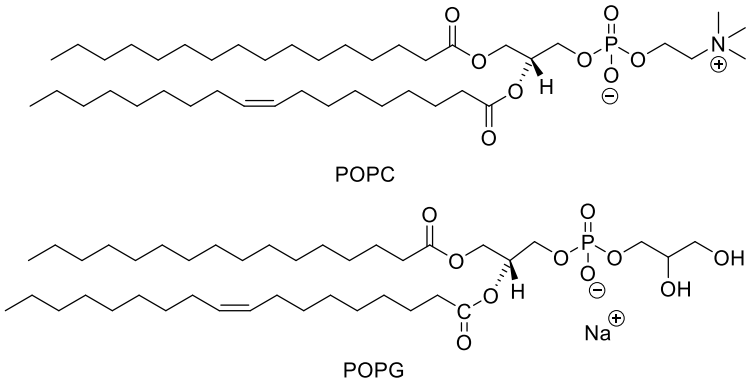

Scheme 6. Structures of POPC and POPG.

Syntheses

Syntheses of compounds **1**,[30] **2**,[30] **5**,[30] **6**,[30] **7**,[30] **8**,[30] **11**,[20] **12**,[20] **13**,[20] **14**,[20] **15**,[20] **16**,[20] **17**,[20] **18**,[20] **19**,[42] **20**,[42] **21**,[42] and **22**[42] were previously reported.

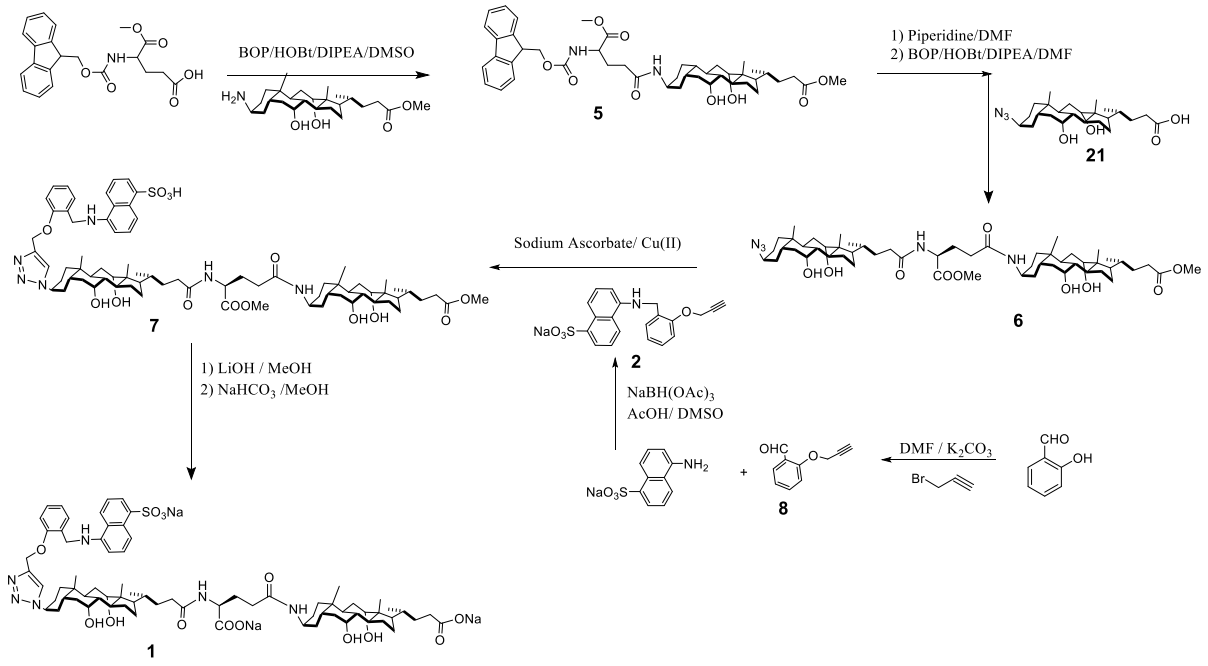

Scheme 7. Synthesis of compound **1.**

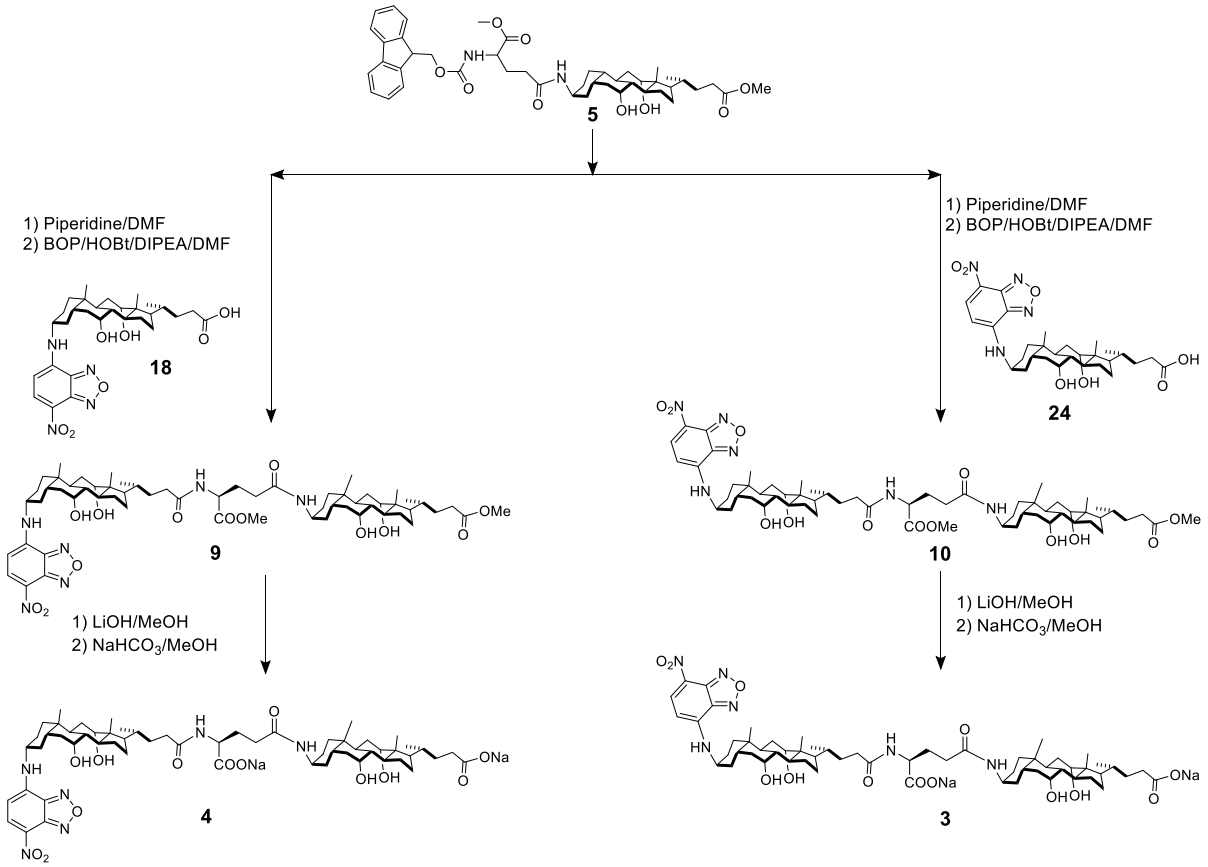

Scheme 8. Synthesis of compound **3** and compound **4.**

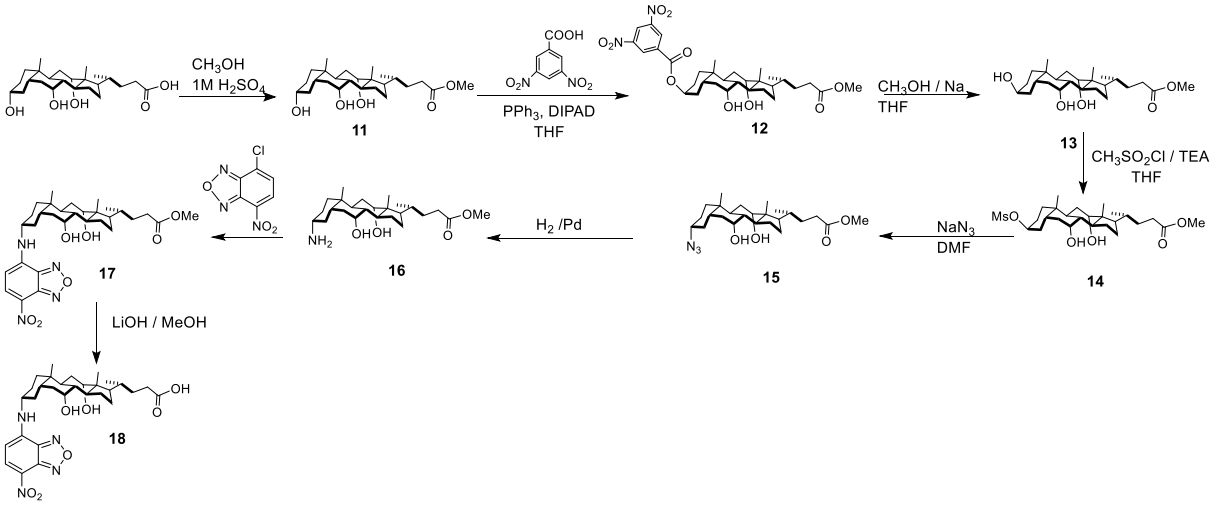

Scheme 9. Synthesis of compound **18.**

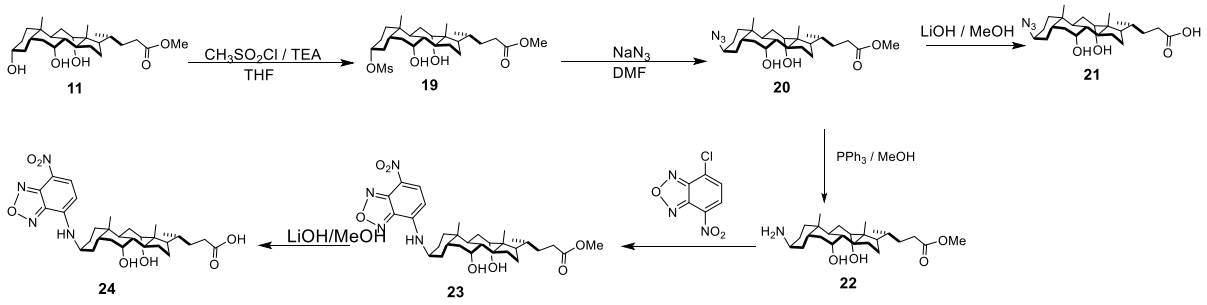

Scheme 10. Synthesis of compound **21** and compound **24.**

Compound 23. Compound **22** (0.30 g, 0.7 mmol) and NBD Chloride (4-Chloro-7-Nitrobenzofurazan, 0.29 g, 1.1 mmol) were dissolved in methanol (10 mL). Sodium bicarbonate (0.12 g, 1.4 mmol) was added to the solution. The reaction mixture was stirred at room temperature for 20 h. Solvent was removed in vacuo. The residue was diluted with water (20 mL) and extracted with ethyl acetate (2 × 30 mL). The combined organic phase was washed with brine (40 mL), dried over $MgSO_4$, filtered, concentrated *in vacuo*, and purified by column chromatography over silica gel using 1:2 ethyl acetate/hexane as the eluent to give an orange color powder (0.249 g, 60%). ^{1}H NMR (600 MHz, $CDCl_3/CD_3OD$ =

1:1, δ): δ 8.46 (d, *J* = 8.8 Hz, 1H), 6.28 (s, 1H), 3.96 (d, *J* = 3.4 Hz, 1H), 3.83 (s, 1H), 3.64 (s, 3H), 2.76 (td, *J* = 14.4, 4.1 Hz, 1H), 2.51-0.80 (series of m), 0.69 (s, 3H). ^{13}C NMR (150 MHz, $CD_3OD/CDCl_3$, 1:1, δ): 175.4, 170.9, 144.4, 144.1, 137.1, 122.2, 99.4, 98.3, 77.7, 77.5, 77.3, 76.7, 72.7, 67.8, 51.2, 50.1, 48.7, 48.6, 48.5, 48.3, 48.2, 48.0, 47.9, 46.8, 46.3, 41.6, 39.4, 37.1, 35.3, 35.1, 34.0, 32.3, 30.9, 29.5, 28.4, 27.4, 26.2, 23.5, 23.0, 22.6, 20.6, 16.8, 12.2. ESI-MS (m/z): $[M+H]^+$ cacld for $C_{31}H_{45}N_4O_7$, 585.3283; found, 585.3285.

Compound 24. Compound **23** (0.23 g, 0.38 mmol) was dissolved in methanol (4.00 mL) and 2.00 M lithium hydroxide (1.88 mL, 3.80 mmol) was added to it. The mixture was stirred overnight at room temperature. Upon completion of the reaction as indicated by TLC, the organic solvent was removed by rotary evaporation. After addition of a dilute HCl solution (0.05 M, 20 mL), the precipitate formed was collected by suction filtration or centrifugation, washed with cold water, and dried *in vacuo* to get an orange powder (0.21 g, 99%). ^{1}H NMR (600 MHz, $CDCl_3/CD_3OD$ = 1:1, δ): δ 8.46 (d, *J* = 8.8 Hz, 1H), 6.28 (s, 1H), 3.96 (d, *J* = 3.4 Hz, 1H), 3.83 (s, 1H), 2.76 (td, *J* = 14.4, 4.1 Hz, 1H), 2.51-0.80 (series of m), 0.69 (s, 3H). ESI-MS (m/z): $[M+H]^+$ cacld for $C_{30}H_{43}N_4O_7$, 571.3053; found, 571.3126.

Compound 9. Compound **5** (0.62 g, 0.79 mmol) was dissolved in an aqueous solution of piperidine (0.7 mL, 20%). After the reaction mixture was stirred for 2 h at room temperature, it was concentrated by rotary evaporation. The residue (0.050 g, 0.089 mmol) was then mixed with compound **18** (0.056 g, 0.097 mmol), (benzotriazol-1-yloxy)tris(dimethylamino)phospho-nium hexafluorophosphate (0.078 g, 0.177 mmol), 1-hydroxybenzotriazole hydrate (0.024 g, 0.177 mmol), and N,N-diisopropylethylamine (DIPEA, 0.123 mL, 0.708 mmol) in dry DMF (2 mL). The reaction was stirred for 2 h in a microwave reactor at 90 °C (150 W), extracted with ethyl acetate (3 × 10 mL), washed with

water (5 mL), and dried with $MgSO_4$. The solvent was removed by rotary evaporation, and the residue was purified by column chromatography over silica gel with 20:1 dichloromethane/methanol as the eluent to give a yellow powder (74 mg, 75%).^{1}H NMR (600 MHz, $CD_3OD/CDCl_3$, 1:1, δ): 8.49 (d, *J* = 9.1 Hz, 1H), 8.08(s, 1H) 7.57 (d, *J* = 7.1 Hz, 1H), 6.29 (d, *J* = 8.7 Hz, 1H), 4.40 (dq, *J* = 7.3, 3.9, 2.2 Hz, 1H), 4.01 (dq, *J* = 6.4, 3.1 Hz, 2H), 3.94 (d, *J* = 3.4 Hz, 1H), 3.83 (dq, *J* = 16.0, 3.1 Hz, 2H), 3.69 (s, 6H), 2.59-0.80 (series of m), 0.71 (d, *J* = 20.9 Hz, 6H). ^{13}C NMR (150 MHz, $CD_3OD/CDCl_3$, 1:1, δ): 175.4, 172.5, 144.5, 137.5, 121.2, 98.5, 77.8, 77.6, 77.4, 72.8, 72.7, 67.9, 67.7, 54.6, 52.2, 51.9, 51.1, 47.8, 46.8, 46.7, 46.3, 46.2, 45.9, 42.6, 41.9, 41.7, 41.6, 39.5, 39.4, 36.9, 35.5, 35.3, 35.0, 34.8, 34.4, 34.1, 33.2, 32.7, 32.2, 31.6, 30.9, 30.8, 30.7, 28.4, 28.1, 27.5, 27.4, 27.4, 26.6, 25.9, 24.2, 23.0, 22.5, 22.2, 16.7, 16.7, 12.2, 12.1, 12.1. ESI-MS (*m/z*): $[M+H]^+$ cacld for $C_{61}H_{93}N_6O_{13}$, 1117.6722; found 1117.6781.

Compound 4. Compound **9** (0. 102 g, 0.091 mmol) was dissolved in methanol (2.00 mL) and 2.00 M lithium hydroxide (0.912 mL, 1.82 mmol) was added to it. The mixture was stirred overnight at room temperature. Upon completion of the reaction as indicated by TLC, the organic solvent was removed by rotary evaporation. After addition of a dilute HCl solution (0.05 M, 20 mL), the precipitate formed was collected by suction filtration or centrifugation, washed with cold water, and dried *in vacuo* to get yellow powder (101 mg, 99%). To obtain the sodium salt of this compound, the above acid was mixed with saturated sodium bicarbonate (0.8 mL) and methanol (5 mL). The mixture was stirred for 5 h. After the solvents were removed by rotary evaporation, the residue was dissolved in methanol (5 mL). The solution was filtered and then concentrated by rotary evaporation to give the sodium salt as a yellow powder. For the acid derivative: ^{1}H NMR (400 MHz, $CD_3OD/CDCl_3$, 1:1, δ):

8.49 (d, *J* = 9.1 Hz, 1H), 8.08(s, 1H) 7.57 (d, *J* = 7.1 Hz, 1H), 6.29 (d, *J* = 8.7 Hz, 1H), 4.40 (dq, *J* = 7.3, 3.9, 2.2 Hz, 1H), 4.01 (dq, *J* = 6.4, 3.1 Hz, 2H), 3.94 (d, *J* = 3.4 Hz, 1H), 3.83 (dq, *J* = 16.0, 3.1 Hz, 2H), 2.59-0.80 (series of m), 0.71 (d, *J* = 20.9 Hz, 6H). ESI-MS (*m/z*): $[M+H]^+$ cacld for $C_{59}H_{89}N_6O_{13}$, 1089.6482; found 1089.6462.

Compound 10. Compound **5** (0.62g, 0.79 mmol) was dissolved in an aqueous solution of piperidine (0.7 mL, 20%). After the reaction mixture was stirred for 2 h at room temperature, it was concentrated by rotary evaporation. The residue (0.148 g, 0.26 mmol) was then mixed with compound **24** (0.136 g, 0.24 mmol), (benzotriazol-1-yloxy)tris(dimethylamino)phospho-nium hexafluorophosphate (0.211 g, 0.48 mmol), 1-hydroxybenzotriazole hydrate (0.064 g, 0.48 mmol), and N,N-diisopropylethylamine (DIPEA, 0.32 mL, 1.88 mmol) in dry DMF (2 mL). The reaction was stirred for 2 h in a microwave reactor at 90 °C (150 W), extracted with ethyl acetate (3 × 10 mL), washed with water (5 mL), and dried with $MgSO_4$. The solvent was removed by rotary evaporation, and the residue was purified by column chromatography over silica gel with 20:1 dichloromethane/methanol as the eluent to the yellow color powder (213 mg, 80%). ^{1}H NMR (400 MHz, $CD_3OD/CDCl_3$, 1:1, δ): 8.52 (d, *J* = 8.8 Hz, 1H), 6.34 (s, 1H), 4.43 (dd, *J* = 9.2, 4.8 Hz, 1H), 3.99 (m, 3H), 3.85 (m, 2H), 3.74 (s, 3H), 2.59-0.80 (series of m), 0.72 (s, 6H). ^{13}C NMR (100 MHz, $CD_3OD/CDCl_3$, 1:1, δ): 176.1, 173.4, 144.8, 137.9, 122.8, 100.1, 78.6, 78.2, 77.9, 77.6, 73.5, 68.6, 68.5, 52.9, 52.6, 51.9, 50.8, 48.1, 47.4, 47.0, 46.9, 46.5, 43.0, 42.3, 40.1, 40.0, 37.7, 37.6, 36.8, 36.2, 36.0, 35.7, 34.9, 34.7, 34.4, 33.9, 33.4, 32.9, 32.4, 31.6, 31.4, 31.0, 30.5, 30.2, 29.9, 29.6, 29.3, 29.1, 28.3, 28.1, 28.0, 26.9, 26.6, 24.9, 24.1, 23.7, 23.2, 22.4, 17.5, 17.4, 12.8. ESI-MS (*m/z*): $[M+H]^+$ cacld for $C_{61}H_{93}N_6O_{13}$, 1117.6722; found 1117.6788.

Compound 3. Compound **10** (0. 122 g, 0.109 mmol) was dissolved in methanol (3 mL) and 2.00 M lithium hydroxide (1.09 mL, 2.18 mmol) was added to it. The mixture was stirred overnight at room temperature. Upon completion of the reaction as indicated by TLC, the organic solvent was removed by rotary evaporation. After addition of a dilute HCl solution (0.05 M, 20 mL), the precipitate formed was collected by suction filtration or centrifugation, washed with cold water, and dried *in vacuo* to get yellow powder (121 mg , 99%). To obtain the sodium salt of this compound, the above acid was mixed with saturated sodium bicarbonate (0.8 mL) and methanol (5 mL). The reaction mixture was stirred for 5 h. After the solvents were removed by rotary evaporation, the residue was dissolved in methanol (5 mL). The solution was filtered and then concentrated by rotary evaporation to give the sodium salt as a yellow powder. For the acid derivative: ^{1}H NMR (400 MHz, CD_3OD, 1:1, δ): 8.49 (d, J = 9.1 Hz, 1H), 8.08(s, 1H) 7.57 (d, J = 7.1 Hz, 1H), 6.29 (d, J = 8.7 Hz, 1H), 4.40 (dq, J = 7.3, 3.9, 2.2 Hz, 1H), 4.01 (dq, J = 6.4, 3.1 Hz, 2H), 3.94 (d, J = 3.4 Hz, 1H), 3.83 (dq, J = 16.0, 3.1 Hz, 2H), 2.59-0.80 (series of m), 0.71 (d, J = 20.9 Hz, 6H). ESI-MS (*m/z*): $[M+H]^+$ cacld for $C_{59}H_{89}N_6O_{13}$, 1089.6482; found 1089.6462.

Liposome Size analysis

30 nm- 0 hrs

30 nm- 5 hrs

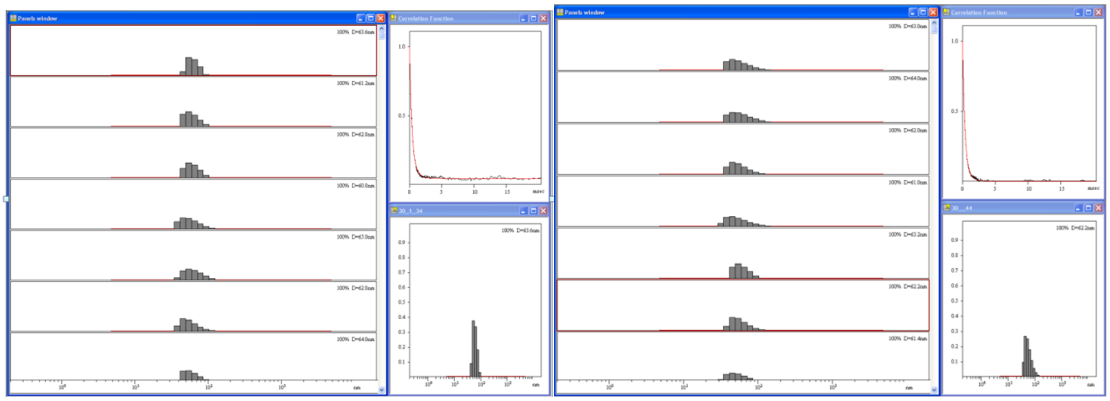

Figure 5. Average size obtained from DLS: 58 ± 5 nm.

100 nm- 0 hrs

100 nm- 5 hrs

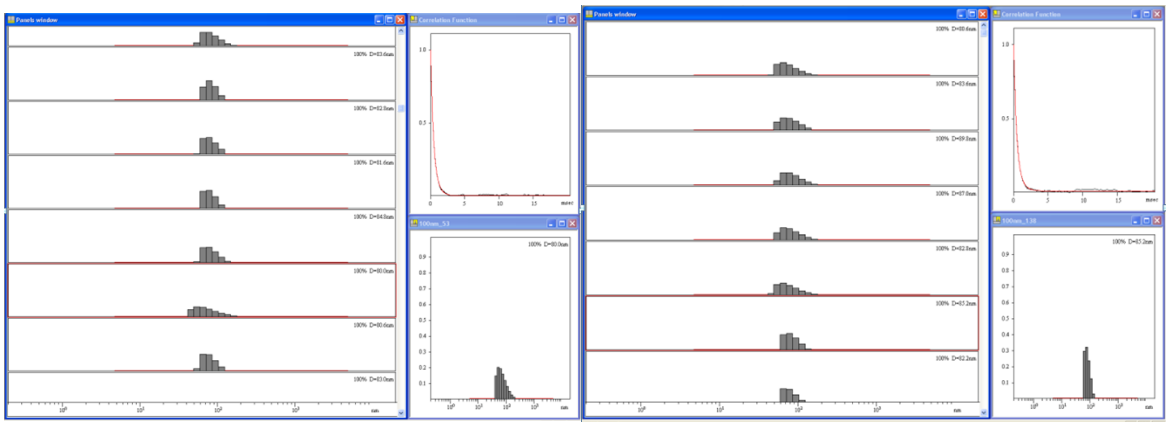

Figure 6. Average size obtained from DLS: 83 ± 7 nm.

400 nm- 0 hrs

400 nm- 5 hrs

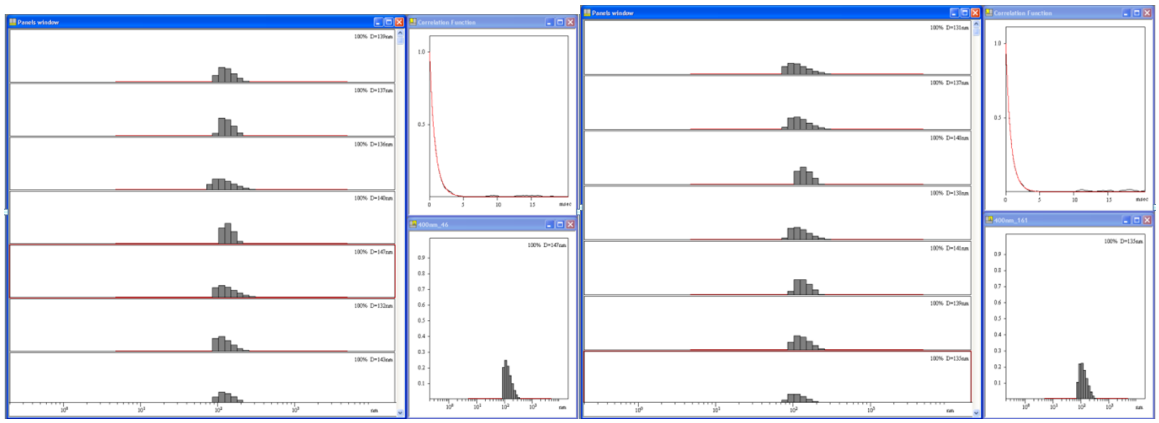

Figure 7. Average size obtained from DLS: 141 ± 8 nm.

Fluorescent enhancement data

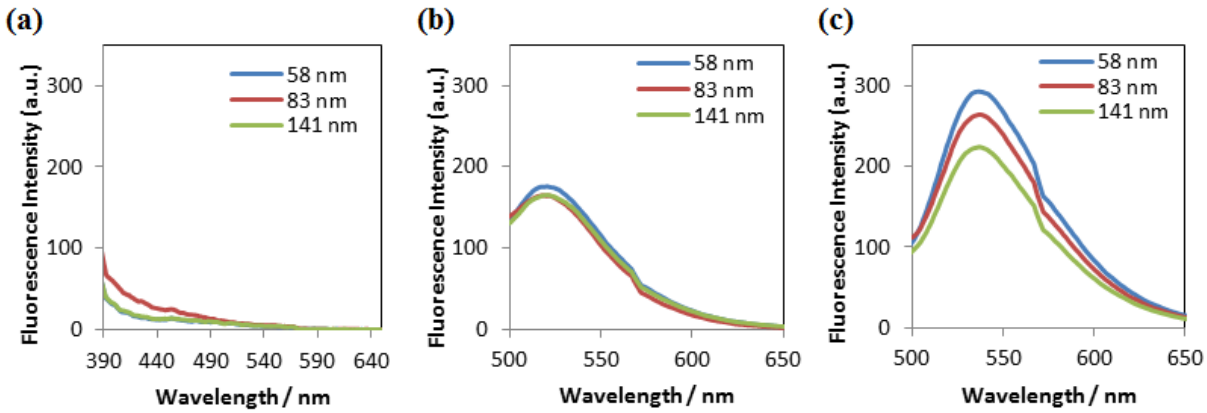

Figure 8. Emission spectra of bischolate foldamer **1** (a), **3** (b), and **4** (c) in the presence of different-sized LUVs made of 10:1 POPC/POPG in PBS buffer (pH 7.4). The experiments were typically run in duplicates and the errors in the two runs were generally <5%. [bischolate] = 0.10 μM. [lipids] = 300 μM. The excitation wavelength (λ_{ex}) was 340, 470, and 470 nm for bischolate **1**, **3**, and **4**, respectively.

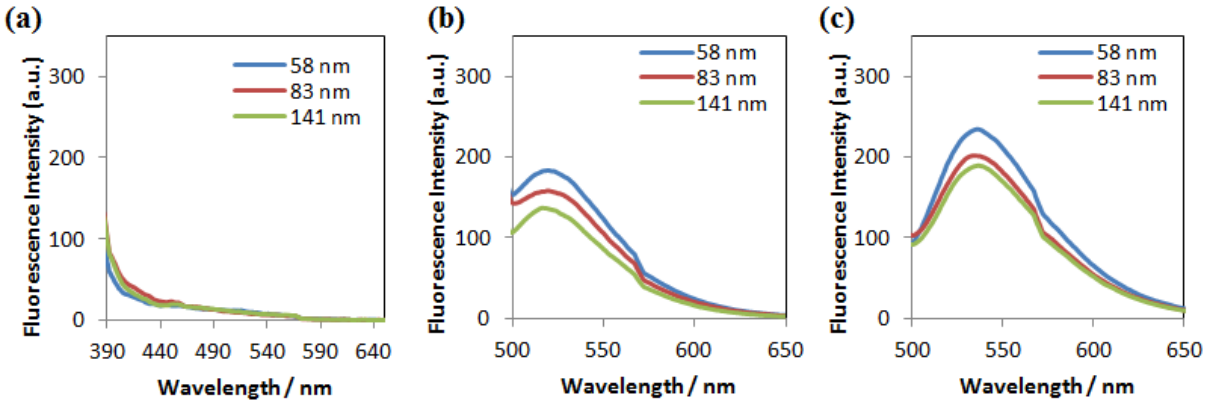

Figure 9. Emission spectra of bischolate foldamer **1** (a), **3** (b), and **4** (c) in the presence of different-sized LUVs made of 10:1 POPC/POPG containing 10% cholesterol in PBS buffer (pH 7.4). The experiments were typically run in duplicates and the errors in the two runs were generally <5%. [bischolate] = 0.10 μM. [lipids] = 300 μM. The excitation wavelength (λ_{ex}) was 340, 470, and 470 nm for bischolate **1**, **3**, and **4**, respectively.

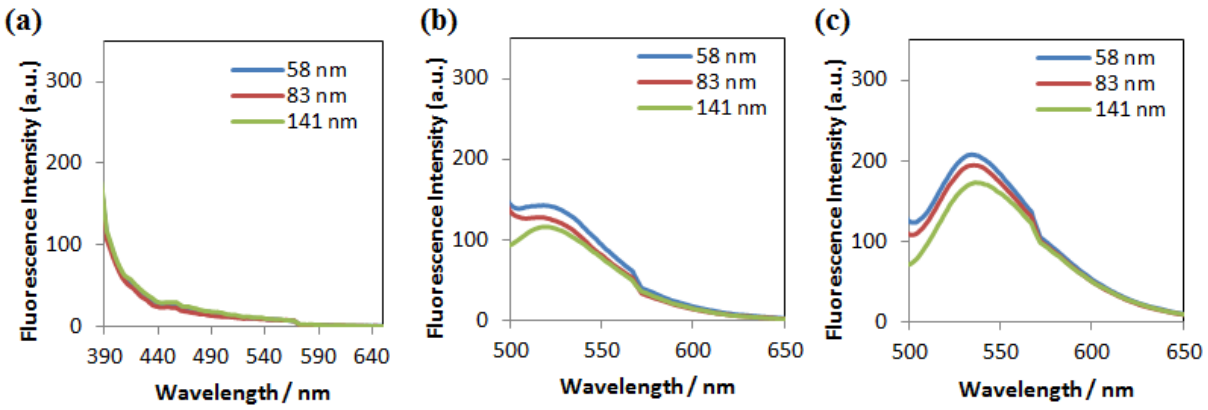

Figure 10. Emission spectra of bischolate foldamer **1** (a), **3** (b), and **4** (c) in the presence of different-sized LUVs made of 10:1 POPC/POPG containing 30% cholesterol in PBS buffer (pH 7.4). The experiments were typically run in duplicates and the errors in the two runs were generally <5%. [bischolate] = 0.10 μM. [lipids] = 300 μM. The excitation wavelength (λ_{ex}) was 340, 470, and 470 nm for bischolate **1**, **3**, and **4**, respectively.

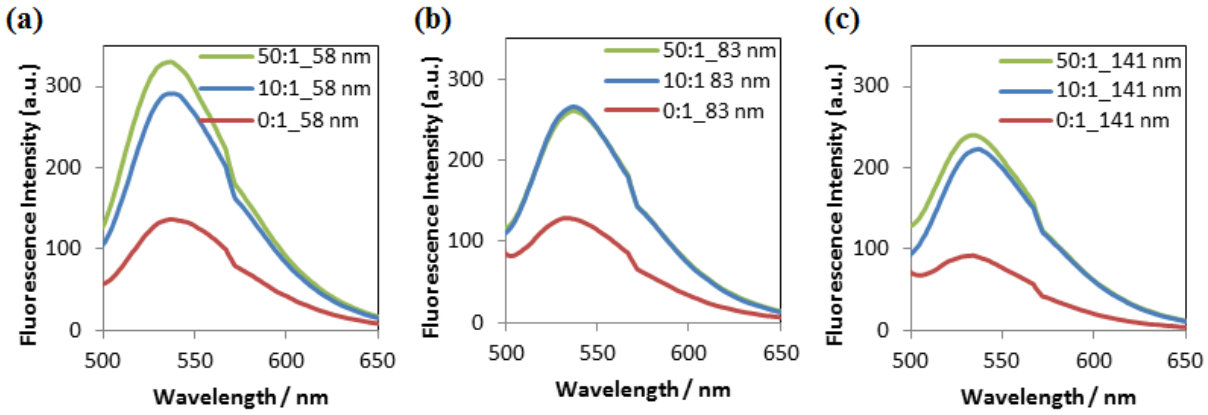

Figure 11. Emission spectra of bischolate foldamer **4** in the presence of LUVs of 58 (a), 83 (b), and 141 nm (c) containing different amounts of POPG in PBS buffer (pH 7.4). The experiments were typically run in duplicates and the errors in the two runs were generally <5%. [bischolate] = 0.10 μM. [lipids] = 300 μM. The excitation wavelength (λ_{ex}) was 470 nm.

^{1}H and ^{13}C NMR spectra

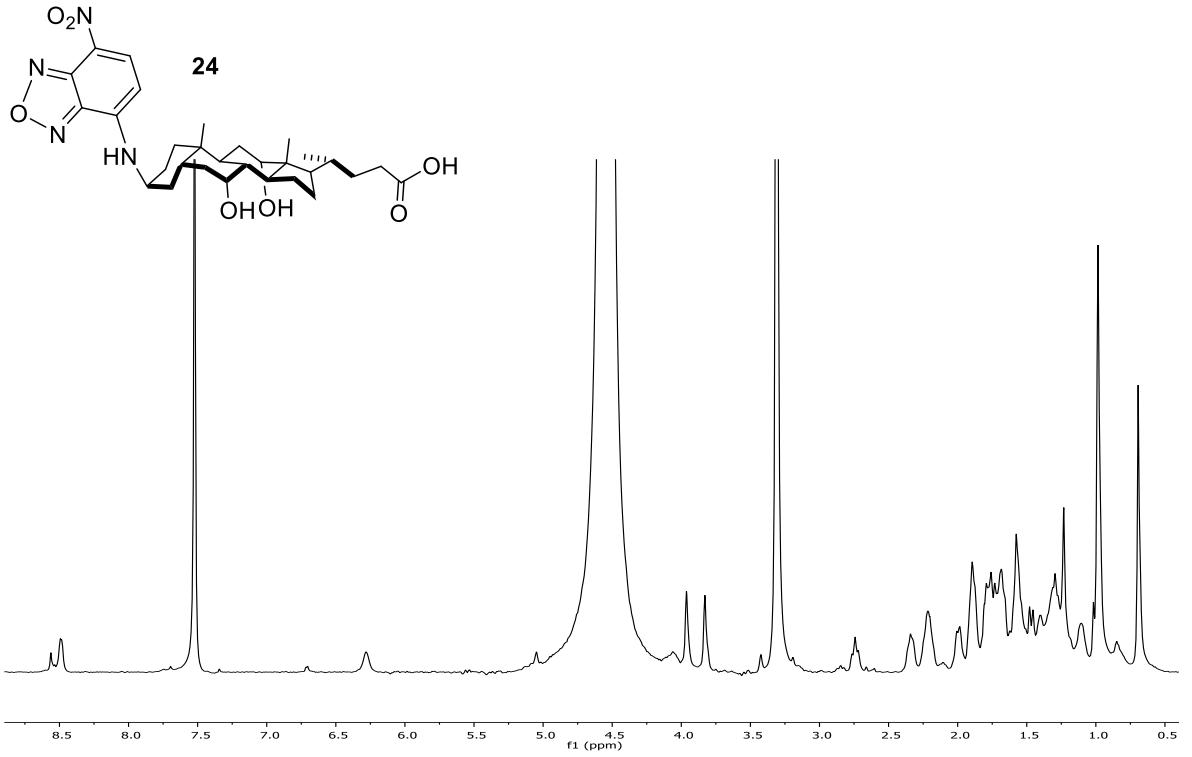

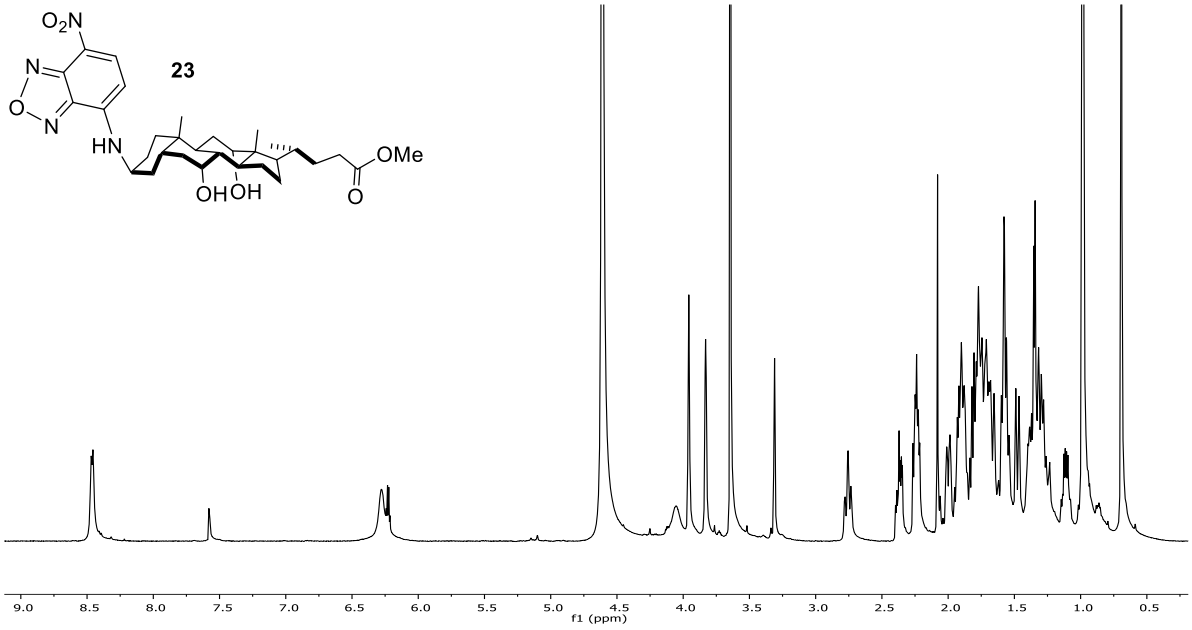

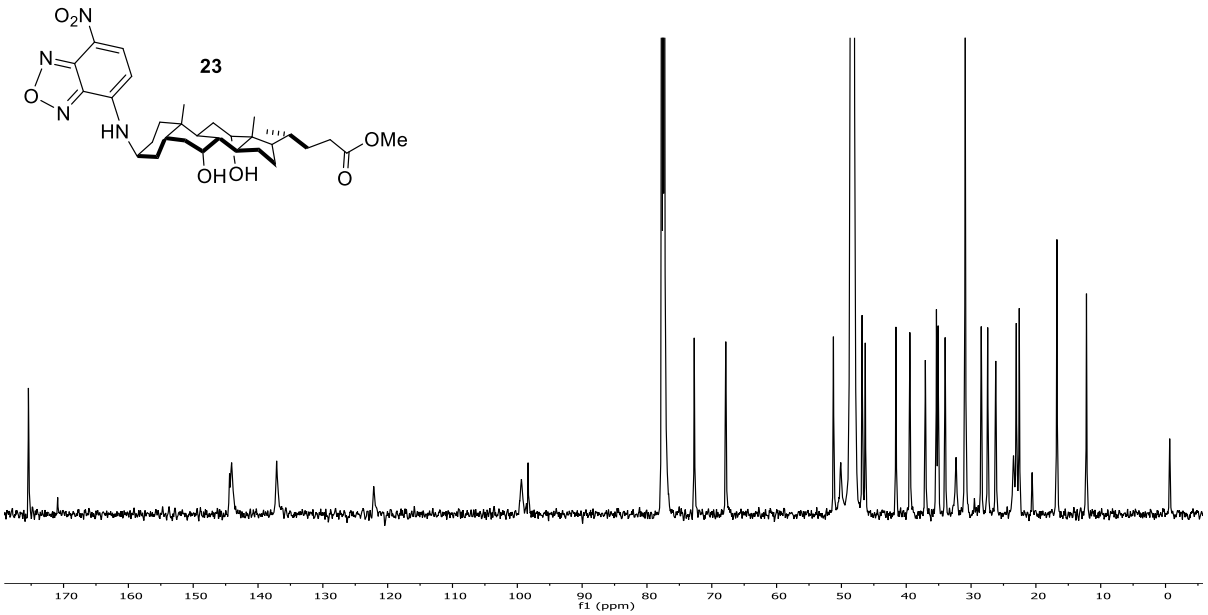

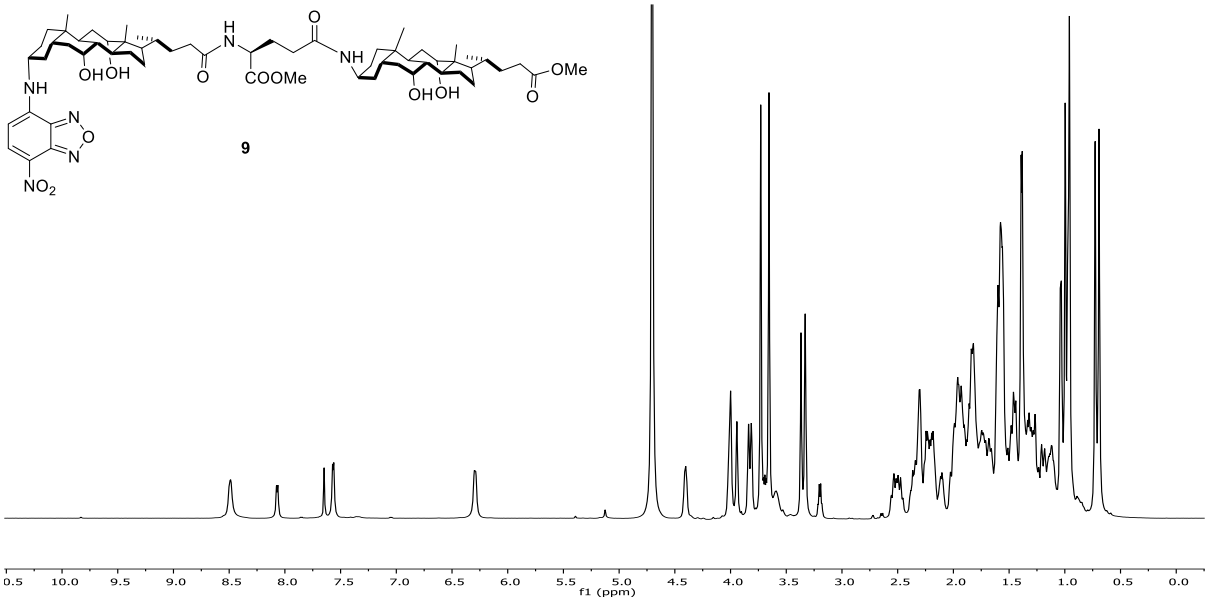

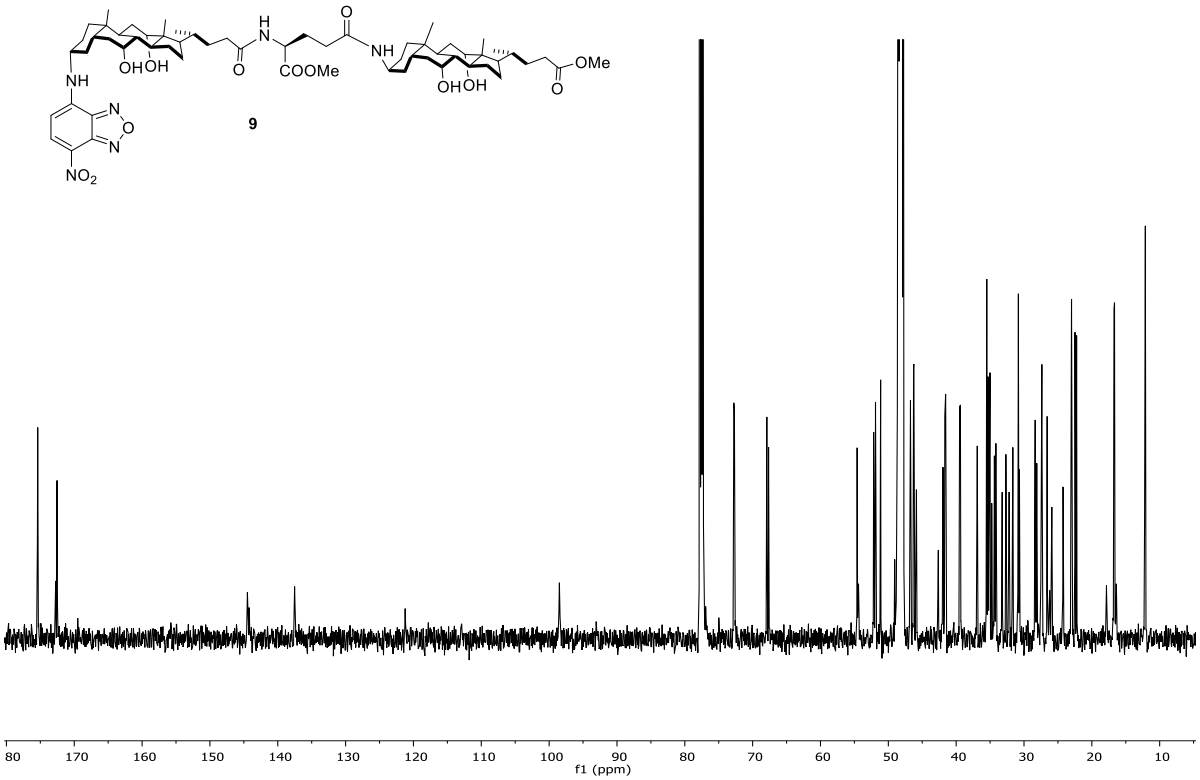

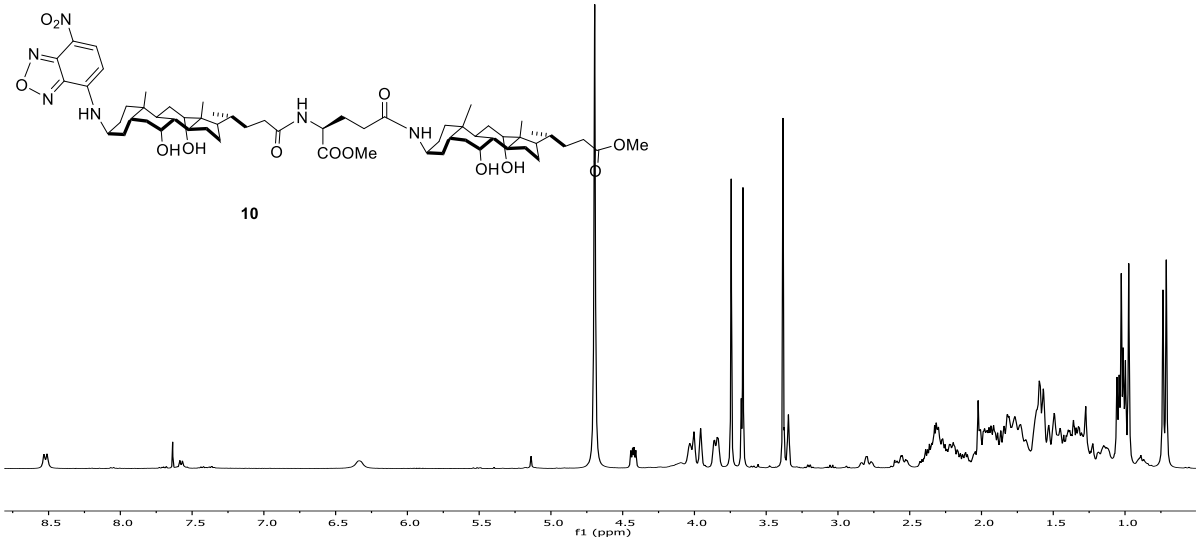

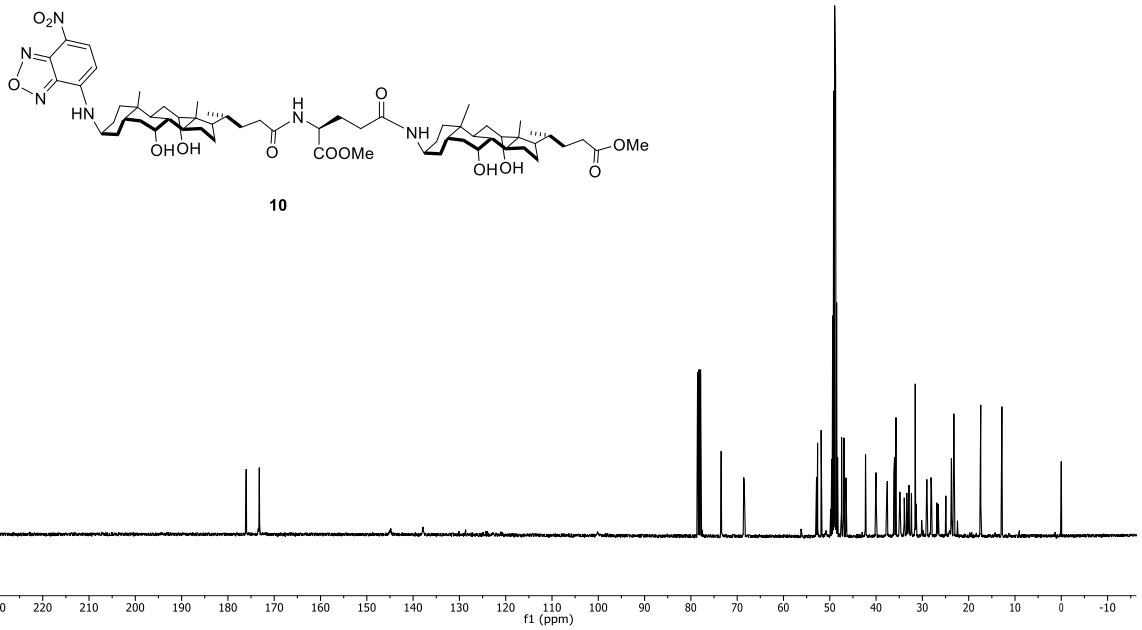

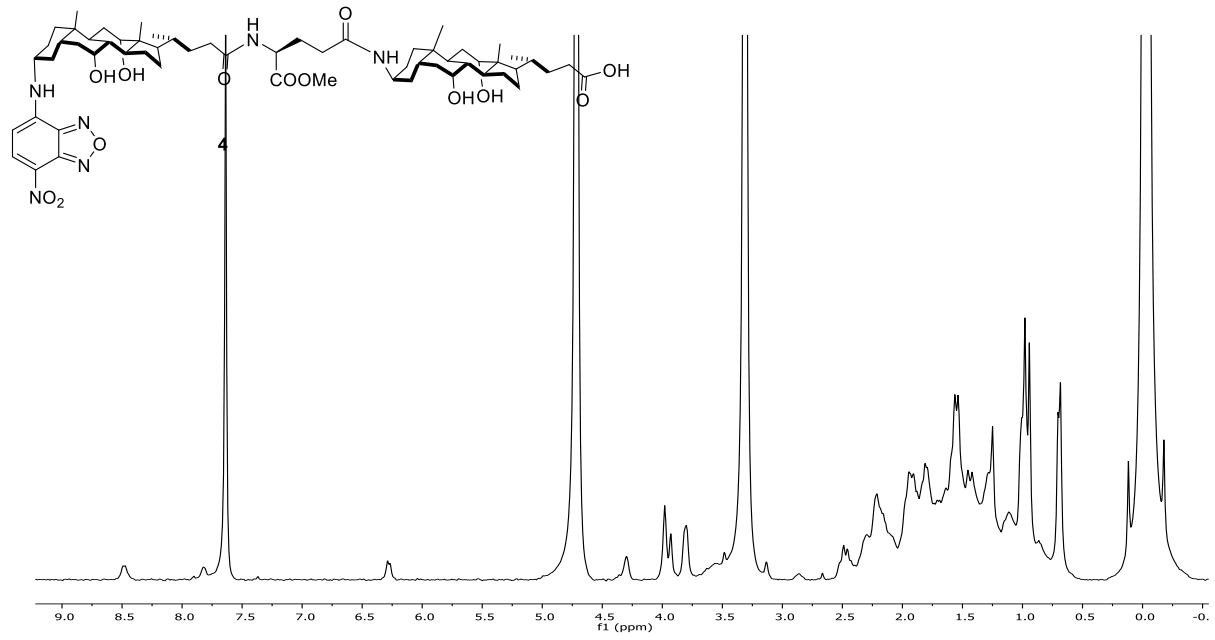

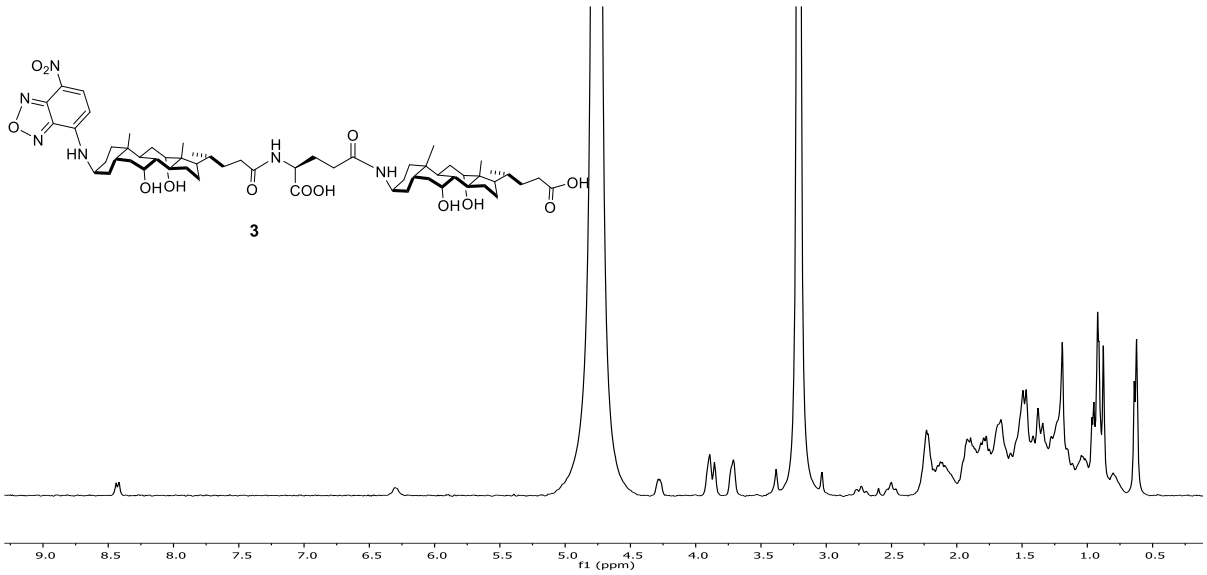

Notes and References

(1) Lee, A. G. *Biomembranes: A Multi-Volume Treatise*. JAI Press: Greenwich, 1995.

(2) Simons, K.; Vaz, W. L. C. Model Systems, Lipid Rafts, and Cell Membranes. *Annu. Rev. Biophys. Biomol. Struct.* **2004**, *33*, 269-295.

(3) Wenk, M. R. The Emerging Field of Lipidomics. *Nat. Rev. Drug Discov.* **2005**, *4*, 594-610.

(4) Edidin, M. The State of Lipid Rafts: From Model Membranes to Cells. *Annu. Rev. Biophys. Biomol. Struct.* **2003**, *32*, 257-283.

(5) Binder, W. H.; Barragan, V.; Menger, F. M. Domains and Rafts in Lipid Membranes. *Angew. Chem. Int. Ed.* **2003**, *42*, 5802-5827.

(6) McMahon, H. T.; Gallop, J. L. Membrane Curvature and Mechanisms of Dynamic Cell Membrane Remodelling. *Nature* **2005**, *438*, 590-596.

(7) Kozlov, M. M.; McMahon, H. T.; Chernomordik, L. V. Protein-Driven Membrane Stresses in Fusion and Fission. *Trends Biochem. Sci.* **2010**, *35*, 699-706.

(8) Antonny, B. Mechanisms of Membrane Curvature Sensing. *Annu. Rev. Biochem.* **2011**, *80*, 101-123.

(9) Baumgart, T.; Capraro, B. R.; Zhu, C.; Das, S. L. Thermodynamics and Mechanics of Membrane Curvature Generation and Sensing by Proteins and Lipids. *Annu. Rev. Phys. Chem.* **2011**, *62*, 483-506.

(10) Peter, B. J.; Kent, H. M.; Mills, I. G.; Vallis, Y.; Butler, P. J.; Evans, P. R.; McMahon, H. T. Bar Domains as Sensors of Membrane Curvature: The Amphiphysin Bar Structure. *Science* **2004**, *303*, 495-499.

(11) Frost, A.; Unger, V. M.; De Camilli, P. The Bar Domain Superfamily: Membrane-Molding Macromolecules. *Cell* **2009**, *137*, 191-196.

(12) Bigay, J.; Casella, J. F.; Drin, G.; Mesmin, B.; Antonny, B. Arfgap1 Responds to Membrane Curvature through the Folding of a Lipid Packing Sensor Motif. *EMBO J.* **2005**, *24*, 2244-2253.

(13) Drin, G.; Casella, J. F.; Gautier, R.; Boehmer, T.; Schwartz, T. U.; Antonny, B. A General Amphipathic Alpha-Helical Motif for Sensing Membrane Curvature. *Nat. Struct. Mol. Biol.* **2007**, *14*, 138-146.

(14) Saludes, J. P.; Morton, L. A.; Ghosh, N.; Beninson, L. A.; Chapman, E. R.; Fleshner, M.; Yin, H. Detection of Highly Curved Membrane Surfaces Using a Cyclic Peptide Derived from Synaptotagmin-I. *ACS Chem. Biol.* **2012**, *7*, 1629-1635.

(15) Hui, E.; Johnson, C. P.; Yao, J.; Dunning, F. M.; Chapman, E. R. Synaptotagmin-Mediated Bending of the Target Membrane Is a Critical Step in Ca(2+)-Regulated Fusion. *Cell* **2009**, *138*, 709-721.

(16) Morton, L. A.; Yang, H.; Saludes, J. P.; Fiorini, Z.; Beninson, L.; Chapman, E. R.; Fleshner, M.; Xue, D.; Yin, H. Marcks-Ed Peptide as a Curvature and Lipid Sensor. *ACS Chem. Biol.* **2013**, *8*, 218-225.

(17) Gellman, S. H. Foldamers: A Manifesto. *Acc. Chem. Res.* **1998**, *31*, 173-180.

(18) Hill, D. J.; Mio, M. J.; Prince, R. B.; Hughes, T. S.; Moore, J. S. A Field Guide to Foldamers. *Chem. Rev.* **2001**, *101*, 3893-4012.

(19) Hecht, S.; Huc, I. *Foldamers: Structure, Properties, and Applications*. Wiley-VCH: Weinheim, 2007.

(20) Zhao, Y.; Zhong, Z. Oligomeric Cholates: Amphiphilic Foldamers with Nanometer-Sized Hydrophilic Cavities. *J. Am. Chem. Soc.* **2005**, *127*, 17894-17901.

(21) Cho, H.; Zhao, Y. Environmental Effects Dominate the Folding of Oligocholates in Solution, Surfactant Micelles, and Lipid Membranes. *J. Am. Chem. Soc.* **2010**, *132*, 9890-9899.

(22) Zhao, Y.; Cho, H.; Widanapathirana, L.; Zhang, S. Conformationally Controlled Oligocholate Membrane Transporters: Learning through Water Play. *Acc. Chem. Res.* **2013**, *46*, 2763-2772.

(23) Cho, H.; Widanapathirana, L.; Zhao, Y. Water-Templated Transmembrane Nanopores from Shape-Persistent Oligocholate Macrocycles. *J. Am. Chem. Soc.* **2011**, *133*, 141-147.

(24) Cho, H.; Zhao, Y. Translocation of Hydrophilic Molecules across Lipid Bilayers by Salt-Bridged Oligocholates. *Langmuir* **2011**, *27*, 4936-4944.

(25) Zhang, S.; Zhao, Y. Oligocholate Foldamers as Carriers for Hydrophilic Molecules across Lipid Bilayers. *Chem. -Eur. J.* **2011**, *17*, 12444-12451.

(26) Hatzakis, N. S.; Bhatia, V. K.; Larsen, J.; Madsen, K. L.; Bolinger, P.-Y.; Kunding, A. H.; Castillo, J.; Gether, U.; Hedegard, P.; Stamou, D. How Curved Membranes Recruit Amphipathic Helices and Protein Anchoring Motifs. *Nat. Chem. Biol.* **2009**, *5*, 835-841.

(27) Chong, S. S.; Taneva, S. G.; Lee, J. M.; Cornell, R. B. The Curvature Sensitivity of a Membrane-Binding Amphipathic Helix Can Be Modulated by the Charge on a Flanking Region. *Biochemistry* **2014**, *53*, 450-461.

(28) Taotafa, U.; McMullin, D. B.; Lee, S. C.; Hansen, L. D.; Savage, P. B. Anionic Facial Amphiphiles from Cholic Acid. *Org. Lett.* **2000**, *2*, 4117-4120.

(29) Walker, S.; Sofia, M. J.; Kakarla, R.; Kogan, N. A.; Wierichs, L.; Longley, C. B.; Bruker, K.; Axelrod, H. R.; Midha, S.; Babu, S.; Kahne, D. Cationic Facial Amphiphiles: A Promising Class of Transfection Agents. *Proc. Natl. Acad. Sci. U. S. A.* **1996**, *93*, 1585-1590.

(30) Gunasekara, R. W.; Zhao, Y. Rationally Designed Cooperatively Enhanced Receptors to Magnify Host–Guest Binding in Water. *J. Am. Chem. Soc.* **2015**, *137*, 843-849.

(31) Zhao, Y. Conformation of Oligocholate Foldamers with 4-Aminobutyroyl Spacers. *J. Org. Chem.* **2009**, *74*, 834-843.

(32) Li, Y. H.; Chan, L. M.; Tyer, L.; Moody, R. T.; Himel, C. M.; Hercules, D. M. Study of Solvent Effects on Fluorescence of 1-(Dimethylamino)-5-Naphthalenesulfonic Acid and Related Compounds. *J. Am. Chem. Soc.* **1975**, *97*, 3118-3126.

(33) Zhao, Y.; Zhong, Z.; Ryu, E.-H. Preferential Solvation within Hydrophilic Nanocavities and Its Effect on the Folding of Cholate Foldamers. *J. Am. Chem. Soc.* **2007**, *129*, 218-225.

(34) Ryu, E.-H.; Yan, J.; Zhong, Z.; Zhao, Y. Solvent-Induced Amphiphilic Molecular Baskets: Unimolecular Reversed Micelles with Different Size, Shape, and Flexibility. *J. Org. Chem.* **2006**, *71*, 7205-7213.

(35) Janout, V.; Lanier, M.; Regen, S. L. Molecular Umbrellas. *J. Am. Chem. Soc.* **1996**, *118*, 1573-1574.

(36) Janout, V.; Lanier, M.; Regen, S. L. Design and Synthesis of Molecular Umbrellas. *J. Am. Chem. Soc.* **1997**, *119*, 640-647.

(37) Fery-Forgues, S.; Fayet, J.-P.; Lopez, A. Drastic Changes in the Fluorescence Properties of Nbd Probes with the Polarity of the Medium: Involvement of a Tict State? *J. Photochem. Photobiol. A* **1993**, *70*, 229-243.

(38) Olson, F.; Hunt, C. A.; Szoka, F. C.; Vail, W. J.; Papahadjopoulos, D. Preparation of Liposomes of Defined Size Distribution by Extrusion through Polycarbonate Membranes. *Biochim. Biophys. Acta* **1979**, *557*, 9-23.

(39) Murray, D.; Hermida-Matsumoto, L.; Buser, C. A.; Tsang, J.; Sigal, C. T.; Ben-Tal, N.; Honig, B.; Resh, M. D.; McLaughlin, S. Electrostatics and the Membrane Association of Src: Theory and Experiment. *Biochemistry* **1998**, *37*, 2145-2159.

(40) The binding was weak in all three cases for the largest liposomes.

(41) Taylor, K. M. P.; Roseman, M. A. Effect of Cholesterol, Fatty Acyl Chain Composition, and Bilayer Curvature on the Interaction of Cytochrome B5 with Liposomes of Phosphatidylcholines. *Biochemistry* **1995**, *34*, 3841-3850.

(42) Ryu, E.-H.; Ellern, A.; Zhao, Y. *Tetrahedron* **2006**, *62*, 6808-6813.

CHAPTER 6

CONCLUSIONS

The work presented in this dissertation demonstrates how cooperatively enhanced receptors (CERs) and molecularly imprinted nanoparticles (MINPs) could be used for biomimetic molecular recognition. Moreover this dissertation illustrates a convenient method to synthesize protein-like sensors to detect curvature and the lipid composition of a membrane.

Rationally designed CERs displayed a high affinity and selectivity towards aromatic tris-amines, citric acid, and aromatic acids. The overall binding energy of CERs has contribution from the direct host-guest interactions and intra-host hydrophobic interactions. These receptors could be further investigated in recognition of branched amines and acids in order to get a library of affinities to compare and contrast with biological counterparts.

MINPs have demonstrated a rather simple way to imprint almost any sugar in water by benzoxaborole. The binding affinities of these nanoparticles were comparable to those of natural lectins. The template-specific MINPs showed 1:1 binding with the sugar and the main binding seemed to have happened in a hydrophobic pocket. The process can be further extended for glycolipid and nucleotide detection that are important in biology.

Conformationally flexible fluorescently labeled bischolate foldamers have reflected a biomimetic process in cell membrane. The NBD (7-nitrobenz-2-oxa-1, 3-diazole-4-yl) fluorophore connected to bischolate foldamer on the α-face has shown a higher affinity for curved lipid membranes. It is possible this bischolate foldamer could be used to understand lipid-peptide binding in membrane like environments.